ENGINEERING INTERACTIONS WITH DISTINCT ENTROPIC ATTRIBUTES: PREDETERMINING NANOPARTICLE ASSEMBLY PATHWAYS AND PROMOTING MIXING IN PHOTORESISTS

A Dissertation

Presented to the Faculty of the Graduate School

of Cornell University

In Partial Fulfillment of the Requirements for the Degree of

Doctor of Philosophy

by

Prajwal Bangalore Prakash

August 2025

ENGINEERING INTERACTIONS WITH DISTINCT ENTROPIC ATTRIBUTES: PREDETERMINING NANOPARTICLE ASSEMBLY PATHWAYS AND PROMOTING MIXING IN PHOTORESISTS

Prajwal Bangalore Prakash, Ph. D.

Cornell University 2025

Recent advances in synthesis of nanoparticles with anisotropic interactions and sequence-controlled oligomers with diverse chemistries have enabled the rational design of novel nanomaterials for applications in photonics, plasmonics, catalysis, and next-generation computer chips. Designing such functional nanomaterials requires fundamental understanding of the complex interplay between the entropic and enthalpic forces. Molecular simulations techniques have provided us with a tool to elucidate such complex behaviors in systems with intricate interactions and external stimuli; thus, revealing many nontrivial correlations between molecular design of the building block and the resulting complex morphologies having interesting properties. In this thesis, I will demonstrate how entropic forces, which are sometimes overlooked during design strategies, can be used to assemble structures with target properties, where in some scenarios we can pave an efficient kinetic pathway and in other cases we can promote compatibility and mixing homogeneity between the components.

The first part of the thesis examines my recent work on nanoparticle assembly kinetics, where we validate that mesophases with intermediate entropies, such as nematic, rotator, and micro-segregated phases can enhance crystallization rates from the disordered phase. Such design rules can be used to steer the assembly away from phenomena like polymorphism and vitrification. Further, I have detailed the computational and experimental efforts that we undertook to provide evidence of a novel “mosaic-like” mesophase orderings in the monolayer systems, that could potentially act as a switch between hexagonal and square structures. The last study describes the industrial collaborative project that was focused on developing a computational framework using atomistic models to rank polymer and salt chemistries with

enhanced homogeneity to improve the quality of the features printed through extreme ultraviolet light processing.

Overall, the findings in my work can guide future studies for ‘reverse engineering’ target structural properties by predicting suitable system design parameters and explore unique spectral responses of structures having complex morphologies.

BIOGRAPHICAL SKETCH

Prajwal Bangalore Prakash was born in Mysore, India in 1990. After completing his schooling in 2008, he moved to Mangalore for his undergraduate studies. In 2012, he completed his bachelor's degree in chemical engineering from the National Institute of Technology, Karnataka, Surathkal. After completing his undergraduate studies, he worked as a Research Assistant under Prof. Ganapthy Ayappa at Indian Institute of Science, Bangalore, where had the opportunity to work on continuum modeling of adsorbed natural gas systems, and soon developed a strong interest to work on problems focusing on understanding molecular level properties and phenomena. Pursuing this interest, he joined Prof. Fernando Escobedo's research group at Cornell University as a master's student and later transitioned to the PhD program in 2018. Under the guidance of Prof. Fernando Escobedo, he investigated phase behavior and transition kinetics of nanoparticle assembly and developed a computational framework to predict the aggregation tendency of salt in polymeric systems. After PhD, he will be joining IBM Research Lab as computational patterning research engineer.

To my family, friends, mentors, and collaborators who contributed to this work

ACKNOWLEDGMENTS

I express my heartfelt gratitude to my advisor, Prof. Fernando Escobedo, for his unwavering support and encouragement throughout my graduate studies at Cornell University. His guidance and patience while explaining complex concepts have helped me throughout my research work. Prof. Escobedo has consistently encouraged critical thinking and inspired me to explore new research ideas, which have been invaluable to my growth as a researcher. He has always made time to discuss my findings and provided valuable feedback which significantly improved my work. I have always looked forward to our insightful discussions. I really appreciate the stimulating environment he fosters in the research group, which allows students to share ideas freely. I admire his choice of research problems, and the rigorous and elegant approaches he employs to solve such complex problems. During the pandemic, he demonstrated exceptional dedication to his students' well-being. I am very fortunate to have had the opportunity to pursue my PhD under his guidance. I look forward to applying the valuable lessons learned on this journey to future research challenges and wish to continue working on many interesting research problems with Prof. Escobedo.

I am grateful to Prof. Abraham Duncan Stroock for helping me gain valuable insight into the experimental aspects of my research project and offering a holistic perspective. I appreciate him taking time to discuss my results and providing thoughtful feedback, despite his busy schedule as director at that time. Our informal interactions in the hallway were always comforting, inspiring and our conversations gave me new ideas and directions that I could explore in my work. I really appreciate his genuine interest in my research progress and well-being. I would also like to thank Prof. Tobias Hanrath for engaging discussions that broadened my understanding on how we could creatively design experiments that could provide evidence for the simulated structures and further extend it to observe other interesting phenomena. I appreciate his support and the opportunity to conduct experiments in his group. I also thank Prof. Itai Cohen, Prof. Chekesha Watson, and Prof. Susan Daniel for their guidance and giving me access to their equipment. Additionally, I thank Dr. Garry Bordonaro, Dr. Chris Alpha, and Dr. Beth Rhoades at the Cornell NanoScale Facility for all the help and valuable feedback on

particle fabrication.

I am also grateful to Dr. Unmukt Gupta for his excellent mentorship during the initial stages of my graduate studies. I would like to thank Dr. Vikram Thapar for all the insightful discussion and guidance, particularly helping me kickstart the nucleation project. I would also like to thank Prof. Carlos Avendano, University of Manchester, for his help with the Floppy Box algorithm. I also thank my research group members, Dr. Yangyang Sun, Mohammed Alshammasi, Dr. Abhishek Sharma, Dr. Ankita Mukhtyar, Dr. Mohammed Alhashim, Dr. Isabela Quintela Matos, Dr. Luis Nieves-Rosado, Dr. Mayank Misra, Manish Kumar Gupta for all the helpful discussions and support throughout my PhD. I appreciate all the help from Dr. Meera Ramaswamy, Dr. Eric Schwen, Dr. Jen-Yu Huang, Dr. Rohit Singh, and Dr. Han-Yuan Liu while conducting the experiments. I also thank Dr. Jay Gandhi, Dr. Vikram Thapar, Dr. Maria Teresa Reinoso-Pérez, Dr. Adarsh Ravi, Dr. Srinath Ranya, Dr. Radhika Ravikumar, and Udayshankar Menon for all their support and friendship, which created a stable community during my time in Ithaca. Lastly, I would like to acknowledge all the funding agencies that supported my PhD research work and the Cornell Computing Facility for managing computational resources.

TABLE OF CONTENTS

PREFACE

This dissertation highlights the competition between entropic and enthalpic forces while engineering nanoscale interactions during the design of functional nanomaterials. Recent advances in experimental techniques and computational models have allowed us to improve the bottom-up design strategy, where the interaction of the molecular building blocks can be tuned to obtain complex morphologies with unique properties.

In the context of bulk assembly of nanoparticles, a challenge still exists to optimize and control the crystallization pathways by circumventing routes that could potentially poison the growth of crystal nuclei from solutions. Advances in molecular simulation methods and computational capabilities have allowed us to investigate these complex kinetic pathways with a large-scale system size. Therefore, providing an understanding on how the competition between enthalpy and entropic contributions at the microscopic level can engender order at the macroscale. In pursuit of designing an efficient roadmap for the nanoparticle crystallization pathways, many previous studies have shown that hard-faceted particle shapes like perfect cubes, prolate gyrobifastigia, and truncated octahedra can readily access their corresponding crystal structures due to the presence of the partially ordered mesophases that act as a steppingstone during the crystallization process. However, the above conclusions are based on empirical evidence and there is a lack of understanding on how developing a particular ordered state, for e.g. rotator or nematic mesophases, can accelerate the crystallization process. Chapter 1 elucidates the role of metastable mesophases on the crystallization kinetics by quantifying the kinetic free energy barriers and transition rates using molecular simulations, and Markovian and transition state theory. Hence, providing direct proof validating the conjecture proposed in F. A. Escobedo, **Soft Matter**, 2014,10, 8388-8400, that mesophases provide a fast lane for crystallization.

The formation of mesophase ordering is not only constrained to the bulk system but can be accessed in both two-dimensional (2D) and quasi-2D systems that could have potential applications in thin film technology. In chapters 2 and 3, we used Monte Carlo simulations and experiments in a wedge-cell to address the question that whether a system can be designed to dynamically bridge the ubiquitous hexagonal and tetragonal lattice symmetries.

In Chapter 2, we revealed a re-entrant melting transition in a single component confined monolayer assembly, where an intervening disordered Flipped-Unflipped (FUN) phase, having mixture of both flipped and unflipped orientations, is sandwiched between a fourfold tetratic and sixfold triangular solid phases. Complementary experiments were conducted with photolithographically fabricated cylindrical microparticles confined in a wedge cell. I was fortunate to have had the opportunity to conduct experiments and publish our work in collaboration with Prof. Abraham Duncan Stroock, Prof. Tobias Hanrath, and Prof. Itai Cohen groups. The soft-repulsive wall model explored in this study exemplifies how tunable particle-wall interactions can provide an experimentally viable strategy to dynamically bridge the flipped and unflipped states. Our work with the hard and soft confinement model is also expected to guide future experimental and modeling efforts to control particle orientation behavior in monolayers using external forces other than slit confinement.

Chapter 3 is authored by me and Prof. Fernando Escobedo, where we report a novel mosaic state in a binary mixture system that manifests a non-homogenous packing that resembles patches having hexagonal order intermingled with other patches having square order. The dual characteristics of the mosaic state have distinct ordered structures that could potentially be leveraged for specialty applications with switchable hexagonal-square packings, e.g., to fabricate synthetic Chameleon skin, optical switches, and optical biosensors.

Overall, the structures reported in both 2D and quasi-2D systems arise from the balance between two competing entropic forces, namely packing entropy that favors like-particle contacts and mixing entropy favoring random contacts between the components, that allow for the coexistence of domains having distinct lattice symmetries.

In pursuit of downsizing the transistor components to a sub-10nm length scale, several experimental and computational efforts are focused on designing chemically amplified resists with a blend of ionic salt and an acid-sensitive polymer medium that have high molecular uniformity, and minimal stochastic defects. Chapter 4 is an attempt to quantify the stochastic defects present in the photoresist systems. It focuses on developing a computational framework using atomistic models to efficiently screen ionic photoacid generators and polymer photoresist chemistries with enhanced homogeneity (or higher mixing entropy) to improve the quality of the features created through extreme ultraviolet light processing. This work was carried out in collaboration with Intel.

The thesis is organized into self-contained chapters, which have been published or in the process of preparation for future publication in a peer-reviewed journal. Each chapter stands alone, with its own numbering for references, equations, figures, tables, and supplementary material.

CHAPTER 1: Mesophases as steppingstones to enhance crystallization kinetics in nanoparticle self-assembly

B. P. Prajwal[a] and Fernando Escobedo[a*]

[a] Robert Fredrick Smith School of Chemical and Biomolecular Engineering,

Cornell University, Ithaca, New York

Abstract

Manipulation of kinetic pathways is essential to self-assemble nanoparticle building blocks into complex ordered structures, as the formation of intermediate metastable states could either facilitate or hinder the crystallization of a target symmetry. Molecular simulations, and Markovian and transition state theory are used to validate our conjecture that intermediate mesophases with partial structural ordering can accelerate crystallization kinetics. Using representative models, it is shown that mesophases with intermediate entropies, such as nematic, rotator, and micro-segregated phases, enhance the overall crystallization rate. This enhancement occurs by effectively splitting a larger isotropic-to-crystal free energy barrier into two smaller barriers corresponding to isotropic-to-mesophase and mesophase-to-crystal transitions, with mesophase macrostates being more favorable than microscopic fluctuations. This effect depends on the interfacial energies between the isotropic, mesophase, and crystal which determine the barrier for the isotropic-to-crystal composite-cluster pathway. Our results illustrate the applicability of our conjecture, providing guidance to nanoparticle designs to achieve efficient crystallization pathways.

1. Introduction

Over the past decades, engineering molecular interactions of nanoparticle (NP) building blocks to control their bottom-up assembly into complex functional nanomaterials has been a focal point of many experimental and computational studies. These nanomaterials have attracted interest for diverse applications in devices used for information storage,[1–3] photonics,[4–7] sensors,[8–10] and plasmonics.[11,12] Despite the current synthetic capabilities to systematically fine-tune NP interactions for assembling them into targeted lattice symmetries,[13,14] a grand challenge remains to control and optimize the crystallization pathways from an isotropic dispersion to the crystalline structure, thereby, circumventing routes leading to undesirable kinetically trapped metastable states.

Observations from our previous studies[15,16] led us to conjecture that for hard-NP systems expected to form a crystal (C) upon gradual concentration of the isotropic (I) phase, the ordering transition occurred more readily if an intermediate mesophase (M) having global partial ordering preceded the fully crystalline phase. Such was the case for perfect cubes and truncated octahedra having M states like liquid crystal (M_{LC}) and plastic solid/rotator (M_R) phases, respectively.[15] In contrast, Gyrobifastigium (GBF) a shape that does not have a M and forms a space-filling ABCD type crystal (C_{ABCD}), tends to get trapped in a dense "glassy" state.[15] Similar observations apply to other oblate and prolate shapes,[17,18] where the particles able to form a M_{LC} more readily crystallized upon densification. Complementary to the above instances of entropy-driven self-assembly, recent investigations[19–21] have demonstrated that tuning the NP-NP energetic interactions can also lead to the formation of M intermediates that facilitate assembly of the C phase. For example, mixture of silicates and structure directing agents (SDAs)[22,23] have been found to mediate the nucleation of porous Zeolite crystal (C_Z) through a metastable double-gyroid mesophase (M_G). Similar strategies have been posited in various experimental and simulation models, for example, when investigating the crystallization of triblock Janus particles,[20] DNA-functionalized NPs,[29] and globular proteins,[30,31] revealing the presence of pre-existing amorphous and dense liquid macro-clusters that facilitate the growth of the stable crystal nucleus within them. The aforementioned examples provide empirical evidence that M acts as a steppingstone for a two-step crystallization process, lowering the I →

$M \rightarrow C$ transition free energy barriers, $\beta\Delta G^*$, as depicted in Figs. 1a and 1b, where $\beta = 1/k_bT$, k_b is Boltzmann's constant, T is temperature, and the degree of supersaturation, DSS, is the difference in chemical potential between I and C phases:

$$\text{DSS} = |\beta\Delta\mu_{IC}| = |\beta\mu_I - \beta\mu_C|, \quad (1)$$

Modulating the NP design parameters and DSS influences the characteristics of the M basin by varying stability, entropy (*S,* depictable as the basin's width or curvature radius), and its position along the reaction coordinate relative to the I and C basins (Figs. 1c to 1e). NP-NP directional binding interactions can be designed to favor the formation of certain crystalline motifs whereas entropic forces can favor structures that enhance motion along selected degrees of freedom, e.g., to lead to the emergence of M and faster two-step crystallization processes. However, there is an incomplete understanding of what makes the M state kinetically beneficial (as some intermediates could become kinetic traps) and a lack of direct quantification of any such benefit through, e.g., the estimation of $\beta\Delta G^*$and transition rates involving the I, M, and C phases. Note that while a simplified one-dimensional free-energy landscape like that in Fig. 1 provides a qualitative guide, a proper description of phase transitional pathways for most systems requires a multidimensional representation as exemplified later (in Figs. 2 and 5).

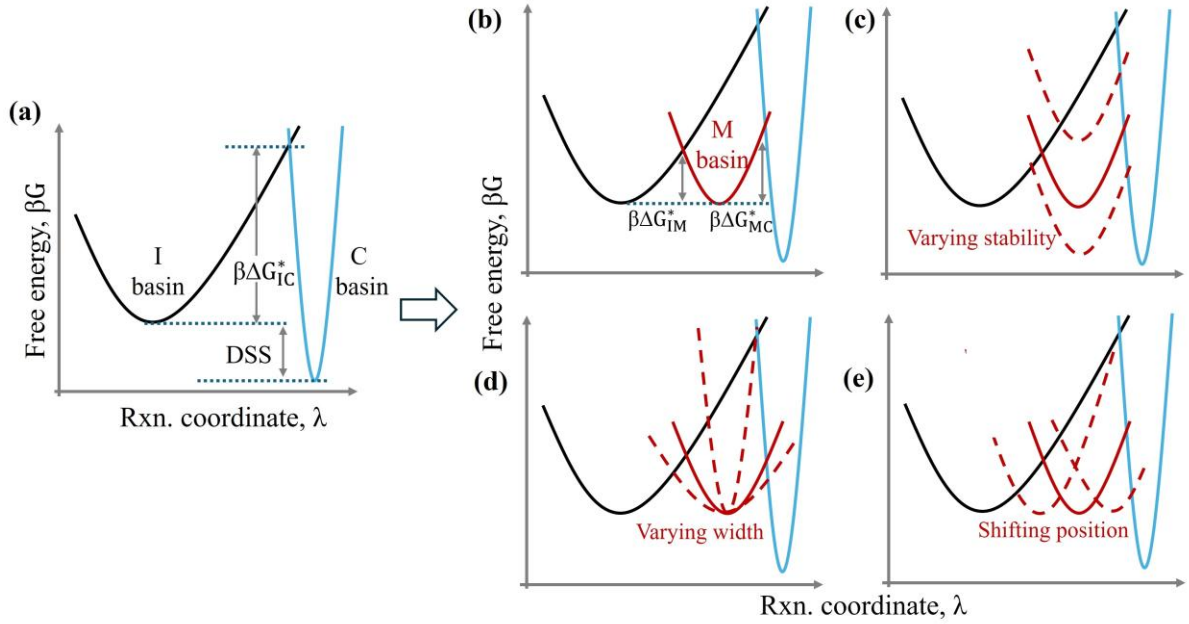

Figure 1| Free energy landscape features and kinetics. Qualitative free energy, βG profiles as a function of reaction coordinate, λ for I (black), C (blue), and M (red) phases. Basins depicting the phases are shown as parabolas where the well depth and width (or curvature radius) represents its G and basin entropy, *S,* respectively. A larger (or smaller) configurational *S* correlates to a wider (or narrower) basin in a 1D λ region since $S \sim -p(\lambda) \ln p(\lambda)$; where p is the probability distribution function of λ values for a given basin: $p(\lambda) \sim e^{-\beta G(\lambda)}$. The degree of supersaturation, DSS between I and C is kept constant. (a) and (b) illustrate rough estimation of kinetic barrier, $\beta\Delta G^*$ for I → C, I → M, and M → C transitions from the intersection of the corresponding basin branches. The presence of M (red solid curve) splits the I → C barriers into smaller I → M, and M → C barriers. As reference, the M basin is shown to have similar well depth as the I basin with its λ position and *S* (well-width) being intermediate between those of I and C. (c-e) Illustrate the effect on $\beta\Delta G^*$ due to the variations (depicted as dashed red curves) in the M basin's (c) vertical position, (d) width, and (e) lateral position.

To elucidate the role of M on the crystallization kinetics, we employed rigorous simulation techniques and theory to validate our previously proposed hypothesis[16] which henceforth will be referred to as our "conjecture". This conjecture posits that the presence of a M having macroscopic translational, orientational, or topological partial ordering like in M_{LC}, M_R, and M_G provides a *"fastlane"* for the I → C transition (Figs. 2). The validity of the above conjecture is expected to apply to various classes of systems having intermediate-ordered phases between I and C like in densified-amorphous,[21,24] polycrystalline,[19,25] and micro-segregated phases like the lamellar (M_{LAM}), cylinder,[26] and bicontinuous phases (like the M_G). The underlying

heuristic in the conjecture is that the crystallization rate should be enhanced when a high free energy nucleation barrier between I → C is "split" into two smaller barriers corresponding to I → M and M → C transitions (Figs. 1a to 1b). Hence, the M would act as a structural template that lowers the bulk and interfacial free energy to ease the nucleation of the crystal structure. This sequential formation of increasingly stable phases, illustrated in Fig. 2, is consistent with the heuristic Oswald's rule of stages[27,28] which states that the nucleating phase is not the most stable phase at the target conditions but rather the metastable phase closest in free energy to the parent phase.

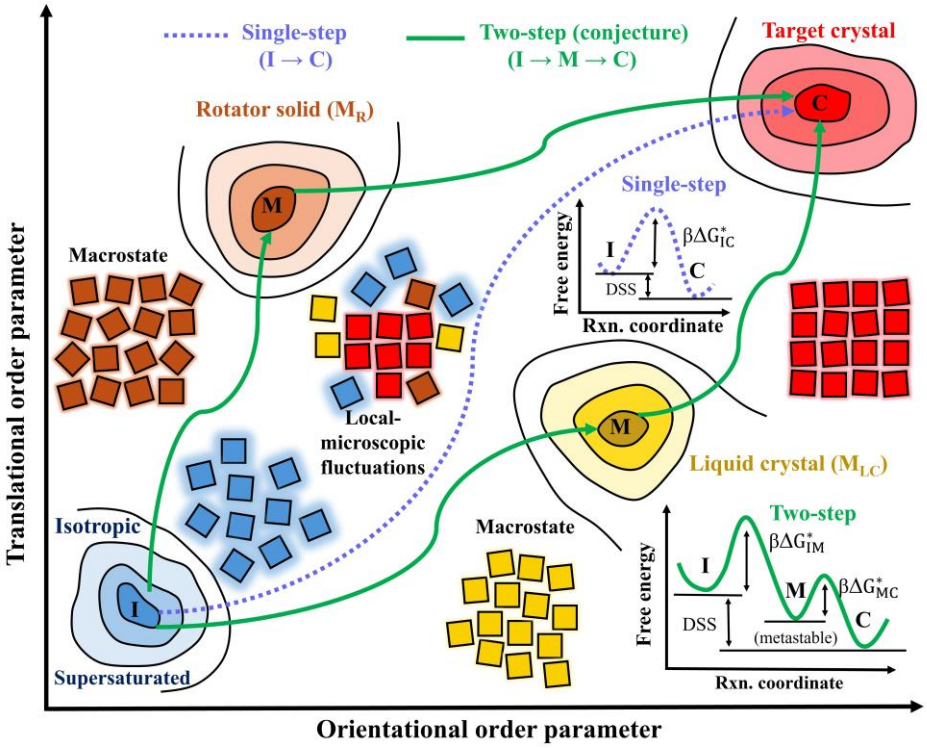

Figure 2| Illustration of free energy landscape, and nucleation barriers. 2D landscape using order parameters (OPs) that resolve the I, M, and C basins for NP systems in a single-step (blue dotted arrow) and two-step (green solid arrow) pathways toward crystallization. Cartoons with squares depict M state as being a local transient microstate or a macrostate *en route* to the C phase. The free energy barrier $\beta\Delta G^*_{IC}$ for I → C at a given DSS is split into two smaller barriers corresponding to I → M and M → C transitions with $\beta\Delta G^*_{IM}$ and $\beta\Delta G^*_{MC}$ barriers, respectively, where $\beta = 1/k_bT$. The 2D landscape can be adapted to represent the lamella/double-gyroid (M) and crystal lamella/Zeolite (C) structures by using suitable translational OPs as coordinates.

In this work, we chose to test our conjecture using both athermal and thermal NP model testbeds, namely, gyrobifastigia (GBF), Truncated cubes (TC), and binary coarse-grained mixtures that form distinct crystalline phases and, more crucially, exhibit different types of M intermediates (and associated $\mathrm{I} \rightarrow \mathrm{M} \rightarrow \mathrm{C}$ transition pathways). As indicated earlier, while regular hard GBFs did not spontaneously crystallize upon concentrating the I phase, recent computational work[17] has shown that by increasing the particles' aspect ratio, AR, an intermediate nematic mesophase (M_N) occurs before spontaneous formation of C_{ABCD} (a multilayered, space tessellating, body center tetragonal lattice similar to the Beta-Sn structure[32]). In contrast to this assembly route where orientational degrees of freedom freeze in M, the "octahedra-like" TC family exhibits a transition pathway where translational degrees of freedom first partially freeze to engender M_R having body centered cubic (BCC) order, which then transforms into a rhombohedral Bravais Minkowski crystal (C_{Mink}).[33] In this $\mathrm{M_R} \rightarrow \mathrm{C_{Mink}}$ transition the increase in orientational ordering is coupled with a slight shearing of the lattice from BCC to C_{Mink}. Thirdly, we investigated an AB mixture model which forms a lamella mesophase (M_{LAM}), with stacks of alternate disordered monolayers of A and B components, that transitions into a layered crystal (C_{LXA}). Lastly, we simulated a TS mixture of coarse-grained particles representing silica-like (T) and SDA (S) that was already alleged to conform with our conjecture where the M_G network directs the growth of C_Z. Overall, the above testbeds allow us to conveniently tune the geometric and interaction parameters to study the kinetics associated with both $\mathrm{I} \rightarrow \mathrm{C}$ and $\mathrm{I} \rightarrow \mathrm{M} \rightarrow \mathrm{C}$ transitions. While such a tunability is not generally feasible, it can be realized in some experimental systems by transient changes brought about by NP swelling,[34,35] external electric fields or chemical triggers,[36,37] so that after crystallization, the original target state of the NPs could be restored.

For our simulations, we selected GBFs with AR = 2.7 and TC with vertex truncation, $s = 0.90$ to be henceforth referred to as GBF27 and TC90, respectively (see Fig. 3). In the case of AB and TS mixtures, we selected the interaction parameters developed by Kumar et. al.,[26] and Bertolazzo et. al.,[22] respectively. While many other NP design parameter combinations and conditions could be used, these choices were made for convenience in computing the target quantities. Umbrella sampling (US) using standard and hybrid Monte Carlo simulations were

performed to estimate the free energy barriers, $\beta\Delta G^*$, to nucleate the critical cluster with size, n_c between I, M, and C phases. The size of the clusters, n, was detected using local translational, orientational (I_4), and nematic (P_2) order parameters (OP), while global translational and orientational OPs were used to identify the spontaneous transition between the phases of interest.[15,38–40] Using the predicted $\beta\Delta G^*$ values, we estimated the speed-up factor, S_{up}, defined as the ratio of the rate of crystallization of the two-step process, $k_{I\to M\to C}$, to the single-step transition, $k_{I\to C}$ by using our theoretical rate expression [see equation (8) in Methods Section] derived by adopting a Markovian framework for a process undergoing a serial transition among I, M, and C states; values of $S_{up} > 1$ would be consistent with our conjecture. We also estimated transition rate constants as the reciprocal mean first-passage time numerically calculated from the Fokker-Planck equation applied to the nucleation free-energy curves. More information on simulation model parameters, protocols, and details on OPs and DSS calculations can be found in the Methods Section and supplementary information (SI).

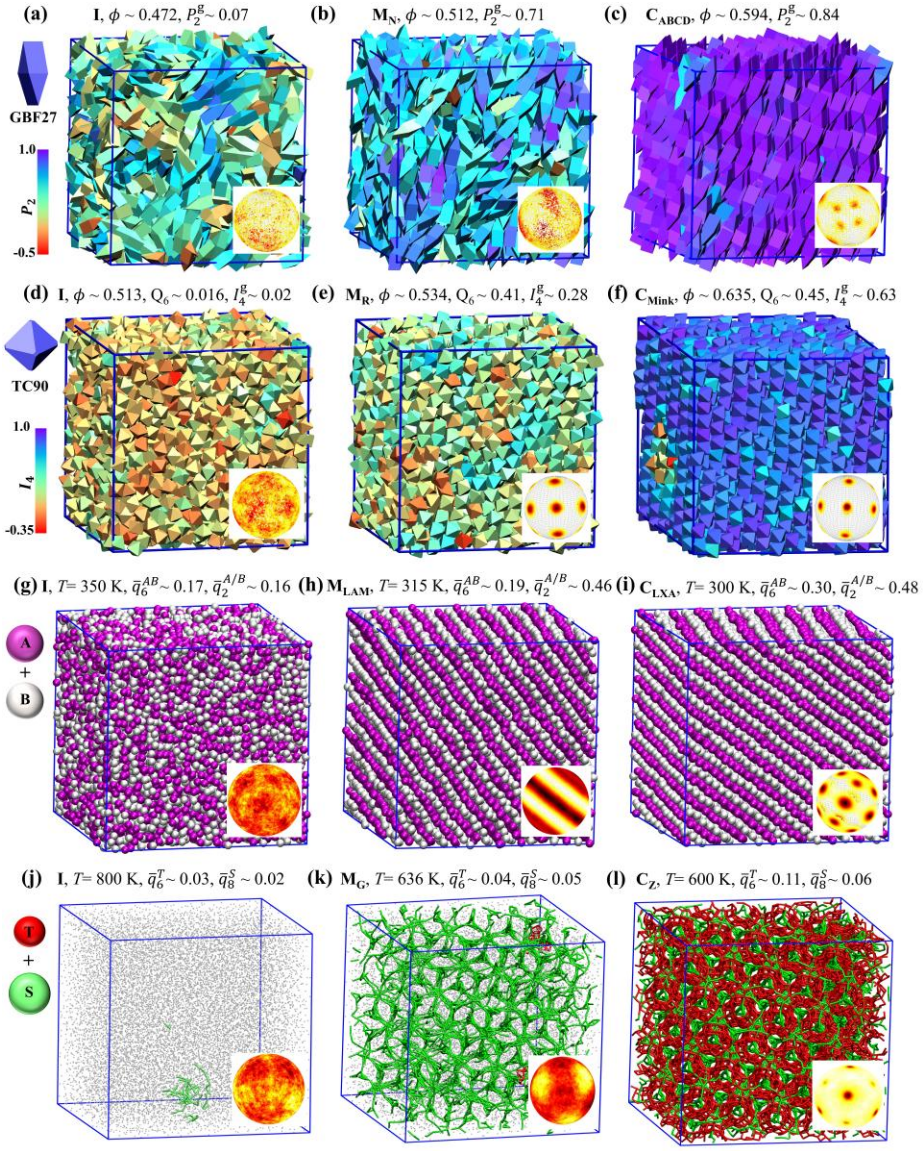

Figure 3| Simulation snapshots for two-step transition assembly of GBF27, TC90, AB, and TS models. Testbeds undergoing two-step transitions: (a-c) I → M_N → C_{ABCD} for prolate gyrobifastigium GBF27, (d-f) I → M_R → C_{Mink} for truncated cubes TC90, (g-i) I → M_{LAM} → C_{LXA} for AB mixture, and (j-k) I → M_G → C_Z for TS mixture of silicates (T) and structure directing agent (S). Packing fraction, ϕ, Temperature, T (K), and relevant global order parameters (OP) for each phase are shown. (a-f) Particles are colored based on local P_2 or I_4 OP values as indicated by color bars. (g-i) Assembly of A (magenta) and B (white) components showing disordered and crystalline lamella structures upon I phase cooling. (j-l) T and S particles are colored based on amorphous (grey), double-gyroid (green), and Zeolite (red) order. (Inset) Distribution of the bond unit vectors with darker red regions showing higher density of points on the sphere.

2. Results

2.1 Phase behavior and characteristics of I, M, and C phases

The equation of state and metrics of the relative stability between the I, M, and C phases for GBF, TC, AB, and TS models, are detailed in Sec. IV of the SI. Our calculations show that all M phases have entropy values, S_{M}, intermediate between those of the I and C phases (see Table S3 and Fig. S11), consistent with intermediate structural ordering, as corroborated by the OPs. For GBF27, Figures 3a to 3c show representative snapshots along with the global average packing fraction, ϕ and P_2^{g} values estimated for the I, $\mathrm{M_N}$, and $\mathrm{C_{ABCD}}$ phases obtained from unbiased simulations. As a visual guide for changes in ordering, we colored the particles based on their local orientational order and plotted the density scatter of the unit bond vectors (BV) connecting a particle and its neighbors (see Sec. IIIB3 in the SI for more details on OP color scheme). Movie S1 shows the spontaneous $\mathrm{I} \rightarrow \mathrm{M_N} \rightarrow \mathrm{C_{ABCD}}$ transition tracked by local orientational order upon compressing the supersaturated I phase. The color map of Fig. 3a also shows the local alignment of GBFs along the long axis (also shown using the distribution in Fig. S9). This reveals that microscopic pre-nucleation motifs present in I act as potential loci for the formation of $\mathrm{M_N}$. The particle alignment in $\mathrm{M_N}$ is stronger than in I but weaker than in $\mathrm{C_{ABCD}}$ (Figs. 3b and 3c). In $\mathrm{M_N}$, the local regions of translationally ordered BV induce facet-facet contacts between already aligned particles that facilitate the crystallization into $\mathrm{C_{ABCD}}$.

For TC90, the I phase showed transient, translationally ordered $\mathrm{M_R}$-like motifs as revealed by dense but diffused regions in the BV plot (Fig. 3d). $\mathrm{M_R}$ gained global translational order upon compression attaining $\mathrm{Q_6} \sim 0.41$ (close to the ideal BCC signature of 0.511) and showed distinct BCC peaks in the BV plot (Fig. 3e). Additionally, $\mathrm{M_R}$ has weak global orientational ordering (I_4^{g}) and small grains of orientationally aligned particles as detected by the local orientational OP. During the $\mathrm{M_R} \rightarrow \mathrm{C_{Mink}}$ transition, the particles give up their rotational degrees of freedom to pack into the $\mathrm{C_{Mink}}$ lattice with high $\mathrm{Q_6}$ and I_4^{g} values (see Fig. 3f and Movie S2 with particles color-coded by local orientational OP).

For the AB mixture, Figures 3g to 3i illustrate the $\mathrm{I} \rightarrow \mathrm{M_{LAM}} \rightarrow \mathrm{C_{LXA}}$ transitions observed during cooling. The translational ordering is detected using average bond-order parameters, $\bar{q}_l$

(where l= 2, 6, or 8). M_{LAM} has high $\bar{q}_2$ value for each component, indicating layering of A and B particles, while its low $\bar{q}_6$ and diffused BV plot for all particles suggests weak intralayer and interlayer translational ordering of components. Upon further cooling, the particles gain translational order and transition into the C_{LXA} phase.

For the TS model, Figures 3j to 3l show the $I \rightarrow M_G \rightarrow C_Z$ transitions upon cooling. The M_G network is characterized by high $\bar{q}_8$ of S particles and the ordering of T particles in C_Z is indicated by high $\bar{q}_6$ and distinct peaks in the BV plot. M_G is an unusual mesophase in that the ordering occurs in only one of the components (S); indeed, the T particles are disordered in the M_G porous structure while having slightly higher local density than the I phase (Figs. 3k and S6a). At low temperatures, the C_Z phase is stable, where the T particles order into the zeolite structure while the S particles remain mobile in the M_G network (Figs. 3l and S6e).

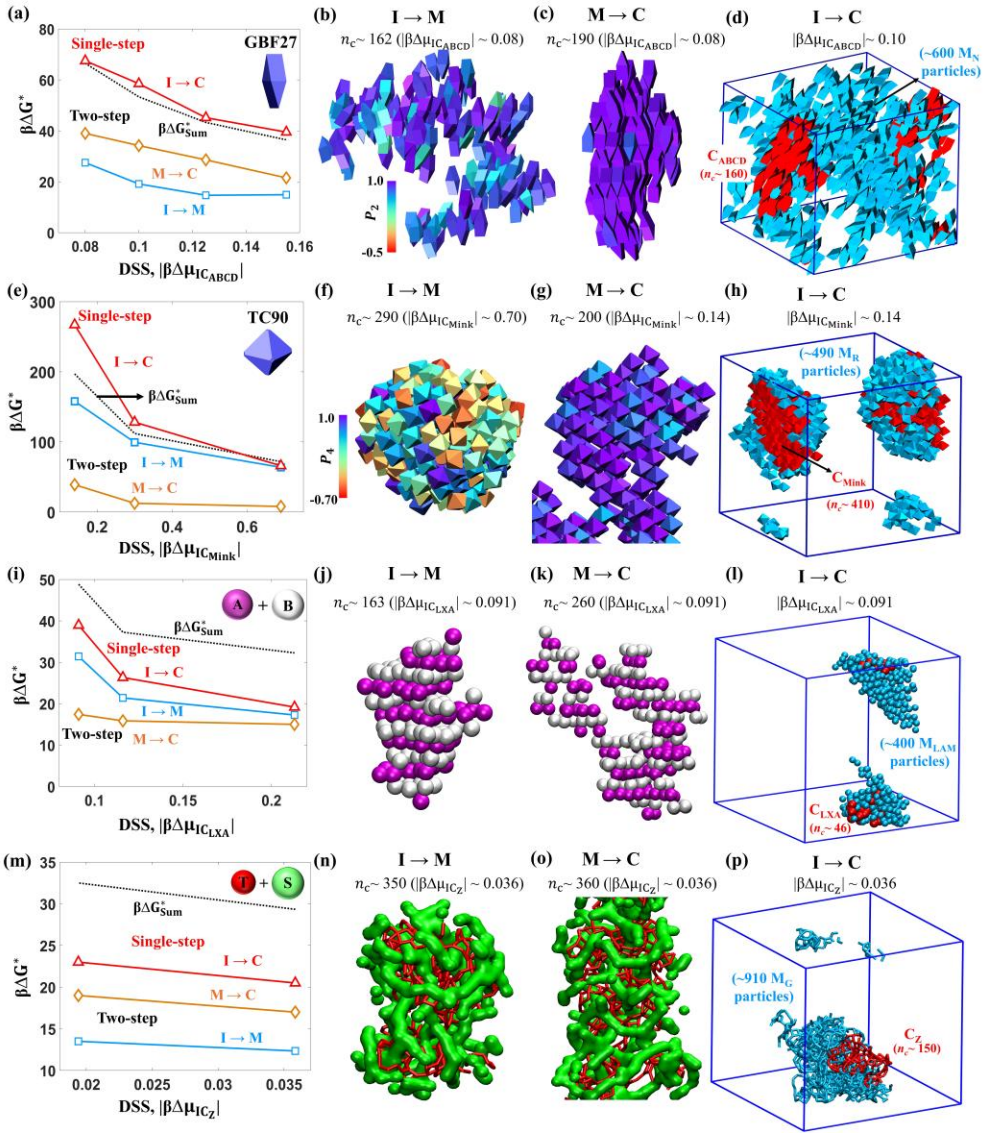

Figure 4| Nucleation free energy barriers and near-critical nuclei morphologies. (a, e, i, m) Free energy barriers, $\beta\Delta G^*$, estimated at different DSS for GBF27, TC90, AB, and TS models during single-step (I → C) and two-step (I → M and M → C) transitions. (Black dashed line) $\beta\Delta G^*_{Sum}$ is the sum of I → M and M → C barriers. (b-c/f-g/j-k/n-o) Simulated near-critical nuclei of M in I → M and of C for M → C for GBF (b)-(c), TC90 (f)-(g), AB mixture (j)-(k), and TS model (n)-(o). The critical nucleus size, n_c, and the corresponding DSS values are shown, with particles colored based on P_2 (b-c) and P_4 (f-g) OP values as per the color side bars. The corresponding M and C nuclei formed by (j, k) A (magenta) and B (white), and (n,o) T (red) and neighboring S (green) particles are shown. (d, h, l, p) Composite cluster pathway consisting of C nuclei (red) surrounded by clusters of M-like particles (cyan) formed during single-step I → C transition. I phase particles are not shown for clarity.

2.2 M lowers the crystallization barrier

Figure 4 shows the variation in $\beta\Delta G^*$ at different DSS (Eq. 1) for GBF27, TC90, AB, and TS systems undergoing a $I \rightarrow C$ and $I \rightarrow M \rightarrow C$ transitions. The complete $\beta\Delta G^*$ profiles as a function of nucleus size *n* for different transitions and DSS are shown in Figs. S12 to S20.

For GBF27 (Figs. 4b-4d), we observe that the barrier associated with gaining orientational ordering in $I \rightarrow M$ is ~28% lower than that for gaining translational ordering in $M \rightarrow C$, and the latter being ~55-65% lower than that for the $I \rightarrow C$ for the simulated DSS, hence providing support our conjecture (Fig. 4a). For $I \rightarrow M$, we find a loosely packed nematic nucleus with grains having high and intermediate particle alignment with respect to a global director, whereas for $M \rightarrow C$ and $I \rightarrow C$ we observe a compact elongated ABCD crystal nucleus having a distinct solid-nematic interface (see Figs. 4b to 4d and Sec. IIIB3 in the SI for OP color scheme). For comparison, we also estimated the single-step crystallization barriers for GBFs with AR = 2.6 (denoted GBF26) where M_N does not occur spontaneously; the results are discussed in Sec. VB in the SI.

For TC90 (Figs. 4e-4g), we estimated that the translational ordering barrier for $I \rightarrow M$ is about 4-8 times higher than that for rotational ordering attained during $M \rightarrow C$ transition. At low DSS, $\beta\Delta G^*_{I\rightarrow C} \sim 1.7\ \beta\Delta G^*_{I\rightarrow M}$, in line with our conjecture, whereas for high DSS values, the $I \rightarrow M$ and $I \rightarrow C$ transitions exhibit similar barriers (Fig. 4e), indicative of comparable kinetics. At these conditions, M is nearly unstable (see Fig. S10b) and the low $M \rightarrow C$ barriers indicate a spinodal-like transition. Figure 4f shows a compact M nucleus with no orientational order with respect to a global director, while figure 4g reveals a C cluster having orientationally aligned particles forming a central core with sparse branches.

For the AB model (Figs. 4i-4k), the $I \rightarrow M$ barrier associated with layering of particles is 40-80% larger than the $M \rightarrow C$ barrier, where the particles within each layer are crystallized (Fig. 4i). For all the simulated DSS, $\beta\Delta G^*_{I\rightarrow C} > \beta\Delta G^*_{I\rightarrow M}$, conforming with our conjecture. We observe compact elongated M and sparse C cluster morphologies during $I \rightarrow M$ (Fig, 4j) and $I \rightarrow C$ (Fig. 4k) transitions. At high DSS where M is nearly unstable (see Fig. S10c), the trends are similar to those for TC90 where the barriers between $I \rightarrow M$ and $I \rightarrow C$ become comparable.

For the TS model, Figs. 4m-4o show results that, as purported,[22] are consistent with our conjecture, but the $I \rightarrow C$ barrier is only about 3-4k_bT higher than $M \rightarrow C$ barrier, suggesting

that the single-step I → C transition could be favorable for larger DSS. For the DSS conditions examined, the barrier associated with the formation of M network for I → M transition is ~5-6k_bT smaller than the barrier for forming M → C nucleus (Fig. 4m). Figures 4n and 4o illustrate the near-critical cluster morphologies depicting the M and C nuclei with disordered and ordered T particles during I → M and M → C transitions, respectively.

The single step $\beta\Delta G^*_{I\rightarrow C}$ can be generally expressed as,

$$\beta\Delta G^*_{I\rightarrow C} = \beta\Delta G^*_{Sum} + \beta\Delta G^*_{IMC}, \quad (2)$$

where $\beta\Delta G^*_{Sum}$ is the sum of I → M and M → C barriers with near-critical cluster sizes formed at their respective DSS:

$$\beta\Delta G^*_{Sum} = \beta\Delta G^*_{I\rightarrow M} + \beta\Delta G^*_{M\rightarrow C}, \quad (3)$$

and $\beta\Delta G^*_{IMC}$ is a correction term for non-additivity. Interestingly, our simulations find that for all systems and conditions studied, the growth of the C nucleus during I → C transition occurs via a composite cluster pathway, where it is largely enclosed by a local microscopic M domain (see Fig. 4). In such a scenario, the composite-cluster theory predicts that[41,42]

$$\beta\Delta G^*_{IMC} = 4\pi R^2 \gamma_{eff}\, e^{-(R-r)/\xi} \quad (4)$$

which accounts for the interaction range between I-M and M-C interfaces formed by the local M domain; here, R and r are the radii of the composite and crystalline cluster, respectively, ξ is the range of interaction, and γ_{eff} is the spreading parameter, which is related to the interfacial surface energies, γ, between phase pairs,

$$\gamma_{eff} = \gamma_{IC} - \gamma_{IM} - \gamma_{MC}, \quad (5)$$

For the simulated DSS range, our results encompass cases where $\beta\Delta G^*_{I\rightarrow C}$ is equal to, greater than, and less than $\beta\Delta G^*_{Sum}$ as shown by the dashed black lines in the plots of Fig. 4. For GBF27, $\beta\Delta G^*_{I\rightarrow C_{ABCD}} \sim \beta\Delta G^*_{Sum}$ indicating that $\gamma_{eff} \sim 0$ and since $\gamma_{IM_N} < \gamma_{M_N C_{ABCD}}$ (as predicted by classical nucleation theory, CNT, in Fig. S22a), it follows that $\gamma_{IM_N} < \gamma_{M_N C_{ABCD}} < \gamma_{IC_{ABCD}}$. Since interfaces with the lowest γ will tend to be favored when I, M, and C phases are present, the M_N domains would not be localized around the GBF27 crystal nucleus but will extensively infiltrate the I phase, as seen in Fig. 4d. For TC90, $\beta\Delta G^*_{I\rightarrow C_{Mink}} > \beta\Delta G^*_{Sum}$ and thus $\gamma_{eff} > 0$ at low DSS, and since $\gamma_{IM_R} > \gamma_{M_R C_{Mink}}$(see Fig. S22b), it follows that $\gamma_{M_R C_{Mink}} < \gamma_{IM_R} < \gamma_{IC_{Mink}}$. Therefore, the lower γ between M_R and C_{Mink} will favor the wetting of a compact C_{Mink}

nucleus by a tight, thin layer of M_R particles as shown in Fig. 4h (similar to the case of NaCl nucleation from solution where the solid cluster is wetted by amorphous domains[41]). For the AB and TS models, we find that $\beta\Delta G^*_{I\to C} < \beta\Delta G^*_{Sum}$, implying $\gamma_{eff} < 0$, and since $\gamma_{MC} < \gamma_{IM}$ (as per Turnbull's[43] correlation, see Table S4), then γ_{IC} may or may not be larger than γ_{MC} or γ_{IM} (i.e. $\gamma_{IC}, \gamma_{MC} < \gamma_{IM}$). Unlike the TC90 case, the M cluster may not uniformly spread around a C nucleus partially wet by I, but rather grow uncorrelated with the C nucleus size, as seen in Figs. 4l and 4p. The growth of the C nucleus of different sizes is shown in the SI Sec. V. Overall, our results suggest that although the concurrent local M fluctuations aid in the growth of C nuclei, it is the serial nature of the I → M and M → C macroscopic events (as pertinent to our conjecture) that provides the most unambiguous kinetic benefit as supported by our theoretical analysis encapsulated by Eq. (8) below.

Model	$\lvert\beta\Delta\mu_{IC}\rvert$	$S_{up}=\frac{k_{I\to M\to C}}{k_{I\to C}}$	γ_{eff}	$D_o^{-1}k'_{I\to M\to C}$	$D_o^{-1}k'_{I\to C}$
GBF27	0.08-0.16	1.2×10^{12} - 3.0×10^{6}	~ 0	8.5×10^{-19}-2.0×10^{-11}	1.0×10^{-31}-2.3×10^{-20}
TC90	0.14-0.70	2.2×10^{47}- 1.0×10^{1}	> 0	2.1×10^{-52}-5.2×10^{-30}	8.6×10^{-118}-2.1×10^{-30}
AB	0.09-0.21	1.0×10^{3}- 3.3×10^{1}	< 0	3.1×10^{-15}-1.0×10^{-9}	3.7×10^{-18}-2.0×10^{-9}
TS	0.019-0.036	3.0×10^{1}- 1.6×10^{1}	< 0	4.2×10^{-11}-1.5×10^{-10}	1.3×10^{-12}-1.0×10^{-11}

Table 1| Speed-up, S_{up} ratios for GBF27, TC90, AB, and TS models. Comparison of rates, k and k' associated with a single I → C and two-step I → M → C transitions at different DSS ranges. Predicted range of the spreading parameter, γ_{eff} for different models are indicated. D_o is the constant rate of attachment of particles to the cluster.

2.3 Transition speed-up for two-step process

Our theoretical expression, embodied by Eq. (8) comparing the single-step and two-step rates, predicts that the two-step transition rate will be larger as long as $\beta\Delta G^*_{I\to C} > \max(\beta\Delta G^*_{I\to M}, \beta\Delta G^*_{M\to C})$, provided that the exponential factor (in CNT-like rate equations) is the dominant contributor to the transition rate values (i.e., large $\beta\Delta G^*$'s, small DSS). We also estimated the relative transition rates, k' using Eq. (10) to capture the effect of the entire nucleation free-energy profiles (and not just $\beta\Delta G^*$). Table 1 shows the variation in the speed-up factor, $S_{up} = \frac{k_{I\to M\to C}}{k_{I\to C}}$ and k' between single-step and two-step transitions at different DSS conditions. Qualitatively, the trends observed in S_{up} values are comparable to the ratios in k' between transitions. In general, one would expect S_{up} to increase when: (i) the difference, $\Delta^* = \beta\Delta G^*_{I\to C} - \max(\beta\Delta G^*_{I\to M}, \beta\Delta G^*_{M\to C})$ is larger, or, (ii) $\beta\Delta G^*_{IMC}$ (from Eq. (2)) is larger, which implies (as per Eq. (4)) that (iii) γ_{eff} is more positive. For GBF27, the $I \to C$ barrier splitting results in a $S_{up} \sim 10^{12}$ at low DSS where $\Delta^* \approx 28.5k_bT$, whereas S_{up} drops to $\sim 10^6$ for a larger DSS where $\Delta^* \approx 16k_bT$. For DSS ~ 0.1, we estimated that the kinetic prefactors have a minimal effect on S_{up} since their magnitudes for all the transitions were similar (see Sec. IIB in the SI). For TC90, we estimated a very high S_{up} value $\sim 10^{47}$ for low DSS due to the large $\Delta^* \approx 110k_bT$; however, S_{up} decreases very quickly with increasing DSS, reaching a value of $S_{up} \sim 10$ where $\Delta^* \approx 3k_bT$. For the AB and TS models, the values corresponding to S_{up} and the ratio in k' are smaller: at low DSS they range from 10^3 to 10 , suggesting that the difference is due to the smaller $\Delta^* \approx$ 8-3k_bT; and at high DSS, $S_{up} \sim 10$ with comparable k' (similar to TC90) indicating that the single-step pathway competes with the two-step transition. Overall, the trends predicted for S_{up} and γ_{eff} can be relevant to other systems exhibiting transition intermediates, e.g., for the TS-λ Zeolite model "B" proposed by Bertolazzo et. al.[22] we estimate $S_{up} \sim 10^7$ for conditions where $\gamma_{eff} \geq 0$.

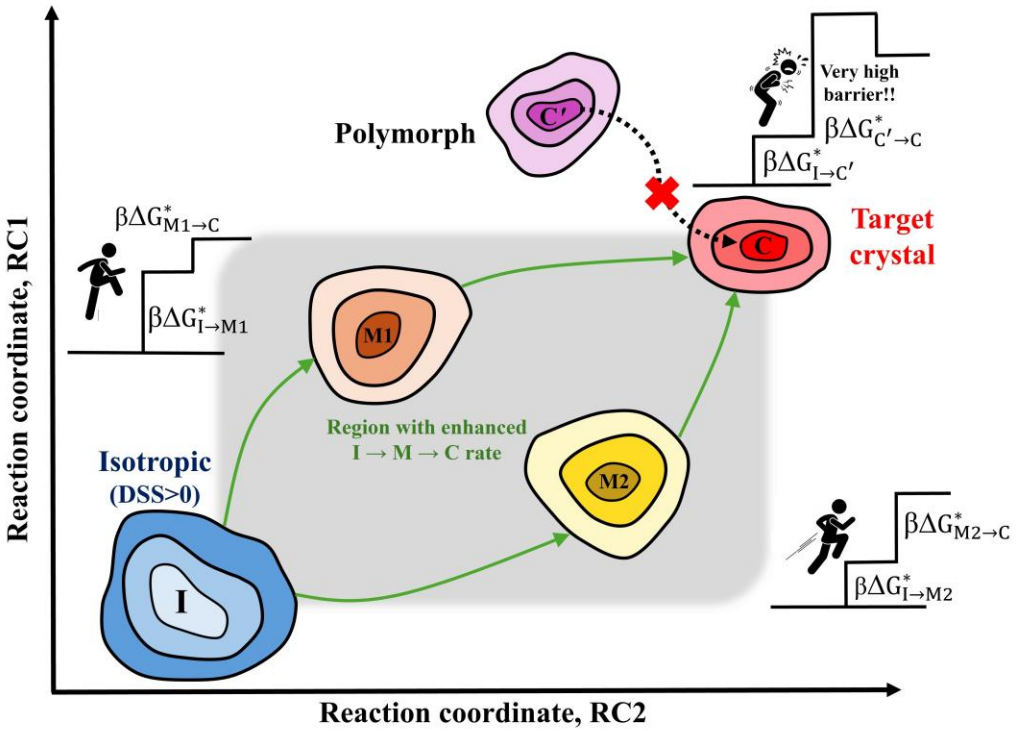

Figure 5| Schematic roadmap of 2D free energy landscape and pathways between I and target C phase. The gray region represents the section of landscape where a mesophase M basin can enhance the crystallization rate. M1 and M2 have distinct characteristics defined by the reaction coordinates (RC). M1/M2 would depict a rotator solid/nematic phase if RC1 and RC2 correspond to translational and orientational OPs, respectively. If C is a porous Zeolite/ordered lamella crystal, the double-gyroid/lamella mesophase could be represented by M2 with translational OPs defining RC1 and RC2. The roadmap shows cartoons for distinct scenarios where the kinetic barrier, $\beta\Delta G^*_{I\to M1}$ (or $\beta\Delta G^*_{I\to M2}$) is higher (or lower) than $\beta\Delta G^*_{M1\to C}$ (or $\beta\Delta G^*_{M2\to C}$). C′ correspond to a polymorph with very large $\beta\Delta G^*_{C'\to C}$ transition barrier.

3. Discussion

Overall, our simulations and theoretical framework predict that the crystallization rate from the supersaturated I phase is significantly enhanced when the system undergoes a two-step global transition with M having an intermediate structural and entropic order between the I and C phases, thus providing a quantitative validation of our conjecture. Our results indicate that the effective interfacial energy between I, M, and C phases influences the single-step $\mathrm{I} \rightarrow \mathrm{C}$ crystallization kinetics, thus providing a potential guide for designing NPs that leverage two-step $\mathrm{I} \rightarrow \mathrm{M} \rightarrow \mathrm{C}$ process.

The kinetic benefit of a two-step $\mathrm{I} \rightarrow \mathrm{M} \rightarrow \mathrm{C}$ crystallization route is more predictable when M occurs as a macrostate (at low DSS) rather than localized transient microscopic fluctuations (at high DSS). This relates to the topology of the free energy landscape, e.g., the relative depth of M basin and the pathways connecting the basins. The optimal crystallization pathway, whether through microscopic or macroscopic M intermediates, reflects the time scale of its occurrence, which depends on DSS and NP model parameters that controls the depth and relative location of the I, M, and C free energy wells in the OP landscape (Figs. 1b to 1e). Figuratively, the barriers involved in the $\mathrm{I} \rightarrow \mathrm{M} \rightarrow \mathrm{C}$ process will need to climbed more times if M is confined to be transient microscopic fluctuations compared to the two-step process where M is a macroscopic state or forms a large enough domain to fully encompass critical sized nuclei of the C phase, with the two barriers thus being crossed serially (as reflected in our treatment in Eqs. 7-8).

Importantly, if a system is designed to engender a M state with an intermediate macroscopic entropy or OP values between I and C phases, then the $\mathrm{I} \rightarrow \mathrm{C}$ barrier is likely to be broken down into smaller $\mathrm{I} \rightarrow \mathrm{M}$ and $\mathrm{M} \rightarrow \mathrm{C}$ barriers. Generally, the $\max(\beta\Delta G^{*}_{\mathrm{IM}}, \beta\Delta G^{*}_{\mathrm{MC}})$ is reduced when the metastable M basin is positioned ~*halfway* between I and C basins along a *good* reaction coordinate with a well-depth lower than I and an entropy larger than C. In our simulations, we kept DSS constant in probing the different barriers to allow direct comparisons; in practice, however, once the M state is reached, one could change the DSS (through, e.g., changes in pressure or temperature) to expedite its transition toward the C phase. Such an approach would of course be in order if M is first stable for $\mathrm{I} \rightarrow \mathrm{M}$ at DSS_1 and then M is metastable for $\mathrm{M} \rightarrow \mathrm{C}$ at DSS_2.

In the examples examined, we show that the dimensionless ratio, $\beta\Delta G^*_{I\to M}/\beta\Delta G^*_{M\to C} < 1$ for GBF27 and TS models, whereas it is > 1 for TC90 and AB models. This indicates that the barrier to nucleate M_N and M_G order from the I phase is lower than that to nucleate a translationally ordered M_R and M_{LAM} phases, suggesting that a wider free energy well associated with larger entropy in M_N and M_G would be kinetically beneficial during crystallization (as depicted in Fig. 1d).[15]

Many systems that undergo $I \to C$ ordering transitions are known to be able to access a competing ordered phase, say C′, which could in principle act as a productive intermediary as the M phase described here (Fig. 5). However, the known problem of polymorph selection, e.g., suggests that such C′ phases can act more as a *poisonous* than a *catalytic* pathway to the attainment of the target C phase by trapping the system in a deep (metastable) well. Hence the key question is: What heuristics can help identify a putative M as a favorable kinetic intermediate for attaining the C phase? Generally, the M should not be a fully ordered crystal or else the $M \to C$ transition would require a costly process of destruction and reconstruction of crystalline order. But even a partially ordered M may not necessarily lie in a productive pathway toward the target C phase; e.g., a recent kinetic study for TCs with $s = 0.527$ revealed the formation of an "orientationally" salt-like polymorph that sidetracks the rotator → crystal nucleation pathway.[47] In the case of longer rods, the formation of a multilayered stacked smectic phase can be suppressed by nematic spinodal instabilities.[48] A qualitative heuristic for a productive M is that it should attain part of the order that the I phase requires to form C, without incurring in any ordering that steers it away from the C basin. Quantitatively, this could be ascertained (without performing expensive free energy calculations) by the analysis of appropriate OPs to track how different types of structural order evolve as the system goes from $I \to M \to C$ as depicted in Fig. 5. Crucially, this may require the availability of multiple high-quality OPs to resolve the structural relations between I, M, and C. A complementary and cheaper guide to attain $S_{up} > 1$ is to look for designs with a more positive spreading parameter γ_{eff}. Our conjecture, embodying a more specialized rule that complements the widely employed Ostwald's rule of stages, should be tested in a broader class of systems[44–46] that can engender an intermediate M *en route* to the C phase, whose basin position may be tuned to lie in a region in the OP landscape that enhances the crystallization rate (as depicted in Figs. 1 and 5).

Online Methods

a. Theoretical rate estimation

Consider a Markovian process with sequential transitions among states I (essentially reflective state), M, and C (absorbing state) such that going from I to C involves a two-step process with an intermediate metastable M state (see Figs. 1a and 1b). The mean first passage time $\tau_{\mathrm{I}\to\mathrm{M}\to\mathrm{C}}$ from I to C states through the M intermediate can be obtained from:

$$\tau_{\mathrm{I}\to\mathrm{M}\to\mathrm{C}} = \tau_{\mathrm{I}} + \langle \text{time for M} \to \text{I} \to \text{M events} \rangle + \tau_{\mathrm{M}\to\mathrm{C}} \qquad (6)$$

where τ_{I} is the mean first escape time from state I, $\tau_{\mathrm{M}\to\mathrm{C}}$ is the mean first passage time from M to C, and the 2nd term is the average time associated with all possible recurrent $\mathrm{M} \to \mathrm{I} \to \mathrm{M}$ transitions (before the $\mathrm{M} \to \mathrm{C}$ transition happens). All these terms can be evaluated in terms of the single-step transition rates $k_{i\to j}$ as shown in SI Sec. IIA. The total rate, $k_{\mathrm{I}\to\mathrm{M}\to\mathrm{C}}$ can be described as the reciprocal of $\tau_{\mathrm{I}\to\mathrm{M}\to\mathrm{C}}$ with the result given as,

$$k_{\mathrm{I}\to\mathrm{M}\to\mathrm{C}} = \frac{k_{\mathrm{I}\to\mathrm{M}} \times k_{\mathrm{M}\to\mathrm{C}}}{[k_{\mathrm{I}\to\mathrm{M}} + k_{\mathrm{M}\to\mathrm{C}} + k_{\mathrm{M}\to\mathrm{I}}]} \qquad (7)$$

where $k_{i\to j}$ is the individual transition probability per unit time to go from *i* to *j* (and *i*, *j* = I, M, or C). According to CNT, the transition rate, $k_{i\to j} \propto \exp(-\beta\Delta \mathrm{G}^*_{i\to j})$ where $\beta\Delta \mathrm{G}^*_{i\to j}$ is the free energy barrier associated with the first-order transition from state *i* to *j* for a given degree of supersaturation, $|\beta\Delta\mu_{\mathrm{IC}}|$ (see Fig. S3). Assuming the pre-exponential factors in the transition rates have a similar order of magnitude and their differences are small compared to those of the exponential terms (which are often used as a surrogate rate constants), we can express Eq. 7 as,

$$k_{\mathrm{I}\to\mathrm{M}\to\mathrm{C}} \approx \frac{\exp(-\beta(\Delta \mathrm{G}^*_{\mathrm{I}\to\mathrm{M}} - \Delta \mathrm{G}^*_{\mathrm{M}\to\mathrm{C}}))}{[\exp(-\beta\Delta \mathrm{G}^*_{\mathrm{I}\to\mathrm{M}}) + \exp(-\beta\Delta \mathrm{G}^*_{\mathrm{M}\to\mathrm{C}}) + \exp(-\beta\Delta \mathrm{G}^*_{\mathrm{M}\to\mathrm{I}})]}$$

and since $k_{\mathrm{I}\to\mathrm{C}} \propto \exp(-\beta\Delta \mathrm{G}^*_{\mathrm{I}\to\mathrm{C}})$, then,

$$\mathrm{S_{up}} = \frac{k_{\mathrm{I}\to\mathrm{M}\to\mathrm{C}}}{k_{\mathrm{I}\to\mathrm{C}}} \approx \frac{\exp(\beta(\Delta \mathrm{G}^*_{\mathrm{I}\to\mathrm{C}} - \Delta \mathrm{G}^*_{\mathrm{I}\to\mathrm{M}} - \Delta \mathrm{G}^*_{\mathrm{M}\to\mathrm{C}}))}{[\exp(-\beta\Delta \mathrm{G}^*_{\mathrm{I}\to\mathrm{M}}) + \exp(-\beta\Delta \mathrm{G}^*_{\mathrm{M}\to\mathrm{C}}) + \exp(-\beta\Delta \mathrm{G}^*_{\mathrm{M}\to\mathrm{I}})]} \qquad (8)$$

To estimate the effect of kinetic prefactors, *A* on the speed-up factor, $\mathrm{S_{up}}$, we performed pseudo-dynamic MC simulations to track the attachment rate of the critical nucleus, f_{n_c} (see SI Sec. IIB for more details and modified version of Eq. (8)). These calculations were carried out for GBF27 as testbed, using 2916 particles at P* = 6.44 and $|\beta\Delta\mu_{\mathrm{IC}}| \sim 0.10$.

To account for the effect of the entire nucleation free-energy profiles (shown in Figs. S12 to S20), we numerically estimate $\tau(n_c)$ up to the transition state derived from the Fokker-Planck equation,[49,50]

$$\tau\,(n_c) = \int_0^{n_c} \frac{1}{D_o}\, dy\, e^{[\beta G(y)]} \int_0^{y} dz\, e^{[-\beta G(z)]} \tag{9}$$

where D_o is the constant rate of attachment of particles to the cluster and the relative rate for barrier-crossing for different transitions is expressed as,

$$k' = \frac{1}{2\tau(n_c)} \tag{10}$$

where $\tau_{\mathrm{I}\to\mathrm{M}\to\mathrm{C}} = \tau_{\mathrm{I}\to\mathrm{M}} + \tau_{\mathrm{M}\to\mathrm{C}}$ and the τ values at critical conditions are reported in Table S5 in the SI.

b. Estimating kinetic barriers

Nucleation barriers between I, M, and C phases, were found using umbrella sampling (US) using standard MC for hard particle models and hybrid MC simulations for the AB and TS mixtures. The size of the largest cluster detected using clustering-based on local translational and orientational OP was used as the reaction coordinate to bias sampling in a particular window of OP values. The translational order was calculated based on the coordinates of the particles' center of mass, and the orientational order was based on all the particle orientation unit vectors for TCs and only the long axis unit vector for GBFs (see Fig. 3).

The reaction coordinate was partitioned into overlapping windows with rigid reflective walls at their respective boundaries. The equilibrium probability distribution of different cluster sizes, $P(N_n)=\langle N_n\rangle/N$ within the US windows were collected during the simulations and the Gibbs free energy was determined using: $\beta\Delta G = -\ln P(N_n)$ where N_n is the average number of clusters with n particles. $\beta\Delta G^*$ is the free energy corresponding to the critical cluster size n_c. Each US windows was run for at least 2.0×10^6 MC and 10^5 HMC cycles. More details on the simulation protocols, OPs used to detect the clusters for different transitions are given in the supplementary information (SI) Secs. IIIA, and IIIB.

c. Simulation models and protocols to map phase diagrams

The GBFs and TCs are defined by pair-wise excluded volume interactions where the overlap between the particles is checked using the Gilbert-Johnson-Keerthi (GJK)[51] algorithm. We tuned the aspect ratio, AR= $\frac{h}{\sigma}$ in GBFs (where h is the GBF height and σ is the length of the square base) and vertex truncation, s, in TCs to explore the region of phase space where the intermediate M state was reportedly observed.[17,33] The equation of state for I, M, and C phases was mapped by carrying out compression and expansion simulations in the isobaric-isothermal (NPT) ensemble. We varied the reduced pressure, $\hat{P}= PL^3/k_bT$, and estimated the average packing fraction, $\phi= NV_p/V$ of the particles, where N is the number of particles, V is the system volume, V_p is the volume of each particle, T is temperature, and L is the length scale set as σ for GBF and $\sqrt[3]{V_p}$ for TC. Compression/expansion runs were carried out with 1728/1210 GBFs and 2744/2574 TCs. At each pressure step, we performed 3 $\times 10^6$ MC cycles with the last 1.5 $\times$ 10^6 cycles used for production runs, where each MC cycle consisted of N translational, N rotational, N/10 flip, and 2 volume moves. Longer runs with 6 $\times 10^6$ MC cycles were carried out at conditions near first-order transitions. For GBFs, the coexistence pressure, $\hat{P}_{coex}$ between I-M_N and I-C_{ABCD} phases in the equation of state were estimated using interfacial pinning (IP)[52,53] simulations where the coexisting phases of interest were simulated in an elongated 3D periodic box. The coexistence conditions between I-M_R, and M_R-C_{Mink} for TCs were obtained from a previous study.[33]

For the TS model, the two- and three-body interaction parameters for T and S components were obtained from Bertolazzo et. al.[22] We performed molecular dynamics (MD) simulations using LAMMPS software[54] (stable August 3rd 2020 version) in NPT ensemble using Nosé-Hoover[55,56] thermostat and barostat with a damping time of 1 and 5 ps, respectively. The Verlet algorithm with 4 fs timestep was used to integrate the equations of motion. The pressure was set to 0 atm and the I, M_G, and C_Z phases were mapped by varying T using a total of 16,337 beads with 74% network former T-particles and 26% structure directing S-particles.

The AB mixtures were modeled using the two-body interaction parameters of Kumar et. al.[26] We performed MD simulations in NPT ensemble with 13824 particles, comprising of a 50-50 mixture of A and B. The pressure was set to 0 and the timestep to 0.05fs. The Nosé-Hoover thermostat and barostat had a damping time of 0.025 and 0.125ps, respectively.

The coexistence conditions between I-M_{LAM}, M_{LAM}-C_{LXA}, I-M_G, and M_G-C_Z are discussed in Sec. IC in SI. Using equation of state data, we estimated the difference in chemical potentials, $(\beta\mu_i - \beta\mu_j(\hat{P}))= \int_{\hat{P}_{coex}}^{\hat{P}} \hat{v}_i - \hat{v}_j d\hat{P}$ and the entropies, $(s_i - s_j)/k_b= \beta(u_i - u_j) + \hat{P}\ (\hat{v}_i - \hat{v}_j)$ where i, j = I, M, or C, $\beta\mu_i - \beta\mu_j(\hat{P}_{coex}) = 0$, $\hat{v}$ is the reduced specific volume per particle, μ and u is the chemical and total potential energy per particle, respectively.

More details on the models, interaction parameters, simulation protocols for mapping phase behavior, and IP calculations can be found in the supplementary information (SI) Secs. IA, IB, and IC.

Acknowledgment

Funding support from NSF award No. CBET-2402416 is gratefully acknowledged. Support to F. A. E. from grant NSF PHY-1748958 to the Kavli Institute for Theoretical Physics (KITP) is also acknowledged. The authors thank Dr. Vikram Thapar for insightful discussions and for sharing the base simulation code, and Mohammed Alshammasi, Manish Kumar Das, and Dr. Luis Nieves-Rosado for useful exchanges. We also thank Prof. Valeria Molinero and Eli Martinez for sharing LAMMPS input scripts and valuable assistance in validating the Zeolite system.

References

1. Church, G. M., Gao, Y. & Kosuri, S. Next-Generation Digital Information Storage in DNA. *Science (80).* **337**, 1628–1628 (2012).
2. Gu, M., Zhang, Q. & Lamon, S. Nanomaterials for optical data storage. *Nat. Rev. Mater.* **1**, (2016).
3. Yu, J. *et al.* Recent advances in optical and optoelectronic data storage based on luminescent nanomaterials. *Nanoscale* **12**, 23391–23423 (2020).
4. Kim, H. *et al.* Biomimetic chameleon soft robot with artificial crypsis and disruptive coloration skin. *Nat. Commun.* **12**, 4658 (2021).

5. M.E.Zoorob, M.D.B.Charlton, G.J.Parker, J.J.Baumberg & M.C.Netti. Complete photonic bandgaps in 12-fold symmetric quasicrystals. *Nature* **404**, 740–743 (2000).
6. Wang, P. *et al.* Localization and delocalization of light in photonic moiré lattices. *Nature* **577**, 42–46 (2020).
7. Wu, Y., Wang, Y., Zhang, S. & Wu, S. Artificial Chameleon Skin with Super-Sensitive Thermal and Mechanochromic Response. *ACS Nano* **15**, 15720–15729 (2021).
8. Uniyal, S., Choudhary, K., Sachdev, S. & Kumar, S. Nano-bio fusion: Advancing biomedical applications and biosensing with functional nanomaterials. *Opt. Laser Technol.* **168**, 109938 (2024).
9. Kabashin, A. V. *et al.* Plasmonic nanorod metamaterials for biosensing. *Nat. Mater.* **8**, 867–871 (2009).
10. Altug, H., Oh, S. H., Maier, S. A. & Homola, J. Advances and applications of nanophotonic biosensors. *Nat. Nanotechnol.* **17**, 5–16 (2022).
11. Sherman, Z. M. *et al.* Plasmonic Response of Complex Nanoparticle Assemblies. *Nano Lett.* **23**, 3030–3037 (2023).
12. Green, A. M. *et al.* Structural Order and Plasmonic Response of Nanoparticle Monolayers. *ACS Photonics* **11**, 1280–1292 (2024).
13. Jo, I.-S. *et al.* DNA-Coated Microspheres with Base Mismatches for Stepwise Programmed Assembly. *Chem. Mater.* **36**, 3820–3828 (2024).
14. Lu, F., Yager, K. G., Zhang, Y., Xin, H. & Gang, O. Superlattices assembled through shape-induced directional binding. *Nat. Commun.* **6**, 6912 (2015).
15. Agarwal, U. & Escobedo, F. A. Mesophase behaviour of polyhedral particles. *Nat. Mater.* **10**, 230–235 (2011).
16. Escobedo, F. A. Engineering entropy in soft matter: the bad, the ugly and the good. *Soft Matter* **10**, 8388–8400 (2014).
17. Sharma, A. K. & Escobedo, F. A. Effect of particle anisotropy on the thermodynamics and kinetics of ordering transitions in hard faceted particles. *J. Chem. Phys.* **158**, (2023).
18. Lim, Y., Lee, S. & Glotzer, S. C. Engineering the Thermodynamic Stability and Metastability of Mesophases of Colloidal Bipyramids through Shape Entropy. *ACS*

Nano **17**, 4287–4295 (2023).

19. Zhong, Y., Allen, V. R., Chen, J., Wang, Y. & Ye, X. Multistep Crystallization of Dynamic Nanoparticle Superlattices in Nonaqueous Solutions. *J. Am. Chem. Soc.* **144**, 14915–14922 (2022).
20. Eslami, H. & Müller-Plathe, F. Self-Assembly Pathways of Triblock Janus Particles into 3D Open Lattices. *Small* **20**, 1–12 (2024).
21. Mao, R. *et al.* Regulating phase behavior of nanoparticle assemblies through engineering of DNA-mediated isotropic interactions. *Proc. Natl. Acad. Sci.* **120**, 2017 (2023).
22. Bertolazzo, A. A., Dhabal, D., Lopes, L. J. S., Walker, S. K. & Molinero, V. Unstable and Metastable Mesophases Can Assist in the Nucleation of Porous Crystals. *J. Phys. Chem. C* **126**, 3776–3786 (2022).
23. Kumar, A. & Molinero, V. Two-Step to One-Step Nucleation of a Zeolite through a Metastable Gyroid Mesophase. *J. Phys. Chem. Lett.* **9**, 5692–5697 (2018).
24. Du, J. S., Bae, Y. & De Yoreo, J. J. Non-classical crystallization in soft and organic materials. *Nat. Rev. Mater.* **9**, 229–248 (2024).
25. Avendaño, C. & Escobedo, F. A. Phase behavior of rounded hard-squares. *Soft Matter* **8**, 4675–4681 (2012).
26. Kumar, A. & Molinero, V. Self-Assembly of Mesophases from Nanoparticles. *J. Phys. Chem. Lett.* **8**, 5053–5058 (2017).
27. Ten Wolde, P. R. & Frenkel, D. Homogeneous nucleation and the Ostwald step rule. *Phys. Chem. Chem. Phys.* **1**, 2191–2196 (1999).
28. Ostwald, W. Studien über die Bildung und Umwandlung fester Körper. *Zeitschrift für Phys. Chemie* **22U**, 289–330 (1897).
29. Mao, R. *et al.* Regulating phase behavior of nanoparticle assemblies through engineering of DNA-mediated isotropic interactions. *Proc. Natl. Acad. Sci.* **120**, e2302037120 (2023).
30. Wolde, P. R. ten & Frenkel, D. Enhancement of Protein Crystal Nucleation by Critical Density Fluctuations. *Science (80-.).* **277**, 1975–1978 (1997).
31. Vekilov, P. G. The two-step mechanism of nucleation of crystals in solution.

Nanoscale **2**, 2346 (2010).

32. Zhou, Y., Cersonsky, R. K. & Glotzer, S. C. A route to hierarchical assembly of colloidal diamond. *Soft Matter* **18**, 304–311 (2022).
33. Gantapara, A. P., de Graaf, J., van Roij, R. & Dijkstra, M. Phase behavior of a family of truncated hard cubes. *J. Chem. Phys.* **142**, (2015).
34. Champion, J. A., Katare, Y. K. & Mitragotri, S. Making polymeric micro- and nanoparticles of complex shapes. *Proc. Natl. Acad. Sci.* **104**, 11901–11904 (2007).
35. Yoo, J.-W. & Mitragotri, S. Polymer particles that switch shape in response to a stimulus. *Proc. Natl. Acad. Sci.* **107**, 11205–11210 (2010).
36. Liu, B. *et al.* Switching plastic crystals of colloidal rods with electric fields. *Nat. Commun.* **5**, 1–8 (2014).
37. Cimada daSilva, J., Balazs, D. M., Dunbar, T. A. & Hanrath, T. Fundamental Processes and Practical Considerations of Lead Chalcogenide Mesocrystals Formed via Self-Assembly and Directed Attachment of Nanocrystals at a Fluid Interface. *Chem. Mater.* **33**, 9457–9472 (2021).
38. Steinhardt, P. J., Nelson, D. R. & Ronchetti, M. Bond-orientational order in liquids and glasses. *Phys. Rev. B* **28**, 784–805 (1983).
39. Lechner, W. & Dellago, C. Accurate determination of crystal structures based on averaged local bond order parameters. *J. Chem. Phys.* **129**, 114707 (2008).
40. Cuetos, A. & Dijkstra, M. Kinetic Pathways for the Isotropic-Nematic Phase Transition in a System of Colloidal Hard Rods: A Simulation Study. *Phys. Rev. Lett.* **98**, 95701 (2007).
41. Bulutoglu, P. S. *et al.* An investigation of the kinetics and thermodynamics of NaCl nucleation through composite clusters. *PNAS Nexus* **1**, 1–11 (2022).
42. Iwamatsu, M. Nucleation pathway of core-shell composite nucleus in size and composition space and in component space. *Phys. Rev. E* **86**, 041604 (2012).
43. Turnbull, D. Formation of Crystal Nuclei in Liquid Metals. *J. Appl. Phys.* **21**, 1022–1028 (1950).
44. Gim, M.-J., Beller, D. A. & Yoon, D. K. Morphogenesis of liquid crystal topological defects during the nematic-smectic A phase transition. *Nat. Commun.* **8**, 15453 (2017).

45. Smeets, P. J. M. *et al.* A classical view on nonclassical nucleation. *Proc. Natl. Acad. Sci.* **114**, E7882–E7890 (2017).
46. Nishida, K. *et al.* In situ observations of the mesophase formation of isotactic polypropylene—A fast time-resolved X-ray diffraction study. *Polym. J.* **44**, 95–101 (2012).
47. Sharma, A. K. & Escobedo, F. A. Diffusionless rotator–crystal transitions in colloidal truncated cubes. *J. Chem. Phys.* **161**, 34509 (2024).
48. Ni, R., Belli, S., van Roij, R. & Dijkstra, M. Glassy Dynamics, Spinodal Fluctuations, and the Kinetic Limit of Nucleation in Suspensions of Colloidal Hard Rods. *Phys. Rev. Lett.* **105**, 088302 (2010).
49. Reguera, D., Rubí, J. M. & Vilar, J. M. G. The Mesoscopic Dynamics of Thermodynamic Systems. *J. Phys. Chem. B* **109**, 21502–21515 (2005).
50. Wedekind, J., Strey, R. & Reguera, D. New method to analyze simulations of activated processes. *J. Chem. Phys.* **126**, 1–7 (2007).
51. Gilbert, E. G., Johnson, D. W. & Keerthi, S. S. A Fast Procedure for Computing the Distance Between Complex Objects in Three-Dimensional Space. *IEEE J. Robot. Autom.* **4**, 193–203 (1988).
52. Pedersen, U. R., Hummel, F., Kresse, G., Kahl, G. & Dellago, C. Computing Gibbs free energy differences by interface pinning. *Phys. Rev. B* **88**, 094101 (2013).
53. Thapar, V. & Escobedo, F. A. Extensions of the interfacial pinning method and application to hard core systems. *J. Chem. Phys.* **141**, (2014).
54. Thompson, A. P. *et al.* LAMMPS - a flexible simulation tool for particle-based materials modeling at the atomic, meso, and continuum scales. *Comput. Phys. Commun.* **271**, 108171 (2022).
55. Nosé, S. A unified formulation of the constant temperature molecular dynamics methods. *J. Chem. Phys.* **81**, 511–519 (1984).
56. Hoover, W. G. Constant-pressure equations of motion. *Phys. Rev. A* **34**, 2499–2500 (1986).

SUPPLEMENTARY INFORMATION

Mesophases as steppingstones to enhance crystallization kinetics in nanoparticle self-assembly

B.P. Prajwal and Fernando A. Escobedo*

Robert Fredrick Smith School of Chemical and Biomolecular Engineering,

Cornell University, Ithaca, New York

I. Simulation model and protocols

A. Simulation Models

A1. Hard particle systems

We simulated gyrobifastigia (GBF) and truncated cubes (TC) defined by the pair-wise excluded volume interactions, $U(r_{ij})$, given as,

$$U(r_{ij}) = \begin{cases} \infty, & \text{if } r_{ij} < r_{ij}^{max} \\ 0, & \text{otherwise} \end{cases} \qquad \text{(S1)}$$

where, r_{ij} is the distance between the particle center of mass, r_{ij}^{max} is the maximum r_{ij} distance beyond which overlap cannot occur.

For GBFs, we varied the aspect ratio, AR= $\frac{h}{\sigma}$ (where h is the GBF height and σ is the length of the square base) to explore the region of phase space having single and two-step transitions. The AR for regular gyrobifastigium is $\sqrt{3}$ and the AR values were tuned by varying the edge length of the triangular facets while fixing the dimensions of the square base.

In the case of TC, we tuned the vertex truncation to induce the two-step transition. The vertex truncation was constructed using a simple mathematical expression as reported in a previous study[1] that relates the truncation parameter, s with the location of vertices and diameter of the circumcircle, σ defining the shape with unit volume.

A2. TS mixture model

We simulated a mixture of coarse-grained particles representing silica-like (T) and structure directing agents (S) developed by Bertolazzo et. al.[2] The composition was fixed with 74% network former T and 26% structure directing S. Interaction potential energy, U between all particles is modeled with the SW potential[3] defined as,

$$U = \sum_i \sum_{j>i} U_2(r_{ij}) + \sum_i \sum_{j\neq i} \sum_{k>j} U_3(r_{ij}, r_{ik}, \theta_{ijk}) \quad \text{(S2)}$$

Where the two-body term, $U_2(r_{ij})$ is given by,

$$U_2(r_{ij}) = A_{ij}\varepsilon_{ij}\left[B_{ij}\left(\frac{\sigma_{ij}}{r_{ij}}\right)^{p_{ij}} - \left(\frac{\sigma_{ij}}{r_{ij}}\right)^{q_{ij}}\right]\exp\left(\frac{\sigma_{ij}}{r_{ij} - a_{ij}\sigma_{ij}}\right) \quad \text{(S2}')$$

And the repulsive three-body term, $U_3(r_{ij}, r_{ik}, \theta_{ijk})$,

$$U_3(r_{ij}, r_{ik}, \theta_{ijk}) = \lambda_{ijk}\,\varepsilon_{ijk}\left[\cos\theta_{ijk} - \cos\theta_0\right]^2 \exp\left(\frac{\gamma_{ij}\sigma_{ij}}{r_{ij} - a_{ij}\sigma_{ij}}\right)\exp\left(\frac{\gamma_{ik}\sigma_{ik}}{r_{ik} - a_{ik}\sigma_{ik}}\right) \quad \text{(S2}'')$$

Where r_{ij} and r_{ik} are the distances and θ_{ijk} is the angle formed by *i*, *j*, and *k* particles. $a\sigma$ defines the cutoff for SW potential. The interaction potential for T particles is represented with the monoatomic water model[4] parameters having both two-body attractive and three-body repulsive terms. The S particles have only a two-body term of the SW potential defining the isotropic S-S and S-T interactions. Masses of T and S components were set as 28.15 g/mol. Table S1 shows the values of SW interaction parameters that are listed according to LAMMPS software[5] input file format.

Table S1. SW parameters for particle interactions. The parameters A= 7.049556277, B= 0.6022245584, p=4.0, q=0.0, a=1.8, γ=1.2, and $\cos\theta_0$ = -0.333333333 for all the interactions.

Interacting particles	ε (kcal/mol)	σ (Å)	a	λ
S-S-S	0.68	5.13	1.8	0.0
S-S-T	0.0	5.13	1.8	0.0
S-T-S	0.0	5.13	1.8	0.0
T-S-S	1.6	5.13	1.8	0.0
S-T-T	1.6	5.13	1.8	0.0
T-S-T	0.0	5.13	1.8	0.0
T-T-S	0.0	5.13	1.8	0.0
T-T-T	12.378	2.7275	1.8	23.15

A3. AB mixture model

The Kumar-Molinero model[6] for the binary mixture of A and B particles interacting through pair potentials modeled with two-body Stillinger-Weber (SW)[3] is given as,

$$U(r_{ij}) = 7.049556277\varepsilon\left[0.6022245584\left(\frac{\sigma}{r_{ij}}\right)^4 - 1\right]\exp\left(\frac{\sigma}{r_{ij} - a\sigma}\right) \qquad \text{(S3)}$$

Where r_{ij} is the distance between particles *i* and *j*, ε is the attraction well depth, σ is the size of the particles, and a=1.8 defines the cutoff of the interaction potential. Masses of A and B components are 1 g/mol. The sizes and interaction strengths of AA and BB were fixed as: σ_{AA}= σ_{BB}=1 and ε_{AA}= ε_{BB}=1 kcal mol^{-1}. The unlike particles have ε_{AB}= 1.45 kcal mol^{-1} and σ_{AB}/σ_{AA}= 1.08.

B. Protocol for mapping phase diagram

B1. GBF and TC systems

To map the phase diagram for the bulk assembly of GBFs and TCs, we performed standard Metropolis Monte Carlo (MC) algorithm in an isothermal-isobaric (NPT) ensemble in a periodic box where N is the total number of particles, V is the volume, and P is the pressure (see Fig. S2). We first mapped the equation of state by varying the dimensionless pressure, $\hat{P}= PL^3/k_bT$, and estimating the average packing fraction, $\phi= NV_p/V$, where V_p is the volume of each particle, T is temperature, L is the particles' length scale which was set as σ and $\sqrt[3]{V_p}$ for GBF and TC, respectively, and k_b is the Boltzmann's constant. We performed a stepwise expansion, and compression runs to map the isotropic (I), nematic/rotator mesophase (M_N/M_R), and ABCD/Minkowski crystal (C_{ABCD}/C_{MINK}) branches of the phase diagram. The initial configurations for the compression runs were the I phase and for the expansion runs we used the densest C structure predicted using Floppy Box Monte Carlo algorithm.[7] To minimize finite size effects, we selected the initial system size having a minimum of 10 particles per layer in all three dimensions. Each MC cycle consisted of N translational, N rotational, $N/10$ *flip*, and 2 volume moves. All moves obey detailed balance and the step size for the translational, rotational, and volume moves are adjusted to have acceptance probabilities of 0.4, 0.4, and 0.3. Volume moves attempt isotropic changes in the box volume during compression runs, while the shape of the box is changed (anisotropic moves) during the expansion runs. Since the rotator (M_R) structure observed in TC assembly is translationally ordered, we carried out anisotropic box moves for both compression and expansion runs. We incorporated *flip* moves that attempt to randomly orient a chosen particle in a plane that is perpendicular to its current orientation. The three-unit vectors defining the particles' orientation were randomly selected. The *flip* move was particularly important for simulating GBFs with different ARs as the standard rotational moves do not effectively sample the long axis orientation states.

B2. TS mixture system

For the TS model, we performed molecular dynamics (MD) simulations using LAMMPS software[5] (stable August 3rd 2020, version) in NPT ensemble using Nosé-Hoover[8] thermostat and barostat with a damping time of 1 and 5 ps, respectively. For all simulations, we used 4 fs timestep to integrate the equations of motion with the velocity Verlet algorithm. The pressure was set to 0 atm, where isotropic box volume move was performed.

We prepared the isotropic (I) amorphous phase by initializing the T and S components on a cubic lattice (without overlaps) in a large periodic cubic box and then equilibrating for 40 ns at 800 K where I phase is stable. Using the final configuration at 800 K, we then performed two independent simulations where a 4 ns linear ramp was used to cool to 636 K and 600 K. Finally, we carried out an equilibration run for 40-50 ns to obtain double-gyroid mesophase (M_G) at 636 K and Zeolite crystal (C_Z) at 600 K, respectively.

Using the above equilibrated I, M_G, and C_Z configurations at 800 K, 636 K, and 600 K, respectively, we mapped the phase diagram using 10 K cooling and heating step sizes and 40 ns equilibration at each temperature (see Fig. S2).

B3. AB mixture system

The AB mixtures were modeled using the two-body interaction parameters developed by Kumar et. al.[6] We performed MD simulations in NPT ensemble with 13824 total particles, comprising of a 50-50 mixture of A and B. The pressure was set to 0 and 0.05fs timestep was used to integrate the equations of motion. The Nosé-Hoover thermostat and barostat with a damping time of 0.025 and 0.125ps, respectively is used in the simulations.

We follow the protocol described in Sec. B2 to prepare the initial I phase configuration at 350 K. We then cooled the system to 325 K and used 5-10 K cooling steps to further cool it to 290 K. Below 290 K, the system transitioned directly to the ordered lamella (C_{LXA}) phase and each temperature step was equilibrated for 10^7 MD cycles.

The C_{LXA} transitions to the disordered lamella mesophase (M_{LAM}) at 325 K and the M_{LAM} transitions to I phase at 345 K. The M_{LAM} obtained at 325 K is used to map the mesophase branch in the phase diagram.

Each temperature step was equilibrated for 10^7 MD cycles. Figure S2 shows the phase diagram for the AB model.

C. Estimating coexistence conditions for GBF, TC, AB, and TS mixture systems

Table S2 shows the coexistence conditions for phases observed in the GBF, TC, AB, and TS mixture models. The coexistence, $\hat{P}_{coex}$ values between I-M_R, and M_R-C_{Mink} phases for s= 0.90 TC system were obtained from a previous study.[1] In the case of TS model, the coexistence temperatures were roughly estimated from the transition regions in the phase diagram (see Fig. S8e). We predicted 645 K and 700 K as the coexistence temperatures (T_{coex}) at which M_{DG}-C_Z and I-M_{DG}, respectively coexist, which is 10 K and 16 K below the values reported by Bertolazzo et. al.[2] For AB model, we obtained the T_{coex} to be 320 K and 312 K for I-M_{LAM} and M_{LAM}-C_{LXA}, respectively.

For GBF system, we performed interfacial pinning (IP)[9,10] calculations using MC simulations where the coexisting phases I and II of interest were simulated in an elongated 3D periodic box. The protocol for preparing the initial configuration for the IP simulations are as follows: 1) single phase configuration of GBF crystal (C_{ABCD}) or nematic (M_N) phase assembled using the compression runs with the system size N=1728 was selected, 2) the simulation box was replicated and elongated in one of the dimensions (say the z-axis) such that the slant plane formed by the GBFs in C_{ABCD} and M_N structures are in contact with the I phase. The interfacial free energy of the slant plane in the GBF crystal structure were estimated in a previous study[11] and was found to be lesser compared to (100) and (001) planes. The box length in the z-axis was selected to accommodate an equal number of particles in the individual coexisting phases, 3) NVT simulations were performed for replicated N particles in the box that melts to form the two-phase interfacial system.

The initial configuration generated from the above protocol is then used to run a biased NP_zT simulations for 6 $\times 10^6$ MC cycles where the box dimension along z was allowed to fluctuate and the xy cross sectional area was kept constant. A harmonic potential, $U(\Omega) = \frac{k_s}{2}(\Omega - a)^2$ is used to pin the two-phase interfacial system where Ω is the value of the order parameter (OP) used to distinguish phases I and II, k_s is the spring constant, and a is the average of Ω_I and Ω_{II} OP values corresponding to phases I and II, respectively. Using $\langle\Omega\rangle$ calculated from the last 1.5 $\times$ 10^6 production cycles, we estimated the free energy difference, $\beta\Delta\mu_{I-II}$ using,

$$\beta(\mu_I - \mu_{II}) = -\frac{\beta\, k_s\, (\Omega_I - \Omega_{II})}{N}\,[\langle\Omega\rangle - a] \qquad \text{(S4)}$$

where $\beta = 1/k_bT$ (k_b is Boltzmann's constant). In this study, we used specific volume, $\upsilon = \frac{V}{N\,V_{GBF}}$ as the OP where V is the box volume, and V_{GBF} is the volume of a GBF particle. The k_s value for the spring was set as 10000 for all the simulations. υ is a cheap OP to compute on-the-fly and was found to be effective in pinning the interfaces between I and M_N or C_{ABCD} phases due to the differences in the packing densities. The P^*_{coex} corresponds to the values where $\beta\Delta\mu_{I-II}$ ~0 (see Fig. S1a). Figures S1b to S1d show the final two-phase configurations after equilibration run in the IP simulation.

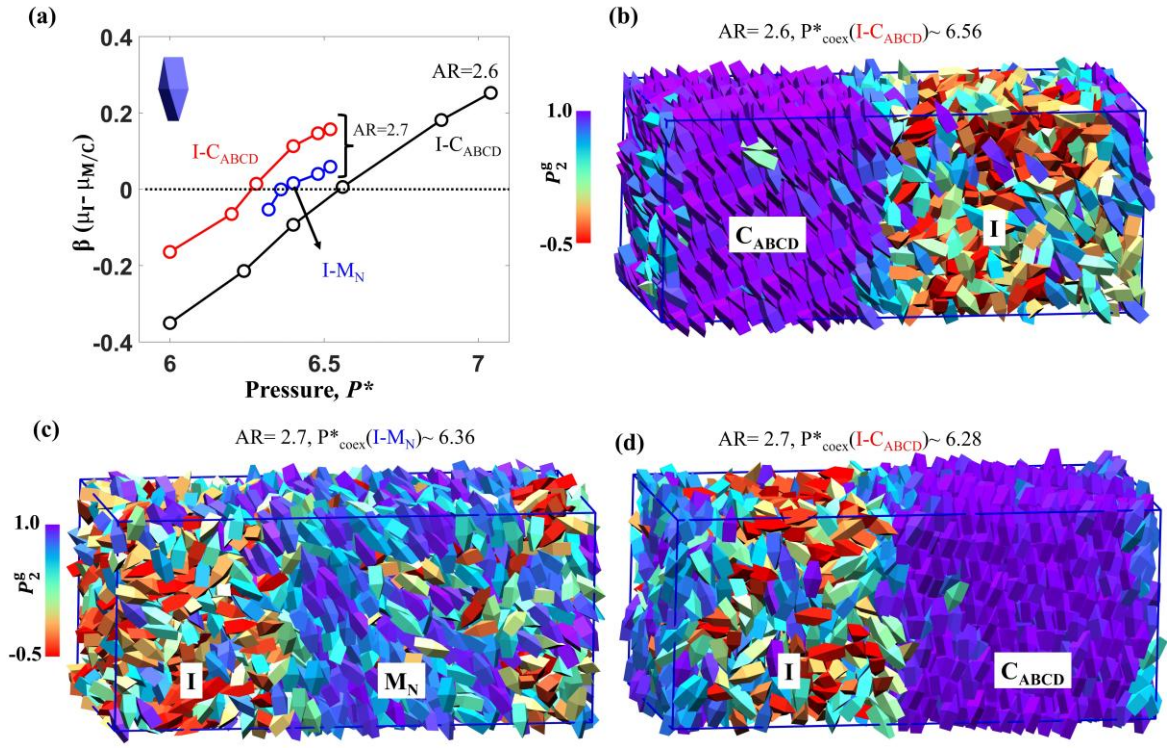

Fig S1: Interfacial pinning simulation results for GBF26 and GBF27 systems. (a) The chemical potential difference between I and M/C phases at different reduced pressures, $\hat{P}$ for aspect ratios, AR= 2.6 and 2.7 are shown. The dotted line marks the coexistence, $\hat{P}_{coex}$ conditions and the representative two-phase simulation snapshots for (b) AR= 2.6 and (c,d) AR= 2.7 at coexistence after equilibration are also shown.

Table S2. Coexistence $\widehat{P}_{coex}$ for TC, and GBF systems and T_{coex} for AB and TS mixture model. I- Isotropic, M_N- Nematic, C_{ABCD}- ABCD crystal, M_R- Rotator, M_G- Double-gyroid, C_Z- Zeolite, M_{LAM}- disordered lamella, C_{LXA}- ordered lamella.

System	Coexisting Phases	Condition ($\widehat{P}_{coex}$/ T_{coex})
GBF27	I-M_N	6.36
	I-C_{ABCD}	6.28
GBF26	I-C_{ABCD}	6.56
TC90	I-M_R	9.5
	M_R-C_{Mink}	10.25
AB model	I-M_{LAM}	320 K
	M_{LAM}-C_{LXA}	312 K
TS model	I-M_G	700 K
	M_G-C_Z	645 K

C1. Equation of state

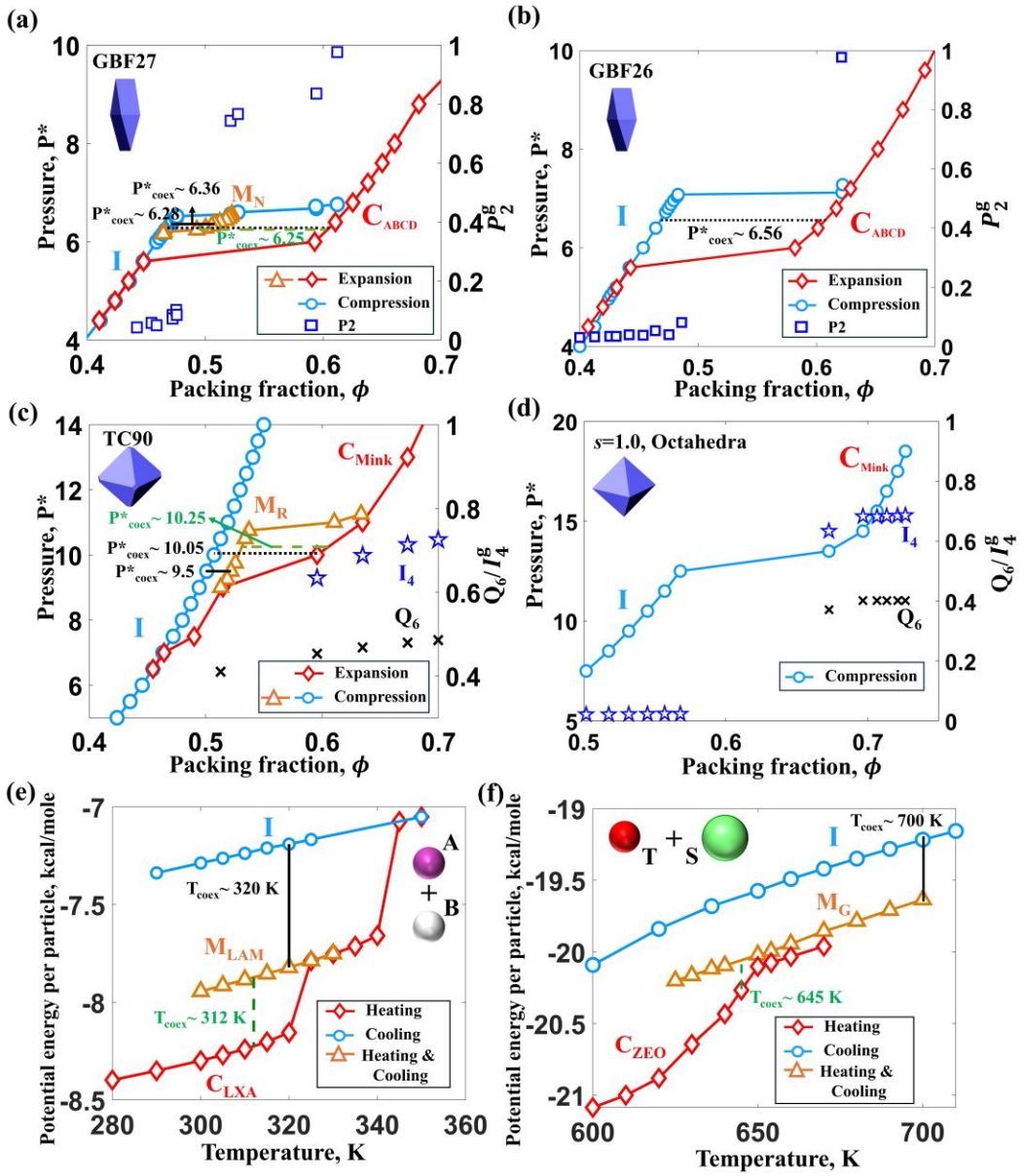

Fig. S2: Variation in $\hat{P}$ vs. ϕ and potential energy vs. temperature for GBF, TC, AB, and TS model systems. (a-d) Hard particle systems showing compression and expansion run for GBF27, GBF26, TC90, and octahedra with *s*=1.0. (e, f) Cooling and heating run for AB and TS model systems. Legends show the markers for the compression and expansion (or cooling and heating) runs. The coexistence condition between I-C phases, I-M, and M-C phases are marked with dotted black, solid black, and dashed green lines, respectively. The variation in global Q_6, I_4^g , and P_2^g order parameters for different phases are shown.

D. Protocol for estimating kinetic barriers

We performed umbrella simulations (US) using standard NPT-MC[12] to estimate the kinetic barriers for GBF and TC systems. We carried out unbiased simulations at the desired conditions to estimate kinetic free energy barriers, $\beta\Delta G$ for the initial range of windows. The largest cluster size is then selected to launch the simulations in the next umbrella window. Within each window, we performed unbiased simulations where any configuration outside the window was rejected. To reduce the computational costs, we compute the cluster size, *n* every 2 MC cycles. The window sizes were incremented with steps of 10-20 cluster sizes. At lower degree of supersaturation, DSS= $|\beta\Delta\mu_{IC}|$ between 0.07 and 0.10, we used steps of 2-5 cluster sizes for the initial windows and then the window size was changed to 10-20 as the slope of the $\beta\Delta G$ becomes less steep. We simulated system sizes with 1728 and 2916 GBFs, and 2744 and 5488 TCs. Each window was equilibrated for 2-3 $\times$ 10^6 cycles and the production statistics were taken from the last 5-8 $\times 10^5$ cycles.

In the case of AB and TS mixture models, we performed hybrid NPT-MC (HMC) simulations[13,14] where each HMC move consisted of either a MD run or volume move. 80% of the total HMC moves consisted of 100 microcanonical (NVE) MD steps and the remaining 20% attempted to change the system's volume isotropically based on the standard NPT MC run. Every NVE MD simulation started with a configuration whose momenta was randomly generated from a Maxwell-Boltzmann distribution at the temperature of interest. The final configuration after MD steps was accepted or rejected based on the Metropolis acceptance criteria: min(1, $e^{-\beta\Delta H}$), where ΔH is the change in the system's Hamiltonian, H which is the sum of potential and kinetic energies. The timestep and volume step size was tuned by increasing/decreasing by 5% every 1000 and 5000 HMC steps, such that the MD and volume move acceptance is about 60% and 30%, respectively. The HMC simulations were carried out using python 2.7.16 and LAMMPS software[5] (stable August 3rd 2020, version). The python wrapper class for LAMMPS (PyLAMMPS) was installed using the instructions detailed in https://github.com/palmergroup/hmcwithlammps. To perform umbrella simulations, we adopted a protocol similar to TC and GBF systems where any configuration outside the umbrella window was rejected. For all the transitions, the cluster size, *n* was computed every 5 HMC cycle except for I $\rightarrow$ M_G where we computed *n* every 10 HMC cycle since the order

parameters to identify M_G phase is computationally expensive. Each HMC cycle consists of either an NVT or a volume move.

For the AB model, the US window widths and step sizes were varied for different transitions and temperatures mainly to constrain the formation of macroscopic M_{LAM} during I → C_{LXA} transition. For I → C_{LXA} transition at 300 K, we used US window width of 20 with *n* increment by 1 (up to cluster size <= 10) and 2 (for cluster size >= 20). At 295 K and 290 K, *n* is increment by 1 and the width of US window width is set as 3 to constrain the formation of macroscopic M_{LAM}. For I → M_{LAM}, we used the *n* step sizes of 3 and 6 up to 30 and after 30, the step size was increased to 10 and for M_{LAM} → C_{LXA}, we used a fixed step size of 20. We used a US window width of 300 for I → M_{LAM} and M_{LAM} → C_{LXA} transitions.

In the case of TS model, the US windows were incremented by steps of 10 cluster sizes to estimate the barrier for I → C_Z and M_G → C_Z transitions, respectively. For I → M_G, we used 50 as the step size for the umbrella window. In all cases, we set the US window width of 300, except for the I → C_Z transition where we used US window width of 50 in the initial 0 and 10 cluster size window to constrain the direct I → M_G transition. The TS system comprises a total of 16,337 beads with 74% network former T-component and 26% structure directing S-component.

Finally, we use the kinetic free-energy barrier, $\beta\Delta G^*$ corresponding to the critical cluster with size, n_c for comparison across different simulated conditions and systems. The free energy curve was obtained by averaging the statistics obtained by dumping the *n* value every 50 and 100 HMC steps for TS and AB models, respectively. Each window was equilibrated for 1-2 × 10^5 HMC cycles and the production statistics were taken from the last 0.5-1 ×10^5 HMC cycles. The configuration having overlapping *n* value with the neighboring window after 10^4 cycles is used to progress the US simulations.

II. Theoretical rate estimation

A. Derivation of mean first passage time for two-step transition

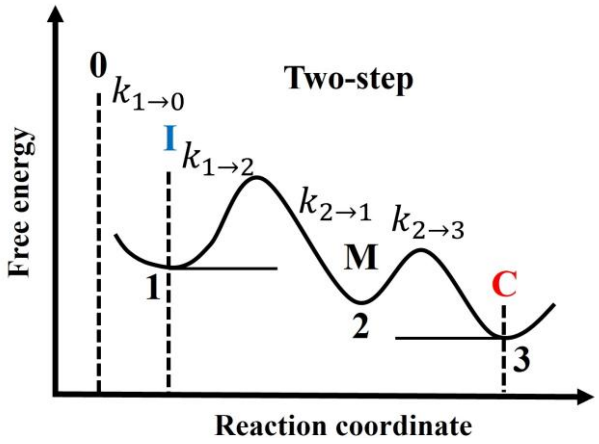

Fig. S3: Schematic representing mean first passage of the Markovian process going sequentially between states 0, 1, 2, and 3. M (or 2) is the intermediate state between I (or 1) and C (or 3). 0 is the reflecting bound with very high energy and C (or 3) is the absorbing state. $k_{i\to j}$ (i,j= 0,1, 2, or 3) are the transition rates.

Consider states i and j (where i,j=1, 2, or 3) that undergoes a two-step process (Fig. S3). Here 1= Isotropic, 2= Mesophase, and 3= Crystal states. Let's consider first the mean escape time from state j, τ_j, given that it can access neighboring states i and m only:

$$\tau_j = p_{j\to i}\tau_{j\to i} + p_{j\to m}\tau_{j\to m} = p_{j\to i}\tau_{j\to i} + (1-p_{j\to i})\tau_{j\to m} = \tau_{j\to m} + p_{j\to i}(\tau_{j\to i} - \tau_{j\to m}) \quad \text{(S5)}$$

Where $p_{j\to i,m}$ are the corresponding split probabilities, which for $p_{j\to i}$ can be estimated as:

$$p_{j\to i} = \frac{k_{j\to i}}{k_{j\to i}+k_{j\to m}} = \frac{\tau_{j\to i}^{-1}}{\tau_{j\to i}^{-1}+\tau_{j\to m}^{-1}} = \frac{\tau_{j\to m}}{\tau_{j\to i}+\tau_{j\to m}} \quad \text{(S6)}$$

and substituting this expression into Eq. S5, we obtain after simplification:

$$\tau_j = 2\tau_{j\to m}\tau_{j\to i}/\left(\tau_{j\to m}+\tau_{j\to i}\right) \quad \text{(S7)}$$

This relation shows when $\tau_{j\to m}/\tau_{j\to i} \to 0$ or $k_{j\to i}/k_{j\to m} \to 0$ then:

$$\tau_j = 2\tau_{j\to m} \quad \text{(S8)}$$

Hence, for a process started at state $j = 1$ as illustrated in Fig. S3, the average time for the system to escape state 1 (regardless of its destination state m) is τ_1 as given by Eq. S8.

Case 1. If the system is going "directly" from 1 to 3 one would write:

$$\tau_1 = 2\tau_{1\to3} \tag{S9}$$

Case 2. If the system is going from 1 to 3 via an intermediate state 2. We could write that the mean first passage time from 1 to 3 is:

$$\tau_{1\to2\to3} = \tau_1 + \langle \text{time for } 2 \to 1 \to 2 \text{ events} \rangle + \tau_{2\to3} \tag{S10}$$

Where the 2nd term is the average time associated with all possible transitions 2→1→2 transitions. To evaluate this term, let $p_{2\to1}^{(n)}$ be the probability of the 2→1 transition happening n successive times, then Eq. (S10) can be written as:

$$\tau_{1\to2\to3} = \tau_1 + \sum_{i=1}^{\infty} p_{2\to1}^{(n)}(\tau_{2\to1} + \tau_1) + \tau_{2\to3} \tag{S11}$$

Since transitions are Markovian, one can write: $p_{2\to1}^{(n)} = (p_{2\to1})^n$, and hence:

$$\tau_{1\to2\to3} = \tau_1 + (\tau_{2\to1} + \tau_1)\sum_{i=1}^{\infty} p_{2\to1}^{n} + \tau_{2\to3} = (\tau_{2\to1} + \tau_1)\sum_{i=0}^{\infty} p_{2\to1}^{n} - \tau_{2\to1} + \tau_{2\to3} \tag{S12}$$

which simplifies upon using the geometric summation formula to:

$$\tau_{1\to2\to3} = (\tau_{2\to1} + \tau_1)\frac{1}{1-p_{2\to1}} - \tau_{2\to1} + \tau_{2\to3} \tag{S13}$$

the split probability $p_{2\to1}$ can be estimated as:

$$p_{2\to1} = \frac{k_{2\to1}}{k_{2\to1}+k_{2\to3}} = \frac{\tau_{2\to1}^{-1}}{\tau_{2\to1}^{-1}+\tau_{2\to3}^{-1}} = \frac{\tau_{2\to3}}{\tau_{2\to1}+\tau_{2\to3}} \tag{S14}$$

Substituting (S14) into (S13) and simplifying:

$$\tau_{1\to2\to3} = (\tau_{2\to1} + \tau_1)\frac{\tau_{2\to1} + \tau_{2\to3}}{\tau_{2\to1}} - \tau_{2\to1} + \tau_{2\to3}$$

$$\tau_{1\to2\to3} = \tau_1 + \frac{\tau_{2\to3}}{\tau_{2\to1}}(\tau_{2\to1} + \tau_1) + \tau_{2\to3}$$

Or

$$\tau_{1\to2\to3} = \tau_1\left(1+\frac{\tau_{2\to3}}{\tau_{2\to1}}\right)+2\tau_{2\to3} \quad \text{(S15)}$$

τ_1 can be estimated from a relation analogous to Eq. (S9) as $\tau_1 = 2\tau_{1\to2}$, and substituting this into (S15):

$$\tau_{1\to2\to3} = 2\left[\tau_{1\to2}\left(1+\frac{\tau_{2\to3}}{\tau_{2\to1}}\right)+\tau_{2\to3}\right] \quad \text{(S16)}$$

The speed-up factor can then be estimated from Eqs. (S16) and (S9) as:

$$\frac{k_{1\to2\to3}}{k_{1\to3}} = \frac{\tau_1}{\tau_{1\to2\to3}} \approx \frac{\tau_{1\to3}}{\tau_{1\to2}\left(1+\frac{\tau_{2\to3}}{\tau_{2\to1}}\right)+\tau_{2\to3}} \quad \text{(S17)}$$

which is the main result where as indicated before one can convert average transition times $\tau_{i\to j}$ into transition probabilities per unit time between two states as $k_{i\to j}\sim\tau_{i\to j}^{-1}$.

B. Protocol for estimating kinetic prefactors

In this section, we present the protocol used to estimate the kinetic prefactors for GBF27 system with 2916 particles undergoing I → M, M → C, and I → C transitions at $\hat{P}$ = 6.44 and $|\beta\Delta\mu_{IC_{ABCD}}|$ ~0.10. We estimated kinetic prefactor, *A* for different transitions to understand its effect on the speed-up factor, S_{up} defined as,

$$S_{up}=\frac{k_{I\to M\to C}}{k_{I\to C}} \approx \frac{A_{I\to M}\,A_{M\to C}\exp\left((\Delta G^*_{I\to C}-\Delta G^*_{I\to M}-\Delta G^*_{M\to C})\right)}{A_{I\to C}\left[A_{I\to M}\exp(-\Delta G^*_{I\to M})+A_{M\to C}\exp(-\Delta G^*_{M\to C})+A_{M\to I}\exp(-\Delta G^*_{M\to I})\right]} \quad \text{(S18)}$$

where $k_{I\to C}$ and $k_{I\to M\to C}$ is the single and two step transition rates, respectively. $A = \rho\, Z\, f_{n_c}$; where Zeldovich factor, $Z = \sqrt{\frac{1}{2\pi}\left|\frac{\partial^2\beta\Delta G^*}{\partial n^2}\right|_{n_c}}$, f_{n_c} is the average attachment rate of the critical nucleus, n_c, and ρ is the number density.[15]

The values of Z shown in Fig. S4 are estimated by fitting the nucleation free energy profile, βΔG vs. n obtained from the umbrella simulation calculations with a third-order polynomial function and taking the double derivative of the function at the top of barriers with n_c= 155, 490, and 160 for I → C_{ABCD}, I → M_N, and M_N → C_{ABCD} transitions, respectively (see Fig. S4). To estimate f_{n_c} for different transitions, we performed pseudo-dynamic MC simulations where the translational and rotational steps sizes are selected such that the average translation and

rotational acceptance is ~80%. The attachment rate, $f_{n_c} = \frac{1}{2} \frac{\langle \Delta n^2(\mathrm{N_{MC}}) \rangle}{\mathrm{N_{MC}}}$ where $\mathrm{N_{MC}}$ is the number of MC cycles and the mean square deviation (MSD) of the cluster size, $\langle \Delta n^2(\mathrm{N_{MC}}) \rangle = \langle (n(\mathrm{N_{MC}}) - n_c)^2 \rangle$. We track the MSD for 15 independent configurations at the top of the barrier by measuring the cluster size for every 100 cycles. Each configuration was simulated for 10^5 MC cycles. The slope of the average MSD vs. $\mathrm{N_{MC}}$ is calculated to obtain f_{n_c}. The A in units of $\mathrm{D_L}/\sigma^5$ for $\mathrm{I} \rightarrow \mathrm{C_{ABCD}}$, $\mathrm{I} \rightarrow \mathrm{M_N}$, and $\mathrm{M_N} \rightarrow \mathrm{C_{ABCD}}$ transitions were estimated as 1.1×10^{-6}, 6.5×10^{-7}, and 4.3×10^{-6}, respectively where $\mathrm{D_L}$ is the long-time diffusion coefficient, and σ is the length of the square base in GBF27. We assume that the $A_{\mathrm{I}\rightarrow\mathrm{M}} = A_{\mathrm{M}\rightarrow\mathrm{I}}$ while calculating the $\mathrm{S_{up}}$ in Eq. S18 and also shown later in Fig. S21.

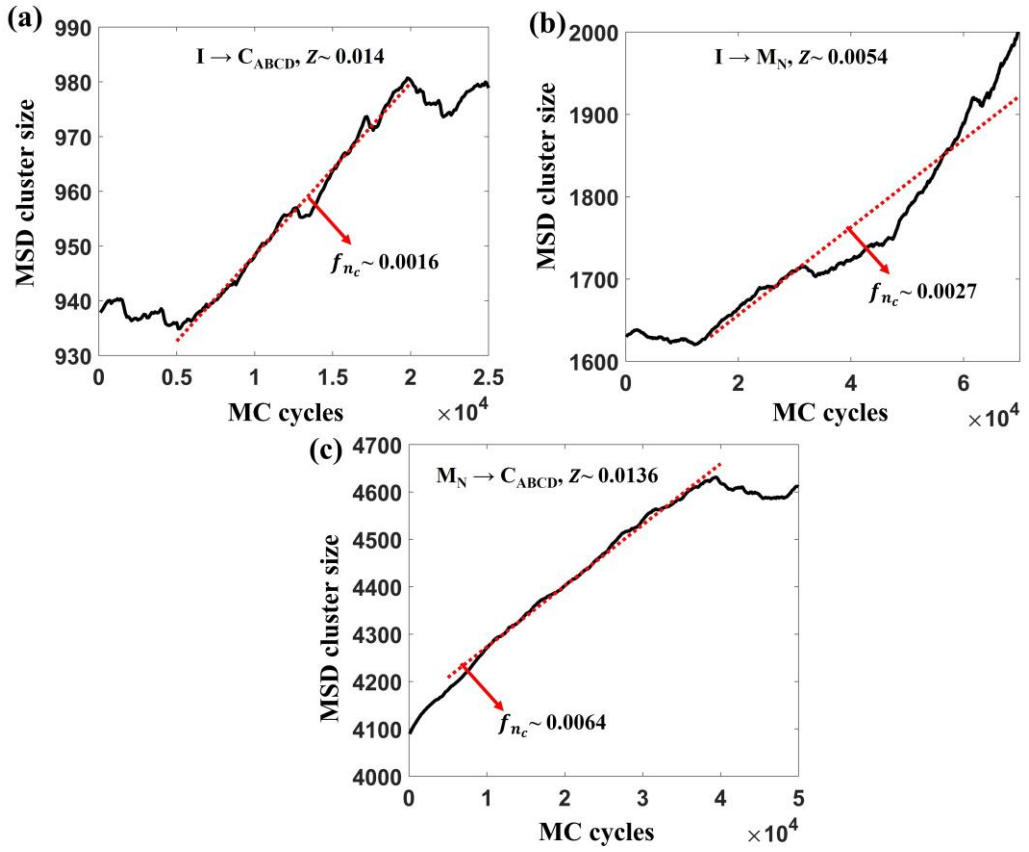

Fig S4: The mean squared deviation (MSD) of the cluster size, $\langle \Delta n^2(\mathrm{N_{MC}}) \rangle$ as function of MC cycles for (a) $\mathrm{I} \rightarrow \mathrm{C_{ABCD}}$, (b) $\mathrm{I} \rightarrow \mathrm{M_N}$, and (c) $\mathrm{M_N} \rightarrow \mathrm{C_{ABCD}}$ transitions. The cluster size was measured and averaged over 100 cycles. The slope of the average MSD vs. $\mathrm{N_{MC}}$ (red dashed line) is twice the attachment rate, f_{n_c}. The estimated Zeldovich factor, Z values for the corresponding transitions are also shown.

III. Local and global order parameters (OPs)

A. Translational Bond OPs

A1. OP to identify M_R and C_{Mink} phases in TCs

Distribution of the translationally ordered clusters with different sizes, *n* was determined using local bond order (BO) parameter proposed by Steinhardt et al.[16] The local BO is effective for US simulations as they provide a metric that indicates the degree of crystallinity irrespective of the crystalline structure. This ensures that the system evolves naturally to their inherent ordered structure during the US simulations. The local BO parameter for particle *i,* $q_{l,m}(i)$, is defined as,

$$q_{l,m}(i) = \frac{1}{N_b(i)} \sum_{j=1}^{N_b(i)} Y_{l,m}(\theta_{i,j}, \phi_{i,j}) \qquad \text{(S19)}$$

where $N_b(i)$ is the number of neighbors of particle *i*, $Y_{l,m}(\theta_{i,j}, \phi_{i,j})$ are the spherical harmonics with polar and azimuthal angles calculated between particle, *i* and neighbors, *j* ($\epsilon\ N_b(i)$). *l* is the symmetry index and *m* ranges from -*l* to *l*. We used *l*= 6 (or q_6) to study the nucleation of TCs as it has been shown to be an effective reaction coordinate for M_R and Minkowski crystal (C_{Mink}) phases.[17,18] The neighbors of particle *i* were identified based on the cutoff distance, r_c<= 1.74 for TCs with *s*= 0.90, which is ~1.2 times the first peak of the radial distribution function, g(r) (see Fig. S5a). The translation correlation function of q_6 in Eq. S19 can be obtained by using,[19]

$$d_6(i,j) = \frac{\sum_{m=-6}^{6} q_{6,m}(i)\, q_{6,m}^*(j)}{\left(\sum_{m=-6}^{6} \left|\left(q_{6,m}(i)\right)^2\right|^2\right)^{1/2} \left(\sum_{m=-6}^{6} \left|\left(q_{6,m}(j)\right)^2\right|^2\right)^{1/2}} \qquad \text{(S20)}$$

Where * denotes the complex conjugate between q_6 of particles *i* and *j* and we consider particles satisfying $d_6(i,j)$> 0.70 as translationally connected. We estimated the number of translationally connected particles, ξ_c from the central particle, *i* and the environment around *i* is considered solid-like if ξ_c>= 7. After detecting all the solid-like particles, we cluster them based on spatial proximity using a recursive clustering algorithm that identifies clusters of different sizes. Our choice of the tunable parameters such as r_c, d_6, and ξ_c were based on our earlier study[18] that was successful in capturing the free energy barriers for I → M_R and I → C_{Mink} transitions for

octahedra and TC family.

To characterize the phases while mapping the phase diagram, we calculated the global, Q_6 value defined as,

$$Q_6 = \left[\frac{4\pi}{2l+1}\sum_{m=-l}^{l}\left|\sum_{i=1}^{N} q_{6,m}(i)\right|^2\right]^{\frac{1}{2}} \quad \text{(S21)}$$

where N is the number of particles.

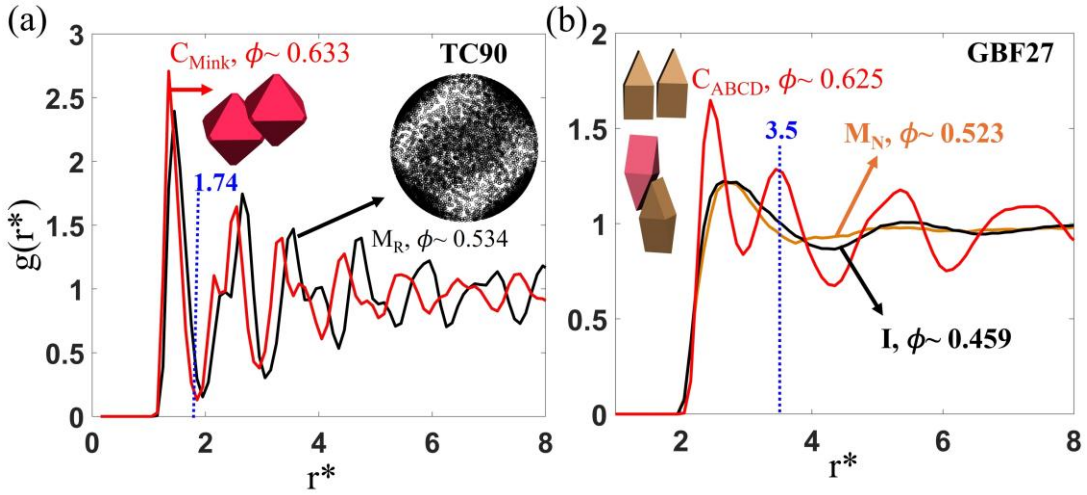

Fig S5: Comparing radial distribution functions, g(r*) for (a) TC90 and (b) GBF27 particles in I, M_R, M_N, C_{ABCD}, and C_{Mink} phases. The corresponding packing fractions, ϕ for different phases are indicated. The neighbor cutoff distance, r_c^* (a) <=1.74 for TC90 and (b) <=3.5 for GBF27 (blue dashed line) are used for US simulations. Representative configurations of particle dimers within r_c^* are also shown. (a) The orientation unit vectors of the particles in M_R phase show weak colocalized orientational ordering with discrete but connected orientational states.

A2. OPs to distinguish amorphous (I), M_G, and C_Z phases

To identify the different phases formed by the TS mixture model, we followed the recipe proposed by Bertolazzo et. al.[2] that uses the average local BO parameters $\bar{q}_l$ defined by Lechner et. al.[20] as,

$$\bar{q}_l = \sqrt{\frac{4\pi}{2l+1}\sum_{m=-l}^{l}|\bar{q}_{6m}(i)|^2} \quad \text{(S22)}$$

and,

$$\bar{q}_{lm}(i) = \frac{1}{N_b(i)} \sum_{k=0}^{N_b(i)} q_{lm}(k) \qquad \text{(S23)}$$

where $N_b(i)$ is the total number of particles, k neighboring central particle, i within a cutoff distance, r_c. $q_{lm}(k)$ is the local BO parameter defined in Eq. S19. The notations in Eqs. S22 and S23 are defined in Sec. A1.

The proposed recipe distinguishes I, M_G, and C_Z phases based on the local ordering attained by T and S particles. The details are as follows.

To identify C_Z order, we compute $\bar{q}_6$ of T particles (or $\bar{q}_6^T$) that are not four-coordinated with r_c <= 11.2 Å. The coordination number of T particles (excluding contribution from S-components) are calculated with a nearest neighbor cutoff of 4 Å. The Zeolite crystal order is detected by considering T particles that are within 8.6 Å of T's with $\bar{q}_6^T$> 0.08. We used $\bar{q}_6^T$> 0.09 at 655 K to avoid the formation of the competing lamella-like motifs.

Since both C_Z and M_G phases have ordered S particles, we distinguish between them by considering T particles (excluding the ones already detected with Zeolite order) that are within 5.7 Å of S-component having gyroid signature. The gyroid network formed by S-component was identified by computing $\bar{q}_8$ (or $\bar{q}_8^T$) and $\bar{q}_{10}$ (or $\bar{q}_{10}^T$) for S beads with r_c <=16.42 Å and selecting all S's having $\bar{q}_8^T$> 0.035 or $\bar{q}_{10}^T$> 0.02.

The remaining T and S particles that are neither identified as Zeolite nor gyroid are characterized as amorphous.

Using the above protocol, we can obtain the fraction of T particles belonging to I, M_G, and C_Z phases. For hybrid MC US simulations, we construct spatially connected clusters of T's having M_G, and C_Z signatures using the second nearest neighbor cutoff of 6 Å (see Fig. S6a). Figures S6b to S6d show the evolution of the fraction of T particles in the largest cluster identified as C_Z and M_G in the I phase while carrying out an independent unbiased MD runs at 636 K, 620 K, and 600 K. At 636 K and 600 K, we observed a spontaneous I→M_G and I→C_Z transitions, respectively and at 620 K, we observed a two-phase system containing both M_G and C_Z clusters.

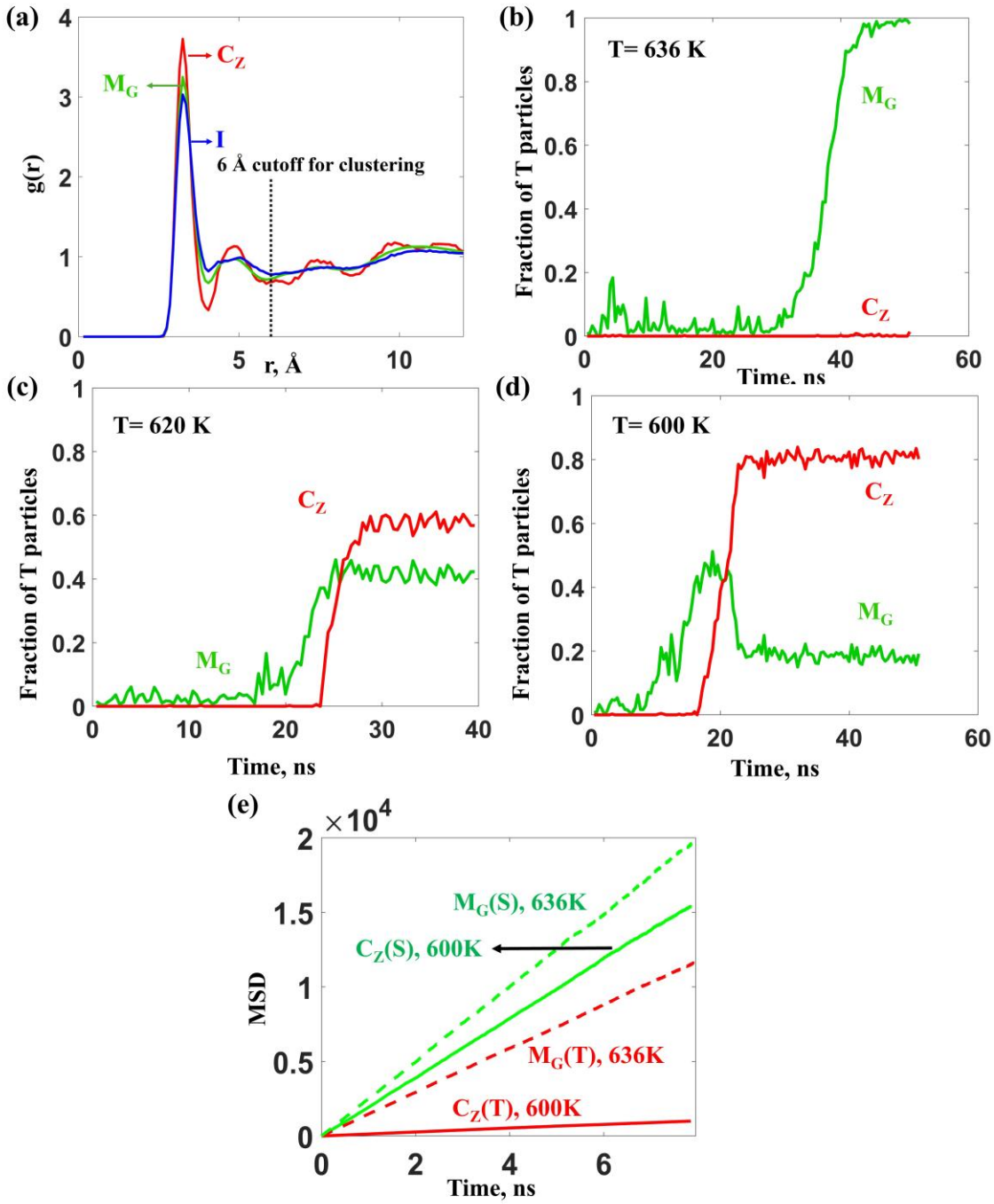

Fig S6: Comparing (a) radial distribution functions, g(r) of T-component particles in C_Z, M_G, and I phases at 600 K, 636 K, and 700 K. The distance cutoff used for clustering algorithm is also shown. (b-d) Evolution of fraction of T particles in the largest cluster identified for C_Z and M_G phases at 636 K, 620 K, and 600 K. (e) Mean square displacement of T and S particles in M_G and C_Z phases at 636 K (dashed line) and 600 K (solid line), respectively.

A3. OPs to distinguish I, M_{LAM}, and C_{LXA} phases

We used d_6 and $\bar{q}_2^{A/B}$ OPs (Eqs. 20 and 22) to estimate the cluster sizes for I → M_{LAM}, M_{LAM} → C_{LXA}, and I → C_{LXA} transitions. The C_{LXA} ordered particles were identified using $d_6(i,j)$> 0.53, where *i* and *j* are neighboring particles considering both A and B components within radial cutoff, r_c < 1.25 Å. The C_{LXA} particles have number of connections, ξ_c >=6 and the lamella ordering is identified with $\bar{q}_2^{A/B}$> 0.42[21] between the AA and BB components with r_c < 1.45 Å. Figure S7 shows the radial distribution function and the distributions of $d_6(i,j)$ and ξ_c for C_{LXA} and M_{LAM} phases at 300 K. The particles having M_{LAM} order were identified with ξ_c <6 (conditions that do not satisfy the C_{LXA} order) but $\bar{q}_2^{A/B}$> 0.42 such that the A and B particles have lamella ordering. Since the barriers are higher for I-C_{LXA} transition, we used a slightly relaxed ξ_c(>= 5) criterion to identify C_{LXA} cluster. For all the transitions, the spatially connected clusters were constructed using the nearest neighbor cutoff of 1.25 Å.

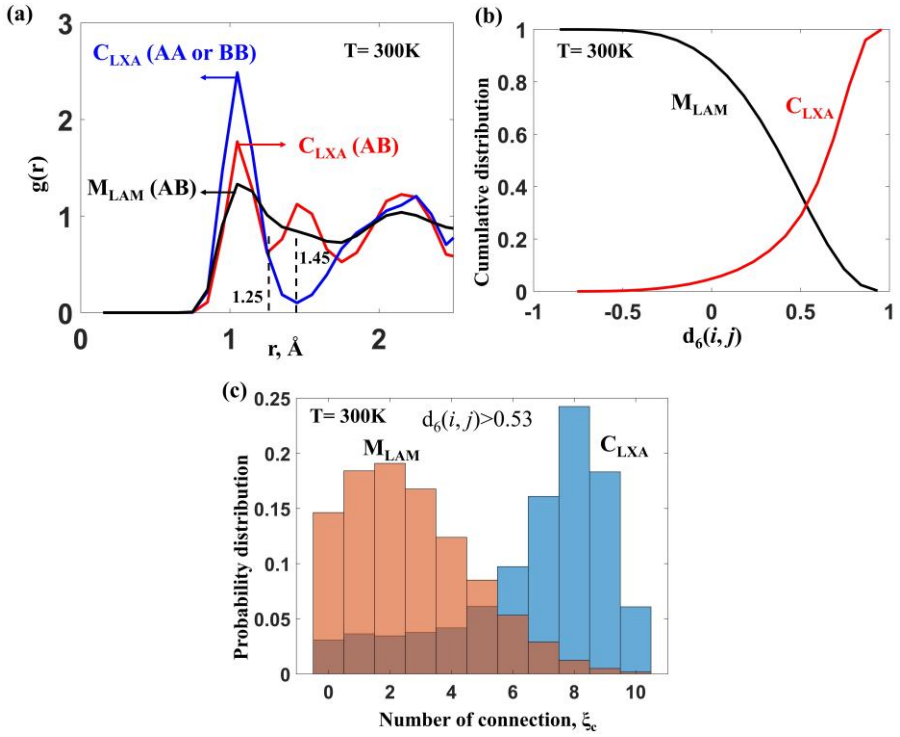

Fig S7: Comparing (a) radial distribution functions, g(r) between AB and AA/BB components in M_{LAM} and C_{LXA} and (b,c) the distributions of the local d_6 values and the number of connections, ξ_c between all particles for M_{LAM} and C_{LXA} phases at 300 K.

B. Orientational order parameters to identify mesophases and crystal structures in GBF and TC systems

B1. Local and global I_4

To capture the kinetic barriers for two-step: I→M_R and M_R → C_{Mink}, and single-step: I → C_{Mink} transitions, we used the I_4 orientational OP that estimates the particle orientation relative to an arbitrary reference coordinate frame.[22,23] Similar to q_6 (in Sec. IIIA), the spherical harmonics function in I_4 is defined as $Y_{4,m}(\Theta_i, \phi_i)$ with symmetry index 4 and Θ_k and ϕ_k are the angles associated with individual particle's axes. The local I_4 for particle i is defined as,

$$I_{4,m}(i) = \frac{\sum_{k=1}^{3} Y_{4,m}(\Theta_k,\phi_k)}{\sqrt{\sum_{m=-4}^{4}\left|\sum_{k=1}^{3} Y_{4,m}(\Theta_k,\phi_k)\right|^2}} \quad \text{(S24)}$$

The dot product for two particles i and j within cutoff r_c<= 1.74 is calculated using,

$$d_4(i,j) = \sum_{m=-4}^{4} I_{4,m}(i)\, I_{4,m}^{*}(j) \quad \text{(S25)}$$

where * implies a complex conjugate. Similar to q_6 OP, solid-like particles are identified and clustered using ξ_c>= 7 along with $d_4(i,j) > 0.70$ condition. In addition to using only I_4 for US simulations, we also used I_4 in conjugation with q_6 (Eqs. S19 and S20) to simulate the kinetic barriers between I→M_R with $d_4(i,j) < 0.70$ and $d_6(i,j) > 0.70$; and M_R→ C_{Mink} with $d_4(i,j) > 0.70$ and $d_6(i,j) > 0.70$.

To estimate the global order, we calculated I_4^{g} defined as,

$$I_4^{\mathrm{g}} = \left[\frac{4\pi}{2l+1}\sum_{m=-l}^{l}\left|\sum_{i=1}^{N} I_{4,m}(i)\right|^2\right]^{\frac{1}{2}} \quad \text{(S26)}$$

where N is the number of particles.

B2. Local and global P_2

For studying the nucleation of GBFs, we used the P_2 orientational OP to evaluate the cluster sizes with high degree of alignment along the long axis of the GBFs. The local correlation between two particles i and j is given as,

$$P_2(i,j) = \frac{3\cos^2\theta_{ij} - 1}{2} \quad \text{(S27)}$$

where θ_{ij} is the angle between the particles' long-axis vectors. The neighbor cutoff, r_c was set

at 3.5 which is ~1.21× $\sqrt{1+AR^2}$ where AR= 2.6 or 2.7 (see Fig. S5b). The optimal threshold $P_2(i,j)$ values for I → M_N, M_N → C_{ABCD}, and I → C_{ABCD} transitions were estimated as 0.60, 0.945, and 0.91, respectively, by comparing the cumulative distributions of $P_2(i,j)$ in the homogenous phases (see Figs. S8a to S8c). Figure S9 shows the $P_2(i,j)$ histograms comparing the I and M_N phases confirming the presence of pre-ordered nuclei in the I phase.

For all the transitions, we used ξ_c>= 5 as the threshold and to test the sensitivity we also used ξ_c>= 7. The ξ_c values were obtained by comparing the histograms in I, M, and C shown in Figs. S8d to S8f. Overall, by fixing the parameter values of r_c, ξ_c constant and by tuning the $P_2(i,j)$ values, we were able to control the reaction coordinate paths between I, M_N, and C_{ABCD} phases in our US simulations. As shown in Fig. S8d, ξ_c =7 is close to the average number of connections found in the nematic phase.

To characterize the phases while mapping the phase diagram, we calculated the global P_2^g value by averaging the local P_2 over all the particles.

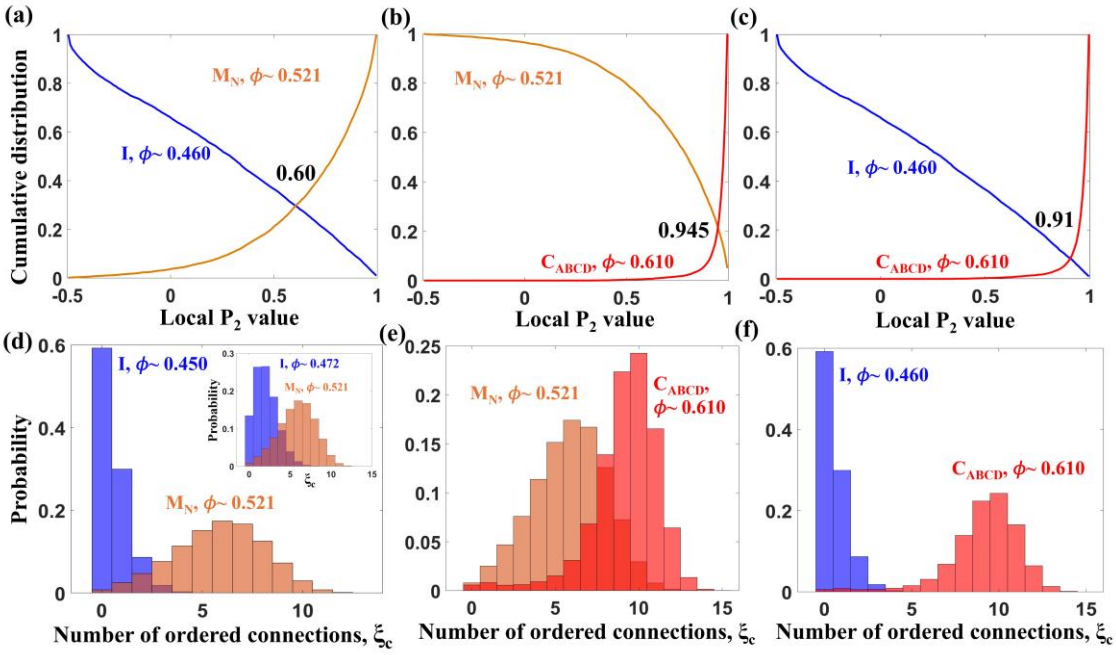

Fig S8: Probability distributions of (a-c) the local P_2 correlation and (d-e) the number of ordered connections, ξ_c for I, M_N, C_{ABCD} phases. The corresponding packing fractions, ϕ for different phases are indicated. The intersection value of the two local P_2 curves are also indicated.

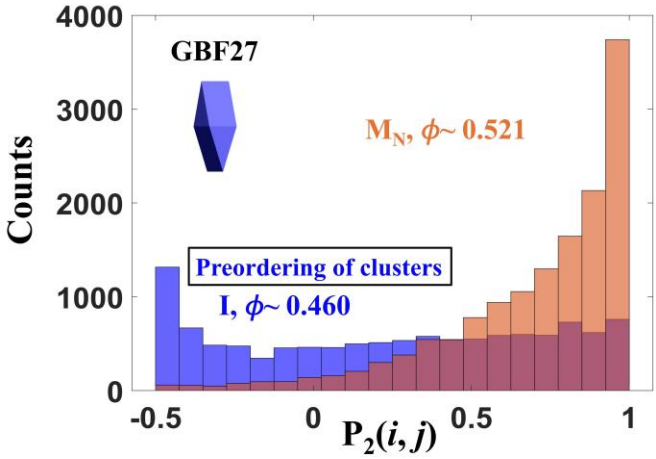

Fig S9: Distribution of local P_2 correlation values between GBF27 particles *i* and neighbor *j* in I and M_N phases. The corresponding densities of the phases are indicated. Wider local P_2 distribution observed in I phase indicates preordering of clusters.

B3. OP color scheme for visualization

To visualize the inherent order in the I, M, and C phases for the GBF and TC systems shown in Fig. 3 in the main text, we colored the particles based on the local orientational I_4 and P_2 (Eqs. S24 and S27) calculated using the protocol detailed in Sec. IIIB. The rainbow color scheme reveals the signature of local orientational ordering due to spontaneous fluctuations in the supersaturated I and M phases. To detect translational ordering, the unit bond vectors (BV) connecting the particle and its first-nearest neighbors are plotted on the surface of the sphere. The points are colored based on density of points scattered on the sphere surface with a gradient from yellow (low) to red (high).

In the TS mixture model, the T and S components identified as amorphous are colored grey. The S-particles having double-gyroid order are colored green and the T-particles identified as having Zeolite order are colored red (see Fig. 3 in the main text). The distinction between amorphous, double-gyroid, and Zeolite orders are made based on the recipe detailed in Sec. IIIA2. The C_Z and M_G cluster are represented by dynamic bonds identified with a cutoff of 4 Å and 6Å, respectively. The BV plots were obtained by identifying the unit bond vectors joining the particles that are not four-coordinated (see Sec. IIIA2) with $r_c <= 11.2$ Å.

For the AB mixture system, the A and B components are colored as magenta and white, respectively. The inter and intra-layer translational ordering is observed in the BV plot which

is obtained by plotting the unit bond vectors joining the particles with r_c <= 1.45 Å.

Figure 4 in the main text shows the critical nucleus predicted from umbrella sampling simulations for I → M and M → C, and the composite cluster for I → C transitions. For GBF and TC systems, the particles are colored based on P_2 (Eq. S27) and P_4 order parameters, respectively. The P_4 function is defined as,

$$P_4 = \max_n \frac{1}{14N} \sum_i (35\ \cos^4(u_i.\vec{n}) - 30\cos^2(u_i.\vec{n}) + 3) \qquad \text{(S28)}$$

where u_i is the unit vector of the particle and the director unit vector, $\vec{n}$ maximizing the P_4 function was obtained by following the recipe mentioned by John et. al.[23] The $\vec{n}$ was calculated for the particles in the critical nucleus. In the case of TC, all the particle axes were used for P_4 calculations. For GBFs, the dot product between particle's long-axis vectors and $\vec{n}$ were used to estimate the P_2 values. The above coloring metric was also used to visualize the interfaces between I-M_N and I-C_{ABCD} in the interfacial simulations for GBFs (see Fig. S1).

In the TS mixture model, the particles in the critical nuclei having I, M_G, C_Z characteristics shown in Fig. 4 in the main text are identified using the clustering recipe detailed in Sec. IIIA2. The T-particles having double-gyroid, and zeolite orders are colored red and represented by dynamic bonds identified with a cutoff of 4 Å. To visualize the gyroid network formed by S-particles (colored green), we used 5.7 Å as the distance cutoff to identify the S-particles neighboring the T's in M_G and C_Z nuclei. The S particles are represented as isosurface density map.

IV. Thermodynamics properties for GBF, TC, and TS model system

B. Free energy calculations

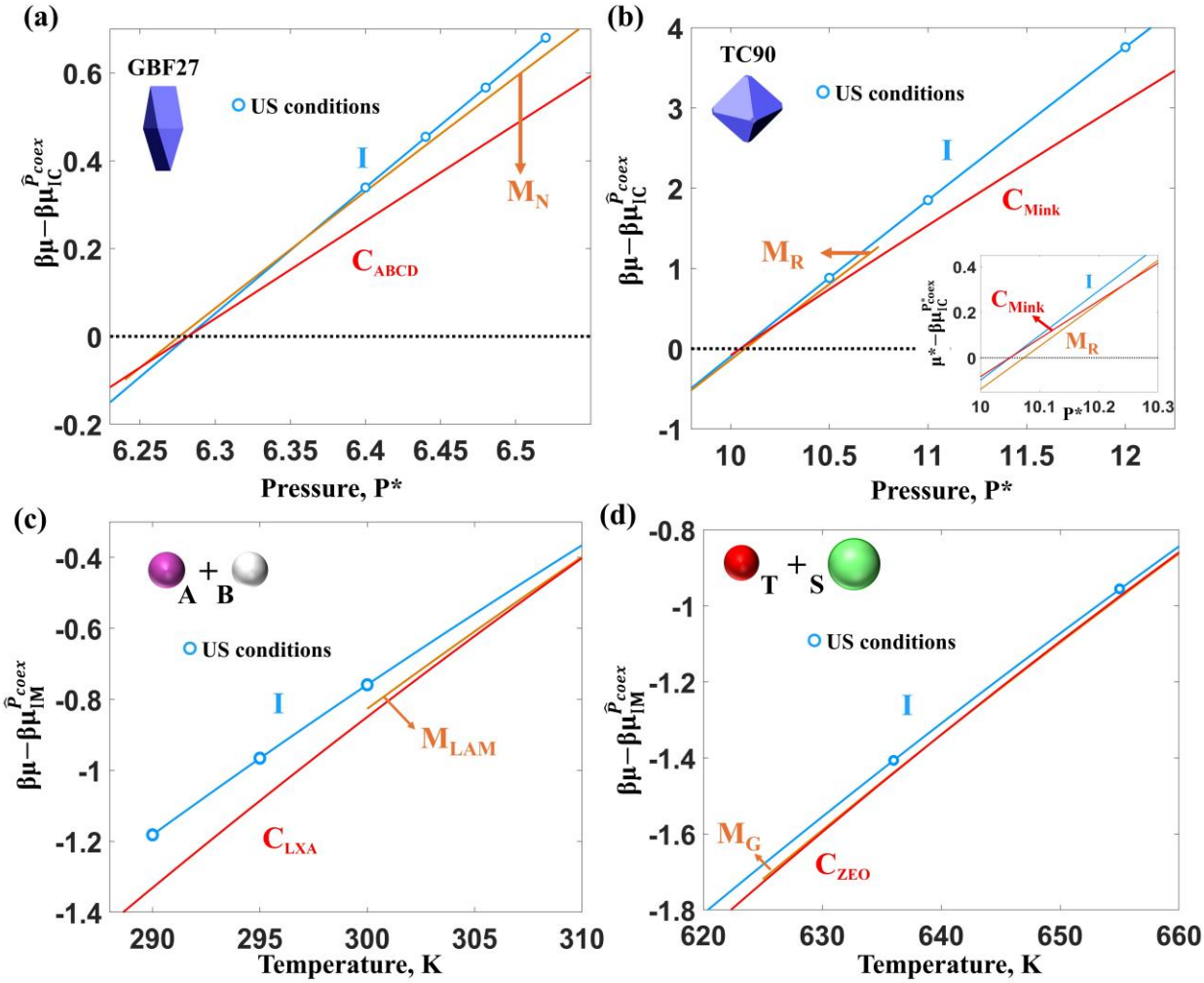

Fig. S10: Phase diagrams for GBF27, TC90, and TS systems. Chemical potential, βμ for I, M_N, M_R, C_{ABCD}, and C_{Mink} phases at different reduced pressures, P* in (a) GBF27, (b) TC90, and (c) TS mixture systems using $\beta\mu_{IC}^{\hat{P}_{coex}}$ and $\beta\mu_{IM}^{\hat{P}_{coex}}$ as the reference condition at the corresponding coexistence pressure, $\hat{P}_{coex}$. The supersaturated conditions where the umbrella sampling (US) simulations are performed are marked with cyan circles. The inset in (b) shows the intersection region of C_{Mink} free-energy curve with I and M_R. We used Second order polynomial to extrapolate the M branch in TS, AB, and TC90 models to estimate the approximate $|\beta\Delta\mu|$ between I, M, and C phases.

For GBF27, our compression simulations revealed a two-step mechanism where the I phase transitions to M_N at $\hat{P}$> 6.52 before crystallizing to C_{ABCD} at $\hat{P}$> 6.60 (see Fig. S8a). Using the equation of state (see Fig. S2a), we calculated the variation in chemical potentials, βμ shown in Fig. S10a for I, M_N, and C_{ABCD} phases using $\beta\mu_{IC}^{\hat{P}_{coex}}$ as a baseline to compare the stability of phases at different $\hat{P}$ values. We estimated that the I phase has the lowest βμ (and therefore higher stability) compared to M_N and C_{ABCD} up to I-C_{ABCD} coexistence point at $\hat{P}_{coex}$(I-C_{ABCD}) ~ 6.26, with corresponding packing densities, ϕ_I~ 0.468 and $\phi_{C_{ABCD}}$~ 0.605 (shown in Fig. S10a). This explains the hysteresis observed between the compression and expansion branches in the equation of state where C_{ABCD} phase melts directly to the I phase at $\hat{P}$< 6.0 and ϕ< 0.592. For $\hat{P}$> 6.26, the C_{ABCD} phase has the lowest βμ values compared to both I and M_N and the βμ of M_N is higher compared to both I and C_{ABCD} until the crossover is reached at $\hat{P}_{coex}$(I-M_N) ~ 6.36 with ϕ_I~ 0.471 and ϕ_{M_N}~ 0.508. For $\hat{P}$> 6.36, M_N occupies a metastable free energy well located closer to the I phase (with 0 <|$\beta\Delta\mu_{IM}$|< 0.04) than to the C_{ABCD} phase (with 0.05 <|$\Delta\mu_{MC}$|< 0.12). As a comparison to GBF27, we also mapped the equation of state for GBF26 where we observed a direct single-step transition from I→C_{ABCD} with $\hat{P}_{coex}$(I-C_{ABCD}) ~ 6.56 (see Fig. S2b).

The phase diagram and the equation of state for TC90 system with I, M_R, and C_{Mink} phases are shown in Fig. S2c and Fig. S10b, respectively. In addition to presenting a different M intermediate compared to GBF27, the $\hat{P}_{coex}$(I-C_{Mink}) which is ~10.0 occurs before the $\hat{P}_{coex}$(M_R-C_{Mink}) ~10.25. Therefore, M_R is metastable only for the narrow range of 10.25 <$\hat{P}$< 10.75, after which it crystallizes to the C_{Mink} phase. The coexistence densities for transitions involving the I, M_R and C_{Mink} are shown in Fig. S2c. For comparison, we also mapped the equation of state obtained from the compression runs for the perfect octahedra (*s*=1.0) case where the M_R phase was not observed (see Fig. S2d).

The free energy profile for the AB system is similar to TC90, where M_{LAM} is metastable for T ranging between 300 K to 320 K and becomes unstable for T<300K (see Fig. S10c). The I phase is metastable between 320 K to 290 K and transitions directly to C_{LXA} on further cooling the system below 290 K.

Figures S2f, S6, and S10d show the metastable and stable branches for I, M_G, and C_Z phases and the corresponding variation in the total potential energies and fraction of T particles in M_G, and C_Z phases during heating and cooling runs for the TS model system. We observed that the M_G phase is stable between 645-700 K, and the I→M_G transition occurred spontaneously after 30 ns equilibration run. At T<645 K, the C_Z phase is stable compared to I and M_G phases and we observed a spontaneous I→C_Z transition at 600 K (see Figs. S10c and S6d).

C. M state has intermediate entropy values between I, and C phases

Table S3. Thermodynamic properties of coexisting phases, *i-j* for GBF27, TC90, and TS model systems. P^*_{coex} and T_{coex} are the coexistence pressure and temperature, respectively. $\hat{v}$ is the specific volume per particle reduced with particle length scale as discussed in Sec. IB1. In the case of AB and TS models, unit length scales are used. u is the potential energy per particle in units of k_bT. s/k_b is the entropy per particle. i and j are the phases under study.

Shape	**Coexisting phases (*i-j*)**	$\hat{P}_{coex}/T_{coex}$	$\hat{v}_i$	$\hat{v}_j$	βu_i	βu_j	$(s_i - s_j)/k_b = \beta(u_i - u_j) + \hat{P}_{coex}(\hat{v}_i - \hat{v}_j)$
GBF27	I-C_{ABCD}	6.28	2.88	2.23	-	-	4.10
	I-M_N	6.36	2.86	2.66	-	-	1.27
	M_N-C_{ABCD}	6.25	2.73	2.24	-	-	3.06
TC90	I-C_{Mink}	10.05	1.97	1.68	-	-	2.91
	I-M_R	9.5	2.0	1.92	-	-	0.76
	M_R-C_{Mink}	10.25	1.88	1.65	-	-	2.36
TS model	I-M_G	700 K	-	-	-13.82	-14.12	0.30
	M_G-C_Z	645 K	-	-	-15.65	-15.81	0.164
AB model	I-M_{LAM}	320 K	-	-	-7.19	-7.82	0.63
	M_{LAM}-C_{LXA}	312 K	-	-	-7.87	-8.23	0.36

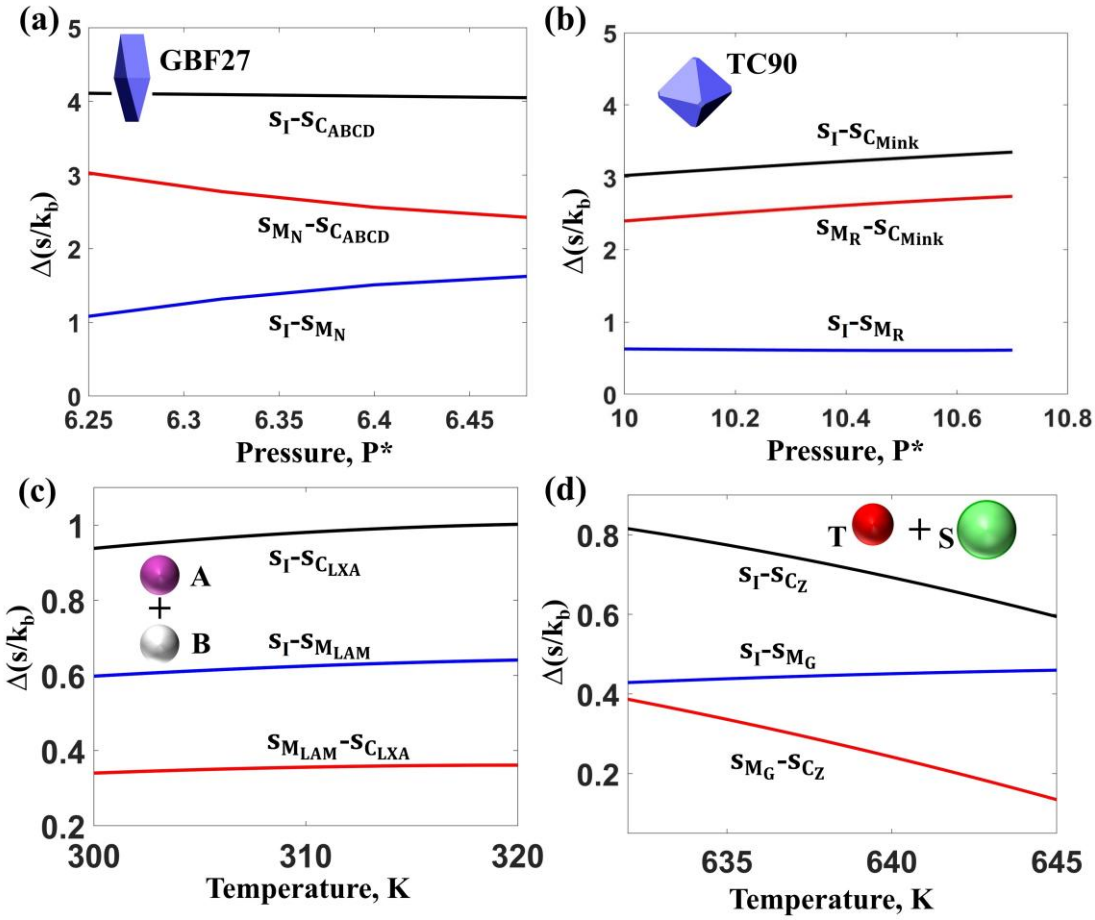

Fig. S11: Entropy difference between I, M, and C phases in (a) GBF27, (b) TC90, (c) AB, and (d) TS model systems.

V. Umbrella sampling results

A. Nucleation free energy barriers and stepwise growth of C_{ABCD} nuclei in a single-step I → C pathway for GBF27

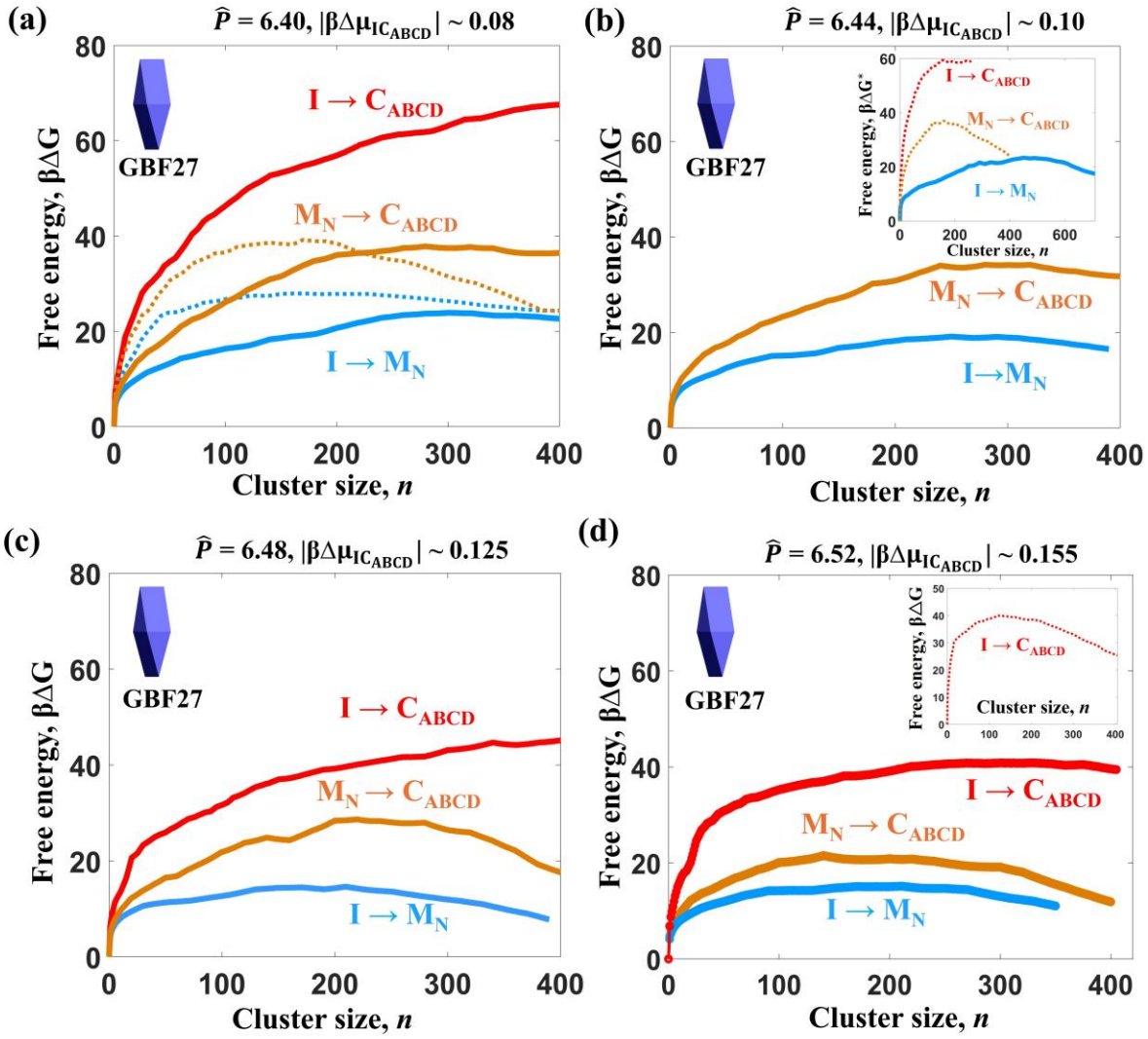

Fig. S12: Nucleation free energy barriers predicted using umbrella sampling for GBF27 at different degree of supersaturation, $|\beta\Delta\mu_{IC_{ABCD}}|$ (or reduced pressure, $\hat{P}$) during I → M_N, M_N→C_{ABCD}, I → C_{ABCD} transitions. The order parameters used to identify different cluster sizes are described in Sec.III B2. Solid and dashed lines are simulated with ξ_c >=5 and 7, respectively. 1728 and 2916 (insets) particles are used for calculations.

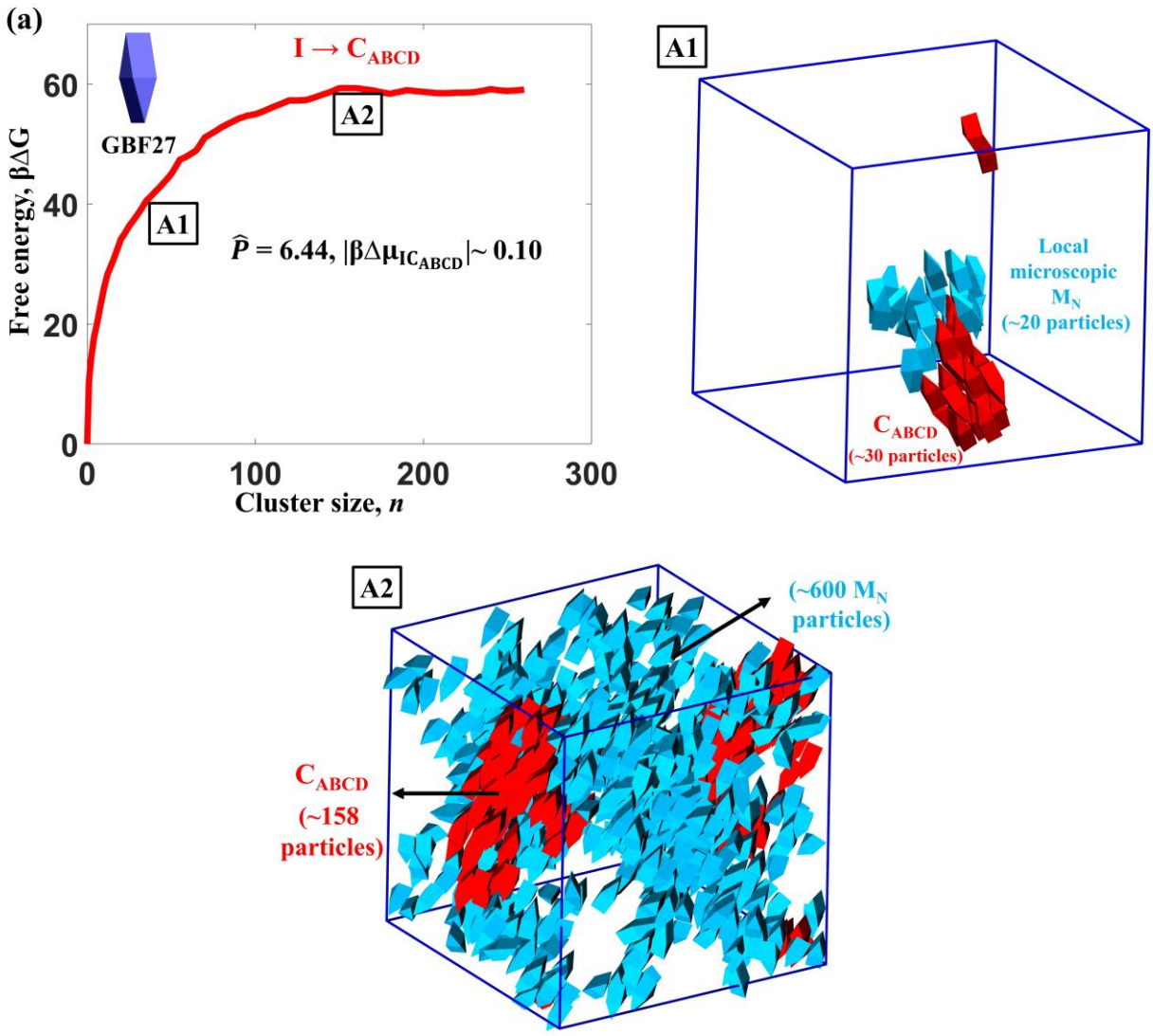

Fig. S13: (a) Nucleation free energy barriers for GBF27 at $|\beta\Delta\mu_{IC_{ABCD}}|\sim 0.10$ (or reduced pressure, $\hat{P}$= 6.44) during I → C_{ABCD} transition. A1 and A2 show the representative snapshot of C_{ABCD} nucleus with local microscopic (A1) and macro clusters (A2) of M_N. The order parameters used to identify different cluster sizes are described in Sec.III B2. M_N particles were identified using 0.60 <$P_2(i,j)$ < 0.91 and ξ_c >=5 for clustering; C_{ABCD} particles were identified with $P_2(i,j)$ > 0.91 and ξ_c >=7.

B. GBF26 has higher I→C_{ABCD} free-energy barriers compared to GBF27

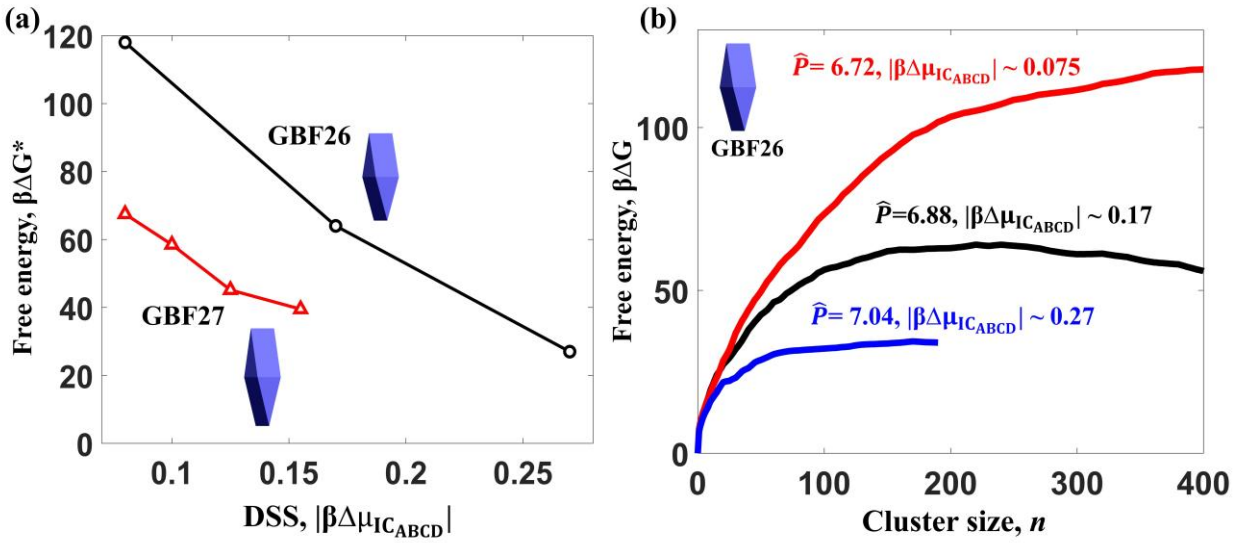

Fig. S14: Single-step I→C_{ABCD} free-energy barriers for (a) GBF26 and GBF27, and (b) the nucleation free-energy profiles for GBF26 at different degree of supersaturation, $|\beta\Delta\mu_{IC_{ABCD}}|$ (or reduced pressure, $\hat{P}$). The equation of state mapped for GBF26 and GBF27 systems are discussed in Secs. IB and IC.

C. Nucleation free-energy barriers and growth of C_{mink} nuclei in a single-step I → C pathway for TC90

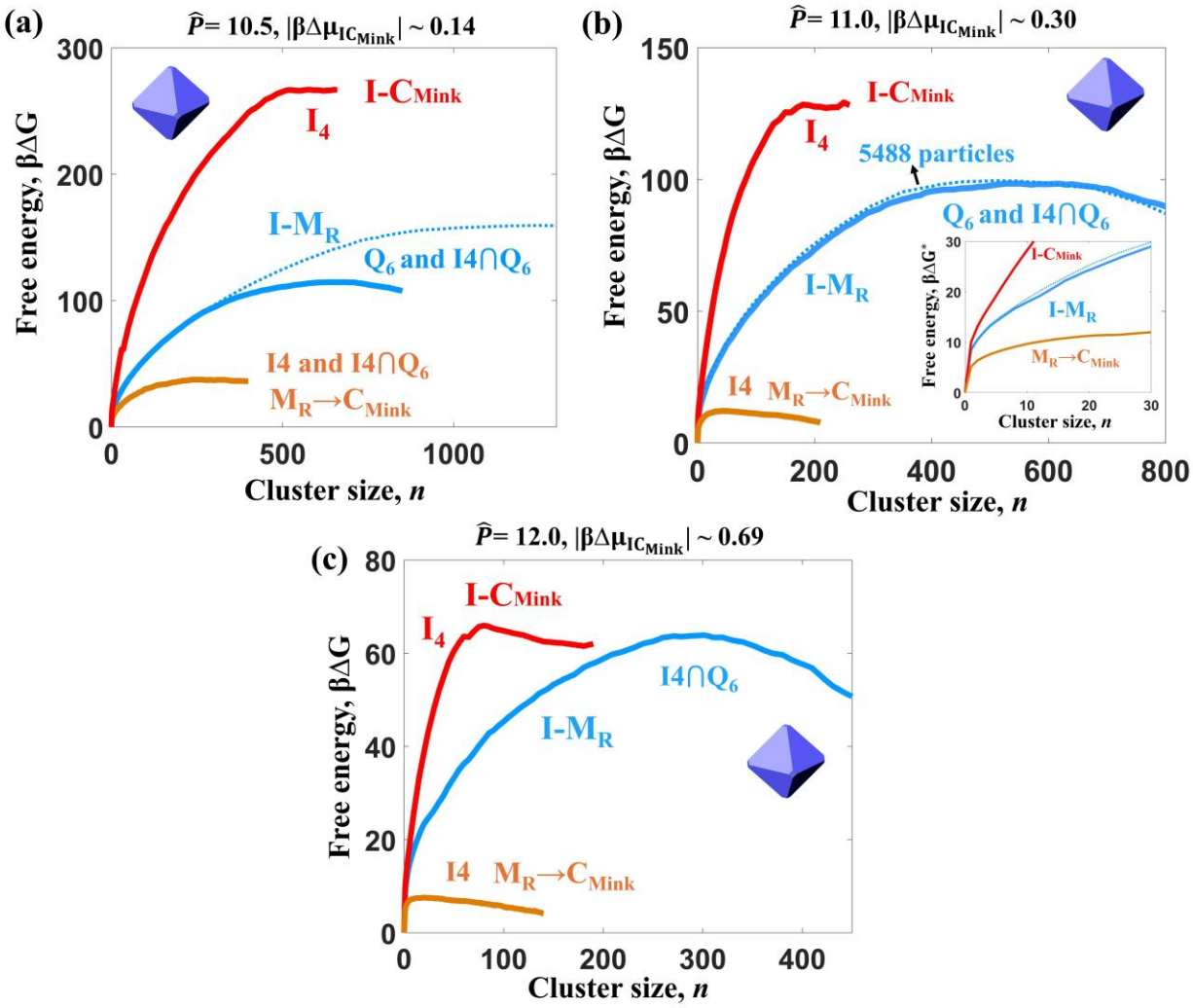

Fig. S15: Nucleation free energy barriers predicted using umbrella sampling simulations for TC90 at different degrees of supersaturation, $|\beta\Delta\mu_{IC_{Mink}}|$ (or reduced pressure, $\widehat{P}$) for I → M_R, M_R → C_{Mink}, I → C_{Mink} transitions. The order parameters used to identify different cluster sizes are described in Secs. III A and B1. System sizes of 2744 (solid curves) and 5788 (dashed curves) particles were simulated. Inset in (b) shows the free energy profiles plotted with a different scale.

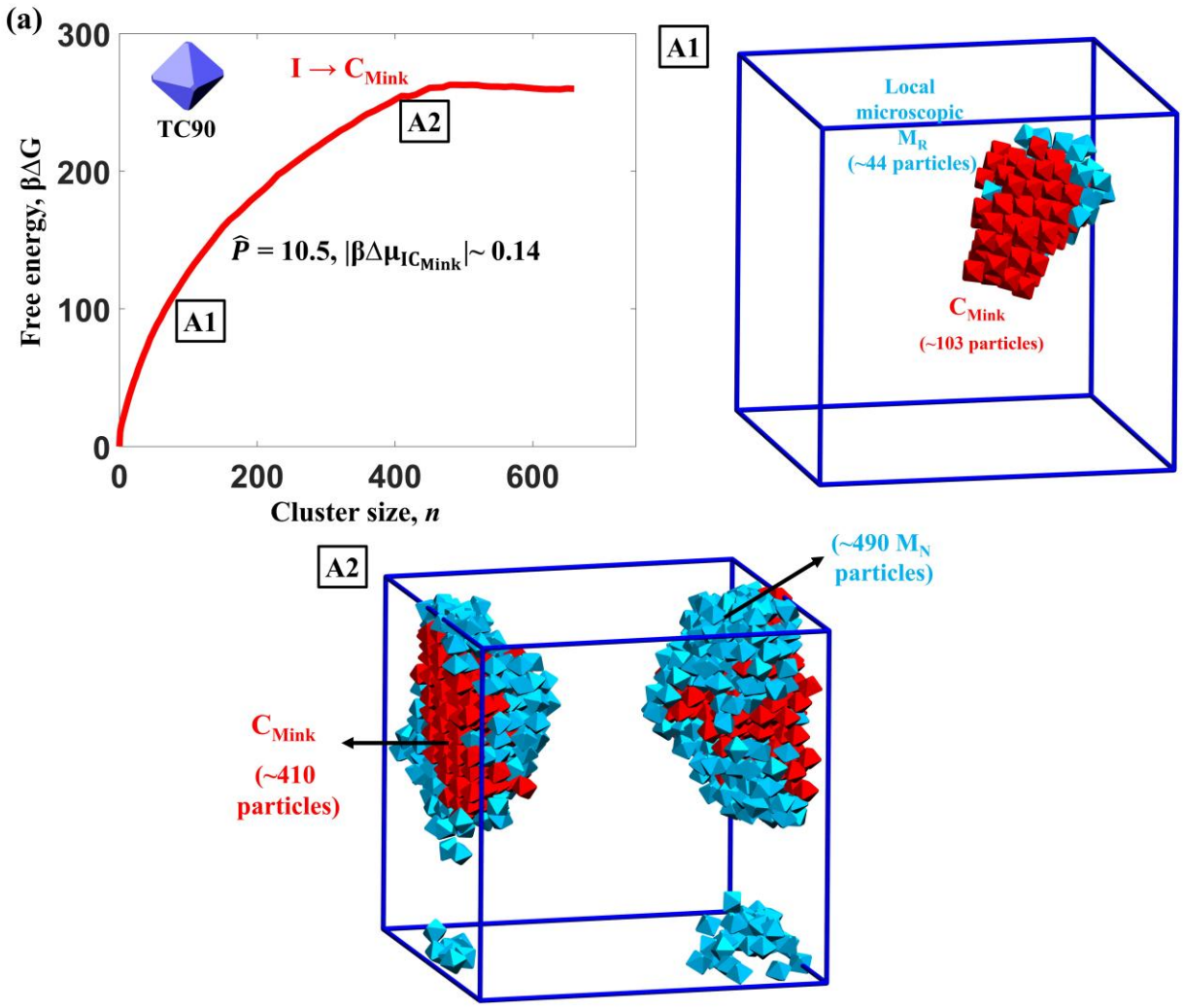

Fig. S16: (a) Nucleation free energy barriers for TC90 at $|\beta\Delta\mu_{IC_{Mink}}|\sim 0.14$ (or reduced pressure, $\hat{P}$= 10.5) during I → C_{Mink} transition with 5488 particles. A1 and A2 show the representative snapshot of C_{Mink} nucleus with local microscopic clusters (A1 and A2) of M_R. I_4 in conjugation with q_6 were used to identify different cluster sizes are described in Sec.III A1 and B1. The M_R and C_{Mink} particles were identified using $d_4(i,j) < 0.70$ and $d_6(i,j) > 0.70$ and $d_4(i,j) > 0.70$ and $d_6(i,j) > 0.70$, respectively. For both cases we selected ξ_c >=7.

D. Nucleation free-energy barriers and growth of CLXA during I → C_{LXA} transition for AB mixture model

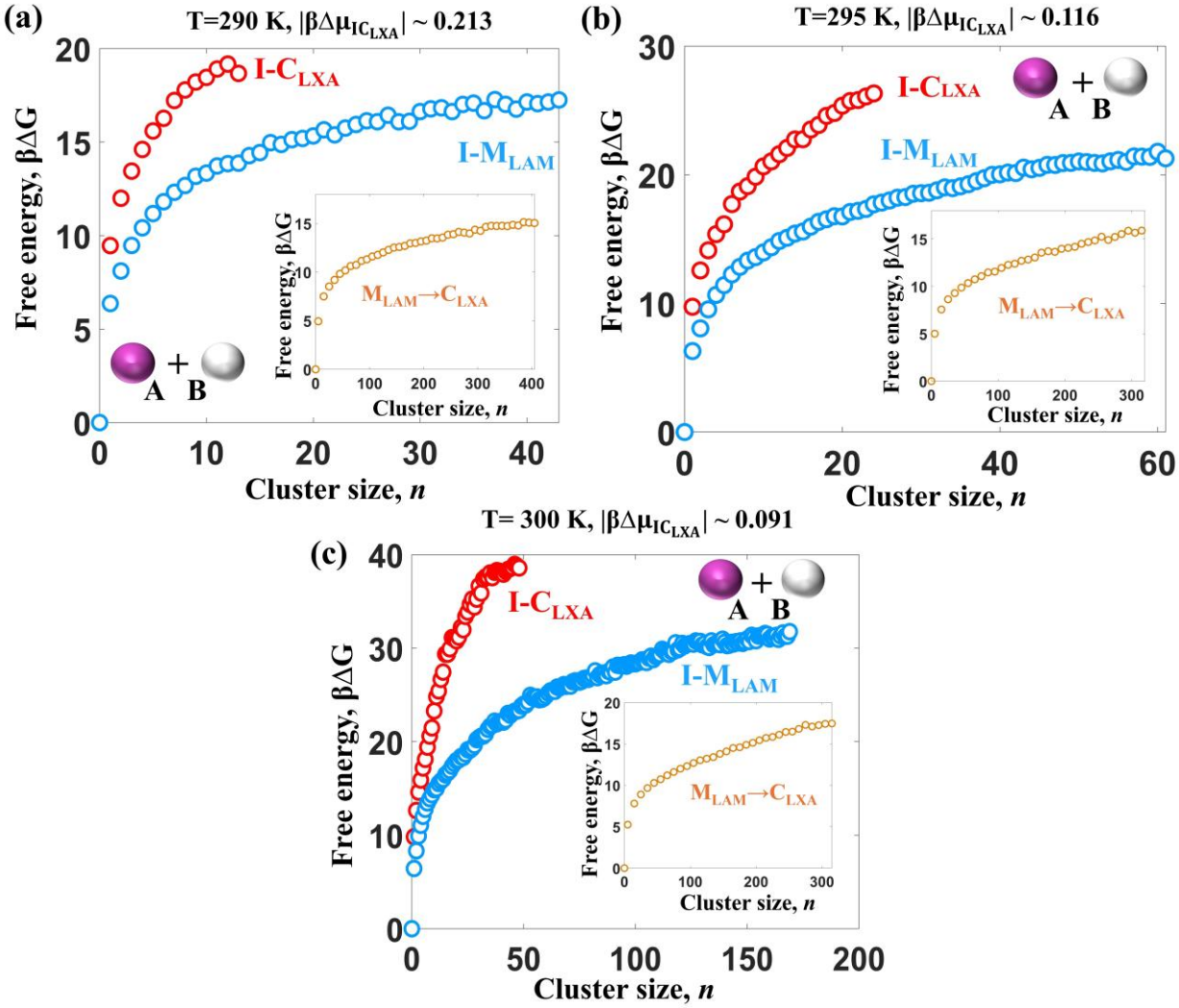

Fig. S17: Nucleation free energy barriers predicted using umbrella sampling simulations for AB model at different degrees of supersaturation, $|\beta\Delta\mu_{IC_{LXA}}|$ (or temperature, T) for I → M_{LAM}, M_{LAM} → C_{LXA}, I → C_{LXA} transitions. The order parameters used to identify different cluster sizes are described in Sec. III A3. Insets show the free energy profiles for M_{LAM} → C_{LXA} transition.

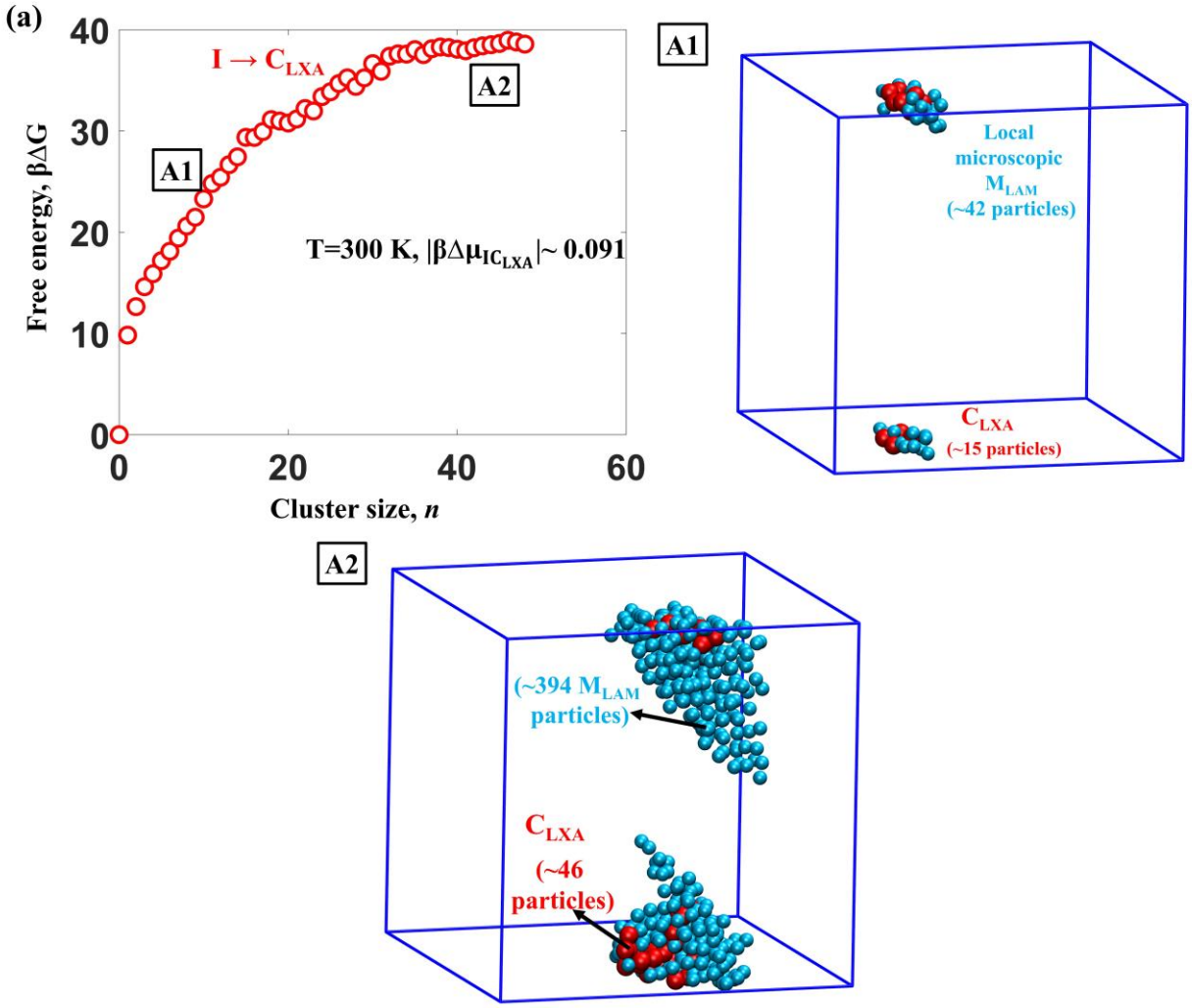

Fig. S18: (a) Nucleation free energy barriers for AB model at $|\beta\Delta\mu_{IC_{LXA}}|\sim 0.091$ (or temperature, T= 300 K) during I → C_{LXA} transition. A1 and A2 show the representative snapshot of C_{LXA} nucleus with local microscopic clusters (A1 and A2) of M_{LAM}. The criterion to identify different clusters are described in Sec. III A3.

E. Nucleation free-energy barriers and growth of CZ nucleus during I → Cz transitions for TS mixture model

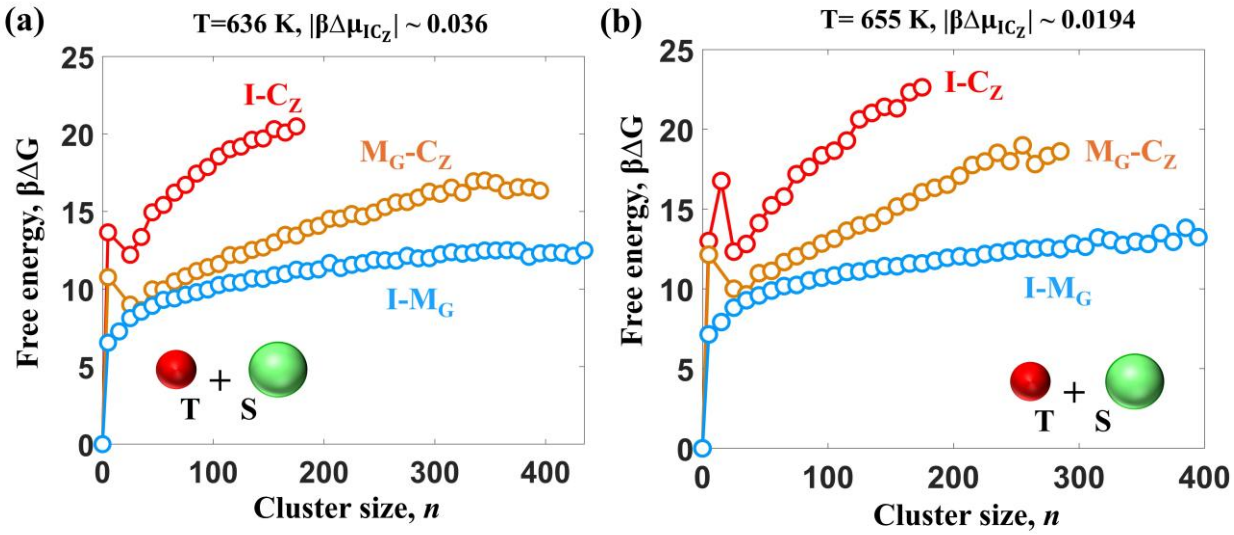

Fig. S19: Nucleation free energy barriers predicted using umbrella sampling simulations for TS mixture model at different degrees of supersaturation, $|\beta\Delta\mu_{IC_Z}|$ (or temperature, T) for I → M_G, M_G → C_Z, I → C_Z transitions. The order parameters used to identify different cluster sizes are described in Sec. III A2.

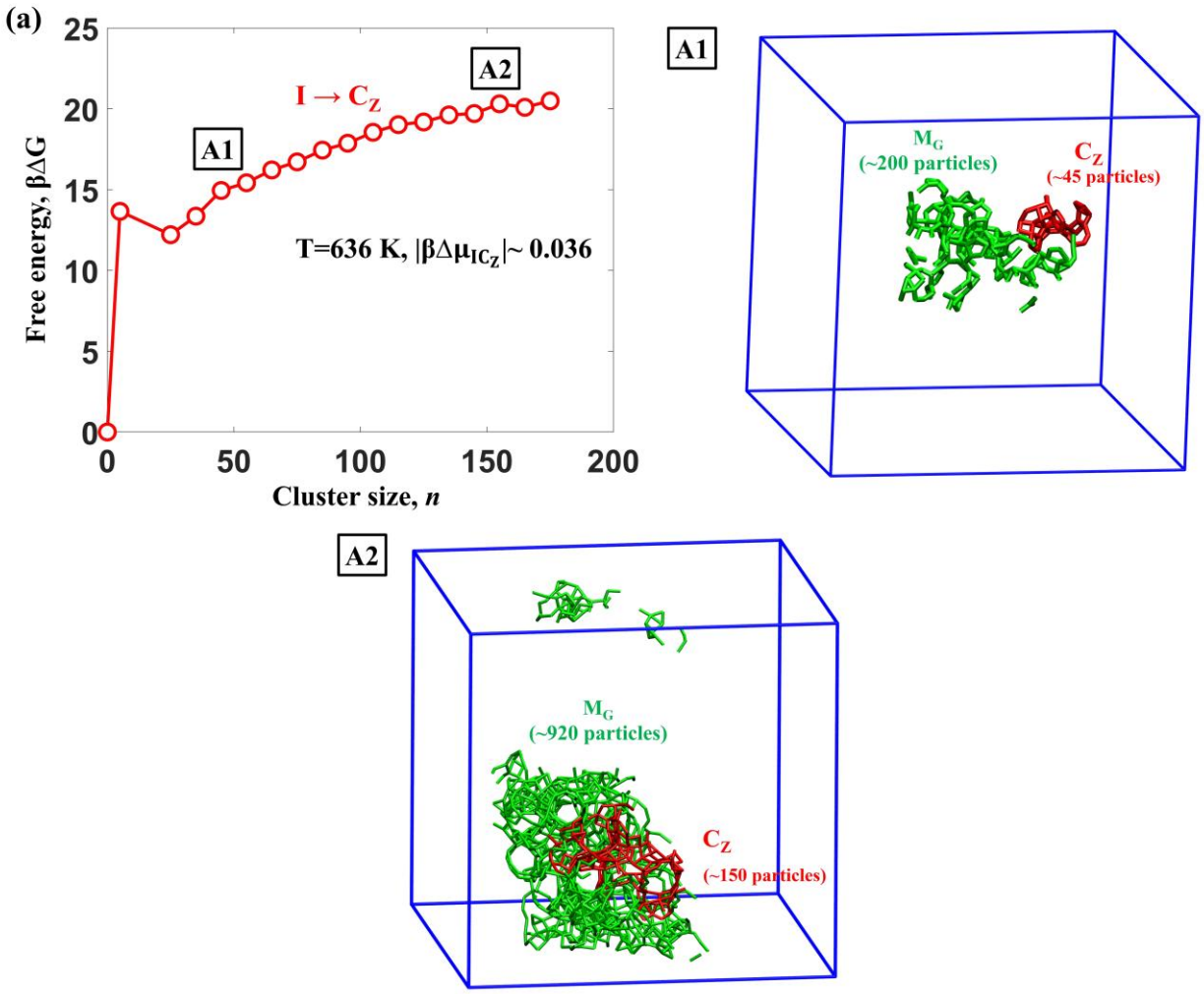

Fig. S20: (a) Nucleation free energy barriers for AB model at $|\beta\Delta\mu_{IC_Z}|\sim 0.036$ (or temperature, T= 636 K) during I → C_Z transition. A1 and A2 show the representative snapshot of C_Z nucleus with local microscopic clusters (A1 and A2) of M_G. The OP to identify different clusters are described in Sec.III A2. The M_G and C_Z clusters are represented by dynamic bonds within a distance cutoff of 4 Å.

F. Speed-up factor for different models

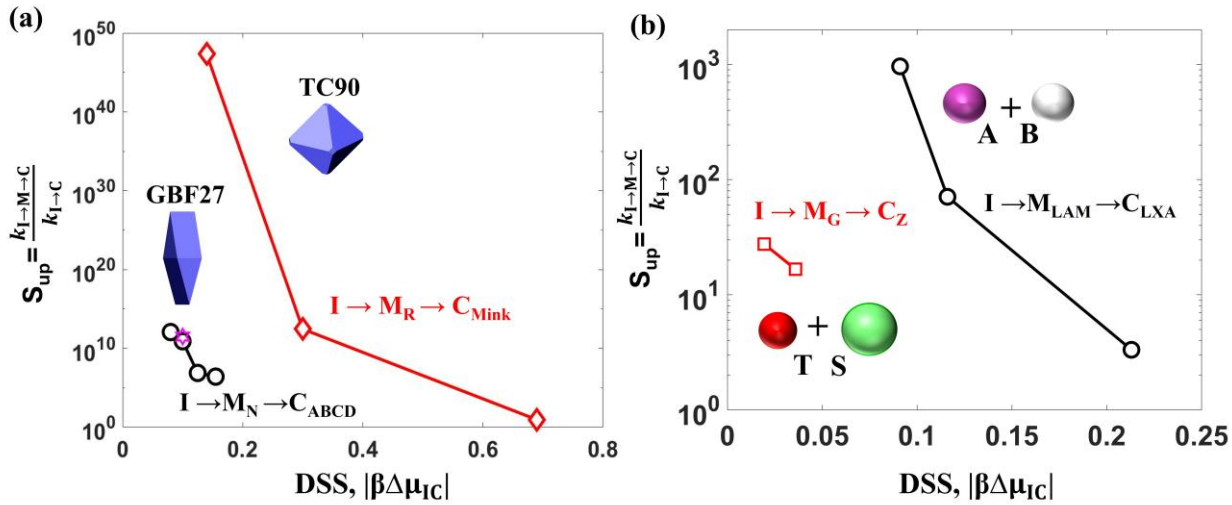

Fig. S21: Speed-up, S_{up} ratios for GBF27, TC90, AB, and TS models. Comparison of rates $\dot{r}$ associated with a single I → C and two-step I → M → C transitions for GBF27 (circles), TC90 (diamonds), and TS mixture (triangles) models at different DSS using Eq. (3). Hexagram marker shows S_{up} for GBF27 at DSS~ 0.10 accounting for the kinetic prefactors.

G. Estimation of interfacial surface energies

Table S4: Interfacial surface energy, γ and enthalpy differences between the phases of interest at 636 K and 300 K for TS and AB models, respectively. Turnbull empirical correlation[24] is used to estimate $\gamma_{ij} = \lambda\ \Delta H_{ij}\ (\nu_j)^{\frac{-2}{3}}\ (N_A)^{\frac{-1}{3}}\ N^{-1}$, where λ= 0.405 is empirically determined constant, ΔH_{ij} is the enthalpy difference between the phases *i* and *j*, ν_j is the molar volume of the phase *j*. N_A and N is the Avogadro's number, and the total number of particles, respectively. We used 28.0855 g/mol for estimating molar volume for TS and AB systems. The γ values for I-GYR and GYR-ZEO are qualitatively similar those reported by Bertolazzo et. al.[2]

Model	Transition phases (*i-j*)	Temperature, K	γ_{ij}, mJ/m^{-2}	υ_j (m^3/mol)	ΔH_{ij} (kJ/mol)
TS	I-GYR	636	9.6	3.47×10^{-5}	34759.793
	GYR-ZEO	636	6.4	3.46×10^{-5}	23039.698
AB	I-LAM	300	22.7	1.38×10^{-5}	37731.121
	LAM-LXA	300	12.3	1.385×10^{-5}	20465.914

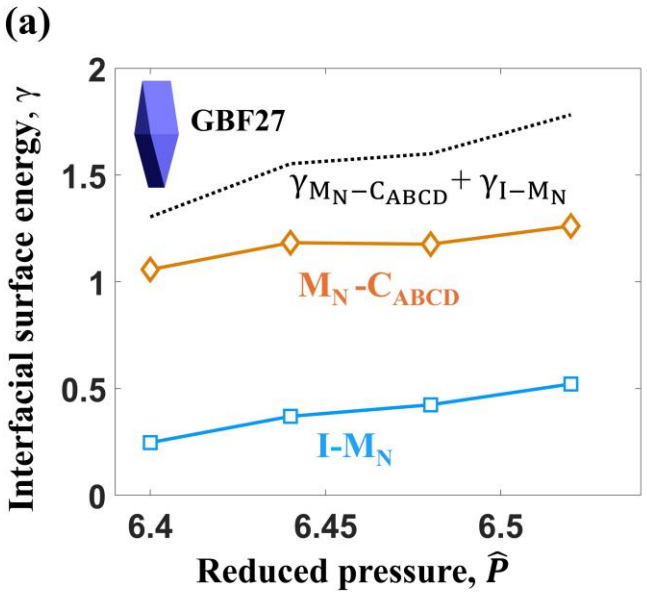

(b)

TC90

$\hat{P}$	Phases	$\lvert\beta\Delta\mu\rvert$	$\beta\Delta G^*$	γ
10.5	I-M_R	0.079	158	1.88
	M_R-C_{Mink}	0.071	40	1.10

Fig. S22: Variation in interfacial free energy, γ for different reduced pressure, $\hat{P}$ between phases of interest in (a) GBF27 and (b) TC90 systems. γ is estimated using approximate classical nucleation theory, where $\gamma = \sqrt[3]{(27/4)\beta\Delta G^* |\beta\Delta\mu|^2}$.

H. Mean first passage time for different transitions

Table S5: Mean first passage time, τ for models with I → C, I → M, and M → C transitions at their respective $|\beta\Delta\mu_{IC}|$ conditions. D_o is the constant rate of attachment of particles to the cluster.

Model	$\lvert\beta\Delta\mu_{IC}\rvert$	$D_o\tau_{IC}$	$D_o\tau_{IM}$	$D_o\tau_{MC}$
GBF	0.08	4.42×10^{30}	6.5×10^{11}	6.0×10^{17}
	0.155	2.2×10^{19}	1.65×10^{8}	2.5×10^{10}
TC	0.14	5.72×10^{116}	2.35×10^{51}	4.3×10^{17}
	0.69	2.34×10^{29}	9.60×10^{28}	1.64×10^{4}
AB	0.091	1.34×10^{17}	1.63×10^{14}	5.2×10^{9}
	0.213	2.80×10^{8}	1.70×10^{8}	3.7×10^{8}
TS	0.036	7.30×10^{10}	7.60×10^{7}	3.15×10^{9}
	0.0194	3.70×10^{11}	1.50×10^{8}	1.16×10^{10}

References

1. Gantapara, A. P., de Graaf, J., van Roij, R. & Dijkstra, M. Phase behavior of a family of truncated hard cubes. *J. Chem. Phys.* **142**, (2015).
2. Bertolazzo, A. A., Dhabal, D., Lopes, L. J. S., Walker, S. K. & Molinero, V. Unstable and Metastable Mesophases Can Assist in the Nucleation of Porous Crystals. *J. Phys. Chem. C* **126**, 3776–3786 (2022).
3. Stillinger, F. H. & Weber, T. A. Computer simulation of local order in condensed phases of silicon. *Phys. Rev. B* **31**, 5262–5271 (1985).
4. Molinero, V. & Moore, E. B. Water modeled as an intermediate element between carbon and silicon. *J. Phys. Chem. B* **113**, 4008–4016 (2009).
5. Thompson, A. P. *et al.* LAMMPS - a flexible simulation tool for particle-based materials modeling at the atomic, meso, and continuum scales. *Comput. Phys. Commun.* **271**, 108171 (2022).
6. Kumar, A. & Molinero, V. Self-Assembly of Mesophases from Nanoparticles. *J. Phys. Chem. Lett.* **8**, 5053–5058 (2017).
7. De Graaf, J., Filion, L., Marechal, M., Van Roij, R. & Dijkstra, M. Crystal-structure prediction via the Floppy-Box Monte Carlo algorithm: Method and application to hard (non)convex particles. *Journal of Chemical Physics* vol. 137 214101 at https://doi.org/10.1063/1.4767529 (2012).
8. Nosé, S. A unified formulation of the constant temperature molecular dynamics methods. *J. Chem. Phys.* **81**, 511–519 (1984).
9. Thapar, V. & Escobedo, F. A. Extensions of the interfacial pinning method and application to hard core systems. *J. Chem. Phys.* **141**, (2014).
10. Pedersen, U. R., Hummel, F., Kresse, G., Kahl, G. & Dellago, C. Computing Gibbs free energy differences by interface pinning. *Phys. Rev. B* **88**, 094101 (2013).
11. Sharma, A. K. & Escobedo, F. A. Effect of particle anisotropy on the thermodynamics and kinetics of ordering transitions in hard faceted particles. *J. Chem. Phys.* **158**, (2023).
12. Auer, S. & Frenkel, D. Numerical prediction of absolute crystallization rates in hard-

sphere colloids. *J. Chem. Phys.* **120**, 3015–3029 (2004).

13. Guo, J., Haji-Akbari, A. & Palmer, J. C. Hybrid Monte Carlo with LAMMPS. *J. Theor. Comput. Chem.* **17**, 1840002 (2018).
14. Gonzalez, M. A. *et al.* Nucleation free-energy barriers with Hybrid Monte-Carlo/Umbrella Sampling. *Phys. Chem. Chem. Phys.* **16**, 24913–24919 (2014).
15. Filion, L., Hermes, M., Ni, R. & Dijkstra, M. Crystal nucleation of hard spheres using molecular dynamics, umbrella sampling, and forward flux sampling: A comparison of simulation techniques. *J. Chem. Phys.* **133**, (2010).
16. Steinhardt, P. J., Nelson, D. R. & Ronchetti, M. Bond-orientational order in liquids and glasses. *Phys. Rev. B* **28**, 784–805 (1983).
17. Thapar, V. & Escobedo, F. A. Localized Orientational Order Chaperones the Nucleation of Rotator Phases in Hard Polyhedral Particles. *Phys. Rev. Lett.* **112**, 048301 (2014).
18. Sharma, A. K., Thapar, V. & Escobedo, F. A. Solid-phase nucleation free-energy barriers in truncated cubes: interplay of localized orientational order and facet alignment. *Soft Matter* **14**, 1996–2005 (2018).
19. Rein ten Wolde, P., Ruiz-Montero, M. J. & Frenkel, D. Numerical calculation of the rate of crystal nucleation in a Lennard-Jones system at moderate undercooling. *J. Chem. Phys.* **104**, 9932–9947 (1996).
20. Lechner, W. & Dellago, C. Accurate determination of crystal structures based on averaged local bond order parameters. *J. Chem. Phys.* **129**, 114707 (2008).
21. Kumar, A. & Molinero, V. Why Is Gyroid More Difficult to Nucleate from Disordered Liquids than Lamellar and Hexagonal Mesophases? *J. Phys. Chem. B* **122**, 4758–4770 (2018).
22. Agarwal, U. & Escobedo, F. A. Mesophase behaviour of polyhedral particles. *Nat. Mater.* **10**, 230–235 (2011).
23. John, B. S., Juhlin, C. & Escobedo, F. A. Phase behavior of colloidal hard perfect tetragonal parallelepipeds. *J. Chem. Phys.* **128**, 044909 (2008).
24. Turnbull, D. Formation of Crystal Nuclei in Liquid Metals. *J. Appl. Phys.* **21**, 1022–1028 (1950).

CHAPTER 2: Re-entrant transition as a bridge of broken ergodicity in confined colloidal hexagonal prisms and cylinders

B.P. Prajwal[1], Jen-Yu Huang[1], Meera Ramaswamy[2], Tobias Hanrath[1], Itai Cohen[2], Abraham D. Stroock[1], Fernando A. Escobedo[*,1]

[1]Department of Chemical and Biomolecular Engineering, Cornell University, Ithaca, New York 14853, USA

[2]Department of Physics, Cornell University, Ithaca, New York 14853, USA

Graphical Abstract

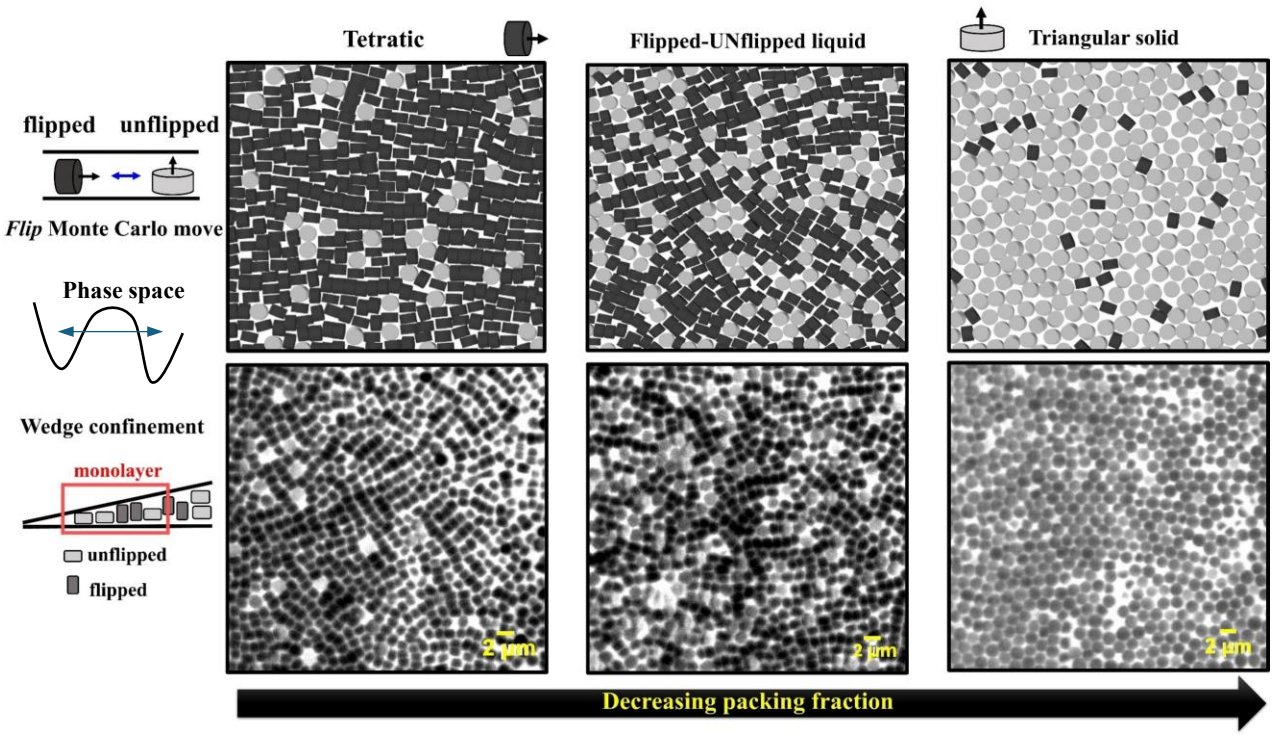

Abstract

The entropy-driven monolayer assembly of hexagonal prisms and cylinders was studied under hard slit confinement. At the conditions investigated, the particles have two distinct and dynamically disconnected rotational states: unflipped and flipped, depending on whether their circular/hexagonal face is parallel or perpendicular to the wall plane. Importantly, these two rotational states cast distinct projection areas over the wall plane that favor either hexagonal or tetragonal packing. Monte Carlo simulations revealed a re-entrant melting transition where an intervening disordered Flipped-Unflipped (FUN) phase is sandwiched between a fourfold tetratic phase at high concentrations and a sixfold triangular solid at intermediate concentrations. The FUN phase contains a mixture of flipped and unflipped particles and is translationally and orientationally disordered. Complementary experiments were conducted with photolithographically fabricated cylindrical microparticles confined in a wedge cell. Both simulations and experiments show the formation of phases with comparable fraction of flipped particles and structure, i.e., the FUN phase, triangular solid, and tetratic phase, indicating that both approaches sample analogous basins of particle-orientation phase-space. The phase behavior of hexagonal prisms in a soft-repulsive wall model was also investigated to exemplify how tunable particle-wall interactions can provide an experimentally viable strategy to dynamically bridge the flipped and unflipped states.

Keywords: Anisotropic colloids, re-entrant phase transition, monolayer confinement, self-assembly

1. Introduction

Assemblies of colloidal particles have promising functional applications as active constituents of photovoltaic devices [1], optical films [2], and catalysts [3]. Recent advances in the synthetic and fabrication approaches of faceted sub-micron particles with different shapes have spurred interest in using these particles as basic building blocks for the assembly of targeted complex structures. The type of order and symmetry of these structures can be tuned by controlling such properties as particle geometry [4,5], interparticle interactions (e.g., chemical patchiness) [5], depletion forces [6–8], and external fields including hard/soft wall confinement [9–13]. Entropic and external forces play a crucial role in the assembly of nanoparticles, and their interplay is being systematically delineated by studies that focus on the effects of each driving force separately.

A large variety of superstructures arises when polyhedral colloidal particles are assembled at fluid interfaces [14] or inside confined geometries such as within parallel hard plate/wedge cell [10,15], spherical [16,17], or square cavities [18]. The confinement effects can drastically change the phase behavior of the system and be dominant when only a few particle layers can be accommodated along at least one direction. For hard spheres, for example, in contrast to the single isotropic to crystal phase transition in the bulk, a rich phase behavior was observed when confined between two parallel hard plates as the plate separation was varied to only accommodate one-to-a-few particle layers [9]. Numerous computational and experimental investigations have been carried out to explore the phase transitions in slit confinement with a variety of particle shapes, including members of the truncated cubes family [10], spherical or mushroom caps [12,19], hard rectangles [20], hard rods [18], hard platelets [21], and dimers [13,22,23]. The results from these studies have provided an understanding of the combined effects of particle anisotropy and confinement length. An interesting attribute associated with the parallel slit confinement model is that it allows access to the two-dimension (2D) and quasi-2D behavior by just altering the confinement separation: The phase behavior can drastically change depending on the particles' accessibility to rotational and translational states across the gap.

This work is focused on mapping the thermodynamic phase behavior of two anisotropic convex shaped particles; namely, hexagonal prisms (HPs), and cylinders (CYLs), under parallel slit

confinement with hard and soft-repulsive walls. The geometry of these shapes is such that the flipped and unflipped particle orientations cast two different projected areas and shapes (Fig. 1) against the confinement wall. The flipped and unflipped orientations corresponds to the particle with its side parallel and perpendicular to the wall plane, respectively (see Fig. 1). Using the hard confinement model, this scenario imposes a hindrance to the different possible rotational and translational states that the particles can populate during self-assembly. By carefully choosing the confinement and the particle dimensions, we can create disconnected regions in the rotational phase space between the flipped and unflipped orientations that causes a non-ergodic dynamic behavior in the system. In simulations, we overcome this dynamic broken ergodicity by using unphysical specialized Monte Carlo (MC) moves that effectively sample all regions of phase space. These MC moves allow particles to transition between flipped and unflipped states, akin to changing the *"type"* of particle in a two-component system, categorized by the projected 2D geometry: hexagon ↔ rectangle for the HPs, and disk ↔ rectangle for the CYLs. Crucially, the transition between these two orientations also provides a mechanism to switch between structures with different packing symmetry and/or lattice spacing. The hexagonal projections of unflipped HPs exhibit a KTHNY-type [24] phase transition with a continuous fluid-hexatic transition and a continuous hexatic-solid transition [25]. Likewise, the disk-shaped projections of the unflipped CYLs have a first-order fluid-hexatic transition and a continuous hexatic-solid phase transition [26]. In contrast, the rectangular projections of flipped HPs and CYLs exhibit a two-stage KTHNY transition with the continuous fluid-tetratic and a continuous tetratic-tetratic solid transitions [27]. The tetratic and hexatic phases are partially ordered phases characterized by a short-range translational order and quasi-long ranged bond orientational order. The tetratic solid phase has long-range translational and bond orientational order.

A challenge associated with the assembly of anisotropic particles in confinement lies in the ability to sample their equilibrated quasi-2D positions and orientations. A "soft" confinement model is proposed in this work as a way to overcome the broken ergodicity by allowing the system to dynamically (and experimentally) bridge the flipped and unflipped particle orientations, but tunable external fields could also be used to control the confinement forces. For instance, application of external electric fields has proven to be an effective approach to

manipulate particle assemblies where the relative polarizability of the particle and the solvent medium controls the particle position, and the relative polarizability of each particle axis controls the particle orientations [28]. For bulk 3D system, a switching transition between the body-centered cubic crystal to a partially ordered plastic crystal structure was achieved for charged rod-like colloidal particles by tuning the electric field [29]. A wide range of structures with hexagonal and tetratic-like symmetries and string fluids were obtained for platelets subjected to varying electric field strengths and confinement separations that allowed particles to access flipped and unflipped orientations [30].

Our simulations predict a re-entrant transition for the HPs and CYLs in hard confinement where an intervening disordered phase occurs between two solid phases: a high-density tetratic phase and a low-density triangular solid (1Δ) phase. We termed this disordered phase as the Flipped-Unflipped (FUN) phase due to the mixture of flipped and unflipped orientations, high particle mobility, and significant degree of disorder. Indeed, the FUN phase has local clusters of flipped and unflipped particles with incompatible footprint areas that are distributed randomly throughout the simulated domain. At narrow separations, we observed a first order transition between the tetratic phase and the 1Δ phase for both HPs and CYLs. In our athermal system, different phases result from the interplay between pressure × volume contributions to the free-energy, which generally favors denser structures at high pressures, and the particles' rotational and translational contributions to the entropy which strongly depend on gap separation. By varying the density and confinement separation, we can tune regions of phase space accessible to the dispersion with our MC moves and experimental preparation (see below). MC simulations were also carried out for polydisperse CYLs in hard confinement to allow comparison of the predicted structures with tetratic, FUN, and 1Δ phases obtained experimentally by assembling fabricated CYLs in a wedge cell confinement. The consistency in the structural characteristics of the assembled phases obtained in experiments and simulations is attributed to both methods being able to comprehensibly sample the accessible orientational phase space. Particles in the wedge confinement cell are able to dynamically explore their flipped and unflipped states at wide separations, and as they migrate to the narrow separations, rearrange laterally to pack more densely; particles in the MC simulations are able to ergodically sample both orientational states through specialized moves at all conditions. Thus, experiments

and simulations produce assembled phases that have similar fraction of flipped/unflipped particles although not necessarily at the exact same confinement conditions (i.e., concentrations), hence providing comparable access to a variety of otherwise disconnected regions of phase space. The re-entrant FUN phase was also observed for HPs simulated in a soft confinement model where a finite transition barrier allows dynamic switching between flipped and unflipped orientations.

The outline of this paper is as follows. Section II details the hard and soft confinement models, simulation method, and the experimental protocol to fabricate the CYL colloids and assembling them in the wedge cell confinement. Section III describes various order parameters used to characterize the phase transitions. Sections IVA/IVB present summary/detailed description of the phase behavior of HPs and CYLs under hard wall confinement, Section IVC discusses the effect of size dispersity and a comparison between the simulated and experimental structures, and Section IVD presents simulation results for HPs under the soft confinement model. Finally, Section V presents closing remarks and an outlook of our study.

2. Methodology

2.1 Simulation model and protocol

Simulations of N hard anisotropic particles under parallel plate confinement were carried out using the standard Metropolis Monte Carlo algorithm in an isothermal-isobaric (NPT) ensemble. Figure 1 shows the hard wall and soft confinement models that corresponds to a case without and with a soft layer of varying thickness, $a^*=a/\sigma$, where σ is the height of the particle. The scaled plate separation is $H^*= H/\sigma$, where H is the distance between the hard walls. We simulated a range of H^* values (imposing periodicity in XY plane) that accommodates only a single particle layer. The aspect ratio of the particles, $R= b/\sigma$ is fixed by varying the characteristic length b, where $b = 2s$ for HPs and $b= d$ for CYLs. s is the edge length of the hexagonal face in the HP and d is the diameter of the circular face in the CYL. The R values chosen for the hard confinement model are 2 for HPs and 1.574 for CYLs and the phase behavior was mapped for H^*= 1.0-1.9 for HPs and H^*= 1.582-1.61 for CYLs. We observed a

quasi-2D phase behavior at $H^* > 1.74$ for HPs and $H^* > 1.574$ for CYLs, where the plate separations are such that the particles can access both flipped and unflipped orientations. The range of H^* values chosen is such that the flipped and unflipped orientations are dynamically disconnected (see Sec. I in the supplementary information, SI). The two orientations are distinguished based on the $|\vec{u}.\ \vec{z}|$ values where $\vec{u}$ is the principal orientation unit vector of the particle and $\vec{z}$ is the unit vector in z direction (see Fig. S1 in the SI). When flipped the $\vec{u}$ is parallel to the wall and perpendicular to the wall when unflipped (see Fig.1). For the soft confinement model, we set R= 1.82 and H^* = 1.95 to allow for the dynamic (or continuous) rotation of the HPs between the flipped and unflipped orientations. The R values for the HPs and CYLs are chosen such that they satisfy two geometric constraints: (i) The particles can access both flipped and unflipped orientations at the confinement separations that only allows formation of monolayers; (ii) The unflipped orientation projects a larger hexagonal/circular area compared to the rectangular area projected by the flipped orientation. The R values chosen for our study are just representative but we expect similar trends in phase behavior for HPs and CYLs with other R values that satisfies both geometric constraints.

The R values of the HPs and CYLs are chosen such that it satisfies two conditions: (i) The HPs and CYLs can access both flipped and unflipped orientations at the confinement separations that allows only formation of monolayer structures. (ii) The unflipped orientation has a larger hexagonal/circular projected area compared to the rectangular area projected by the flipped orientation.

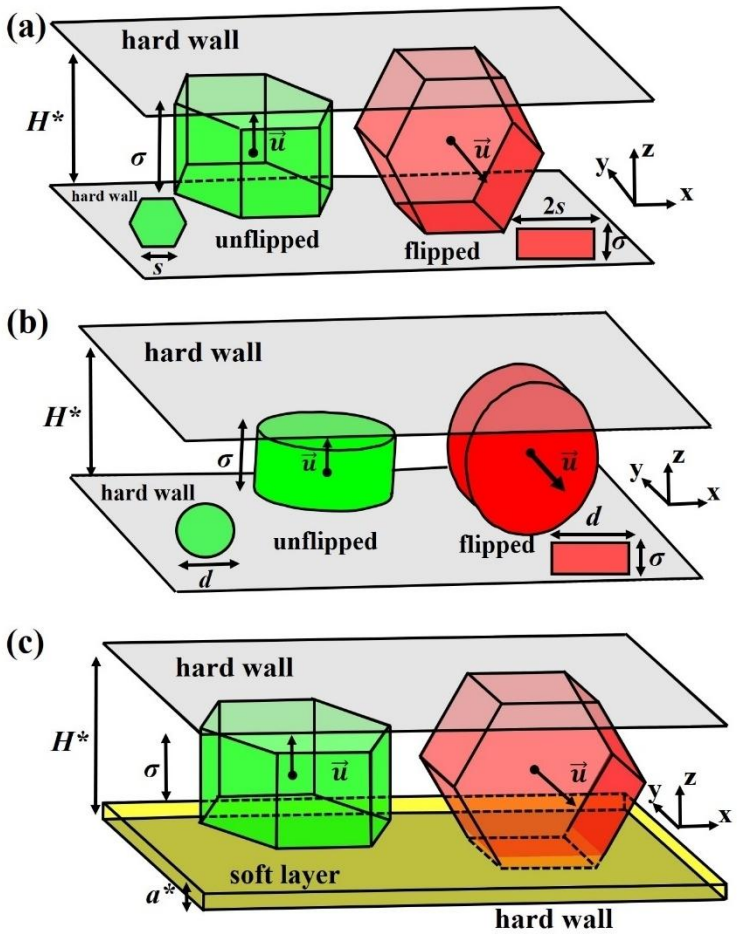

Fig. 1. Schematic of slit-confinement simulation model with (a,b) hard and (c) soft-repulsive walls. H^* is the separation between the hard walls scaled with respect to the height of the particle σ. The flipped (in red) and unflipped (in green) orientations and 2D projected geometries are shown for (a) HPs, and (b) CYLs. The particle's principal orientation unit vector, $\vec{u}$, is parallel/perpendicular to the XY plane when flipped/unflipped. s is the edge length of the hexagon face in HP, d is the diameter of the circular face in CYL. In (c) a^* is the thickness of the soft layer scaled with respect to σ.

We consider excluded volume interaction with the pair potential between the particles, $U(r_{ij})$, given as,

$$U(r_{ij}) = \begin{cases} \infty, & \text{if } r_{ij} < r_{ij}^{max} \\ 0, & \text{otherwise} \end{cases} \qquad (1)$$

where, r_{ij} is the distance between the particle center of mass, r_{ij}^{max} is the maximum r_{ij} distance

beyond which overlap cannot occur. The overlap between the particles is checked using the Gilbert-Johnson-Keerthi (GJK) algorithm [31]. The hard and soft repulsive potentials, $U(r_i)$, between the particle and the hard walls and between the particle and a soft-grafted layer is given by,

$$U(r_i) = \begin{cases} \infty, & \text{if } V_{o,hw}(r_i) \neq 0 \\ \beta V_{o,sw}, & \text{if } V_{o,sw}(r_i) \neq 0 \\ 0, & \text{otherwise} \end{cases} \qquad (2)$$

where, r_i is the particle center of mass position, $V_{o,hw}$ and $V_{o,sw}$ are the volumes of the particle that overlap with the hard walls and soft grafted layer. In this simple soft repulsive potential model, a presumed grafted layer exists with tunable hardness modulus, $\beta^* = \beta\sigma^3$, and thickness a^*. Because of the particle shape anisotropy, the wall-particle interaction potential will depend in a complex way on not only the particle-wall distance but also the particle orientation. Model (2) above can be seen as a first approximation to a soft repulsive potential where the energy required to deform the soft grafter layer is proportional to the particle volume that overlaps with (and pushes out) the soft layer. The 3D simplices was constructed to compute $V_{o,sw}$ using the particle vertices and centroid [32]. The overlap between each particle and the hard walls was detected using separating axis theorem [33].

For the hard confinement model, stepwise expansion/compression runs were carried out at each H^* value by equilibrating the system at each pressure step. These runs were used to map the phase behavior along the solid and liquid branches to detect any hysteresis present between expansion and compression. For the soft confinement model, we studied the phase behavior for HPs at $H^* = 1.95$ for varying a^* and β by performing compression runs and following the same procedure used for the hard confinement model. The dimensionless pressure is $P^* = P\sigma^3/k_bT$, where T is temperature and k_b is Boltzmann's constant. The equation of state was mapped by varying P^* and calculating the volume fraction, $\phi = NV_p/V$, where V_p is the volume of each particle, N is the number of particles and V is the system volume. To minimize finite size effects, we choose the initial system size to have a minimum of 15-35 particles per layer along X and Y dimensions. For the hard confinement model, 1254 and 1352 HPs were used for compression and expansion runs, and 1024 CYLs for both compression and expansion runs. For the system with soft confinement, 1254 HPs were used. We mapped the high-density solid branch of the phase diagram with the expansion runs and the intermediate and lower density branch with the

compression runs. At any H^*, the initial configuration for the compression runs is the isotropic phase and for the expansion runs is the densest crystal phase simulated using Floppy Box Monte Carlo algorithm [34].

At each pressure step, we perform 3×10^7 MC cycles with the last 5×10^6 cycles used for production runs, where each MC cycle consisted of N translational, N rotational, $N/10$ *flip*, $N/10$ two-particle in-plane rotation and 2 volume moves. All move sets obey detailed balance and the step size for the translational, rotational, and volume moves are adjusted to have acceptance probabilities of 0.4, 0.4, and 0.2. We incorporated *flip* moves that attempt to randomly orient a chosen particle in a plane that is perpendicular to its current orientation. The *flip* move was particularly important for our hard confinement model having broken dynamic ergodicity, as it helps to access the flipped and unflipped orientations that are difficult to sample with standard rotational moves. The two-particle in-plane moves improve ergodic sampling for high-density solid phases and were implemented as follows. First, two particles are chosen, the first randomly and the second its closest neighbor. Next, these particles are rotated in the XY plane about their combined center of mass (using z-component unit vector) by 90° (clockwise/anticlockwise) [22]. The move is accepted if: (i) the second particle is still the closest to the first one to maintain reversibility, and (ii) no overlap is incurred. Volume moves attempt changes in XY box area and shape (anisotropic moves) during the expansion runs, while only changes in XY area during compression runs.

2.2 Experimental protocol for fabrication of colloidal CYLs

We used a photolithographic procedure to fabricate colloidal CYLs from an epoxy-based negative photoresist, SU-8 2001 series, which provides high-throughput of different colloidal shapes within narrow size polydispersity [35,36]. The fabrication process includes three key steps: (i) Spin coating of the photoresist on top of a sacrificial Omnicoat layer on a 100 *mm* silicon substrate. The thickness of the photoresist layer controls the height of the particles, σ. (ii) Exposure of the photoresist to ultraviolet light (*i*-line) through a Cr photomask with round holes to control the diameter, d of the particles. (iii) Development of the photopatterned resist layer and release of the particles by dissolution of the Omnicoat layer. The particles were then washed with DI water and suspended in an aqueous solution of Tergitol NP70, a non-ionic

surfactant that adsorbs on the surface of the particles and provides a steric barrier holding the particles outside the *vdW* attraction regime to prevent irreversible aggregation [35,37]. The thickness of the NP70 layer and the zeta potential of the particles were estimated by Badaire et al. [37] to be 8.2 $\pm$ 3.3 nm and -21.0 $\pm$ 6.2 mV, respectively. This route generated particles with d = 1.56 $\pm$ 0.08 μm and σ = 0.96 $\pm$ 0.06 μm and the suspension concentration ~ 4.5×10^8 particles/*ml*. The size dispersity, s_d and s_σ in diameter and height were measured using the SEM micrographs and estimated to be 0.05 and 0.06, respectively. A more detailed description of the fabrication procedure and particle characterization is given in Sec. II of the SI. The suspension was transferred to a 10 ml glass vial and mixed with a small amount of fluorescein dye (2 mg/*ml*) to enable confocal imaging. Finally, the CYLs were assembled in the wedge cell confinement to study the organization of the particles using fast confocal microscopy (see Sec. IID in the SI).

3. Order parameters

3.1 Cubatic orientation order parameter

The global orientational order was measured using the cubatic order parameter, P_4, which is defined as,

$$\langle P_4 \rangle = \max_{\boldsymbol{n}} \frac{1}{N} \sum_i P_4(\overrightarrow{u_i} . \vec{n})$$

$$= \max_{\boldsymbol{n}} \frac{1}{8N} \sum_i (35 \cos^4\theta_i(\vec{n}) - 30 \cos^2\theta_i(\vec{n}) + 3) \qquad (3)$$

where $\overrightarrow{u_i}$ is the principal orientation vector of the particle and the $\vec{n}$ is the director that maximizes $\langle P_4 \rangle$. $\vec{n}$ is found using the numerical recipe reported in [38] which yields two orthogonal directors, $\overrightarrow{n_1}$, $\overrightarrow{n_2}$ and the corresponding values of $\langle P_{41} \rangle$, $\langle P_{42} \rangle$ in decreasing order of magnitude, used to gauge the in-plane and out-plane alignment of the flipped and unflipped particles.

3.2 Bond orientational order parameter

The local *n*-fold bond orientational order, $\Phi_n(\boldsymbol{r_k})$ for each *k* particle is given by,

$$\Phi_n(\boldsymbol{r_k}) = \frac{1}{N_k} \sum_{j=1}^{k} \exp(in\theta_{jk}) \qquad (4)$$

where $i = \sqrt{-1}$ and θ_{jk} is the angle between the vector connecting particle *k* with its neighbor *j* and a fixed reference vector. N_k is the number of nearest neighbors of particles *k.* For *n*= 6, N_k was calculated *via* Voronoi tessellation, while for *n*= 4, the four closest neighbors were used to avoid the degeneracy in the Voronoi construction [39]. Note that the $\Phi_n(\boldsymbol{r_k})$ are evaluated considering the center of mass coordinates of the particles projected on the 2D plane of the slit confinement.

To analyze the correlation length of the local bond order parameters, we compute the *n*-fold local bond orientational correlation function given by,

$$g_n(r) = \langle \Phi_n(0)\, \Phi_n^*(\boldsymbol{r}) \rangle \qquad (5)$$

where * indicates the complex conjugate of $\Phi_n(\boldsymbol{r})$ for the particle at a distance r from the reference particle.

3.3 Translational and rotational mobility analysis

We tracked particle mobility by carrying out *NVT* ensemble simulations of the equilibrated phases at different densities with a fixed set of translation and rotation moves using fixed step size that yield acceptance probabilities between 85%-95% to mimic pseudo diffusive particle dynamics. The translational mobility coefficient, μ_m is defined as the mean square displacement over N_s MC cycles,

$$R_s = \frac{\sum_{i=1}^{N} \sum_{j=0}^{N_{MC}-N_s} \left|\Delta r_{(j+s,j)}^{i}\right|^2}{N(N_{MC} - N_s)} \qquad (6)$$

where $\Delta r^{i}_{(j+s,j)}$ is the center of mass displacement of the i^{th} particle between the j^{th} and $(j+s)^{th}$ MC cycles, and N_{MC} is the total number of MC cycles in the simulation. μ_m quantifies the average in-plane local translational fluctuations for the phases under study. The rotational mobility is gauged by the autocorrelation function of particle orientation vectors over the MC cycles, defined as,

$$\theta_s = \frac{\sum_{i=1}^{N}\sum_{j=0}^{N_{MC}-N_s}\overrightarrow{u_j^i}.\overrightarrow{u_{j+s}^i}}{N(N_{MC}-N_s)} \qquad (7)$$

where, $\overrightarrow{u^i}$ is the principal orientation vector of particle *i*, and N_s is the number of MC cycles over which the axes alignment is measured.

4. Results and discussions

4.1 Brief overview of the phase diagram under hard confinement

Figure 2 shows the quasi-2D behavior of HPs and CYLs that was mapped by tracking ϕ for different phases found at $1.74 < H^* < 1.9$ for HPs and $1.581 < H^* < 1.61$ for CYLs, where the available space only allows the formation of a monolayer. At these plate separations both HPs and CYLs can access the flipped and unflipped orientations that have distinct projected footprints on the confinement planes. The flipped HPs and CYLs cast a smaller rectangular area and hence at the highest concentrations pack into the tetratic solid (TS) and partially ordered tetratic phase which are structurally similar to those of hard rectangles at 2D-close packing [27]. The forbidden region encloses inaccessible state points at higher packing fractions due to wall overlap (see Figs. 2a and 2b) and the boundary between the TS and the forbidden region represents the packing fraction of the densest structure predicted from the Floppy Box Monte Carlo algorithm [34]. The TS is classified into Uniaxial (Uni-TS) and Biaxial (Bi-TS), based on the alignment of the orientation $\vec{u}$ of the flipped particles. At intermediate concentrations, the unflipped orientations project a larger hexagonal and circular areas for the HPs and CYLs, respectively, thus forming 2D phases consistent with the assembly of hard hexagons [25] and hard disks [26]. At $1.8 < H^* < 1.865$ and $0.375 < \phi < 0.535$ for HPs and at $1.581 < H^* < 1.605$

and $0.458 < \phi < 0.614$ for CYLs, we observed an interesting re-entrant melting transition where the intervening disordered FUN phase occurs between the tetratic phase at high concentrations and the 1Δ phase at the intermediate concentrations. We observed a continuous tetratic→FUN phase transition and a first order FUN phase →1Δ phase transition. The FUN phase has local clusters of flipped and unflipped particles that are randomly distributed throughout the system and the particles have relatively high translational and rotational mobility. At $H^* > 1.865$ for HPs and $H^* > 1.605$ for CYLs, the 1Δ phase disappears and the FUN phase transitions to the isotropic (I) phase upon expansion, where any ordering signature disappears as the flipped particles reached ~30% at the lower concentrations. The FUN phase is hence an extension of the I phase but with higher concentration of flipped particles and forms a continuous boundary with the I phase at $1.865 < H^* < 1.9$ for HPs and at $1.605 < H^* < 1.61$ for CYLs (see Fig. 2). Figure 3 show the equilibrated snapshots, 2D structure factor plot, and $\vec{u}$ distribution plot of the tetratic, FUN, and 1Δ phases for the HPs at $H^*= 1.84$ and CYLs at $H^*= 1.595$. The change in the structural symmetry from fourfold to disorder to hexagonal symmetry can be observed with the concentration of the flipped particles. The 2D structure factor was defined as, $S(\boldsymbol{k}) = \frac{1}{N}\langle[\sum_{i=1}^{N}\cos(\boldsymbol{k}.\boldsymbol{r_i})]^2 + [\sum_{i=1}^{N}\cos(\boldsymbol{k}.\boldsymbol{r_i})]^2\rangle$, where $\boldsymbol{k}= (2\pi\, n_x/L_x, 2\pi\, n_y/L_y)$ with integers n_x and n_y chosen so that the wave vector $\boldsymbol{k}$ corresponds to the Bragg peak for the particles position $\boldsymbol{r_i}$.

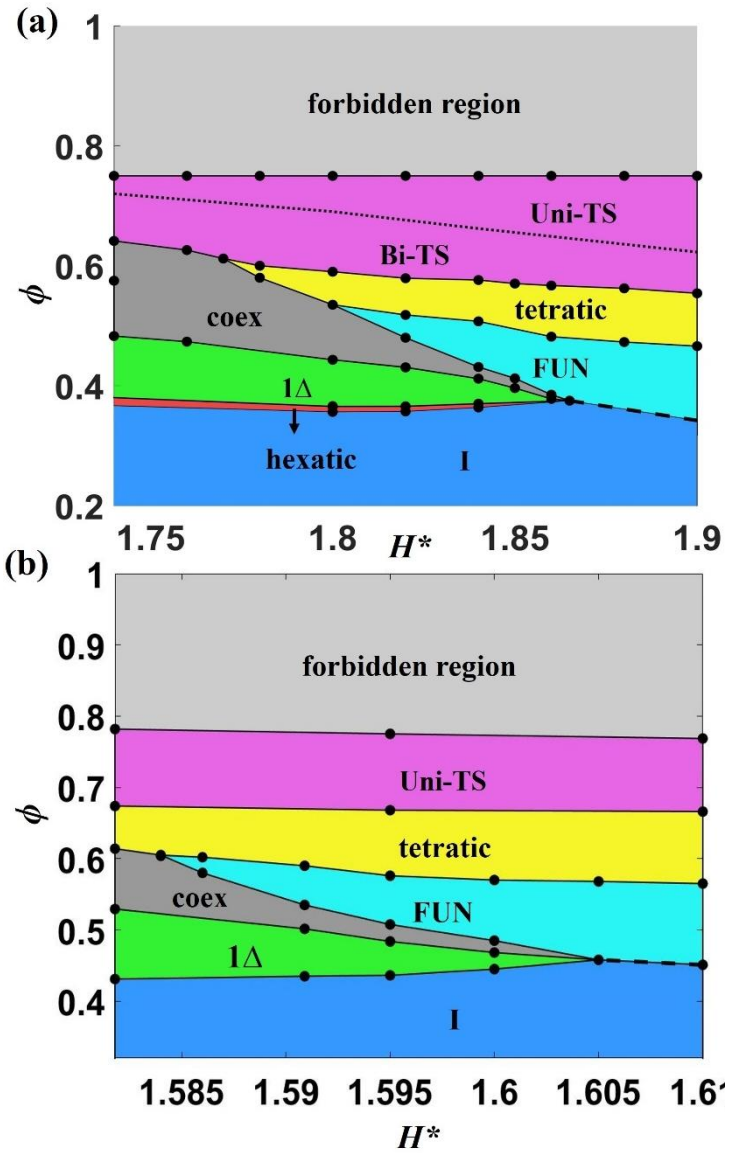

Fig. 2. Quasi-2D phase diagram for (a) HPs and (b) CYLs under hard wall confinement for varying H^* and ϕ. The dashed black line indicates a continuous boundary between the FUN and I phases. In (a) the dotted black line marks boundary between the Uni-TS and Bi-TS phases. Symbols: 1Δ = triangular solid phase, I = isotropic phase, Bi-TS = biaxial tetratic solid, Uni-TS = uniaxial tetratic solid, FUN = disordered phase with the mixture of flipped and unflipped particles, and coex= two-phase coexistence region. The forbidden region encloses inaccessible state points.

For the HPs, the hexatic and 1Δ phases occurred at $H^* > 1.74$ and $0.35 < \phi < 0.48$, where the phase regions narrow with increasing H^* and disappear at $H^* \sim 1.865$. For the CYLs, the 1Δ

phase region was observed for $0.46 < \phi < 0.53$ and $H^* < 1.605$. The HPs exhibit a 2D phase behavior for $H^* < 1.74$ and is discussed in Sec. III of the SI. We expect the CYLs to also exhibit the 2D phase behavior associated with hard disks [26] for $H^* < 1.574$.

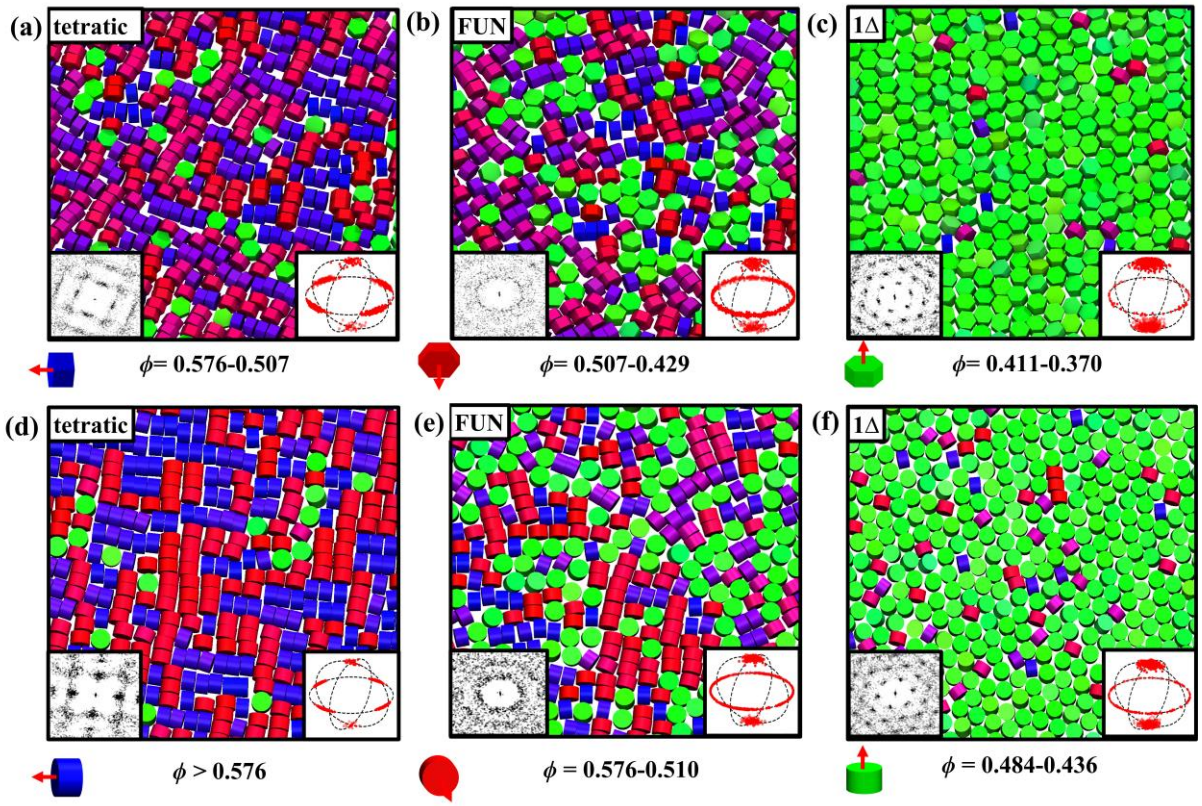

Fig. 3. Equilibrium structures of (a-c) HPs at $H^* = 1.84$ and (d-f) CYLs at $H^* = 1.595$ under hard confinement over different ranges of ϕ. Representative snapshots are shown with insets for the structure factor and $\vec{u}$ distribution plots. Flipped particles are colored red or blue if most or least aligned with the in-plane P_4 director. Unflipped particles are colored green. Single particle $\vec{u}$'s are also depicted in x axis.

The following section IV.B provides a more detailed description of the characterization and properties of the different phases in Fig. 2.

4.2 Phase behavior of HPs and CYLs in hard confinement model

4.2.1 The (Uni- and Bi-) TS phases form at the highest densities

For the HPs at $\phi > 0.6$ and $1.74 < H^* < 1.9$ shown in Fig. 2a, we observed two sub-phase TS regions: Uni-TS and Bi-TS phases. The transition boundary between these phases was determined using the cubatic orientational order parameters P_{41} and P_{42} [defined in Eq. (3)]. Figure 4a shows the equation of state with P^* vs. ϕ for HPs at $H^*= 1.84$ (filled circles for compression and filled squares for expansion), where the Uni-TS phase formed at the higher concentration transitions into the Bi-TS phase upon expansion at $\phi\sim 0.662$ and $P^*\sim 12.4$. We observed a sharp drop in the values of P_{41} from 1.0 and a rise in the P_{42} from 0.375 that flattens to $0.66 < P_{41} < 0.71$ and $0.62 < P_{42} < 0.63$ as the system transitions from the Uni-TS to the Bi-TS that was observed at $0.576 < \phi < 0.662$. This drop indicates that the percolating network of the orientationally aligned cluster of the flipped particles present in the Uni-TS dissolves into the Bi-TS where the size of clusters is about a few particles across and are randomly distributed along the two XY perpendicular directors (see Fig. S11 in the SI). The varying length scales of the coexisting clusters having perpendicular alignment along the XY plane suggests that the Uni-TS $\leftrightarrow$Bi-TS transition is continuous. The analysis using the positional pair-correlation, $g(r^*)$, and fourfold local bond orientational correlation functions, $g_4(r^*)$ [defined in Eq. (5)], shows that both Uni-TS and Bi-TS have long-range translational and fourfold bond orientational order (see Fig. S12 and Sec. ID in the SI describing the associated square lattice structure construction). We note that the mixed bi-orientational states in the Bi-TS is stabilized by the transition between degenerate in-plane orientations of the flipped particles (sampled by the two-particle MC moves) that increases the mixing entropy, with grain boundaries contributing to increase the local free-volume. At higher ϕ, the free energy is minimized by enhancing the packing efficiency (manifested as $P\Delta V < 0$) that drives the system to the more uniformly aligned columnar structure of the flipped particles in the Uni-TS.

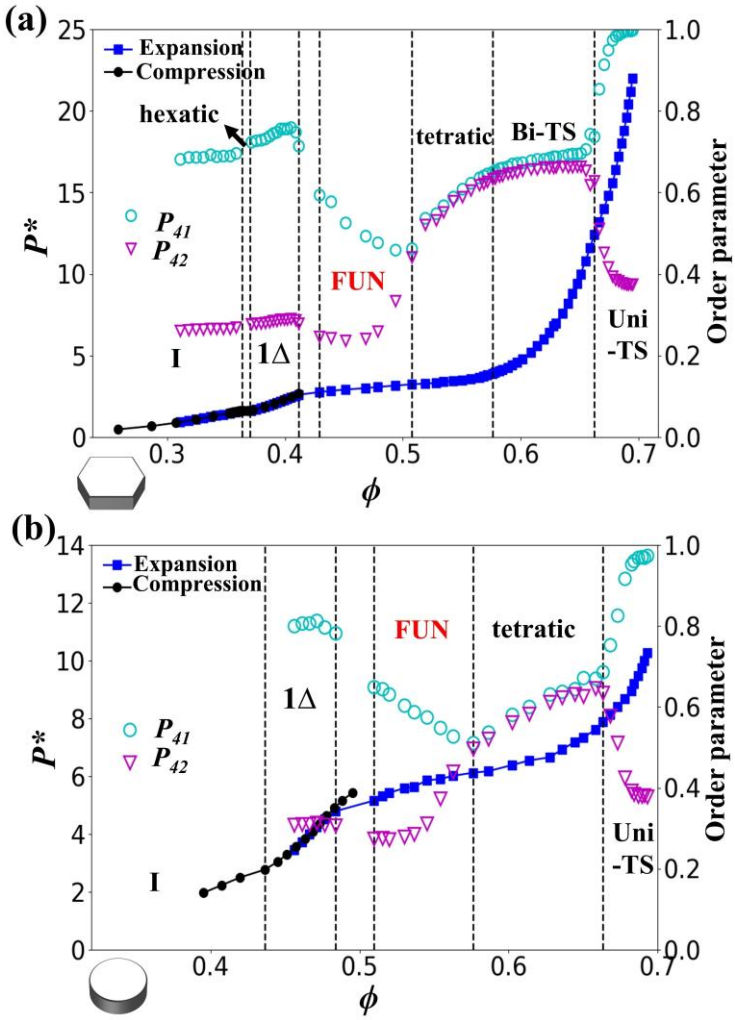

Fig. 4. Equation of state, P^* vs. ϕ, showing the compression and expansion runs for (a) HPs at $H^* = 1.84$ and (b) CYLs at $H^* = 1.595$. Dotted lines mark approximate phase boundaries. The variation of cubatic order parameters P_{41} and P_{42} with ϕ is also shown. Phase symbols as in caption of Fig. 2.

For CYLs, the tetratic phase precedes the Uni-TS (see Fig. 2b) instead of the Bi-TS whose inherent square lattice structure cannot be realized with the CYL aspect ratio adopted here. The Uni-TS and the tetratic phase occurred at $0.66 < \phi < 0.768$ and $0.565 < \phi < 0.674$, respectively for $1.582 < H^* < 1.61$. For the $H^* = 1.595$ case shown in Fig. 4b, the Uni-TS transitions into the tetratic phase at $\phi \sim 0.663$ and $P^* \sim 7.88$. However, the tetratic phase in the range of $0.627 < \phi < 0.663$ close to the Uni-TS→tetratic transition boundary has P_{41} and P_{42} characteristics similar to those of the Bi-TS. For the HPs, the tetratic phase occurred at $1.77 < H^* < 1.9$ and $0.466 <$

$\phi < 0.612$, where a continuous transition from the Bi-TS to the tetratic phase was observed upon expansion. To distinguish the tetratic phase from the Uni-TS and Bi-TS, we examined $g_4(r^*)$ and $g(r^*)$ selecting the $-¼$ exponent value as threshold to align with the KTHNY theory prediction for the scaling parameter lower-bound for the fluid to tetratic phase transition [25]. For the tetratic phase occurring at ($H^*= 1.84$, $\phi = 0.534$) for HPs and at ($H^*= 1.595$, $\phi = 0.627$) for CYLs, $g_4(r^*)$ reveals a long-ranged order with the exponent value $> -¼$, while $g(r^*)$ shows short range translational order with a quick decay of peak amplitude with distance (see Figs. 5 and S13). The long-range translational order in the tetratic phase is disrupted by the delocalized defects created by the weaker alignment of the local flipped particle clusters hence lowering the values of $P_{41} < 0.66$ and $P_{42} < 0.63$ compared to the Bi-TS for HPs and the Uni-TS phase for CYLs (see Fig. 4). This misalignment of the flipped particles and associated grain boundaries between fourfold clusters with biaxial orientation creates more free volume for the unflipped particles to occupy. Upon expanding the tetratic phase to $\phi = 0.507$ for HPs and to $\phi = 0.576$ for CYLs, P_{41} and P_{42} drop to moderate values in the range 0.44-0.52 as more particles attain the unflipped orientations, further destroying the translational order and the orientational alignment of the flipped particles, while still retaining the quasi-long ranged $g_4(r^*)$ order.

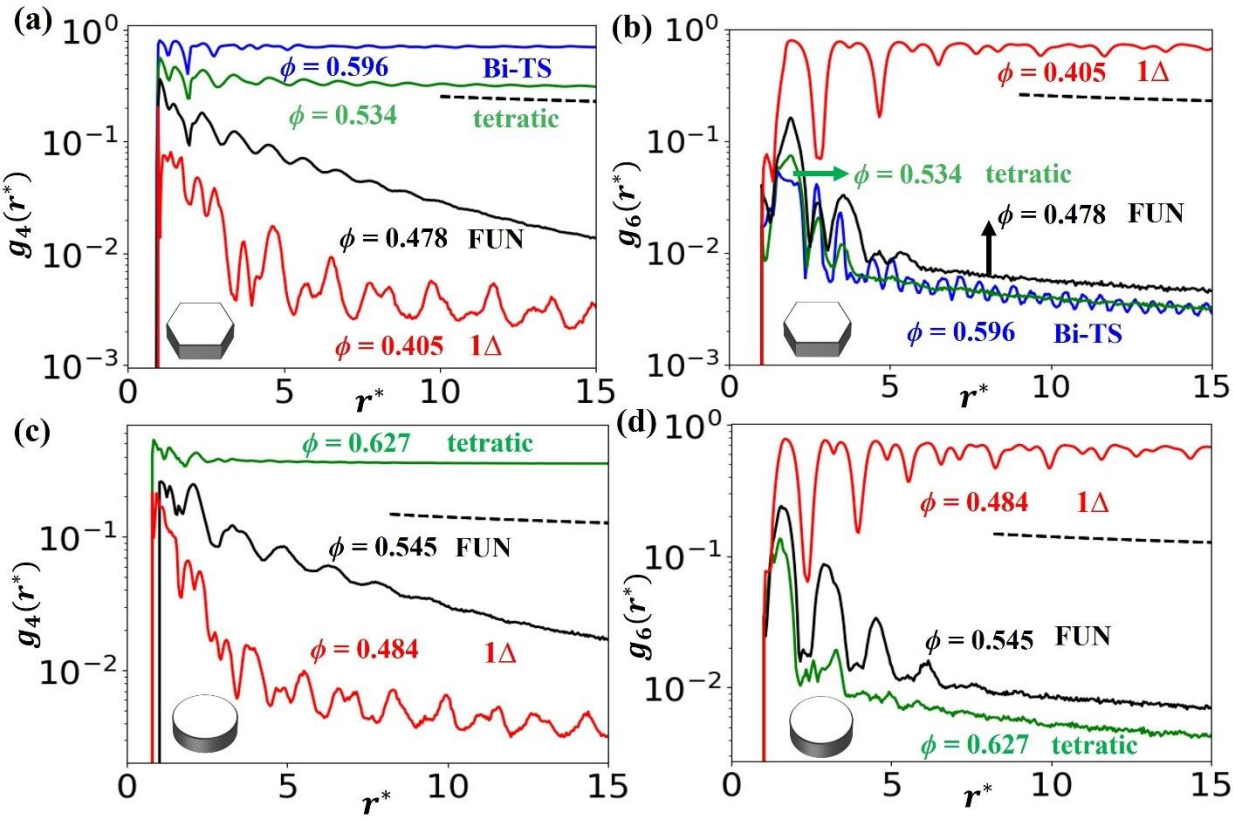

Fig. 5. Bond orientational correlation functions $g_4(r^*)$ and $g_6(r^*)$ of different phases for (a,b) 1352 HPs at H^*= 1.84 and (c, d) 1024 CYLs at H^*= 1.595 under hard confinement. r^* is the scaled radial distance. Phase symbols as in Fig. 2. The black dashed lines indicate algebraic decay of the orientational correlation with exponent −¼ corresponding to the KTHNY theory prediction for the tetratic phase.

4.2.2 The FUN phase reenters into the 1Δ solid on expansion

As the tetratic phase transitions to the FUN phase, the P_{41} shows an inflection at (ϕ = 0.507, H^*= 1.84) for HPs and at (ϕ = 0.576, H^*= 1.595) for CYLs (see Fig. 4). After the inflection point, P_{41} (or P_{42}) in the FUN phase continues to increase (or decrease) with decreasing ϕ as more particles attain the unflipped orientation that disrupts the orientational order of the flipped particles. This indicates that the disorder observed in the FUN phase occurs due to the presence of clusters of flipped and unflipped particles randomly distributed throughout the system. On further expanding the FUN phase to ϕ < 0.43 for HPs and to ϕ < 0.510 for CYLs, the concentration of unflipped particles increases thus forming local solid-like clusters having sixfold bond orientation order that eventually nucleate the 1Δ phase. The distribution plots of

$\vec{u}$ shown in Fig. 3 indicate that the concentration of the particles with unflipped orientation increases upon expansion. To rule out the possibility that the FUN phase is a two-phase mixed state that lies within a two-phase coexistence region having metastable tetratic and 1Δ phases with incomplete melting of solid clusters, we performed an *NVT* ensemble interfacial simulation at H^*= 1.84 and $\phi \approx 0.45$ with N = 9600 HPs. The initial configuration for this simulation consisted of a well-separated two-phase state within an elongated box, with the high-density Bi-TS at $\phi \approx 0.60$ at one side, and the I phase formed at low-densities at the other side. We found that regardless of the initial conditions, the interface between the two phases vanished and the system ended up forming the FUN phase (see Movie 1). The FUN phase showed short-range orientational order in $g_4(r^*)$ and $g_6(r^*)$, and short-range translational order in $g(r^*)$ that transitions to the 1Δ phase with long range $g_6(r^*)$ and pronounced peaks persisting over long distances for $g(r^*)$ which is indicative of solid-like behavior (see Figs. 5 and S13). The $g(r^*)$ function also shows an increase in the lattice spacing for the 1Δ phase compared to the tetratic phase at higher concentrations.

4.2.3 The FUN and 1Δ phases have distinct pseudo dynamical signatures.

To analyze and compare the dynamical properties of the FUN phase with the tetratic and 1Δ phases, we carried out the *"pseudo dynamic"* Monte Carlo simulations in the *NVT* ensemble (see Sec. IIIc for details). We thus obtained the translational mobility coefficient, μ_m and the rotational autocorrelation function of the particle orientation $\vec{u}$ for the tetratic, FUN, and 1Δ phases at different ϕ values for HPs at H^*= 1.84 and CYLs at H^*= 1.595 (see Fig. 6). The μ_m values for different phases were estimated from the mean square displacement plots shown in Fig. S14 in the SI. As the system transitions from the tetratic to the FUN phase, μ_m increases and the rotational autocorrelation function of $\vec{u}$ changes from a roughly linear to a fast exponential decay. The higher mobility in the FUN phase can be attributed to the incompatible footprint area between the flipped and unflipped particle that precludes efficient packing between local clusters. Overall, we observed that the μ_m for the FUN phase and the tetratic phase closer to the tetratic-FUN phase boundary was higher for HPs than those for CYLs, likely due to the HP facets creating more local free volume for the particles to both translate and rotate.

As the FUN phase transitions to the 1Δ phase, μ_m drops as expected, indicating that the 1Δ phase has low XY translational mobility. The particles have higher μ_m in the I phase compared to the FUN phase for both HPs and CYLs. To compare the pseudo dynamical properties at different ϕ, we rescaled the MC step with the acceptance rates and the maximum step sizes and observed a higher translational and rotational mobility of the HPs and CYLs in the FUN phase compared to the tetratic and 1Δ phases (see Fig. S15). Similar behavior was observed by fixing the translational and rotational acceptance ratios that determines the maximum steps sizes of the particles. We note that by fixing maximum translational and rotational step sizes in the pseudo dynamic simulations we qualitatively compare the local free volume available for the particle in different phases. More detailed analysis is required to compare the MC time scale with the Brownian time scale that couples both translational and rotational trajectories and account for the effects of confinement on the rotation of the biaxial particle shapes in a monolayer.

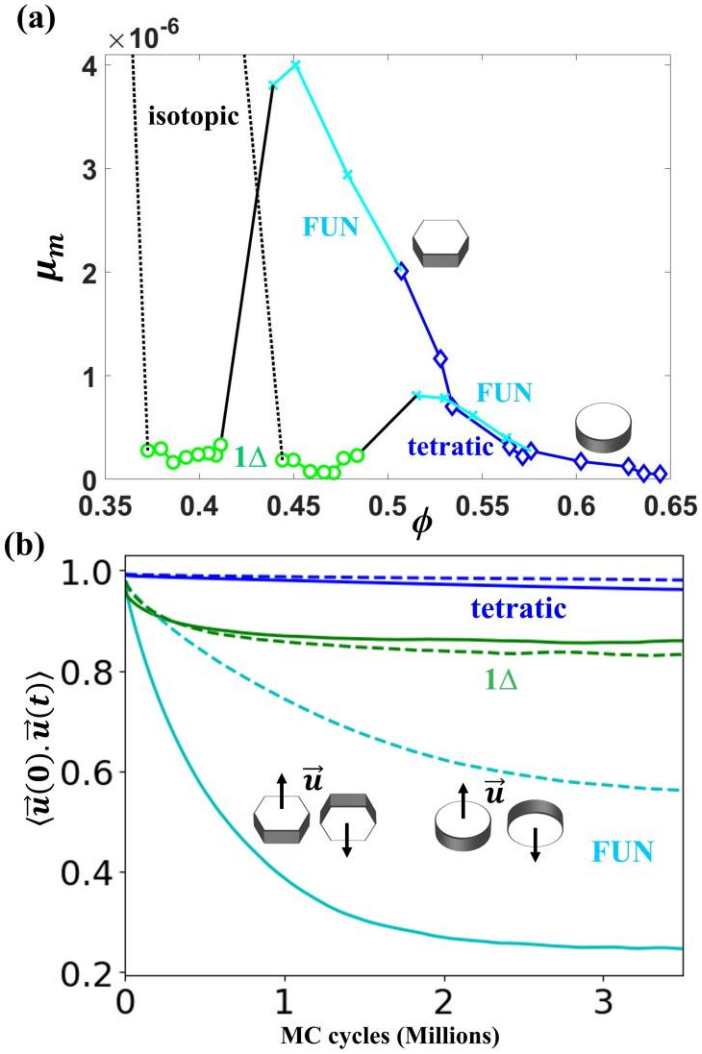

Fig. 6. Dynamic properties of the simulated phases. (a) Variation of translational mobility coefficient, μ_m with ϕ and (b) $\vec{u}$ rotational autocorrelation function vs. Monte Carlo (MC) cycles for 1352 HPs at H^*= 1.84 and 1024 CYLs at H^*= 1.595. In (a) the coexistence region is shown as a solid black line, and the tetratic is represented with filled and open blue diamonds for the HPs and CYLs, respectively. The FUN phase is shown as cyan crosses and the 1Δ phase as green circles. The dotted black line represents the isotropic phase. In (b) the tetratic (blue), FUN (cyan), and 1Δ (green) phases are shown as solid lines for HPs at ϕ= 0.564, 0.478, 0.405, and as dashed lines for CYLs at ϕ= 0.627, 0.515, 0.484, respectively.

Interestingly, the HP 1Δ phase at ϕ= 0.405 reveals an exponential decay of the orientation $\vec{v}$ (parallel to the hexagonal face) with simulation time, albeit the $\vec{v}$ distribution shows discrete sixfold clustering due to the rotational symmetry of the hexagonal facets (see Fig. S16 in the SI). This suggests that through local coordinated motions, HPs are able to dynamically explore all the sixfold rotational states despite being connected by low probability intermediate states. Accordingly, the HP 1Δ phase can also be classified as having discrete rotator-like characteristics given the dynamic particle rotations (connecting a discrete set of orientations) which are similar to the slow hopping motions observed in the 1Δ phase for corner-rounded hexagons [40]. We note that, in our confinement model with perfect HPs, the 1Δ phase formed at intermediate ϕ having significant free volume to allow collective rotational and translational motions.

4.2.4 Greater confinement increases fraction of flipped particles.

To understand the effect of confinement on the relative proportion of flipped and unflipped particles, we computed the variation of the fraction of flipped particles, f_f, with ϕ for different H^* values (see Fig. 7). f_f is the average fraction of particles that satisfies the criterion $|\vec{u}.\vec{z}|< 0.7$ (see Sec. I in the SI). As expected, the tetratic phase has the higher proportion of flipped particles with $f_f > 0.84$ for HPs and $f_f > 0.75$ for CYLs for all plate separations. At H^*= 1.8 and $0.535 < \phi < 0.585$ for HPs and at H^*= 1.582 and $0.614 < \phi < 0.646$ for CYLs, the tetratic → FUN phase transition disappears, and a direct tetratic→1Δ phase transition occurs upon expansion (see Sec. IVD in the SI for more details). The lower density 1Δ phase, having higher fraction of the unflipped particles with f_f ranging between 0.01-0.1, must be stabilized by gains in translational entropy along the z-axis (i.e., the z-translational entropy) to overcome the loss in packing entropy. In our athermal system, the associated pressure × volume (PV) *"enthalpic"* contribution to the free energy acts as a knob that controls the strength of the packing entropy that optimizes local packing arrangement of the particles. At higher pressures, the free energy is minimized by enhancing the $P\Delta V< 0$ effects with the tetratic phase whose tightly packed flipped particles have low entropy associated with their restricted translational and orientational degrees of freedom. Note, however, that an efficient packing does allow gains in particle

vibrational motion (and associated) entropy compared to dense but jammed configurations. The tetratic phase disappears at $H^* \sim 1.77$ for the HPs and a direct Bi-TS to 1Δ phase transition occurs for $1.74 < H^* < 1.77$ (Fig. 2a). At higher plate separations, more free volume is available for the flipped and unflipped particles, and the FUN phase is observed for $H^* \sim 1.84$ with $0.48 < f_f < 0.85$ for HPs and for $H^* \sim 1.595$ with $0.44 < f_f < 0.76$ for CYLs. We posit that the FUN phase engenders when there is a competition between the *z*-translational entropy that favors the presence of unflipped particles and the entropic packing that favors "*flipped-flipped"* and *"unflipped-unflipped"* contacts, resulting in clusters of both flipped and unflipped particles randomly distributed throughout the system. We observed a drop in the f_f values on expanding the FUN phase since the unflipped particles have then more *z*-translational and rotational degrees of freedom which take over the packing entropy and result in the 1Δ phase at lower density. Figure S24 in the SI shows the increase in the spread of the *z*-particle distribution functions during the expansion run as the system undergoes tetratic→FUN and tetratic→1Δ phase transitions. At $H^* = 1.9$ for HPs and $H^* = 1.61$ for CYLs, the FUN phase transitions directly into the I phase upon expansion at $f_f \sim 0.3$ without crossing the stable 1Δ phase regions, with the persistent high fraction of flipped particles impairing the formation of the 1Δ phase. At lower concentrations, we observed a slight increase in the fraction of flipped particles in the HP hexatic phase which eventually transitions to the I phase (see Fig. 7a).

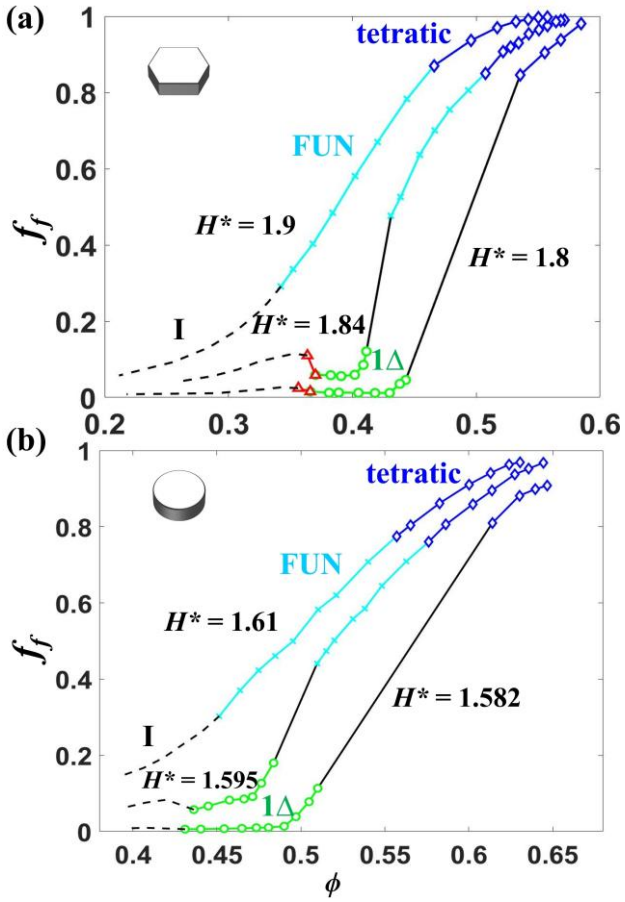

Fig. 7. Variation of the fraction of flipped particles f_f with ϕ for (a) HPs and (b) CYLs at different H^*. Solid and dashed black lines represent the coexistence region and the I phase, respectively. The tetratic, FUN, hexatic, and 1Δ phases are represented by blue diamonds, cyan crosses, red triangles, and green circles, respectively.

5. Size polydisperse CYLs in hard confinement: model and experiment

5.1. Size polydispersity can suppress 1Δ monolayer phase and reentrant behavior

In this section, we explore the effects of size polydispersity on the re-entrant phenomenon of CYLs using MC simulations under the hard confinement model, and compare these results with experimental structures obtained from assembling the fabricated CYLs in a wedge cell confinement. The wedge cell allows us to access phases with varying concentrations of flipped particles occurring at different confinement heights. Compression runs were carried out to obtain the phases at different ϕ and H^* values for different degrees of polydispersity (see Sec.

IC for simulation details). We fixed s_σ = 0.06 and s_d = 0.01 and 0.02 to probe whether the tetratic→FUN→1Δ phase transition is resilient to size imperfections. Note that the phase behavior at narrow plate separations is sensitive to the variation in s_d since the diameter dimension affects the fraction of particles that can access the flipped orientation observed in the FUN and tetratic phases. For s_d= 0.02 and s_σ = 0.06, the re-entrant phenomenon disappears and the tetratic → FUN→ I phase transition persists (see Fig. S25 in the SI). Although the nominal s_d estimated using SEM micrographs is 0.06, the actual s_d estimated from the confocal images for the FUN phase at ϕ~ 0.50 was about 0.026 (see Fig. S6a). This decrease in the size dispersity is likely due to the fractionation process that occurs as the particles sediment into the narrower monolayer confinement separations.

Figure 8 shows the simulated snapshots, $S(\boldsymbol{k})$ plots, and the experimental confocal images for the tetratic, FUN, and 1Δ phases for the CYLs at different densities. The structure factor pattern changes from fourfold tetratic order → no order → sixfold order as the system transitions from tetratic → FUN→ 1Δ phase. The simulated and experimental confocal images of the different phases occurred at the conditions indicated by the square and star markers in Fig. 9a that shows the variation of f_f with ϕ for CYLs with s_d = 0.01 and s_σ = 0.06 at different H^*. The H^* values in the simulations were chosen such that with our MC moves more than 80% of the particles can attain the flipped orientation at higher densities thus forming the tetratic phase. The tetratic phase was observed at f_f > 0.75 for 1.646≤ H^* ≤1.670 (see Fig. 9a). At H^*= 1.646, the re-entrant FUN phase occurs at ϕ < 0.576 and f_f < 0.75 and was stable up to ϕ = 0.48 and f_f = 0.3 before transitioning into the 1Δ phase with ϕ = 0.46 and f_f =0.08. For H^* > 1.646, the 1Δ phase disappears at lower densities and the FUN phase transitions directly to the I phase. The experimental f_f values reported in Fig. 8 were obtained by manually counting the flipped and unflipped particle orientations from the confocal images with 38.6 μm × 37.6 μm field area. The two orientations were distinguished based on the difference in the projected area and geometry. We estimated a total count of about 720, 620, and 540 particles in the tetratic, FUN and 1Δ phases, respectively. The volume of each particle was calculated using $\langle d \rangle$ and $\langle \sigma \rangle$ obtained from the SEM micrographs. The experimental ϕ were roughly estimated by using the average particle diameter $\langle d \rangle$ as the gap size; since the true experimental confinement gap is likely greater than the $\langle d \rangle$, the reported ϕ values can be seen as an upper bound for the tetratic

and FUN phases. The experimental values thus estimated are $\phi \sim 0.60$ and $f_f \sim 0.94$ for the tetratic phase, $\phi \sim 0.50$ and $f_f \sim 0.74$ for the FUN phase, and $\phi \sim 0.44$ and $f_f \sim 0.06$ for the 1Δ phases. Note that the f_f value obtained for the FUN phase lies very close to the predicted tetratic-FUN phase boundary in Fig. 9a. Unflipped ↔ flipped transitions through thermal fluctuations are crucial in the experiments to access the FUN and tetratic phases. For the fabricated CYLs with dimensions $<d>$ and $<\sigma>$ and density mismatch $\Delta\rho$ between the solvent and the particle, we indeed estimated a barrier for unhindered unflipped→flipped rotation to be less than k_bT (i.e., $\Delta U_g \sim 0.4\ k_bT$ as shown in Sec. IIC and Fig. S6b in the SI).

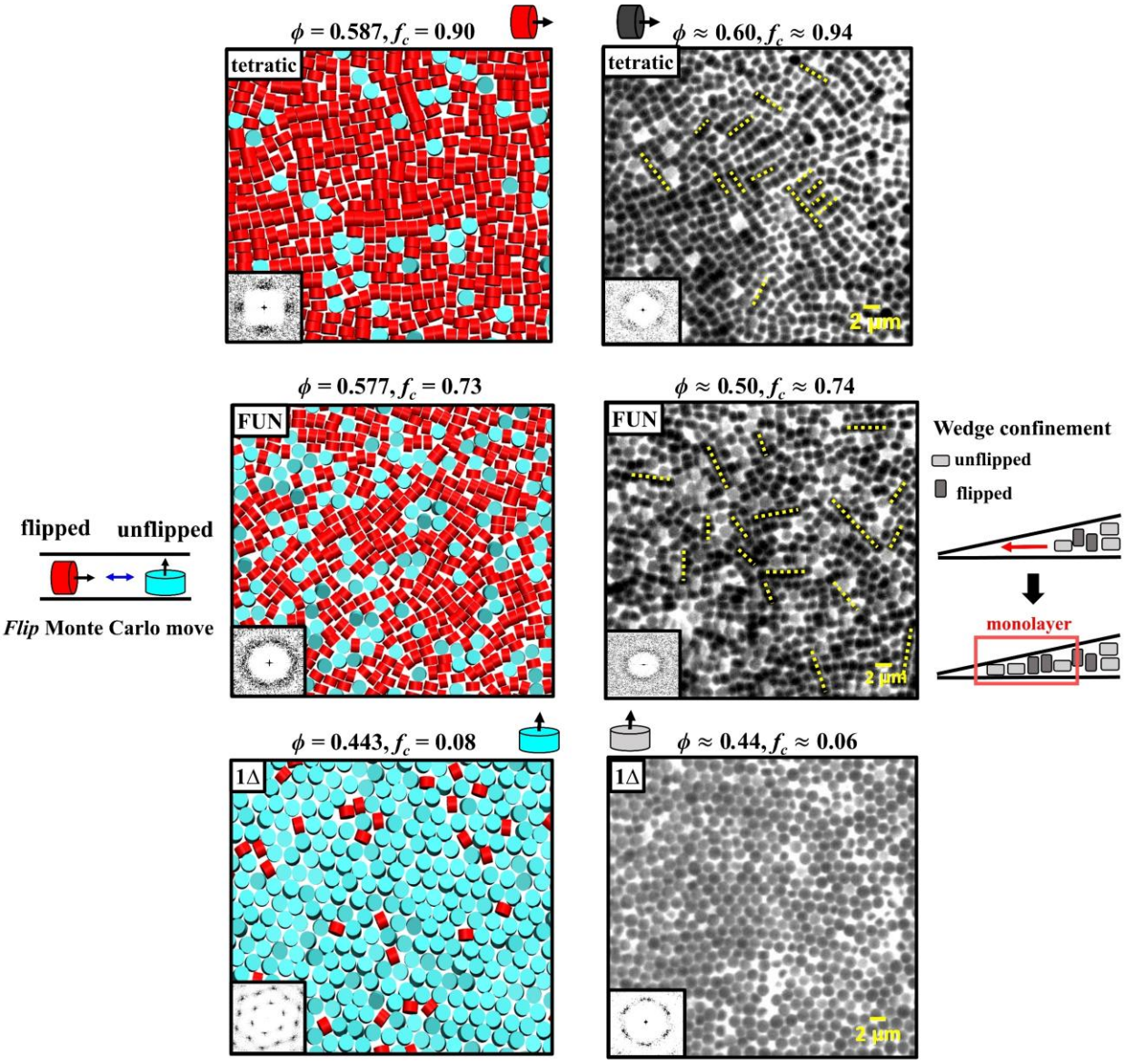

Fig. 8. Simulated (left) and confocal (right) images for CYLs under hard confinement exhibiting tetratic, FUN, and 1Δ structures with the indicated ϕ and f_f values. Insets show the structure factors. Simulated phases have N= 1254 and polydispersity s_d = 0.01 and s_σ = 0.06. Flipped and unflipped particle are colored red and cyan. (Right) The flipped and unflipped particles have different projected geometry and area. The yellow dashed lines show the local column clusters. The tetratic, FUN, and 1Δ phases have 740, 620, and 540 particles within a 38.6 μm × 37.6 μm field area. Lateral schematics represent how sampling of flipped↔unflipped states is accomplished in MC simulations via flip moves (left) and in the wedge confinement cell via migration of flipped and unflipped particles from wide to narrow separations (right).

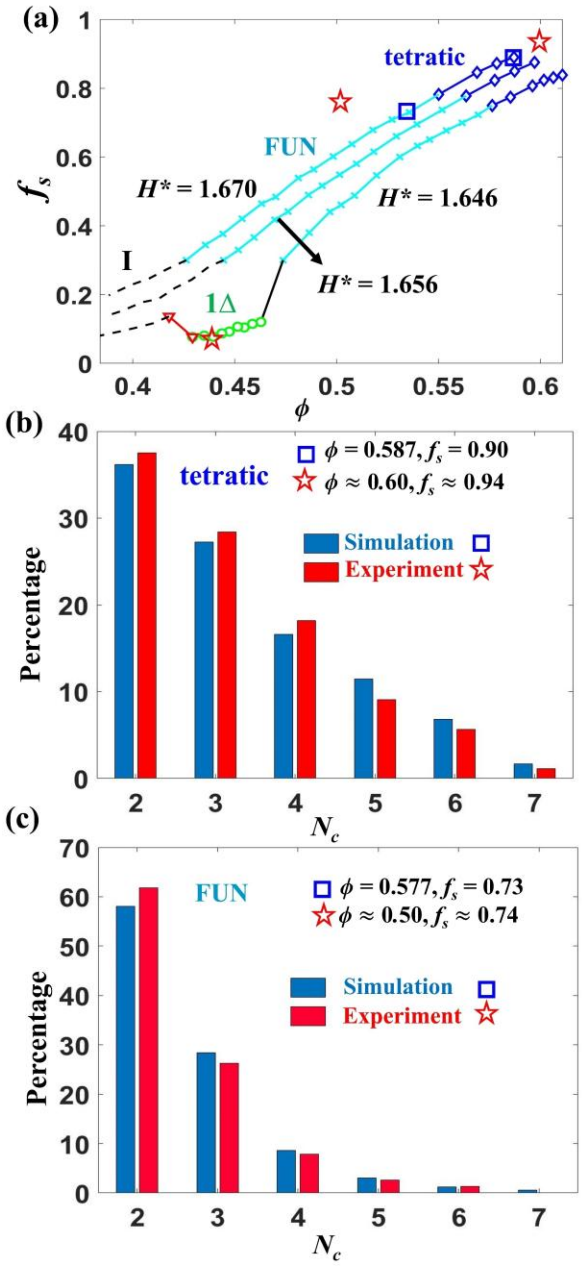

Fig. 9. (a) Variation of f_f with ϕ for CYLs with $s_d = 0.01$ and $s_h = 0.06$ at different H^* values. Black lines represent the coexistence (solid) and I phase (dashed) regions. The tetratic, FUN, hexatic, and 1Δ phases are represented by blue diamonds, cyan crosses, red triangles, and green circles, respectively. The star (red) and square (blue) markers indicate the experimental and simulated state points for the tetratic and FUN phases. (b,c) Percentage of column clusters having different number N_c of flipped particles in column stacks.

5.2 Simulation and experimental phases have similar structural signatures

To investigate the similarities between the experimental and simulated phases, we analyzed the static and dynamic structural properties of the tetratic and FUN phases. The static properties were examined using the local orientational clustering order parameter, $P_i\,(r_c) = \frac{1}{n}\sum_j^n \cos\theta_{ij}$, where *j* identifies flipped particles within the distance cutoff, $r_c \sim 1.25\sigma$ from the position of the flipped particle *i*, *n* is the number of nearest neighbors, θ_{ij} is the angle between the orientations $\vec{u}_i$ and $\vec{u}_j$. We set the threshold for $P_i\,(r_c)$ as 0.7 and identified the number of particles, N_c, forming a continuous network of flipped column clusters. The length of the column clusters in the confocal images were estimated by visual counting. Figure 9b and 9c show the percentage of columns having N_c values ranging between 2 and 7 for the tetratic and FUN phases. To compare with experimental phases having similar f_f values, we used the simulated tetratic phase at ϕ = 0.587 and f_f = 0.90 and the FUN phase at ϕ = 0.577 and f_f = 0.73. The column length distributions from experiment and simulation agree within 10%. The tetratic/FUN phase has about 16%/8% of N_c= 4 columns and 9%/3% of N_c= 5 columns. The tetratic phase also has a higher percentage of longer columns with $N_c > 5$ and a smaller percentage of short columns with $N_c < 3$ than the FUN phase. This indicates that as f_f decreases from 0.90 to 0.73 the long columns found in the tetratic phase break up into shorter columns in the FUN phase, destroying the fourfold features in the system. To probe the dynamic properties of the tetratic and FUN phases, we carried out pseudo dynamic *NVT* simulations and observed a slower decay in the rotational correlation function for the tetratic phase compared to the FUN phase (see Fig. S26 in the SI). Movie 2 in the SI shows the experimental tetratic phase with a well packed bi-orientational structure having more restricted rotational movement than the FUN phase shown in Movie 3, where the particles have more local free volume to rotate and translate. Note that the assemblies in Movies 2 and 3 the particle's motion exhibits Brownian characteristics.

Although the experimental and simulated structures of the FUN phase have similar static and dynamical properties, the experimental ϕ is lower, which could partially be due to the additional interparticle repulsive force created by the particle coating's negative zeta potential as reported in Sec. IIB. Moreover, it is likely that the experimental structures examined had not reached the (denser) equilibrated ϕ and could be kinetically arrested. Indeed, both the 'equilibrium' FUN and tetratic phases found in simulation are only reproducibly attainable regardless of history if

the particles' flipped and unflipped states are ergodically accessed, which could not have happened at the corresponding wall separations in the experiments. This indicates that the FUN and tetratic structures we observe in experiments originated when the flipped and unflipped particles occurring at wider wall separations (and lower ϕ) migrated to the narrower separations where the particles' rotational states were trapped but still had in-plane translational degrees of freedom to form more compact structures (see schematics in Fig. 8). Hence both MC simulations (with its unphysical flip moves) and the wedge-cell experiments (with its gradual narrowing and migration of large particle ensembles) provide a comprehensive sampling of all possible particle "initial states" which can then seed dense structures that "fall" into different basins of phase space.

6. Bridging rotational phase space using soft-repulsive wall model

The re-entrant melting transition observed for the HPs and CYLs under the hard confinement model is associated with the broken ergodicity that results by the disconnected rotational phase space between the flipped and unflipped orientations. As an approach to dynamically bridge the gap between the two rotational states and transform the intermediate forbidden states into low-but-finite probability states, we implement a soft confinement model with a soft repulsive layer coating at the bottom wall (see Sec. IIA for details). By tuning the softness and thickness of a repulsive layer coating, we can control the positional penalty of the particles along the z-axis to find conditions where the reentrant phenomenon observed for the hard confinement scenario can be practically realized. We studied the phase behavior of HPs with R= 1.82 at H^*= 1.95 which allows for dynamic flipping of the particles. The phase transitions were mapped for varying values of the soft layer thickness, a^*, and its modulus parameter, β^*.

Figure 10a shows the phase transition sequences observed for the soft confinement model at different values of soft layer parameters, β^* and a^*. The different types of phase transition sequences were identified by mapping them onto the global phase diagram for the hard wall confinement at varying H^* values shown in Fig. 2a (whose HPs have R= 2):

(i) For a^*= 0.72 and $\beta^* < 6.5$, we observed the phase sequence corresponding to the tetratic→ FUN→ I transition. By decreasing a^*, the β^* required to attain the tetratic→ FUN→ I transition expectedly increases.

(ii) For any value of a^*, increasing β^* pushes the phase behavior into tetratic→ FUN→ 1Δ phase transition

(iii) Further increasing β^* leads to a direct tetratic →1Δ transition. Figure S27 shows the equation of state and the correlation functions for a^*= 0.45 and β^*= 17.3, where the FUN phase occurred within the range of $0.421 < \phi < 0.467$.

(iv) Further increasing β^* leads to the 1Δ→ hexatic phase transition, having 2D phase behavior since then the soft layer is rather "hard" and the effective wall separation effectively corresponds to the hard confinement model having 2D phase behavior.

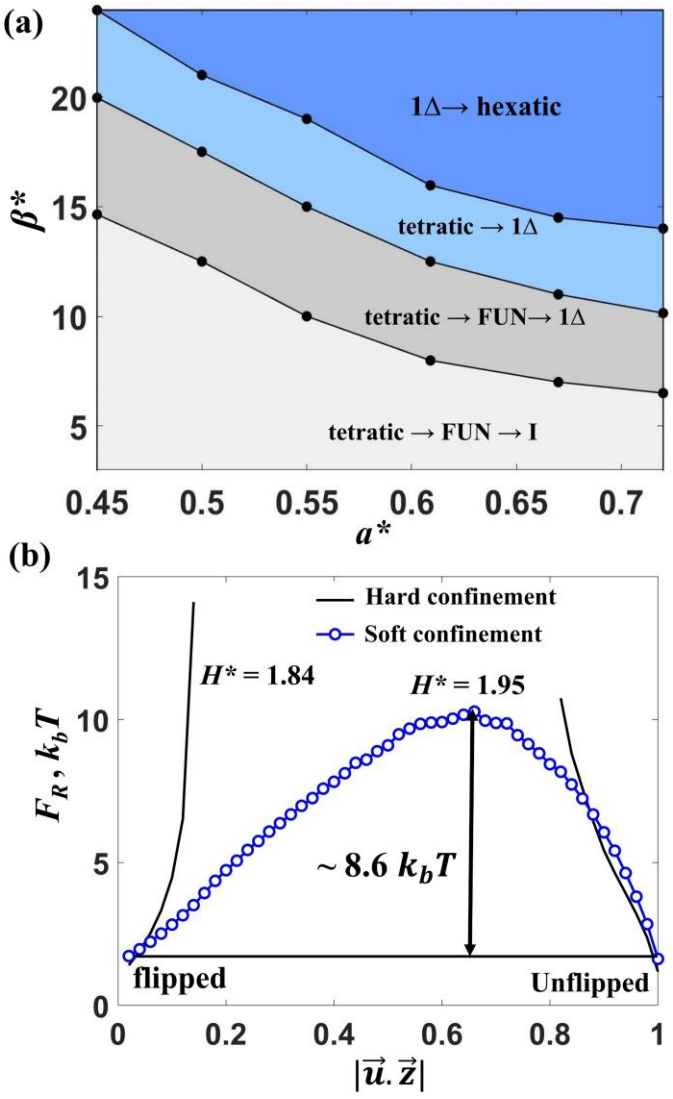

Fig. 10. (a) Different types of phase transition sequences observed using soft confinement model for varying β^* and a^*. (b) Rotational free energy F_R at different rotational states for the

FUN phase with ϕ= 0.439 at H^*= 1.84 under hard confinement and ϕ= 0.432 at H^*= 1.95, β^* = 17.3 and a^* = 0.45 under soft confinement. $\vec{u}$ is the unit vector perpendicular to the flat particle face and $\vec{z}$ is the unit vector in the z direction.

To gauge if the FUN phase is experimentally viable with the soft confinement model, we estimated the transition barrier between the unflipped and the flipped rotational states by calculating the rotational free energy, $F_R = -k_bT \ln(P(|\vec{u}.\vec{z}|))$, where $P(|\vec{u}.\vec{z}|)$ is the probability of occurrence of the indicated rotational state, k_b is the Boltzmann constant and T is the temperature. We compared the F_R between the hard and soft confinement models at the conditions where the intermediate FUN phase was observed; namely at ϕ= 0.432 and H^*= 1.84 (see Sec. IVB Fig. 3) for the hard confinement model and at ϕ= 0.440, β^* = 17.3 and a^* = 0.45 for the soft confinement model. Figure 10b shows the estimated flipped ↔ unflipped particle transition barrier as 8.6 k_bT indicative of events with infrequent but experimentally accessible time scales of the order of 1 hr (estimated by correcting the unhindered rotational tumbling time of microparticles in water [41]). The interaction between the particles and walls and the ensuing particle-rotation barrier can be manipulated based on the soft layer material, e.g., by tuning the grafting density and the length of grafted polymers [42,43].

7. Final remarks and outlook

In summary, we explored the quasi-2D (monolayer) phase behavior of hard HPs and CYLs in slit-pore confinement where the flipped and unflipped orientational states of the particles are dynamically disconnected. Phases with diverse structural order can be realized by coupling the anisotropy associated with particle shape with the restriction of the entropic degrees of freedom of these particles imposed by external potentials like slit confinement. Through specialized MC moves that ergodically sample both orientational states, our simulations mapped out the thermodynamic phase behavior. By varying the separation of the plates, one can effectively tune the z-translational entropy of the particles and hence control the fraction of particles that can access the flipped or unflipped orientations. The chosen particle shapes are such that their footprint changes significantly in area and packing symmetry (i.e., from hexagonal to tetratic) as they go from unflipped to flipped orientations. This unique combination of confinement

effect and particle's orientation creates an interesting re-entrant transition where an intervening disordered FUN phase occurs between two solid phases, namely, a tetratic phase (favored by hard rectangles) and a 1Δ phase (favored by hexagons). The FUN phase has randomly distributed local clusters of flipped and unflipped particles whose incompatible footprint areas create more free volume for the particles to rearrange. The tetratic → FUN phase transition is continuous while the FUN phase → phase transition is first order. At narrow separations, a first order transition is observed between the tetratic phase and the 1Δ phase for both HPs and CYLs. Fast confocal image analysis of fabricated CYLs assembled at different densities inside a wedge-cell was used to identify structures consistent with the FUN phase, the 1Δ phase and the tetratic phase found by simulating particles with 1% and 6% dispersity in diameter and height, respectively. The comprehensive sampling of the accessible orientational phase space afforded by the simulations and experiments resulted in phases having similar fraction of flipped/unflipped particle states and structure, albeit at slightly different conditions. Importantly, our approaches are relevant to practical (often non-equilibrium) processes used to form materials: our simulations were able to unveil near equilibrium states that actually emerged at the end of the non-equilibrium process of filling a wedge cell with a colloidal dispersion. To illustrate alternative, close-to-equilibrium approaches that overcome the broken dynamic ergodicity inherent to the hard confinement, we also proposed a soft confinement model wherein the barrier for the flipped ↔ unflipped transition is large enough to allow the formation of the same phases seen for hard confinement, but not so large to preclude such transitions from occasionally taking place.

An alternative approach to control the flipped ↔ unflipped transitions rates and experimentally bridge the flipped and unflipped orientations would be to use a pre-programmed hard wall actuator that periodically increases and restores the original confinement gap. This time-dependent position of the hard walls could be tuned such that the fraction of time in the large separation is small enough to avoid large structural changes (like bilayer formation) but long enough to allow particle flips. Yet another approach to externally control spatial confinement is by using external electric/magnetic fields that allows for micro-manipulation of positions and orientations of electrically/magnetically active particles to drive the complex assembly of macrostructures [28,44]. The tunable external potential in the above systems allows control of

the fraction of flipped/unflipped particles and can hence provide similar conditions to reproduce the intriguing re-entrant phase behavior observed in our models. The re-entrant phase behavior unveiled in this work for the HPs and CYLs stems from the duality in the projected geometries when the orientation of a particle changes its flip state. In this context, it would be interesting to investigate how the different entropic forces responsible for the re-entrant behavior are affected by varying the aspect ratio of the particles. A re-entrant phase behavior akin to the one described in this work is likely to be associated with concomitant changes in optical properties that could be leveraged to devise photonic band gap crystals [45–47] and optical switches [48]. This unique phase behavior can also provide a template for designing reconfigurable colloidal materials where an external stimulus is used to change the confinement gap and allow the particles to access the flipped and unflipped orientations on command [49,50]. Such an actuator would allow to modulate the structure in the system to have sixfold, fourfold or no symmetry.

Acknowledgments

Funding support from NSF award CBET-1907369 is gratefully acknowledged. IC and MR were supported in part by NSF award CBET-2010118. The authors thank Prof. Chekesha Watson and Eric Schwen for useful exchanges and to Yangyang Sun, Isabela Q. Matos, and Unmukt Gupta for valuable suggestions on the order parameter analysis. Valuable guidance from Dr. Garry Bordonaro and Dr. Beth Rhoades was received for lithoparticle fabrication. The fabrication work was performed at the Cornell NanoScale Facility, a member of the National Nanotechnology Coordinated Infrastructure (NNCI), which is supported by the National Science Foundation (Grant NNCI-2025233).

References

[1] Y. F. Lim, J. J. Choi, and T. Hanrath, J. Nanomater. 2012 (2011) 1-6.

[2] Y. Lu, Y. Yin, Z. Y. Li, and Y. Xia, Nano Lett. 2 (2002) 785-788.

[3] O. D. Velev and S. Gupta, Adv. Mater. 21 (2009) 1897-1905.

[4] U. Agarwal and F. A. Escobedo, Nat. Mater. 10 (2011) 230-235.

[5] S. C. Glotzer and M. J. Solomon, Nat. Mater. 6 (2007) 557-562.

[6] D. Baranov, A. Fiore, M. Van Huis, C. Giannini, A. Falqui, U. Lafont, H. Zandbergen,

M. Zanella, R. Cingolani, and L. Manna, Nano Lett. 10 (2010) 743-749.

[7] K. Yaman, C. Jeppesen, and C. M. Marques, Europhys. Lett. 42 (1998) 221-226.

[8] T. Biben, P. Bladon, and D. Frenkel, J. Phys. Condens. Matter 8 (1996) 10799-10821.

[9] A. Fortini and M. Dijkstra, J. Phys. Condens. Matter 18 (2006) L371.

[10] M. R. Khadilkar and F. A. Escobedo, Soft Matter 12 (2016) 1506-1516.

[11] D. Deb, A. Winkler, M. H. Yamani, M. Oettel, P. Virnau, and K. Binder, J. Chem. Phys. 134 (2011) 214706-214715.

[12] C. Avendaño, C. M. Liddell Watson, and F. A. Escobedo, Soft Matter 9 (2013) 9153-9166.

[13] K. Muangnapoh, C. Avendaño, F. A. Escobedo, and C. M. Liddell Watson, Soft Matter 10 (2014) 9729-9738.

[14] K. Whitham and T. Hanrath, J. Phys. Chem. Lett. 8 (2017) 2623-2628.

[15] E. K. Riley and C. M. Liddell, Langmuir 26 (2010) 11648-11656.

[16] E. G. Teich, G. Van Anders, D. Klotsa, J. Dshemuchadse, and S. C. Glotzer, Proc. Natl. Acad. Sci. U. S. A. 113 (2016) E669-E678.

[17] B. De Nijs, S. Dussi, F. Smallenburg, J. D. Meeldijk, D. J. Groenendijk, L. Filion, A. Imhof, A. Van Blaaderen, and M. Dijkstra, Nat. Mater. 14 (2015) 56-60.

[18] T. Geigenfeind, S. Rosenzweig, M. Schmidt, and D. De Las Heras, J. Chem. Phys. 142 (2015) 174701-174714.

[19] I. D. Hosein and C. M. Liddell, Langmuir 23 (2007) 8810-8814.

[20] P. Gurin, S. Varga, M. González-Pinto, Y. Martínez-Ratón, and E. Velasco, J. Chem. Phys. 146 (2017) 134503-134511.

[21] S. J. Penterman, A. Singh, W. R. Zipfel, and C. M. Liddell Watson, Adv. Opt. Mater. 2 (2014) 1024-1030.

[22] K. W. Wojciechowski, D. Frenkel, and A. C. Brańka, Phys. Rev. Lett. 66 (1991) 3168-3171.

[23] S. J. Gerbode, U. Agarwal, D. C. Ong, C. M. Liddell, F. Escobedo, and I. Cohen, Phys. Rev. Lett. 105 (2010) 13-16.

[24] D. R. Nelson and B. I. Halperin, Phys. Rev. B 19 (1979) 2457-2484.

[25] J. A. Anderson, J. Antonaglia, J. A. Millan, M. Engel, and S. C. Glotzer, Phys. Rev. X 7

(2017) 021001-021015.

[26] E. P. Bernard and W. Krauth, Phys. Rev. Lett. 107 (2011) 1-4.

[27] A. Donev, J. Burton, F. H. Stillinger, and S. Torquato, Phys. Rev. B - Condens. Matter Mater. Phys. 73 (2006) 054109-054121.

[28] B. Rupp, I. Torres-Díaz, X. Hua, and M. A. Bevan, Langmuir 34 (2018) 2497-2504.

[29] B. Liu, T. H. Besseling, M. Hermes, A. F. Demirörs, A. Imhof, and A. Van Blaaderen, Nat. Commun. 5 (2014) 1-8.

[30] A. C. Stelson, S. J. Penterman, and C. M. L. Watson, Small 13 (2017) 1603509-1603519.

[31] E. G. Gilbert, D. W. Johnson, and S. S. Keerthi, IEEE J. Robot. Autom. 4 (1988) 193-203.

[32] H. L. Ong, H. C. Huang, and W. M. Huin, Adv. Eng. Softw. 34 (2003) 351-356.

[33] P. J. Schneider and D. H. Eberly, *Geometric Tools for Computer Graphics* (Morgan Kaufmann, San Fracisco, CA, 2003).

[34] J. De Graaf, L. Filion, M. Marechal, R. Van Roij, and M. Dijkstra, J. Chem. Phys. 137 (2012) 214101-214112.

[35] S. Badaire, C. Cottin-Bizonne, J. W. Woody, A. Yang, and A. D. Stroock, J. Am. Chem. Soc. 129 (2007) 40-41.

[36] C. J. Hernandez and T. G. Mason, J. Phys. Chem. C 111 (2007) 4477-4480.

[37] S. Badaire, C. Cottin-Bizonne, and A. D. Stroock, Langmuir 24 (2008) 11451-11463.

[38] B. S. John, C. Juhlin, and F. A. Escobedo, J. Chem. Phys. 128 (2008) 044909-0044913.

[39] M. Mazars, Epl 84 (2008) 55002-55008.

[40] Z. Hou, K. Zhao, Y. Zong, and T. G. Mason, Phys. Rev. Mater. 3 (2019) 015601-015610.

[41] J. M. Meijer and J. J. Crassous, Small 14 (2018) 1-12.

[42] W. L. Chen, R. Cordero, H. Tran, and C. K. Ober, Macromolecules 50 (2017) 4089-4113.

[43] C. L. Ren and Y. Q. Ma, Phys. Rev. E - Stat. Nonlinear, Soft Matter Phys. 72 (2005) 1-7.

[44] R. Niu, C. X. Du, E. Esposito, J. Ng, M. P. Brenner, P. L. McEuen, and I. Cohen, Proc. Natl. Acad. Sci. U. S. A. 116 (2019) 24402-24407.

[45] K. Busch and S. John, Phys. Rev. E - Stat. Physics, Plasmas, Fluids, Relat. Interdiscip.

Top. 58 (1998) 3896-3908.

[46] E. Yablonovitch, J. Opt. Soc. Am. B 10 (1993) 283-298.

[47] J. Teyssier, S. V. Saenko, D. Van Der Marel, and M. C. Milinkovitch, Nat. Commun. 6 (2015) 1-7.

[48] J. Ge, Y. Hu, T. Zhang, T. Huynh, and Y. Yin, Langmuir 24 (2008) 3671-3680.

[49] M. Lupkowski and F. Van Swol, J. Chem. Phys. 93 (1990) 737-745.

[50] L. B. Krott and J. R. Bordin, J. Chem. Phys. 139 (2013) 154502-154512.

SUPPLEMENTARY INFORMATION

Re-entrant transition as bridges for broken ergodicity in confined colloidal hexagonal prisms and cylinders

B.P. Prajwal[1], Jen-Yu Huang[1], Meera Ramaswamy[2], Tobias Hanrath[1], Itai Cohen[2], Abraham D. Stroock[1], Fernando A. Escobedo[*,1]

[1]Department of Chemical and Biomolecular Engineering, Cornell University, Ithaca, New York 14853, USA

[2]Department of Physics, Cornell University, Ithaca, New York 14853, USA

1. Simulation methods

A. Potential of mean force

The metric for gauging the anisotropic behavior of the hexagonal prisms (HPs) and cylinders (CYLs) under the influence of hard wall confinement was obtained from:

$$PMF(z) = -k_b T \ \ln\left(\langle e^{-U(z)/k_b T}\rangle\right) \quad \text{(S1)}$$

where k_b is Boltzmann's constant, T is temperature, $U(z)$ is the potential energy of interaction between the hard walls and particle centered at z position, and $\langle\rangle$ denote ensemble average. The PMF was calculated by placing a particle with random orientation at different z positions between the hard walls and checking for any overlap between the particle and the walls. For each z value, we sampled 10^5 random particle orientations to calculate the average Boltzmann's factors in Eq. S1. The calculation was repeated for 10^3 different z positions between the walls. Figure S1 shows the PMF for HPs and CYLs for the ranges of plate separations, H^* where the solid-solid and solid-disordered-solid transitions were observed for the hard confinement model (see main text for details). As expected, the PMF profile is symmetric about the center of the plate separation located at 0, with higher probabilities for particles to reside near that center where more free volume is available to access rotational states i.e., flipped and unflipped states. Away from the slit center, the PMF profile tends to diverge as particles encounter a more restrictive space and only unflipped states are accessible.

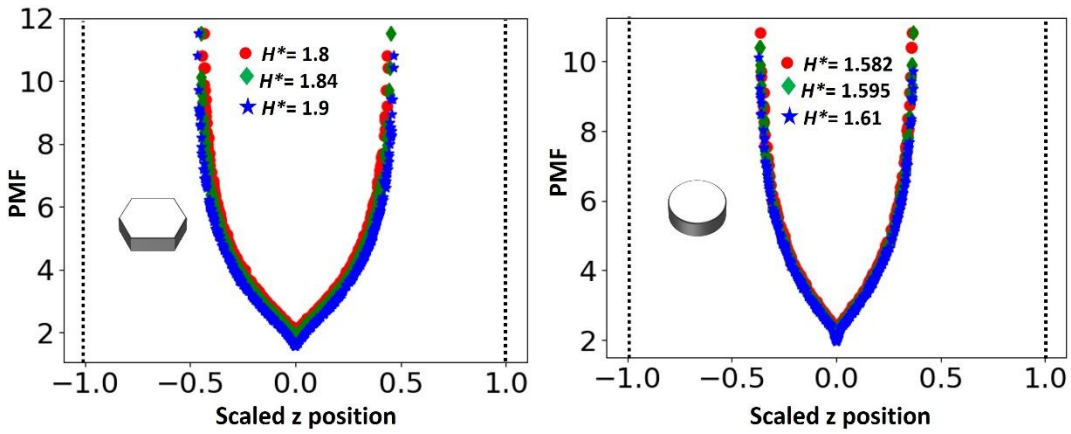

Fig. S1 (color online). Potential of mean force for the HPs and CYLs at different plate separations, H^*. The dashed lines represent the hard wall boundaries.

To obtain the correlation between the particle orientations and the z positions of the center of mass of the particle, we calculate the two-dimensional (2D) histogram of the scaled z positions and $|\vec{u}.\,\vec{z}|$ where $\vec{u}$ is the particle's principal orientation unit vector and $\vec{z}$ is the z direction unit vector. Figure S2 shows the probability distribution of the flipped and the unflipped orientation regions for the plate separations where the two orientation states are dynamically disconnected. At $1.8 < H^* < 1.9$ for HPs and $1.582 < H^* < 1.61$ for CYLs, we observed that the unflipped orientations are more favorable compared to the flipped orientations at lower concentrations since the former can access more z-positions and rotational states. We note that the PMF calculations and 2D histogram analysis carried out in this section pertain to the infinitely dilute limit.

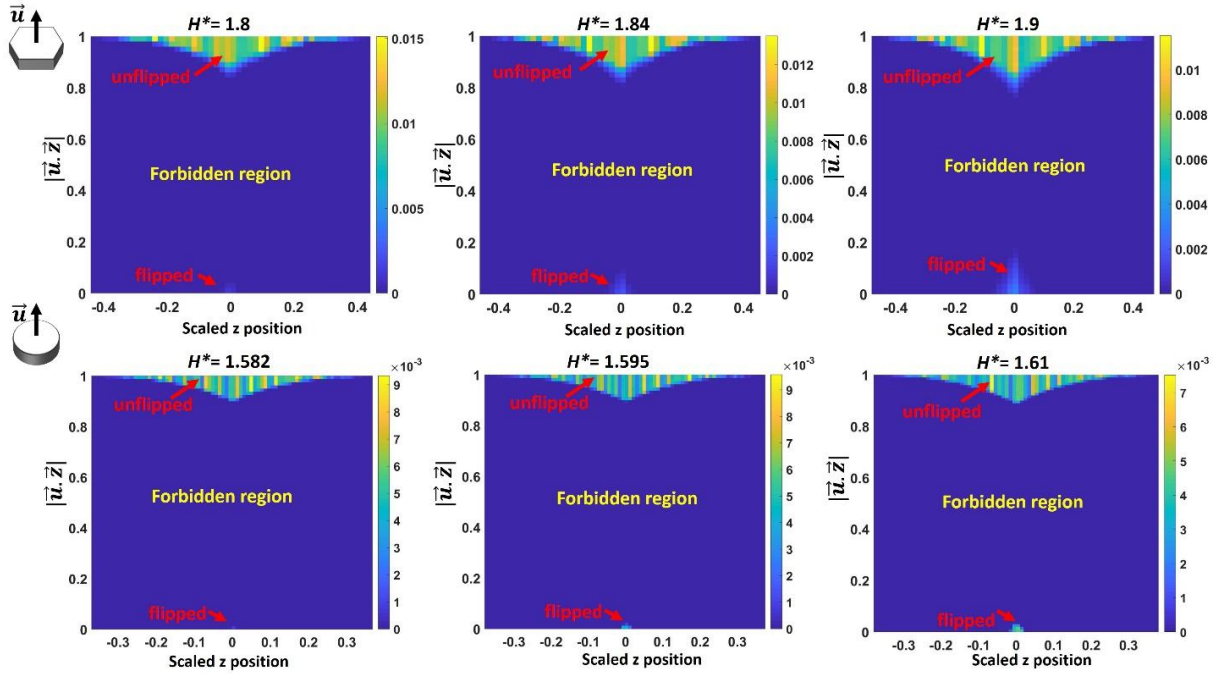

Fig. S2 (color online). Two-dimensional histogram of the scaled z positions and the orientations of the HPs (Top panel) and CYLs (bottom panel). $\vec{u}$ is the principal orientation unit vector that is perpendicular to the flat face of the particle. $\vec{z}$ is the z direction unit vector. The unflipped and flipped regions are marked. The scale bar indicates the probability of occurrence of each state.

B. Floppy Box Monte Carlo method

In the scenario where a predictable densest crystal phase cannot be achieved by simple compression runs of large systems, we adopted the Floppy Box Monte Carlo algorithm [1] to predict the densest crystal phase. Using this algorithm, we simulated systems with a small number of particles (typically $N < 12$) in an isothermal-isobaric (NPT) ensemble, where all the moves were accepted or rejected based on the Metropolis criterion, allowing for changes in the box XY-dimensional area and shape during the volume move attempts. Initially, systems with 4, 6, and 8 particles are equilibrated at low pressures for 3×10^6 MC cycles and the subsequently compressed with small pressure steps until reaching a high pressure, $P^* = 8000$. We perform 30-50 such compression runs with different random number seeds and initial configurations, and the final densest crystal phase is determined from its relative occurrence

frequency in different compression runs. The structure thus obtained was used as the unit cell to construct larger systems, whose stability is further tested by using *NPT* simulations with anisotropic volume moves.

C. Size polydisperse mixture of CYLs in hard confinement

We considered "quenched" size polydispersity wherein the size distribution was discretized and fixed in an *NPT* ensemble simulation. Compression runs were carried out to obtain the phases at different ϕ and H^* values for different degrees of polydispersity in height, s_σ and diameter, s_d. The polydispersity in d and σ, was estimated by,

$$s_a^2 = \frac{\langle a^2 \rangle}{\langle a \rangle^2} - 1 \qquad \text{(S2)}$$

where a is the characteristic length that corresponds to d and σ. $P^* = P\langle\sigma\rangle^3/k_bT$ and $H^*=H/\langle\sigma\rangle$, where $\langle\sigma\rangle$ is the average height of the CYLs obtained from SEM micrographs. We fixed s_σ = 0.06 and s_d = 0.01 and 0.02 to closely match the polydispersity observed in experiments. The desired polydispersity in s_d and s_σ were imposed in the initial random configuration by randomly selecting the sizes of 1254 particles from a Gaussian distribution with $<d_i>$= 1.625 and $<\sigma_i>$= 1.0, and standard deviation δ (see Fig. S3). Each MC cycle consists of N translation, N rotation, N/10 flip, N/10 swap, N/10 two-particle in-plane move and 2 isotropic volume moves, where N is the total number of particles. A swap move randomly chooses a particle pair and swap their positions while preserving the orientation. Each pressure run consisted of 10^7 MC cycles with last 5×10^6 cycles used as production runs.

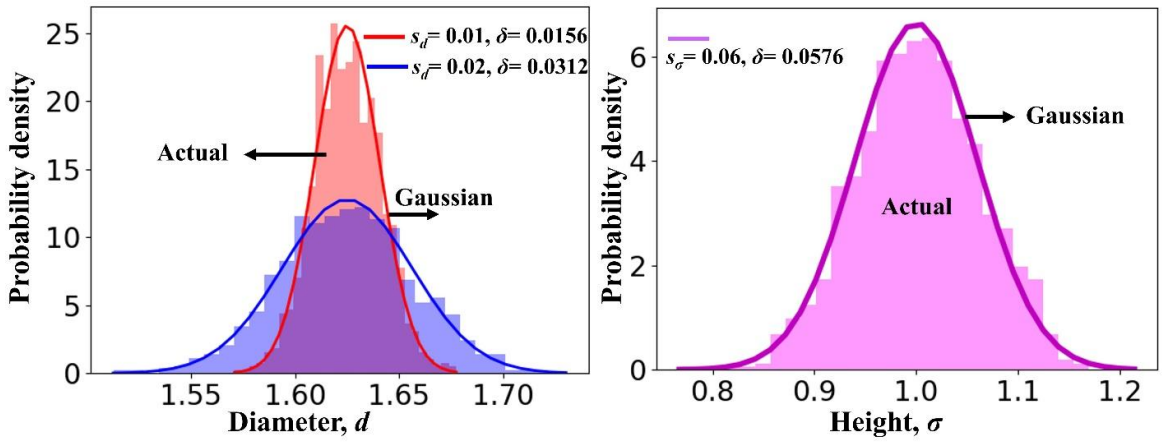

Fig. S3 (color online). Sample size distributions for different nominal polydispersities, δ, in diameter and height for 1254 CYLs. s_d and s_σ are the size dispersity parameters in the diameter and height of the particle. The shaded region represents the actual distribution attained in the quenched polydisperse configuration while the lines are the ideal Gaussian distribution curves

D. Construction of square lattice from the flipped HP particle orientations

To reveal the inherent square lattice in the Uni-TS and Bi-TS phases formed by the HPs with aspect ratio, R= 2, we followed the construction detailed in Ref. [2]. The geometric construction of the square lattice from the HP particle is depicted in Fig. S4. We construct the C2 points which are a unit distance from the center of mass C1 using the orientation $\vec{v}$ and $-\vec{v}$ of the flipped particle ($\vec{v}$ is parallel to the hexagonal face of the particle). For example, for the flipped particle with $\vec{v}$= (1,0,0) or (0,1,0) orientations, the projected domino in the XY plane can be split into two squares with centroids C2. Using this construction, we can detect the long-range translational or bond-orientational order in the Uni-TS and Bi-TS solid phases.

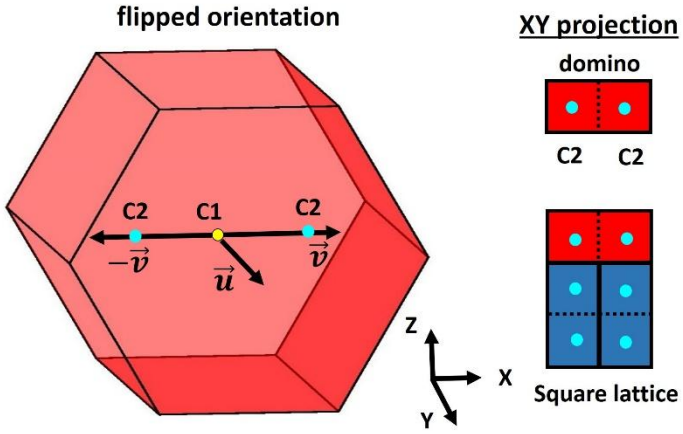

Fig. S4 (color online). Square lattice construction from the flipped HP particle with R= 2. The points C2 are at a unit distance from the center of mass, C1. $\vec{v}$ is the orientation vector of the flipped particle that is parallel to the flat face of the particle. $\vec{u}$ is the principal orientation vector of the flipped particle that is perpendicular to the flat face of the particle. The right panel shows the square lattice constructed by splitting the domino projection on the XY-plane: Blue and red indicate particle with $\vec{v}$ = (1,0,0) and (0,1,0) orientations, respectively.

2 Experimental protocol

A. Materials

SU-8 2001 negative photoresist, Omnicoat, SU-8 developer and Remover PG were purchased from Microchem corp (www.microchem.com). Tergitol NP70 was obtained from Dow Chemical (www.dow.com). Isopropyl alcohol (IPA) was purchased from Sigma-Aldrich (www.sigmaaldrich.com). Fluorescein dye (ACROS organics). 100 mm silicon wafer. 24 × 60 *mm* micro cover glass (www.vwr.com). 2 × 3 *in.* microscope slides. Epoxy Adhesives (HARDMAN). Norland UV optical glue. UV 365 nm lamp 4 WATT (Analytik Jena US).

B. Detailed fabrication process and suspension preparation

1) Silicon wafer preparation: The silicon wafer was dehydrated by heating on a hotplate at 150°C for 30 minutes.
2) Spin coating of a sacrificial layer of Omnicoat:
    a. 4 ml of Omnicoat was applied as a centered and circular puddle on the silicon wafer.
    b. The Omnicoat spreading used 500 rpm (at 100 rpm/s acceleration) for 10 secs and coating used 3000 rpm (at 300 rpm/s acceleration) for 30 secs.
    c. The wafer was then placed on a vacuum hotplate at 200°C for 1 min to remove the solvent. The wafer was cooled to ambient temperature before proceeding to the step 3.
3) Spin coating of SU-8 2001 layer:
    a. 5 ml of SU-8 2001 resist was applied as a centered and circular puddle on the silicon wafer.
    b. To obtain ~ 1 μm layer of the SU-8 2001 resist, spreading was done with 500 rpm (at 100 rpm/s acceleration) for 20 secs and coating with 3000 rpm (at 300 rpm/s acceleration) for 30 secs. The backside of the wafer was carefully cleaned by wiping with an acetone-wetted wipe.
    c. Soft bake: After spinning, the wafer was placed on a levelled vacuum hotplate at 65°C for 2 mins and 95°C for 3 mins to remove the solvent and densify the layer. To ensure uniform heating of the SU-8 layer, we placed the wafer on a pre-heated quartz disk on the hotplate.
4) Exposure of the wafer through a Chromium-on-glass photomask with round holes using 5X stepper (GCA Autostep 200 DSW i-line 365 nm Wafer Stepper). A pattern with 3000 × 3000 arrays of circular holes with diameter ~ 8.6 μm was generated on the Cr photomask using the Heidelberg Mask Write-DWL2000. The exposure time, and the lens focus in the 5X stepper machine were optimized to obtain the final diameter, d and parallel side walls in the cylindrical particles. The exposure time and focus were set as 0.22 secs and -1.4 μm, respectively.

5) Post-exposure bake of the SU-8 layer: the wafer was placed on a vacuum hotplate at 65°C for 2 mins and 95°C for 3 mins to cross link the exposed photoresist. The wafer was cooled to ambient temperature before proceeding to the next step.
6) Development of the SU-8 layer: The wafer was placed in a ~100 ml of SU-8 Developer for 1 min with manual gentle agitation. It was then carefully rinsed with IPA and immersed into a dish of IPA. If a white film persists, the wafer was developed for more time in a fresh SU-8 developer. The wafer was then rinsed carefully with DI water, IPA, and finally dried with nitrogen. Steps 1-6 were repeated for 10 wafers to obtain high concentration of particle suspension.
7) Release of the particles via dissolution of the sacrificial layer: The developed wafers were individually placed in a clean crystallization dish containing 100 mL of Remover PG and sonicated for 2 mins in an ultrasonic cleaner (Branson CPX5800H). The wafers were rinsed in Remover PG after sonication.
8) Suspension preparation: 20 ml suspension of cylinders in Remover PG was placed in 50 ml polypropylene centrifuge tubes. Centrifugation (Beckman Coulter Allegra X-12) was performed for each tube at 3000 rpm for 5 mins. The supernatant was discarded in each tube, and the particles were redispersed by sonication and a vortex mixer in 5 ml DI water. The 5 ml suspensions were then combined in one 50 ml centrifuge tube. The following procedure was repeated three times with DI water: (i) Centrifugation at 3000 rpm for 5 mins, (ii) removal of the supernatant, and (iii) redispersion of the particles in 10 ml DI water by sonication and a vortex mixer. Using the same procedure, the particles were then washed twice with IPA and three times with aqueous solution containing 75 μM (0.015 wt %) of Tergitol NP70. The volume was finally adjusted to ~ 5 ml, which corresponds to a particle concentration ~ 4.5×10^8 particles/ml and the suspension was transferred to a 10 ml glass vial. The sample was observed under optical microscopy after 24 hrs to check for any aggregation. Finally, the stable dispersed suspension was mixed with a small amount of fluorescein dye (2 mg/ml) to enable imaging.

C. Characterization of particles

Figure S5 a and b shows asymmetric features at the edges of the particles: the edges on the flat end in contact with the Omnicoat layer was sharp compared to the more rounded edges in the opposite face. A small sample of particles dispersed in DI water was deposited on a silicon wafer and imaged by SEM (Zeiss Supra 55VP or Zeiss Ultra 55) and the distribution of the height, σ and diameter, d of the particles was measured from 190 sample images (Fig. S5 c and d). We obtained the s_d and s_σ values from the distribution as 0.05 and 0.06, respectively. We also measured the zeta potential as ~ -50.9 $\pm$ 5.14 mV for the released particles in DI water using a light scattering tool (Malvern Zetasize Nano-ZS) and the measured value matches with the zeta potential of the "rough" cylinder particles [3]. The reported density of SU-8, ρ_p is 1200 kg/m^3. To understand the effect of the density mismatch between the CYL lithoparticles and water solvent on the orientation of the particle, we estimated the energy of the particle, U_g using,

$$\frac{U_g}{k_bT} = \frac{\Delta\rho\, V_p\, g}{4.11\times10^3}\left(\frac{\langle d\rangle}{2}\sin\theta + \frac{\langle\sigma\rangle}{2}\cos\theta\right) \qquad \text{(S3)}$$

where $\Delta\rho = \rho_p - \rho_{water}$ (kg/m^3), V_p is the particle volume (μm^3), g is the gravitational acceleration (m/s^2), and θ is the orientational angle between the unit vector perpendicular to the flat particle face and the unit vector in the z direction. We estimated a low transition barrier $\Delta U_g \sim 0.4\ k_bT$ between unflipped and flipped orientations (see Fig. S6).

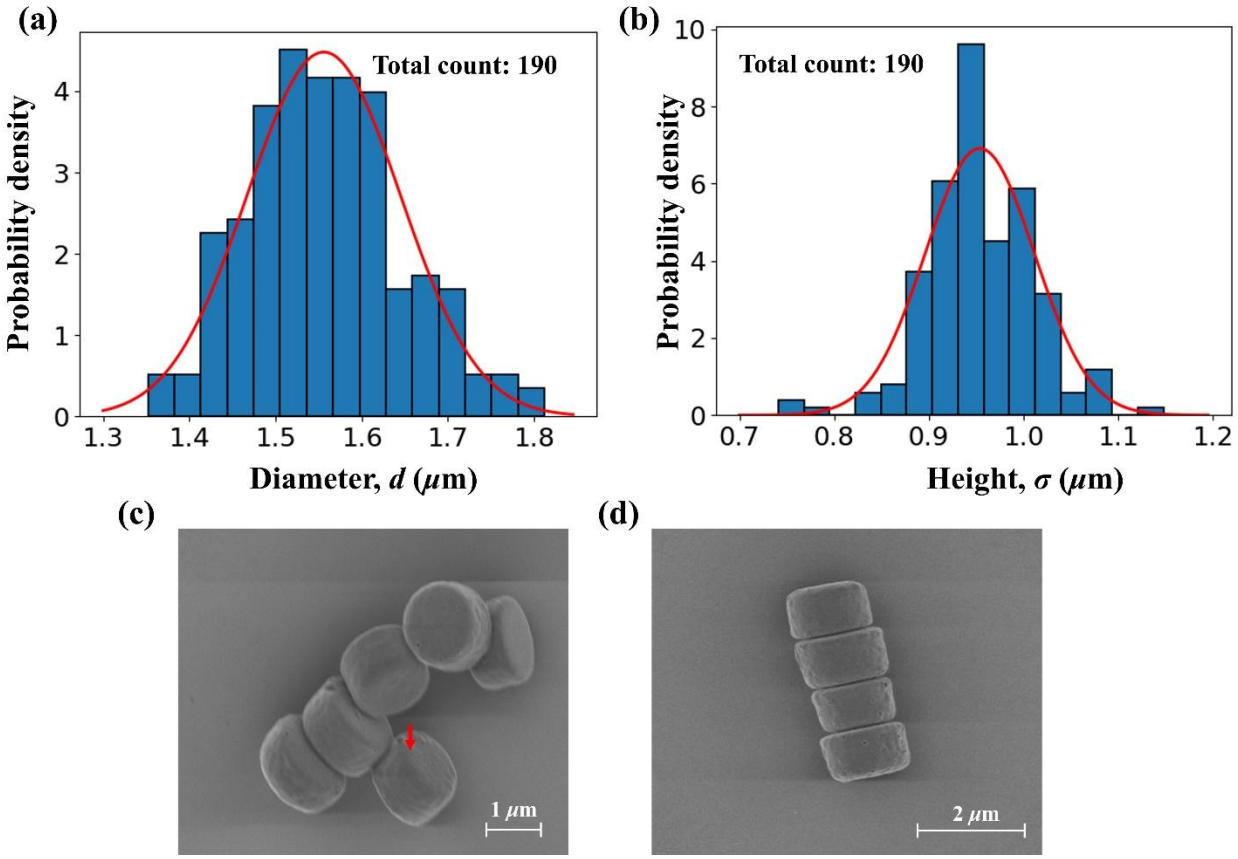

Fig. S5 (color online). Size distribution of particles with aspect ratio ~1.62 (a-b) obtained from scanning electron micrographs and (b-c) structure of the SU-8 2001 CYL lithoparticles. (a-b) The red curves are fits to the data using a Gaussian distribution with d = 1.56 $\pm$ 0.08 μm and σ = 0.96 $\pm$ 0.06 μm. (c) Arrow (red) shows the curved edge of the particle. (d) The end-to-end arrangement of the flipped particles show variation in particle diameter and height.

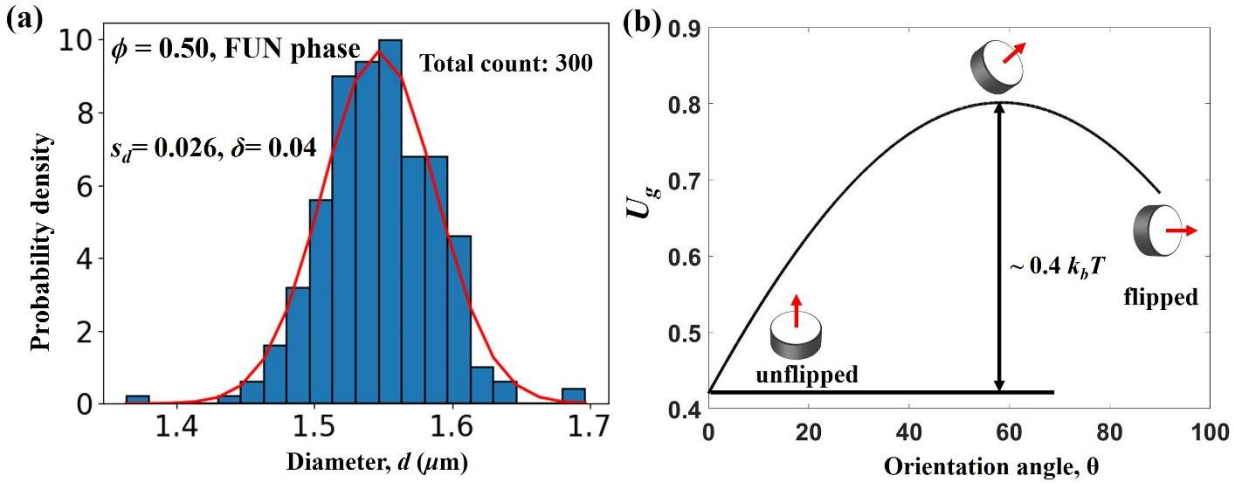

Fig. S6 (color online). (a) Distribution of the particle diameter, d obtained from the confocal images of the FUN phase at ϕ= 0.5. The red curves are fits to the data using a Gaussian distribution with d = 1.55 ± 0.04 μm and s_d= 0.026. (b) The energy, U_g, of the single particle at different rotational states accounting for the density mismatch between the CYL lithoparticle and water solvent (see Eq. S3). The orientational angle θ is the angle between the unit vector perpendicular to the flat particle face and the unit vector in the z direction.

D. Sample preparation

Wedge cell confinement was assembled using 24 × 60 *mm* coverslips with a 2 × 3 *in.* microscope slide that provides mechanical support. The coverslips were cleaned in aqueous NaOH solution for at least 30 mins and thoroughly washed in DI water. A coverslip was glued to the microscope slide using Norland UV adhesive that was cured with 365 nm UV lamp. Two rows of spacer dots (cured UV adhesive) were deposited near the top of the supported coverslip and another coverslip was overlaid. On the opposite end, pressure was applied to create a zero-height separation edge. This edge along with the two other sides were sealed with epoxy, leaving the top edge open for particle injection. Particle suspension was injected into the cell via a micropipette tip and was sealed with epoxy. To sediment the particles into the quasi-2D regions, the confinement cell was tilted at ~ 60° for at least 48 hrs. After sufficient densification, the cell was laid flat for another 48 hrs to equilibrate and the structures in the quasi-2D regions were examined using the Zeiss LSM 5 LIVE confocal microscope.

3 2D phase behavior

A. Hexagonal prisms

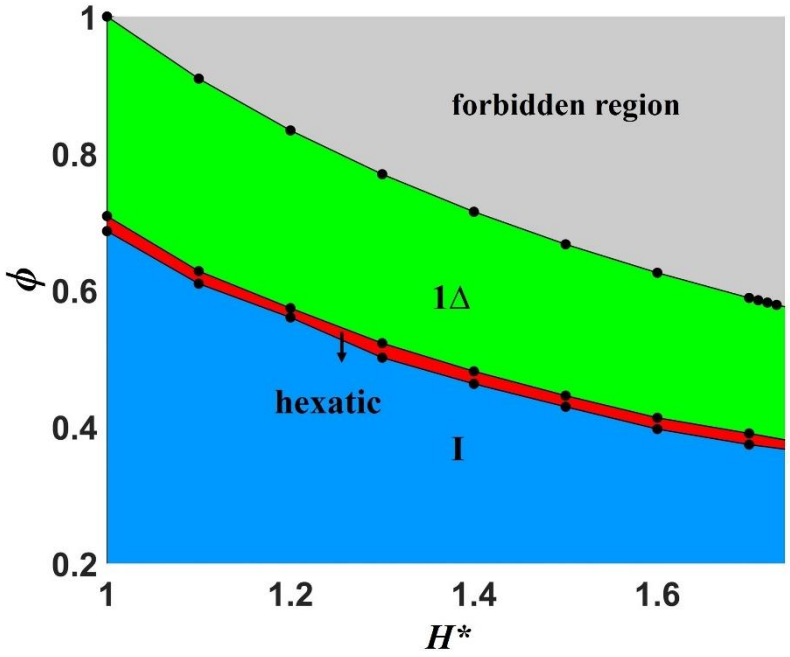

Fig. S7 (color online). Global phase diagram for hexagonal prisms at varying hard wall plate separation, H^*, and volume fraction, ϕ. The I, 1Δ, and hexatic phase boundaries are shown. 1Δ denotes the triangular solid and I is the isotropic phase, respectively. The forbidden region denotes the inaccessible state points in the phase diagram.

Figure S7 shows the phase behavior for the hard confinement model at narrow ranges of plate separation, $1.0 < H^* < 1.74$. The phases observed are similar to those of hard hexagons in a 2D plane, where the system transitions from the isotropic (I) phase to a triangular (1Δ) solid phase with an intermediate hexatic phase upon increasing the volume fraction, ϕ [4]. Figure S8a shows the equation of state for $H^*= 1.1$. As the I phase is compressed to $P^* > 2.0$ and $0.605 <$

$\phi < 0.631$, the particles assemble into a partially ordered structure with the characteristics of the hexatic phase (Ψ_6 = 0.4-0.65) and no four-fold order ($\Psi_4 \approx 0$). The global bond order value, Ψ_n where n=6 or 4, is obtained by calculating $\langle \left| \frac{1}{N} \sum_{i=1}^{N} \Phi_n(\boldsymbol{r_N}) \right| \rangle$ where $\Phi_n(\boldsymbol{r_N})$ is the local n-fold bond orientational order of N particles. At P^*= 2.33 and ϕ= 0.610, the analysis using the six-fold bond orientation correlation ($g_6(r^*)$) and pair correlation ($g(r^*)$) functions shown in Fig. S8b and S8c indicates that the hexatic phase has short ranged translational order, with quickly decaying of $g(r^*)$ peaks, and quasi-long ranged six-fold orientational order, with a $g_6(r^*)$ decaying algebraically with exponent $-¼$. By further increasing P^*, the system assembles into a solid structure forming the 1Δ solid phase that has both long-ranged $g(r^*)$ peaks and long-ranged $g_6(r^*)$ correlation function with Ψ_6 = 0.7-0.98. Figure S9 shows snapshots and associated structure factors, which display six-fold patterns due to the hexagonal order in the hexatic and 1Δ solid phase. Overall, our analysis suggests that the hexatic→1Δ solid transition follow the continuous KTHNY mechanism [5]. However, a rigorous analysis using simulations of much larger systems would be required to establish the mechanism more definitely and accurately map the boundaries of these transitions.

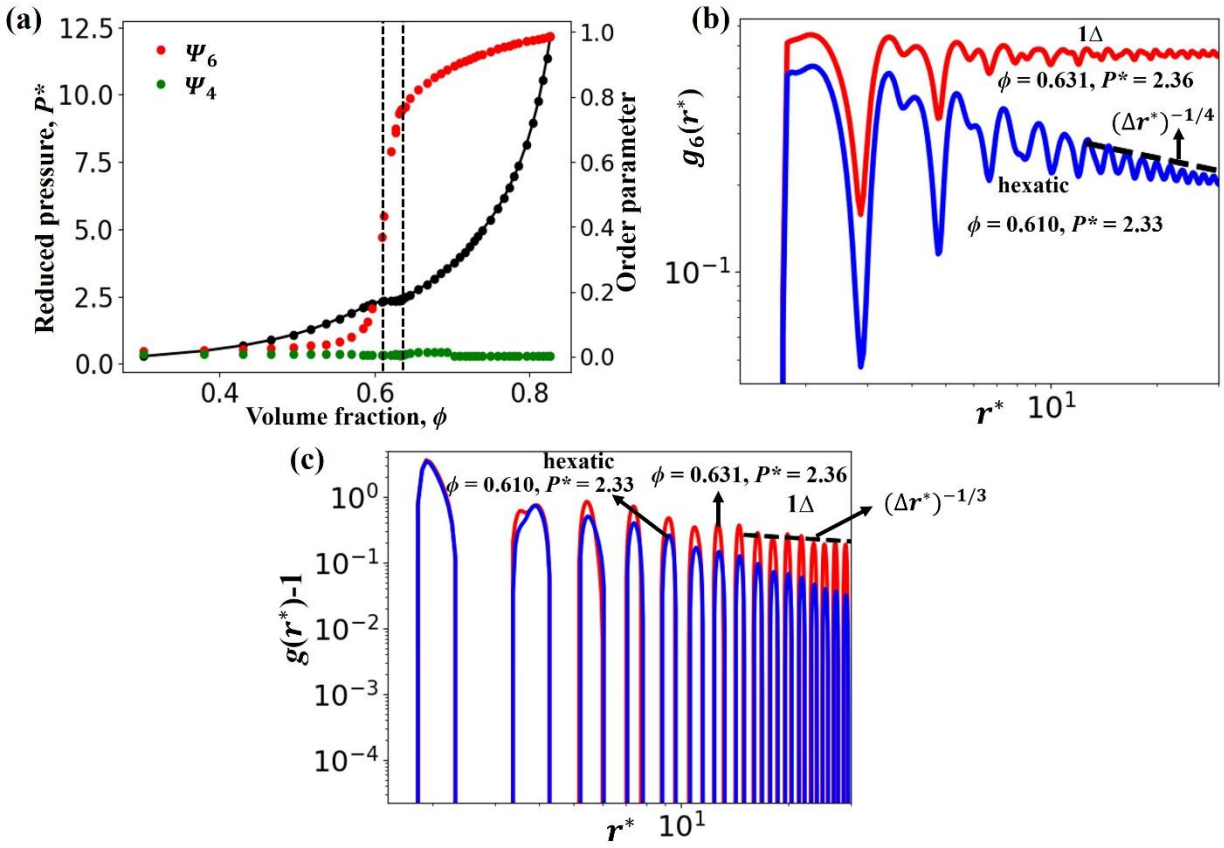

Fig. S8 (color online)**:** Equation of state and correlation functions for N= 1254 hexagonal prisms obtained by compression runs for H^* = 1.1. (a) Variation of P^*, Ψ_6, and Ψ_4 as a function of volume fraction, ϕ. Bond orientational correlation function, $g_6(r^*)$ (b), and radial distribution function, $g(r^*)$ (c) corresponding to the hexatic and 1Δ phases. The dashed line indicates the algebraic decay with exponent $-1/4$ (b) and $-1/3$ (c) corresponding to the KTHNY theory prediction for the hexatic phase and 1Δ solid phase, respectively.

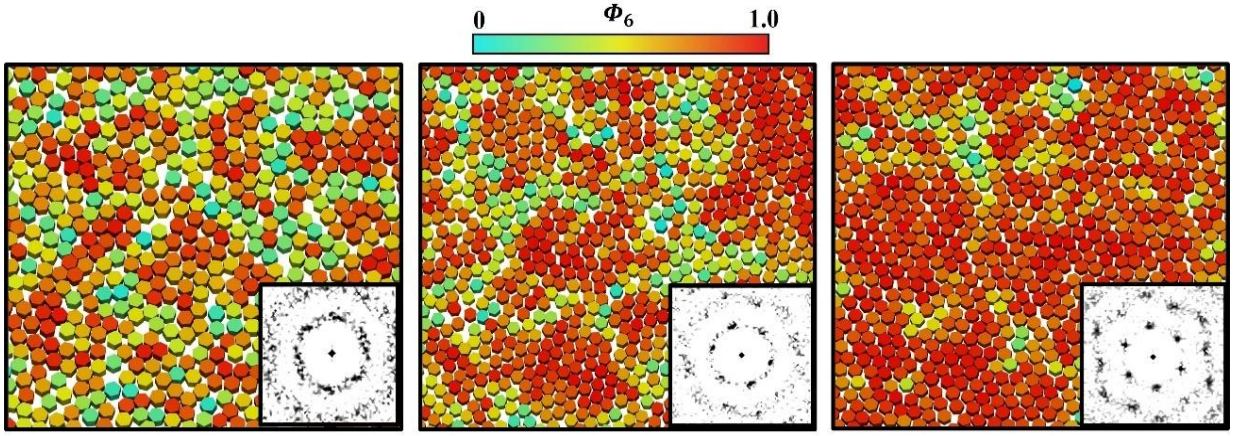

Fig. S9 (color online): Snapshots for left I ($P^* = 1.88$, $\phi = 0.57$), center: hexatic ($P^* = 2.33$, $\phi = 0.610$), and right: 1Δ solid phase ($P^* = 2.36$, $\phi = 0.631$) for a system of $N = 1254$ hexagonal prisms, including the corresponding structure factor, $S(\boldsymbol{k})$. Particles are colored based on the local Φ_6 values shown in the color bar atop.

At $H^*= 1.1$ and $\phi= 0.627$, the z-coordinate distribution is quite narrow, reflecting a small leeway in the z-direction (Fig. S10). As H^* is increased ($1.2 < H^* < 1.74$), the distributions become broader since the system increases configurational entropy by exploring positions available in the z-direction. These larger fluctuations along the z-axis occur even at higher concentrations due to the misalignment of particles within the monolayer. All the distributions shown in Fig. S10 are unimodal and the large fluctuations indicate that the particles have large local displacement modes similar to vibrational normal modes, which is a key contributor to the free energy of hard-core solids.

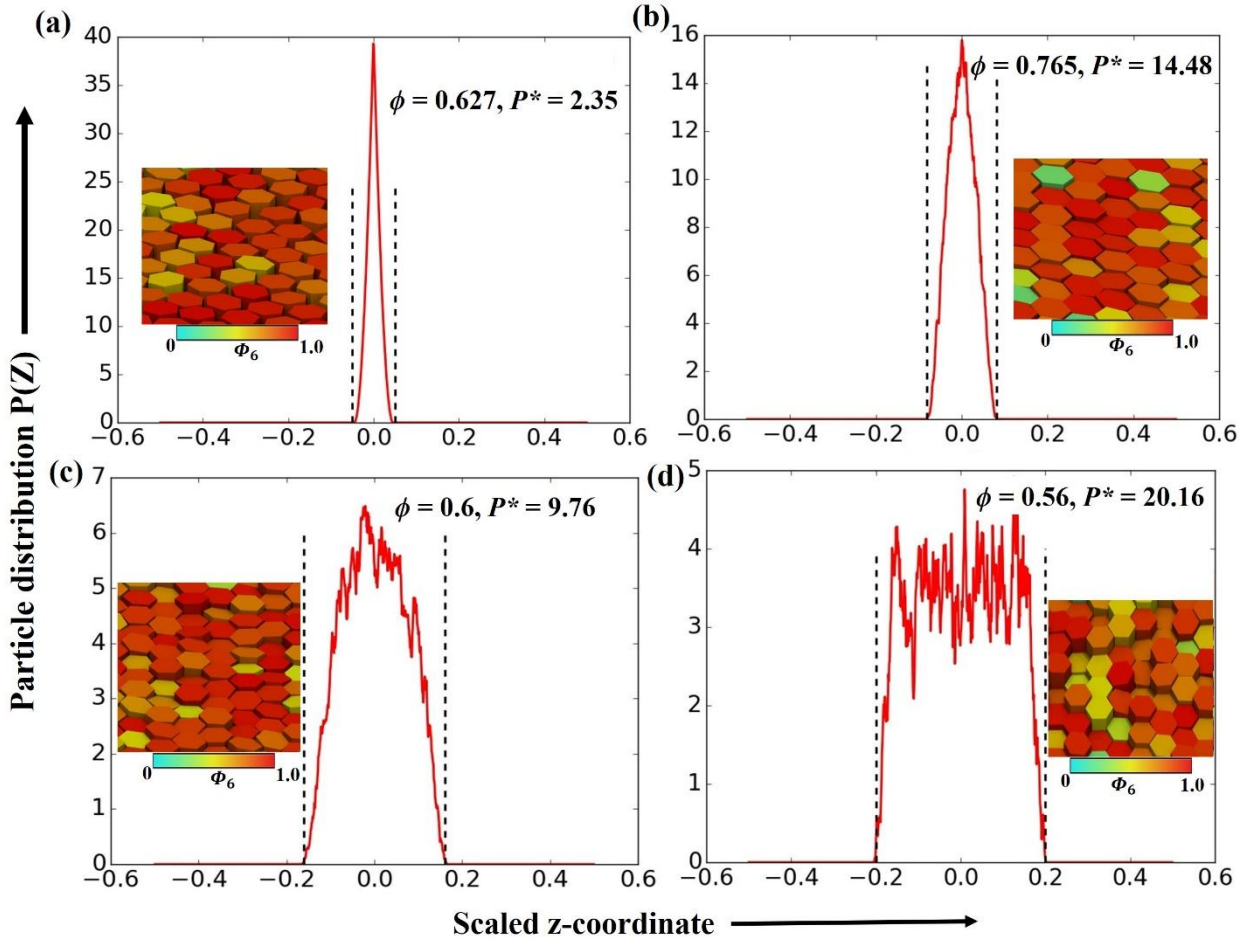

Fig. S10 (color online)**:** Z-coordinate particle distribution for the crystal structures at H^* = 1.1 (a), 1.2 (b), 1.5 (c), and 1.7 (d). The dotted lines show the bounds of accessible states. (Insets) Snapshots showing misalignment of particles along the z-axis.

4 Quasi-2D phase behavior for monodisperse HPs and CYLs

A. Uni-TS phase →Bi-TS phase transition at H^*= 1.84 for HPs in hard confinement

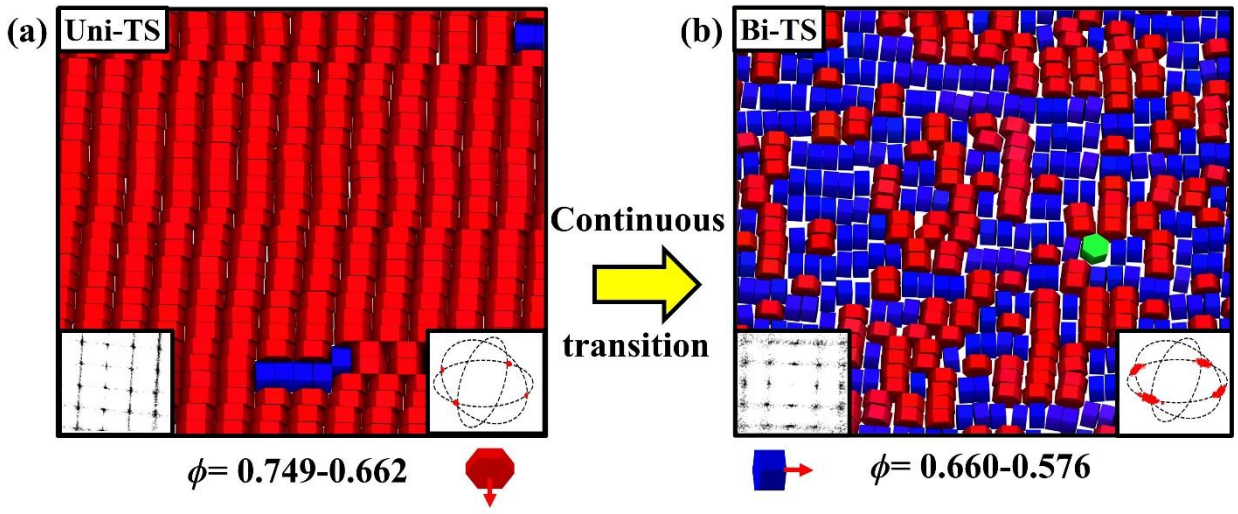

Fig. S11 (color online)**:** Equilibrium snapshots of (a) Uni-TS and (b) Bi-TS phases for 1352 HPs at H^* = 1.84 for the ϕ ranges indicated. Insets show the structure factor, and the orientational $\vec{u}$ distribution plots. The diffused peaks observed in the structure factor plot of the Uni-TS phase is attributed to the sliding/defects between the layers containing the flipped particle. Uni-TS/Bi-TS indicate the uniaxial/biaxial tetratic solid phase.

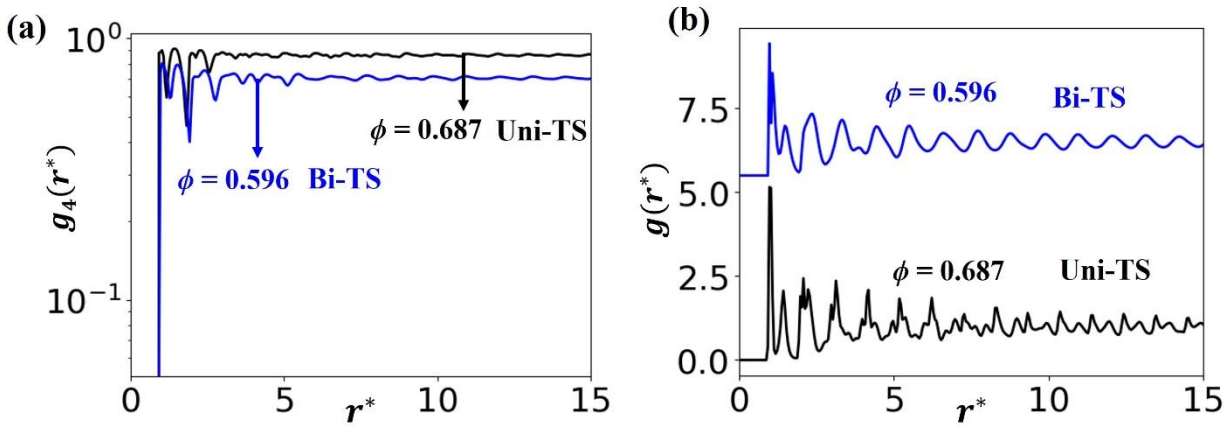

Fig. S12 (color online)**:** Correlation functions of the Uni-TS and Bi-TS phases for 1352 HPs at H^*= 1.84 under hard confinement. Bond orientational correlation, $g_4(r^*)$ and positional pair-correlation, $g(r^*)$ functions are shown, where r^* is the scaled radial distance.

B. Translational and rotational mobility for HPs at H^*= 1.84 and CYLs at H^*= 1.595

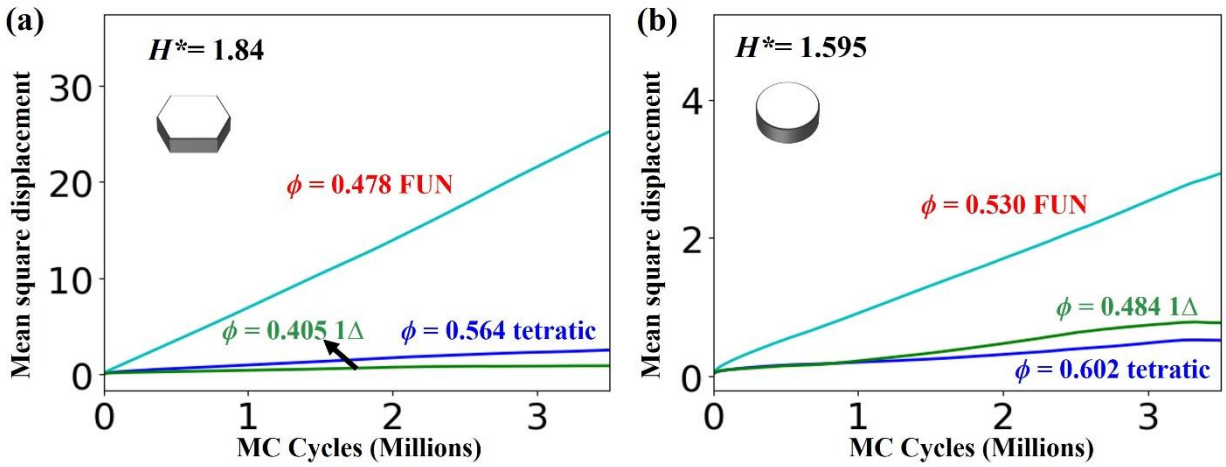

Fig. S13 (color online)**:** Mean square displacement for (a) HPs and (b) CYLs against Monte Carlo cycles for the tetratic phase, FUN phase, and 1Δ phases.

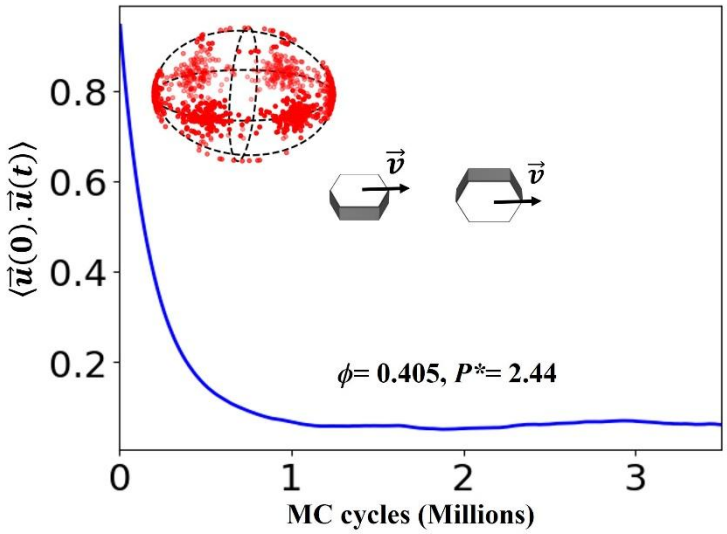

Fig. S14 (color online)**:** $\vec{v}$ rotational autocorrelation function against Monte Carlo cycles for 1352 HPs for the 1Δ phase at ϕ= 0.405, P*= 2.44 and H*= 1.84. The $\vec{v}$ distribution plot in the inset shows discrete sixfold symmetry.

C. Direct tetratic→1Δ phase transition for HPs at H^*= 1.8 and CYLs at H^*= 1.582

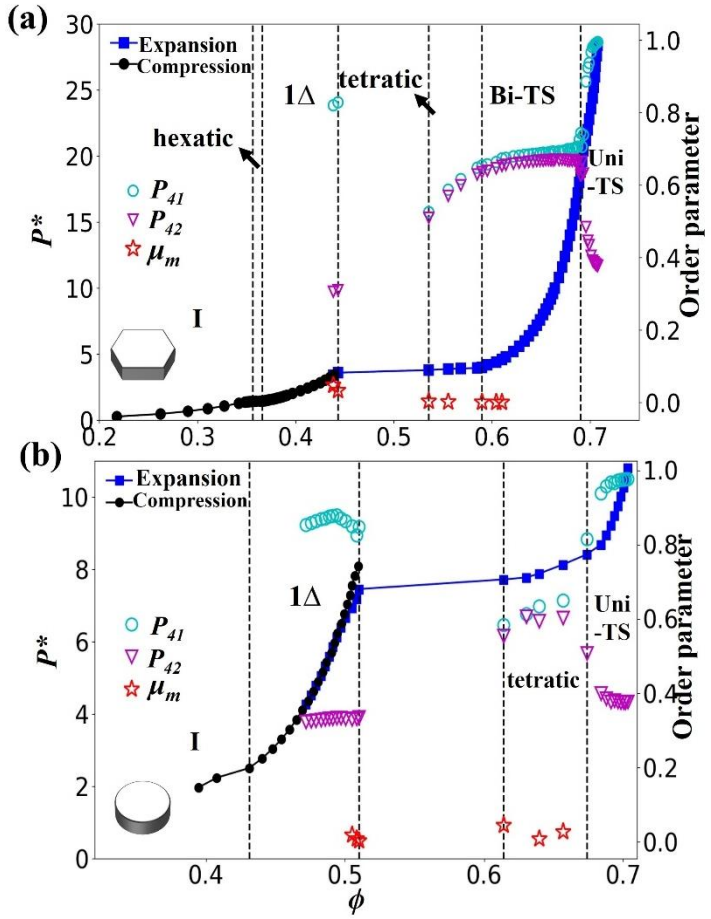

Fig. S15 (color online). Equation of state, P^* vs. ϕ, showing the compression and expansion runs for (a) HPs and (b) CYLs at H^* = 1.8 and 1.582, respectively. Dotted lines mark the approximate phase boundaries. For the HPs, compression/expansions used 1254/1352 particles. For the CYLs, the compression and expansion state points were obtained using 1024 particles. The variation of the cubatic order parameters, P_{41} and P_{42}, and translational mobility coefficient (scaled by a factor of 10^{-5}), μ_m, are also shown. 1Δ = triangular solid phase, Uni-TS/Bi-TS = uniaxial/biaxial tetratic solid phase, and FUN = disordered phase with a mixture of flipped and unflipped particles.

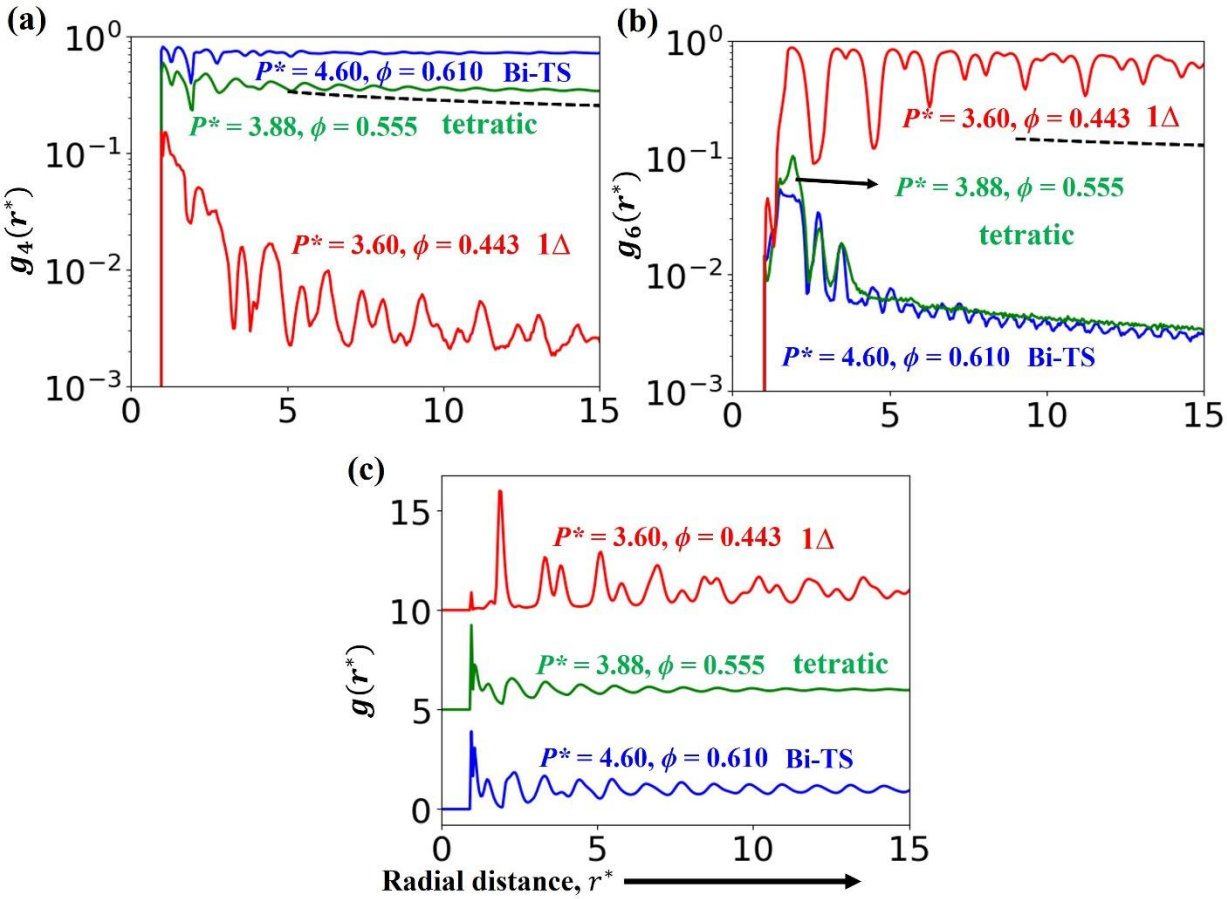

Fig. S16 (color online)**:** Correlation functions for hexagonal prisms under a hard confinement separation, $H^* = 1.8$. (a, b) Bond orientational correlation functions, $g_4(r^*)$ and $g_6(r^*)$, (c) pair-correlation function $g(r^*)$ for the Bi-TS, tetratic and 1Δ solid phases. r^* is the scaled radial distance.

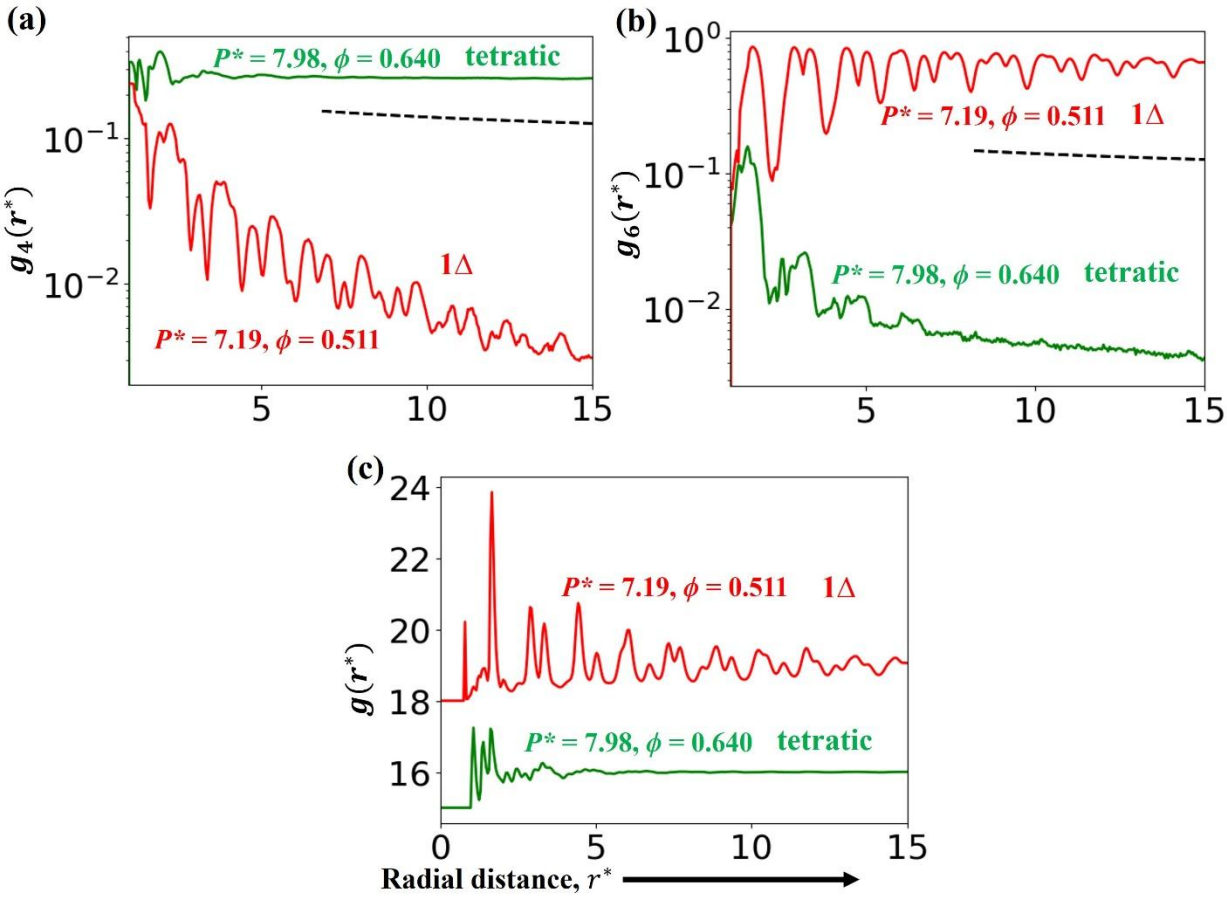

Fig. S17 (color online)**:** Correlation functions for CYLs under hard confinement separation, $H^* = 1.582$. (a, b) Bond orientational correlation functions, $g_4(r^*)$ and $g_6(r^*)$, (c) pair-correlation function $g(r^*)$ for the Bi-TS, tetratic and 1Δ solid phase. r^* is the scaled radial distance.

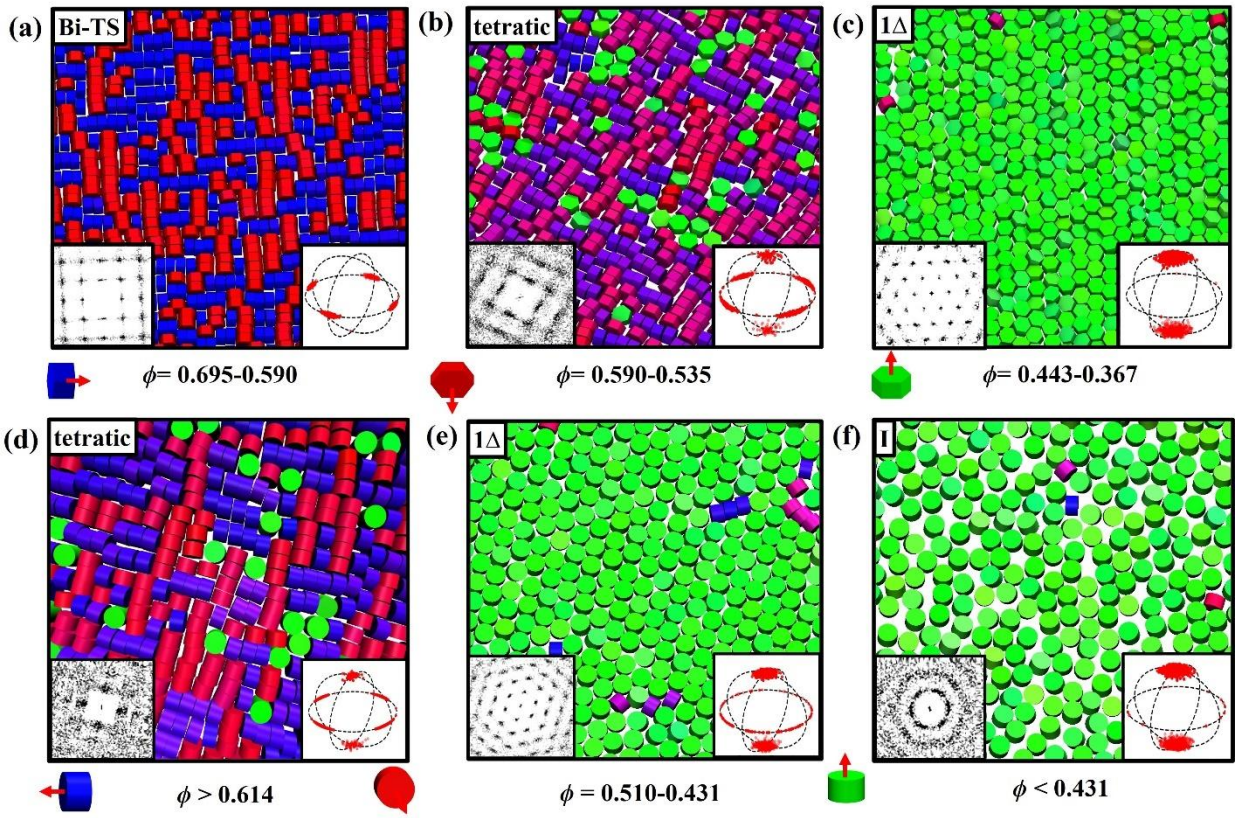

Fig. S18 (color online). Equilibrium structures of (a-c) HPs and (d-f) CYLs under hard confinement for different ranges of ϕ at H^* = 1.8 and 1.582, respectively. Representative snapshots, structure factor, and the $\vec{u}$ distribution plots for the stable phases are shown as insets. The flipped particles are colored based on the alignment with the P_4 in-plane director, where red and blue are the most and least aligned particles. The unflipped particles are colored green. Single particle $\vec{u}$'s are also depicted in x axis. I = isotropic phase.

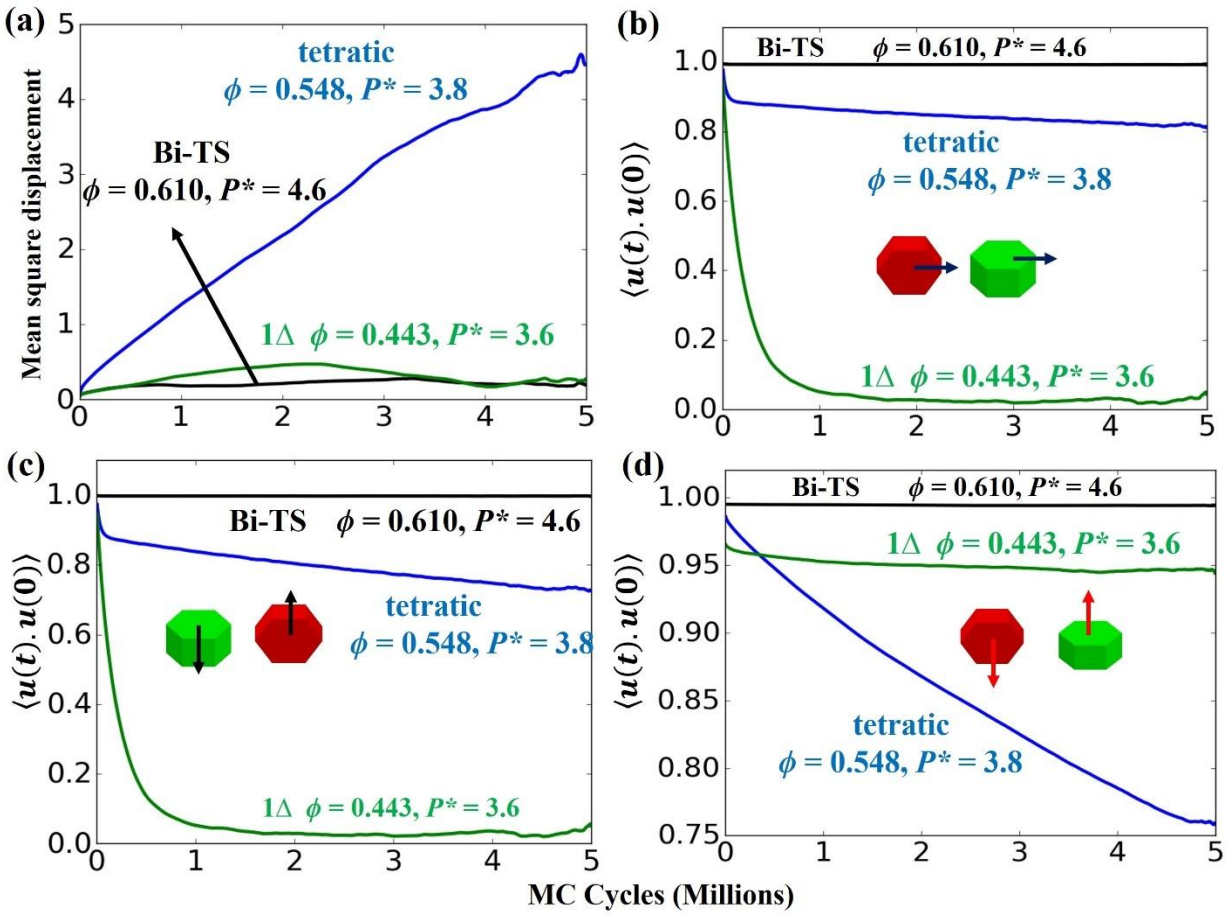

Fig. S19 (color online)**:** Mean square displacement (a) and rotational autocorrelation function for all three particle axes (b), (c), (d) against Monte Carlo Cycles for Bi-TS, tetratic, and 1Δ solid phases at a hard plate separation, H^* = 1.8.

D. Tetratic→FUN→I phase transition for HPs at H^*= 1.9 and CYLs at H^*= 1.61

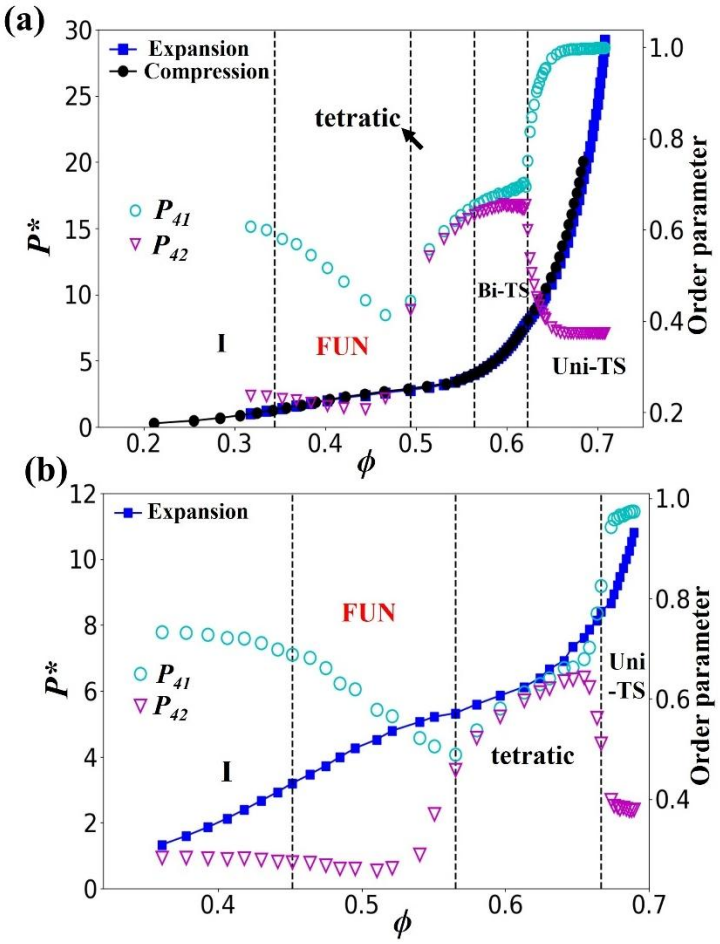

Fig. S20 (color online). Equation of state, P^* vs. ϕ, showing the compression and expansion runs for (a) HPs and the (b) CYLs at H^* = 1.9 and 1.61, respectively. Dotted lines mark the approximate phase boundaries. For the HPs, compression/expansion runs used 1254/1352 particles. For CYLs, the compression and expansion state points were obtained using 1024 particles. The variation of cubatic order parameters, P_{41} and P_{42}, are also shown. 1Δ = triangular solid phase, Uni-TS/Bi-TS = uniaxial/biaxial tetratic solid phase, and FUN = disordered phase with a mixture of flipped and unflipped particle states.

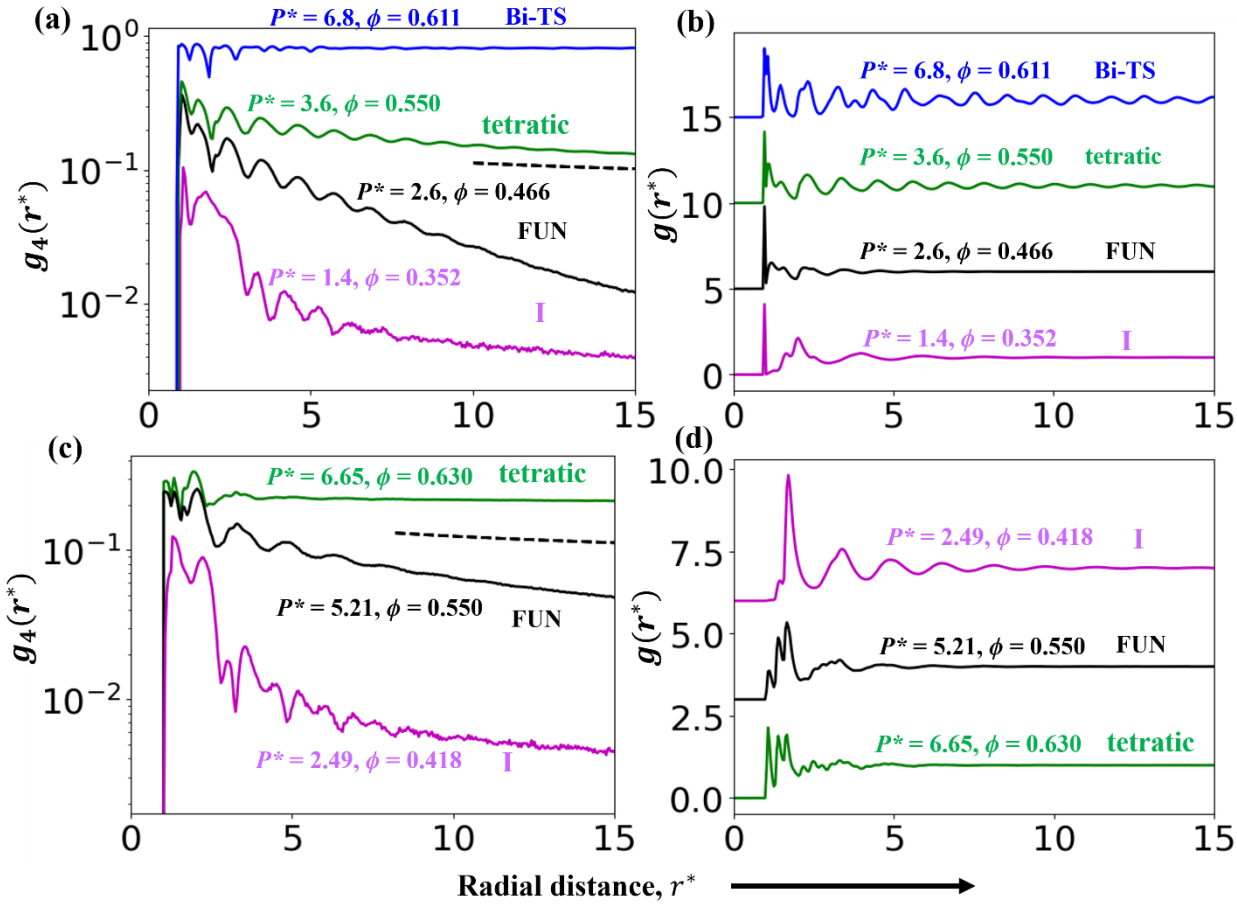

Fig. S21 (color online)**:** Correlation functions for (a, b) HP and (c, d) CYL at H*= 1.9 and 1.61, respectively. (a, c) Bond orientational correlation functions, $g_4(r^*)$ and $g_6(r^*)$, and (c) pair-correlation function $g(r^*)$ for the Bi-TS, FUN, tetratic and 1Δ solid phases. r^* is the scaled radial distance.

E. z-particle distribution function for HPs at H^*= 1.84 and 1.8 and CYLs at H^*= 1.595 and 1.582

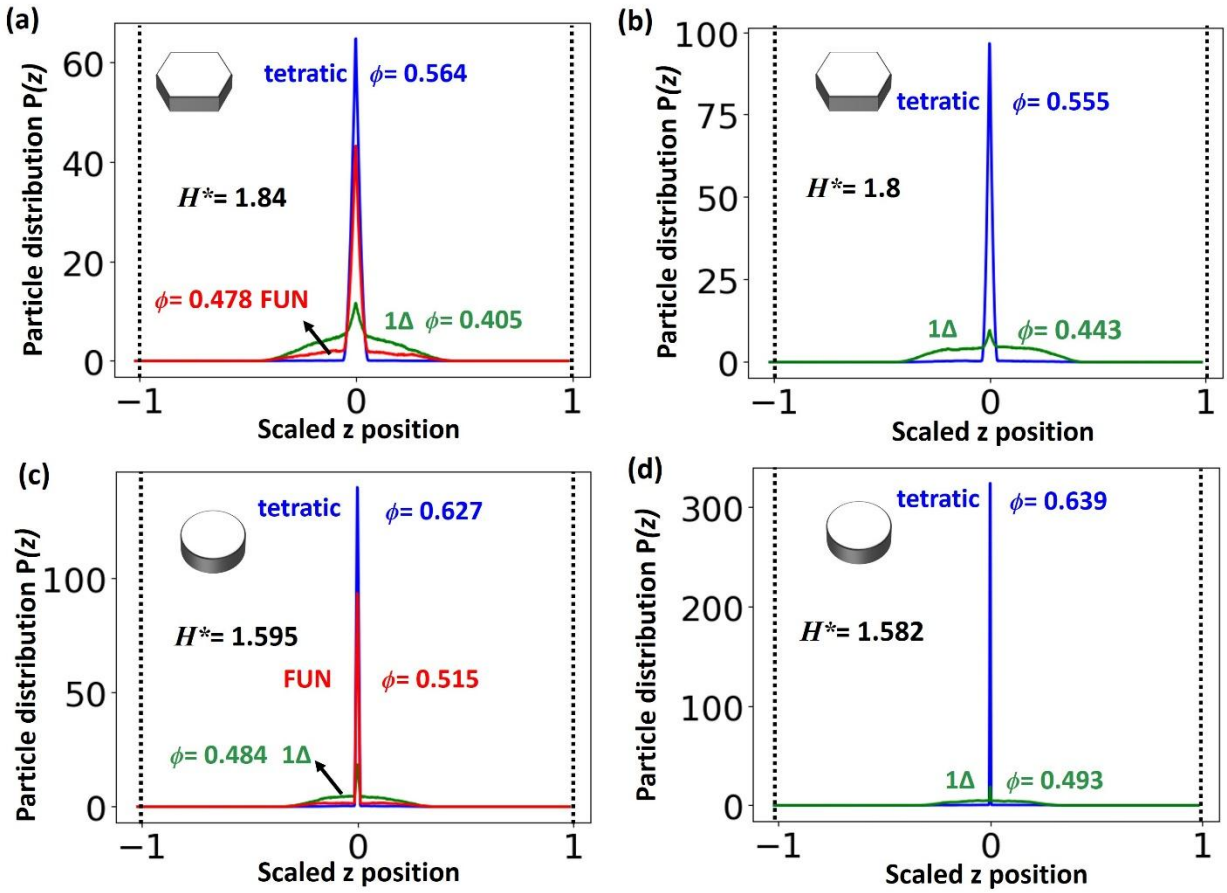

Fig. S22 (color online)**:** Z-coordinate distribution function for (a, b) HPs and (c, d) CYLs under different hard plate separation for the tetratic, FUN, and 1Δ phases.

5 Size polydisperse mixture of CYLs under hard confinement

A. Rotational autocorrelation function

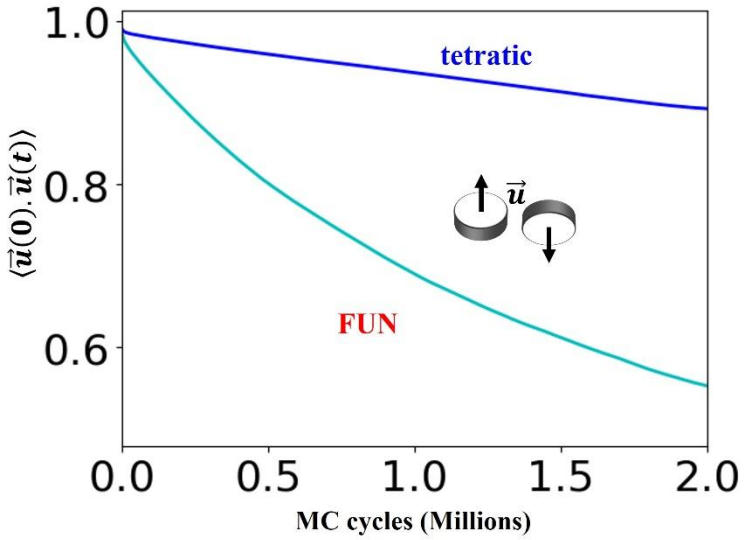

Fig. S23 (color online)**:** Rotational autocorrelation function against Monte Carlo cycles of the orientational vector $\vec{u}$ for 1254 CYLs with $s_d = 0.01$ and $s_\sigma = 0.06$ at $H^* = 1.025$.

B. Phase behavior for $s_d = 0.02$ and $s_\sigma = 0.06$

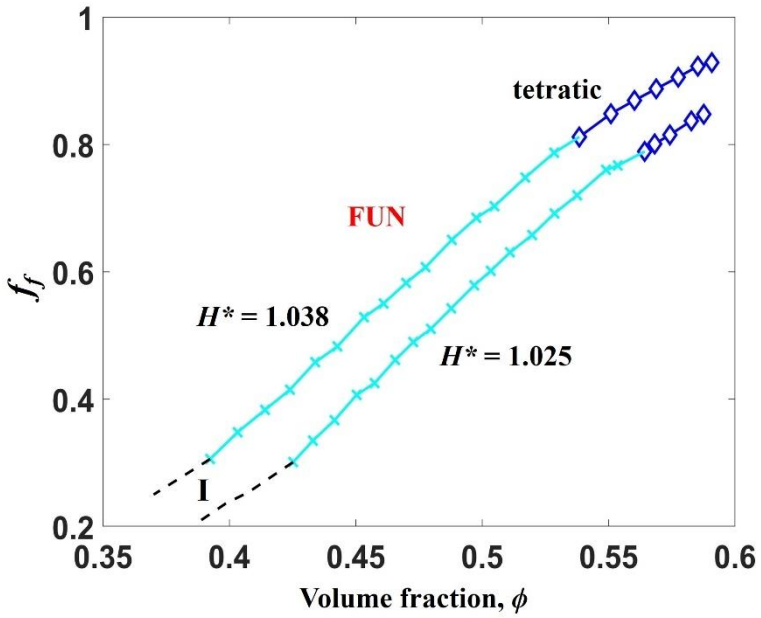

Fig. S24 (color online)**:** Variation of f_f with ϕ for CYLs with $s_d = 0.02$ and $s_h = 0.06$ at different H^* values. Black lines (dashed) represent the I phase regions. The tetratic and FUN phases are represented by blue diamonds, cyan crosses, respectively.

6 Soft confinement model with HPs

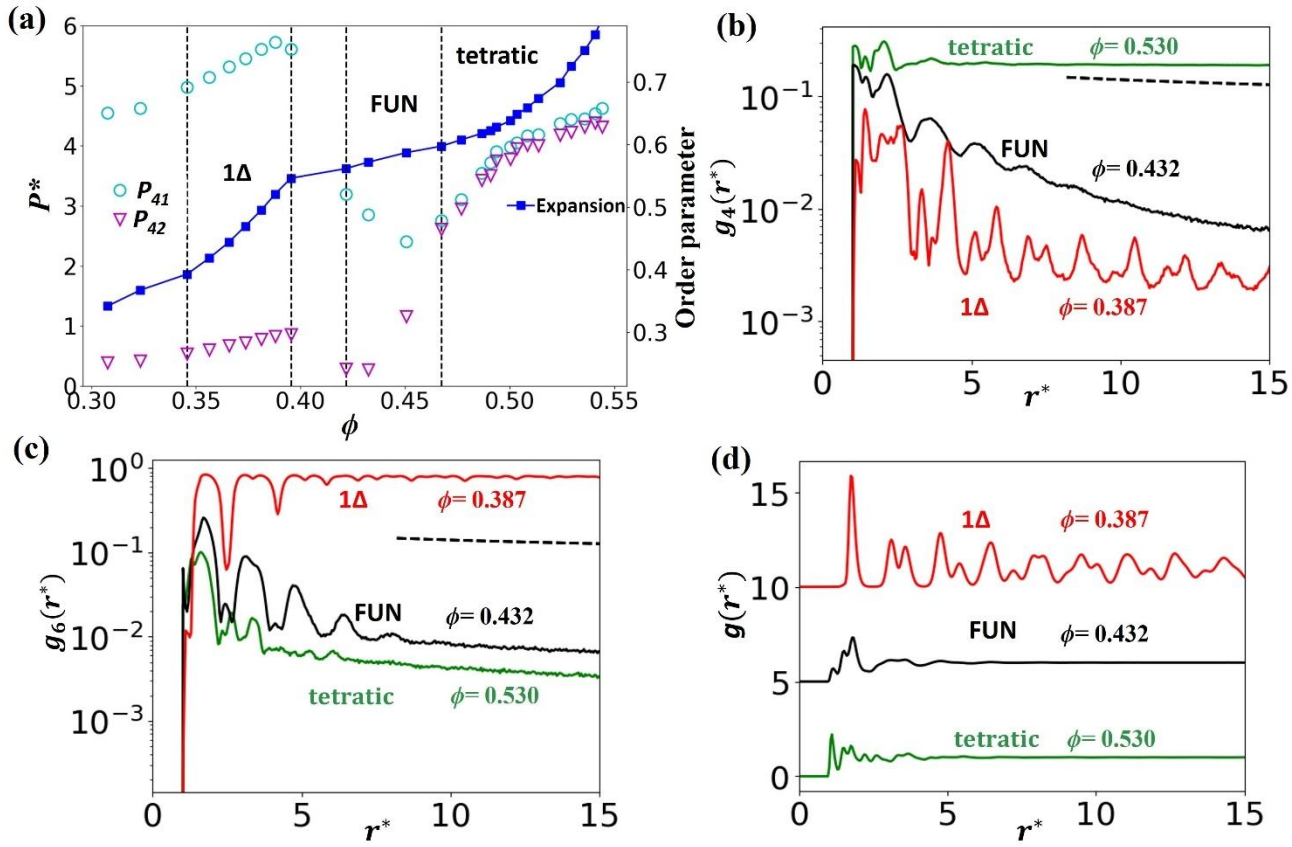

Fig. S25 (color online)**:** (a) Equation of state, P^* vs. ϕ, showing the expansion runs for the HPs at H^*= 1.9 and soft layer parameters β = 17.3 and a^* = 0.45.

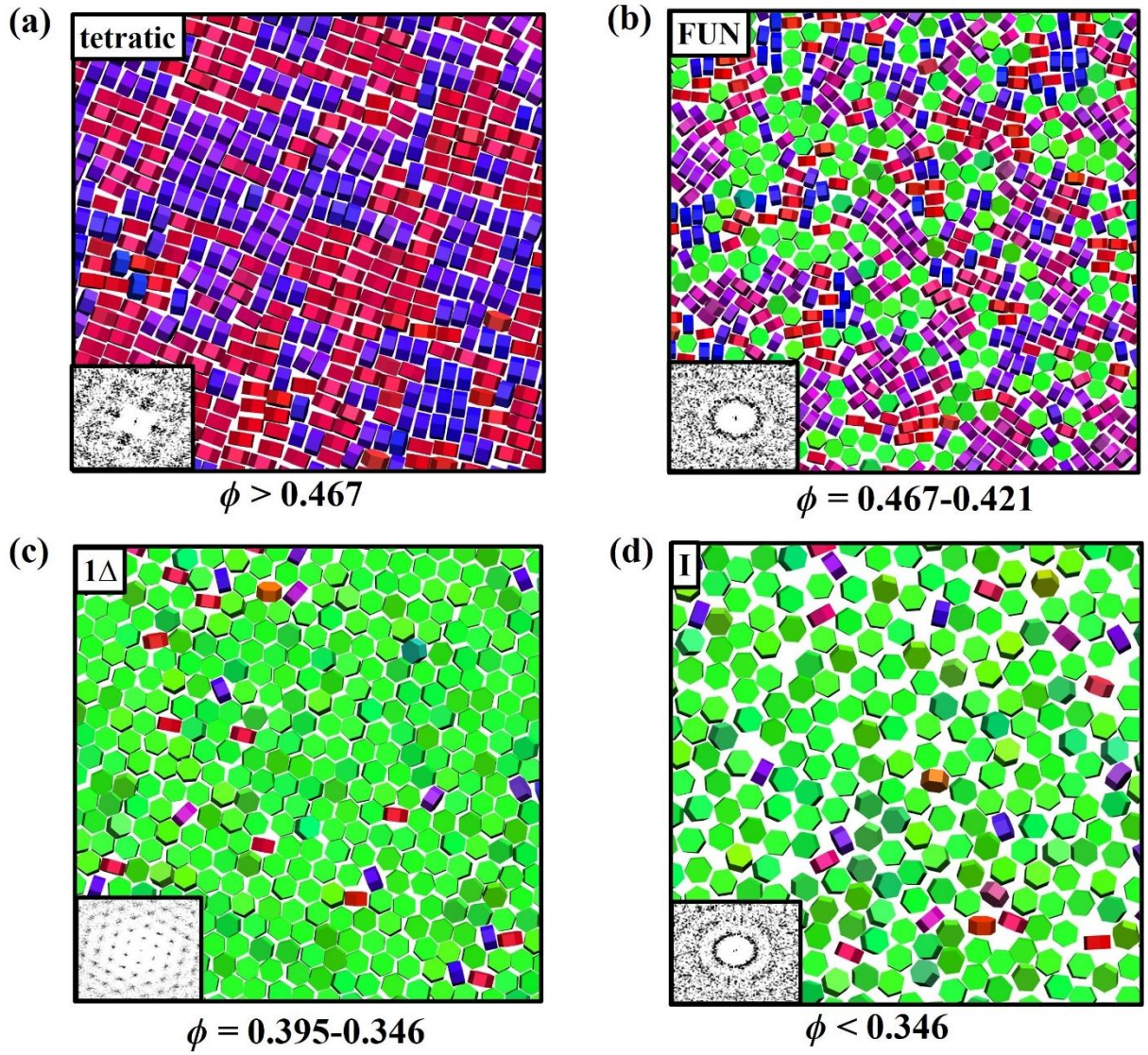

Fig. S26 (color online)**:** Equilibrium structures of HPs under soft confinement at H^*= 1.9 and soft layer parameters β = 17.3 and a^* = 0.45. Representative snapshots and the structure factor for the stable phases are shown as insets. The flipped particles are colored based on the alignment with the in-plane P_4 director, where red and blue are the most and least aligned particles. The unflipped particles are colored green. 1Δ = triangular solid phase, I = isotropic phase, and FUN = disordered phase with a mixture of flipped and unflipped particle states.

References

[1] J. De Graaf, L. Filion, M. Marechal, R. Van Roij, and M. Dijkstra, J. Chem. Phys. **137**, 2141001 (2012).

[2] A. Donev, J. Burton, F. H. Stillinger, and S. Torquato, Phys. Rev. B - Condens. Matter Mater. Phys. **73**, 054109 (2006).

[3] S. Badaire, C. Cottin-Bizonne, and A. D. Stroock, Langmuir **24**, 11451 (2008).

[4] J. A. Anderson, J. Antonaglia, J. A. Millan, M. Engel, and S. C. Glotzer, Phys. Rev. X **7**, 021001 (2017).

[5] D. R. Nelson and B. I. Halperin, Phys. Rev. B **19**, 2457 (1979).

CHAPTER 3: Bridging hexatic and tetratic phases in binary mixtures through near critical point fluctuations

B.P. Prajwal[1] and Fernando A. Escobedo[1]*

[1]Department of Chemical and Biomolecular Engineering, Cornell University, Ithaca, New York 14853, USA

Abstract

Monte Carlo simulations were used to study the assembly of model binary mixtures whose pure components have either distinct or similar crystal order symmetry. Specifically, we simulated mixtures of hard disks with either squares or hexagons, where the components have size ratios that optimize their co-assembly into compositionally disordered solids. For the disks+squares mixture, along with the enhanced regions of solid miscibility, we report a novel continuous-looking transition from the disk-like to the square-like behavior that occurs through a region that seamlessly bridges the regions of hexatic phase of disks and the tetratic phase of squares, which we term the *mosaic* (M) state. For the equimolar composition, this M state is bound by the isotropic phase at low pressures and by the hexatic-tetratic (two-phase) macro-phase segregated region above a critical transition pressure. Our analysis showed that the M state lies in the vicinity of the critical point, manifesting local compositional fluctuations that give rise to micro-phase segregated regions of interspersed square-rich four-fold and rhombic lattice symmetry, and disk-rich six-fold clusters, that coexist across the system. The M state is characterized by a short-ranged translational order and an algebraic decay of the correlation functions for six-fold and four-fold orientational order. A finite size scaling analysis was used to evaluate the dependence of the local compositional susceptibility with the system size to extract the critical exponent associated with the M→two-phase transition. For the disks+hexagons mixture, a fully mixed hexatic phase was observed for all compositions.

1. Introduction

Recent advances in the synthesis [1–3] and fabrication [4,5] of faceted sub-micron particles with different shapes have spurred interest in their use as building blocks for the assembly of targeted complex structures. Several tunable parameters like particle shape [6,7] and inter-particle interactions [7,8], allow the design of a wide range of morphologies having enhanced optical characteristics for potential applications in nanophotonics [9,10], sensing [11], and catalysis [12–14]. Towards designing such materials, recent efforts have focused on predicting phase behavior using theory [15,16] and simulation [6,17–21] for hard polyhedral particles in the bulk (3D) and in monolayers (2D), where the formation of ordered structures entirely depends on the entropic forces encoded in the particle shape. In particular, several experimental protocols leveraging slit confinement or interfacial pinning [22,23] can be deployed to assemble monolayers from different readily synthesizable nano- and micro-sized polyhedral or polygonal particles for applications in thin-film optical and electronic devices [24–28].

Single-component hard-particle superstructures arise at sufficiently high concentrations due to packing entropy manifesting as effective entropic bonds between the constituent particles. Pure systems of squares have been predicted to exhibit a Kosterlitz-Thouless-Halperin-Nelson-Young (KTHNY) [29–32] behavior, wherein the transition is continuous between both isotropic fluid and tetratic phase and tetratic and solid phases [21]. Simulation results reported for the melting behavior of hard disks suggest that the transition occurs in two steps with a first-order fluid-hexatic transition and a continuous hexatic-solid phase transition [33]. The tetratic and hexatic phases are partially ordered phases characterized by a short-range translational order and quasi-long ranged bond orientational order.

By *mixing* particles of different shapes, we can access a wider variety of superstructures having a combination of the constituents' physical properties. For example, ordered superstructures have been predicted for binary mixtures of hexagons+squares, squares+triangles, hexagons+triangles with and without enthalpic patchiness encoded in their facets [34]. The phase behavior of binary mixtures strongly depends on the relative size ratios and contents of the components. This correlation was observed, e.g, in a size-bidisperse system of hard disks, where the liquid-hexatic-solid transition changes to a first order liquid-solid transition upon increasing the composition of the small disks [35]. For binary mixtures of parallel hard squares

having disparate sizes, a fluid-solid phase-separated state was found with small and large squares forming the fluid and solid phases, respectively [36]. These predicted phase transitions reflect the interplay of mixing and packing entropy. At very high pressures, packing entropy dominates over mixing entropy leading to strong segregation of the components into their respective stable structures, separated by an interface. An interesting attribute associated with the phase separation of mixtures is the occurrence of critical behavior, the point where the two phases converge to become a single phase; this critical point can be approached either from the single or the two-phase region. The critical behavior associated with phase transitions is driven by the divergence in the magnitude of (otherwise local) compositional or density fluctuations as the critical point is approached. Critical phenomenon has been observed in a wide range of systems like colloid-polymer mixtures [37,38], active and passive colloid mixtures [39,40], and also in biophysical systems such as multi-component lipid bi-layers, and lipid monolayers [41,42].

In the context of a fundamental understanding of crystalline and partial ordering in 2D systems, the assembly of micro- and nanoparticles on hexagonal and square-lattice arrays [21,43] is well established and has been widely studied; however, much less is known about whether and how a system can be designed to gradually bridge these two types of ubiquitous lattice symmetries. In this work, we tackle this question by studying the entropy-driven assembly of binary mixtures of hard disks with squares using Monte Carlo simulations, where the components have size ratios that optimize their co-assembly into compositionally disordered solids. For reference, we also studied mixtures of disks and hexagons which, in contrast to disks and squares, exhibit pure-component solid phases and partially ordered phases with similar hexagonal lattice symmetry.

The disks+squares mixture with optimized size ratio was found to exhibit broad ranges of compositions where crystalline (with hexagonal and square order) and partially ordered phases (with hexatic and tetratic order) exist. Around the equimolar composition, a novel mosaic (M) state was observed having locally ordered microscopic clusters with square-rich four-fold and rhombic (RB) lattice symmetry, and disk-rich six-fold symmetry, that are distributed randomly throughout the simulated domain. The microscopic ordering of the four-fold and six-fold domains found in the M state are associated with the local compositional fluctuations that occur

in the region closer to the hexatic-tetratic critical point. This coexistence of finite clusters of two different symmetries over a finite range of conditions (pressures and compositions) can be seen as a small region that lies in the vicinity of the critical point, associated with the interplay of the hexatic and tetratic phases observed for the disk-rich and square-rich systems, respectively. For the binary mixtures of hexagons and disks, the hexatic phase is observed for all compositions since the individual pure-components have similar order-disorder transition behavior and lattice symmetry.

2. Methods

2.1 Exchange free energy calculation

We explored the phase behavior of 2D hard binary mixtures of disks+squares and disks+hexagons, when the components have size ratios that optimize their co-assembly into solid solutions. The size ratio is defined as $\xi = \sigma/a$ where σ = disk diameter and a = polygon edge length. For this purpose, we adopted the exchange free-energy method [44] to predict ξ values which tend to maximize the range of compositions and packing fractions where substitutionally disordered solid solutions occur. This general approach was recently introduced and applied to 3D mixtures of spheres and polyhedra. The method is based on finding the ξ value that minimizes an exchange free-energy (ΔF_x) metric, which is obtained by adding the excess chemical potentials associated with substituting one particle in each pure host solid by a guest particle:

$$\Delta F_x = \mu_{ex}^{s_1}(host \rightarrow guest) + \mu_{ex}^{s_2}(host \rightarrow guest) \quad (1)$$

where $\mu_{ex}^{s_i}$ is the reduced excess chemical potential (in units of thermal energy) associated with a single-particle host-to-guest mutation in pure host phase s_i (i = 1 or 2). $\mu_{ex}^{s_i}$ is also a mixing free energy at infinite guest dilution (see connection in Supplementary Information, SI, Sec. I) and hence by minimizing ΔF_x i.e., the *"cost"* for host-guest substitutions in both solid phases, mixing entropy and substitutionally disordered solution behavior are enhanced.

ΔF_x was found by using the unoptimized Bennett's formula, resulting in,

$$\Delta F_x \approx -\ln\left\{\frac{\langle P_{acc}^{s_1}(1 \rightarrow 2)\rangle}{\langle P_{acc}^{s_1}(2 \rightarrow 1)\rangle}\frac{\langle P_{acc}^{s_2}(2 \rightarrow 1)\rangle}{\langle P_{acc}^{s_2}(1 \rightarrow 2)\rangle}\right\}, \quad (2)$$

where $\langle P_{acc}^{s_i}(i \rightarrow j)\rangle$ (or $\langle P_{acc}^{s_i}(j \rightarrow i)\rangle$) is the average acceptance probability of virtually

mutating one particle of type i (or j) into a particle of type j (or i) in phase s_i at pressure, p_m [44]. p_m is the smallest pressure at which both pure components are solid phases for a given ξ. To estimate the p_m value, we selected the isotropic→tetratic transition as the relevant condition for the squares since the tetratic phase is a partially *"ordered"* phase that is stable for a broad range of densities (see SI Sec. II). In the case of disks and hexagons, since the hexatic phase region is narrow and heterogeneous, we choose the conditions for the hexatic→triangular solid (1Δ) phase transition (had we chosen the isotropic-hexatic transition pressure instead would have made no difference). To compute ΔF_x for different ξ, we used system sizes of 5040 particles for the disks+squares system and 6400 particles for the disks+hexagons system. Figure 1a shows the results for ΔF_x vs. ξ for the hard-core mixture of disks+squares. The minimum of ΔF_x occurs for $\xi = 1.04$, which, coincidentally corresponds to ξ where the pure disks and pure squares have equivalent order-disorder transition pressure (ODP) [45]. A relatively flat profile is observed for ΔF_x between $\xi \approx 1.04$ and $\xi \approx 1.2$ (noting that $\xi \approx 1.13$ corresponds to the shapes having equal area), with differences $< 0.2\ k_bT$. This region occurs when the product of the exchange probabilities, shown in the inset of Fig. 1a, are maximized. We choose $\xi = 1.1$ as the representative optimal value expected to promote the formation of regions with substitutionally disordered solid solutions (i.e., for the disk-rich and square-rich solid solutions), being quite near to $\xi = 1.04$ at the ΔF_x minimum. Similar calculations were performed for the disks+hexagons mixture shown in Fig. 1b. We observed the ΔF_x minimum for $\xi = 1.82$ (corresponding to equal-area shapes and quite close to $\xi = 1.84$ prescribed by the equal-ODP rule [45]). The difference in ΔF_x values is $< 0.6\ k_bT$ for $1.6 < \xi < 2.0$, indicating a relatively wide range of ξ expected to promote substitutionally disordered solid solutions.

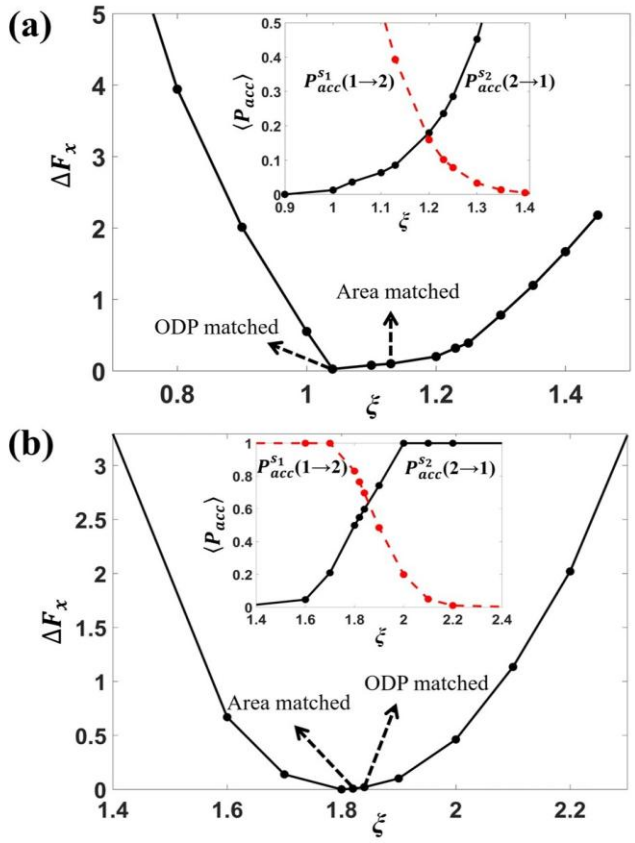

Fig. 1 (color online). Variation of the exchange free energy, ΔF_x, with component size ratio, $\xi = \sigma/a$, for the hard-core mixture of (a) disks and squares and (b) disks and hexagons (σ = diameter of disk, a = polygon edge length). The ξ values corresponding to equal footprint area and equal order-disorder transition pressure (ODP) are indicated. Curves are shifted so that the minimal value corresponds to $\Delta F_x = 0$. The inset shows the average exchange probabilities P_{acc} for mutating a host particle into a guest particle in the two solid phases (s_1-disks (1), s_2- squares or hexagons (2)) which are used to estimate ΔF_x.

2.2 Bond orientational order parameter

For 2D monolayer structures, the local *n*-fold bond orientational order, $\Phi_n(\boldsymbol{r_k})$ for each *k* particle is given by,

$$\Phi_n(\boldsymbol{r_k}) = \frac{1}{N_k} \sum_{j=1}^{k} \exp(in\theta_{jk}) \quad (3)$$

where *i* is the imaginary number and θ_{jk} is the angle between the vector connecting particle *k* with its neighbor *j* and a fixed reference vector. N_k is the number of nearest neighbors of particles *k.* For *n*= 6, N_k was calculated *via* Voronoi tessellation, while for *n*= 4, the four closest neighbors were used to avoid the degeneracy in the Voronoi construction [46]. The global six-fold and four-fold bond order parameter is then obtained by,

$$\langle \Psi_n \rangle = \langle \frac{1}{N} \sum_{k=1}^{N} \Phi_n(\boldsymbol{r_k}) \rangle \quad (4)$$

To analyze the correlation length of the local bond order parameters, we compute the *n*-fold local bond orientational correlation function given by,

$$g_n(r^*) = \langle \Phi_n(0)\, \Phi_n^*(\boldsymbol{r}) \rangle \quad (5)$$

where * indicates the complex conjugate of $\Phi_n(\boldsymbol{r})$ for the particle at a distance $\boldsymbol{r}$ from the reference particle.

2.3 Mapping of pressure-composition phase diagram

At each selected composition of a mixture, we used hard-particle Monte Carlo (MC) simulations in the isothermal-isobaric *NPT* ensemble and serial compression runs with small pressure steps, $\Delta P^* = 0.4$, starting from a low-density disordered state. We simulated systems with sizes in the range $8000 \leq N \leq 11203$ to estimate equation of state data and approximate phase boundaries; e.g., for the hexatic and tetratic phases. Each pressure step entailed 10^7 MC cycles with the last 2.5×10^6 cycles used for analysis, where each cycle includes *N* translations,

N rotations, $N/2$ swaps and 2 volume moves. A swap move randomly chooses a particle pair of different species (disk and polygon) and swap their positions while preserving the orientation of the polygon. Swap moves are imperative to speed-up the equilibration of the systems allowing particles to explore phase space far from their original positions [47]. All trial moves were accepted according to the Metropolis criterion, rejecting any overlaps between two disks, two polygons (via Gilbert-Johnson-Keerthi algorithm [48]) or a disk and a polygon (via the separating axes theorem [49]). The step size for the translational, rotational and volume moves are tuned to target acceptance probability values of 0.4, 0.4, 0.3, respectively.

We verified the formation of solid solutions by mapping the pressure-composition phase diagram for the binary mixtures with the *optimized* components size ratio ξ values (1.1 for disks+squares and 1.82 for disks+hexagons mixtures). The phase boundaries were identified by analyzing the local correlation of the six-fold and four-fold bond-orientational (see Sec. II B for details) and the positional order parameters.

At high pressures, the disks+squares mixture phase-separate into their respective nearly pure component solid phases. The regions where the two phases coexist were mapped based on the results from interfacial simulations (see SI Sec. III). Most interfacial simulations were carried out at the equimolar global composition, with additional runs performed for other compositions to better map out the two-phase coexistence boundaries. Results are reported in dimensionless quantities for distance, $r^* = r/a$, reduced pressure, $P^* = Pa^2/k_bT$ and area fraction/density, $\eta = NA_p/A$, where P is pressure, k_b is Boltzmann's constant, T is temperature, N is the total number for particles, A is the total area of the system, and A_p is the area occupied by the particles.

2.4 Analysis of critical and near critical point behavior in disks+squares system

Finite size scaling (fss) analysis was used to locate the critical point and extract the critical exponents associated with the hexatic-tetratic phase transition. As the critical point is approached the correlation length and the susceptibility, χ, both diverge following a power law. The fss analysis provides a way to extrapolate the diverging properties obtained in finite box size simulation to the thermodynamic limit. In this study, we carry out the fss analysis for the squares+disks mixture with ξ= 1.1 to obtain the critical point and extract the critical exponents at the equimolar composition. The analysis is done for N= 10000 particles and at each value of P^*, the square simulation box with side length, L_b is divided into $N_b \times N_b$ (where N_b=1, 2,…) sub-cells of linear dimension, L (= L_b/N_b) [49]. We note here that the fluctuation observed in L at each P^* due to area-changing moves was less than 1%. We measure the susceptibility χ as a function of P^* for each sub-cell width L, using the fluctuation relation given by [39],

$$\chi(P^*) = L^2 \langle (S - \langle S \rangle)^2 \rangle \qquad (6)$$

where the local order parameter, $S = x_{sq}^L - x_d^L$, x_{sq}^L and x_d^L are the compositions of squares and disks within the sub-cell of width L. The χ for the bimodal distribution observed in the two-phase region is evaluated by assuming a mixture model of two normal distributions [39]. We note here that the local compositional fluctuations gauged using the fss analysis are akin to those that would be observed in a grand canonical ensemble. The sub-cell sizes are carefully chosen such that the length L, assuming $L \geq \mathfrak{E}$ (where $\mathfrak{E}$ is the correlation length), provides a reasonable statistical measure of the local compositional fluctuations.

We also performed large scale simulation of the M state that occurs near the critical point to obtain the long-ranged characteristics of the six-fold and four-fold bond-orientational order parameters. To achieve this, we followed the scale-up protocol described in Ref. [21]. First, we equilibrated the equimolar disks+squares mixture with ξ= 1.1 and N= 6400 particles in the *NPT* ensemble at P^*= 14.9 starting from a random initial particle configuration in a square box. The final equilibrated structure with the target density is replicated 2×2 times to obtain the initial configuration with N= 25600 particles for the second equilibration run in the isochoric (*NVT*) ensemble. In the final stage, the equilibrated structure is again replicated to reach the target

system size with N= 102400 particles and equilibrated in the NVT ensemble. At every stage, the equilibration runs were carried out for 10^7 MC cycles. Results are reported in dimensionless quantities for distance, $r^* = r/a$, reduced pressure, $P^* = Pa^2/k_bT$ and area fraction/density, $\eta = NA_p/A$, where P is pressure, k_b is Boltzmann's constant, T is temperature, N is the total number for particles, A is the total area of the system, and A_p is the area occupied by the particles.

3. Results and discussions

The area fraction-composition and pressure-composition (Figs. 2a and b) phase diagrams exhibit broad stable regions of substitutionally disordered square-rich 1□ (square lattice) and disk-rich 1Δ (triangular lattice) solid solutions along with the hexatic (in disk-rich region) and tetratic (in square-rich region) phases. The disk-rich 1Δ solid phase dissolves up to 30% of squares which do not have any orientational preference and are randomly distributed throughout the underlying 1Δ lattice sites (Fig. S3 in SI Sec. V). In the square-rich side, the 1□ solid phase dissolves up to 26% of disks and is preceded by regions of tetratic and I (isotropic) phases at lower pressures. For $\eta < 0.836$ and $P^* < 19$ and for all x_s values, we observed two main phase transitions: I → hexatic and hexatic → 1Δ solid in the disk-rich region ($x_s < 0.3$) and I → tetratic and tetratic → 1□ solid in the square-rich region ($x_s > 0.74$). The transitions from the I phase to the ordered 1Δ (or 1□) solid, occurring through an intermediate hexatic (or tetratic) phase, are analogous to the well-studied phase transitions in the systems of pure monodisperse hard-disks (or hard-squares). The tetratic phase formed by the pure squares (x_s=1.0) is stable over a range ~ $8.25 < P^* < 15.4$ and $0.72 < \eta < 0.832$ [21] that is wider than the $7.59 < P^* < 7.68$ and $0.716 < \eta < 0.72$ [33,51] range of the hexatic phase formed by pure disks (x_s=0), a difference that can be attributed to the defects being more delocalized in the tetratic phase [21].

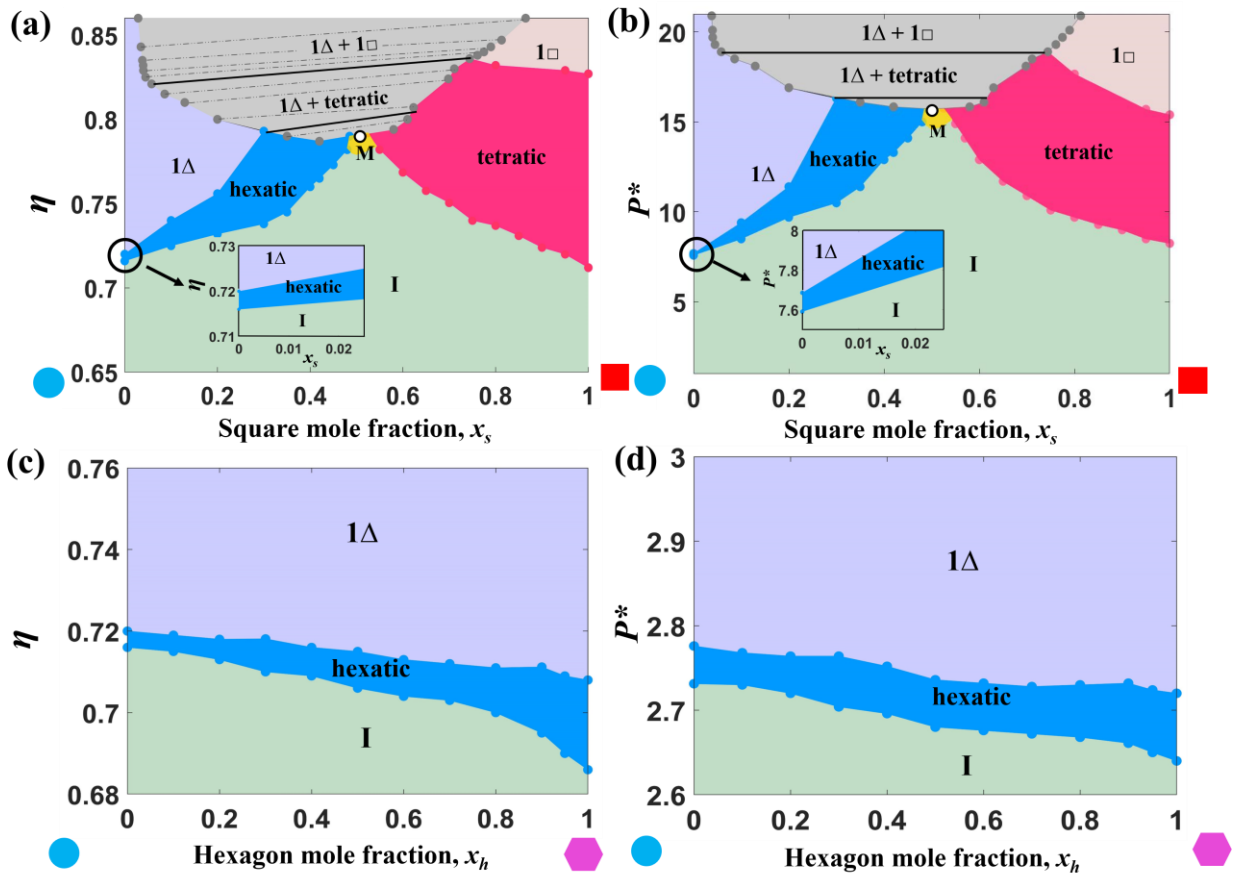

FIG. 2 (color online). Area-composition and pressure-composition phase diagram for mixtures of disks+squares (a and b) and disks+hexagons (b and c) at their corresponding optimal component size-ratio $\xi = \sigma/a$ of 1.1 and 1.82, respectively. In (a and b) the white dot indicates the critical point at equimolar composition and the yellow and grey-shaded area corresponds to the M state and two-phase coexistence region, respectively. In (a) the tie lines in the two-phase regions are shown as dashed lines. The insets in (a) and (b) shows the I, hexatic and 1Δ regions as $x_s \to 0$. The symbols 1Δ, 1□, and I denote the triangular solid, square solid, isotropic phase, respectively and M indicates the mosaic state.

Figure 2a and b also shows that, with increasing molar fraction of squares (disks) in the disk-rich (square-rich) region, the range of η and P^* where the hexatic (tetratic) phase is stable increases significantly compared to the pure disk (square) system. This increase in the stability region for the hexatic phase with x_s suggests that the squares accentuate the hexatic behavior as it persists even for up to $P^* \sim 16.2$, which is approximately twice the pure-disk hexatic →

1Δ solid transition pressure of $P^* \approx 7.68$. The tetratic phase is stable up to $P^* \approx 18.9$ with increasing disk concentration, which is about 1.2 times the pure-square tetratic → 1□ solid transition pressure, $P^* \approx 15.4$. This increase in the stability regions of the hexatic and tetratic phases with the content of the guest component is attributable to the increased concentration of topological defects created by the dissimilarly shaped particles residing in the host-solid lattice. These defects tend to destroy the quasi-long-range positional correlation in the solid phases in favor of the corresponding partially ordered phases.

The disks and hexagons form a *'compatible'* mixture system since both pure components form the hexatic and 1Δ ordered phases. As shown in Figs. 2c and d, this enables a high mixing affinity that leads to the formation of a 1Δ solid solution for the entire range of hexagon compositions, x_h. The hexatic phase was stable for all compositions within the narrow range of $2.70 < P^* < 2.77$ and $0.708 < \eta < 0.72$ in the disk-rich and $2.64 < P^* < 2.73$ and $0.68 < \eta < 0.71$ in the hexagon-rich regions. We identified the boundaries between the hexatic phase and 1Δ solid solution by analyzing the positional pair-correlation and six-fold bond orientational correlation functions (see Sec. VIII and Fig. S14 in the SI for details). We note here that two-1Δ phase-separated states are likely to occur at pressures much larger than those simulated here, and reach conditions where packing entropy would overtake the mixing entropy that favored the 1Δ solid-solution state. Note that for the pure disk limit in the disks+squares and disks+hexagons diagrams shown in Figs. 2b and 2d, the stability P^*-range of the hexatic phase is numerically different because P^* values are reduced with respect to the corresponding polygon edge lengths (i.e., $P^* = Pa^2/k_bT$), rather than the disk diameter. The rest of this section is devoted to analyzing the highly non-trivial results of the disks+squares mixture only.

Figures 2a and b shows a peculiar continuous transition between the disk-like and the square-like behaviors over a range of square molar fractions, $0.48 < x_s < 0.53$, $14.5 < P^* < 15.72$ and $0.779 < \eta < 0.791$. We assign this region bridging the hexatic and the tetratic phases as the mosaic (M) state. Along increasing P^* or η at the equimolar mixture composition, the M state is sandwiched between the I and (hexatic-tetratic) two-phase regions and precedes the critical point (see Fig. 3a). The I → M transition occurs at $P^* = 14.5$ and $\eta \approx 0.779$. As the critical point is reached at $P^* = 15.72$ and $\eta = 0.791$ from the M state, we observed that the distribution width of the local order parameter, S (see Fig. 3b) increases, indicating that the fluctuations of the

local composition grow giving rise to the micro-domains of square-rich tetratic and disk-rich hexatic phases. At P^*= 15.84 and η= 0.793, the distribution of S changes from unimodal to bimodal indicating the onset of a two-phase coexistence state containing macro-segregated six and four-fold ordered domains within the given simulation box size. We used this incipient bimodal state (for the equimolar system at P^*= 15.84) to estimate the approximate x_s values of the two coexistence phases near the lower bound of the two-phase coexistence boundary shown in Figs. 2a and b. We expect a relatively flat boundary closer to the mixture critical point where the composition of the two coexisting phases converge.

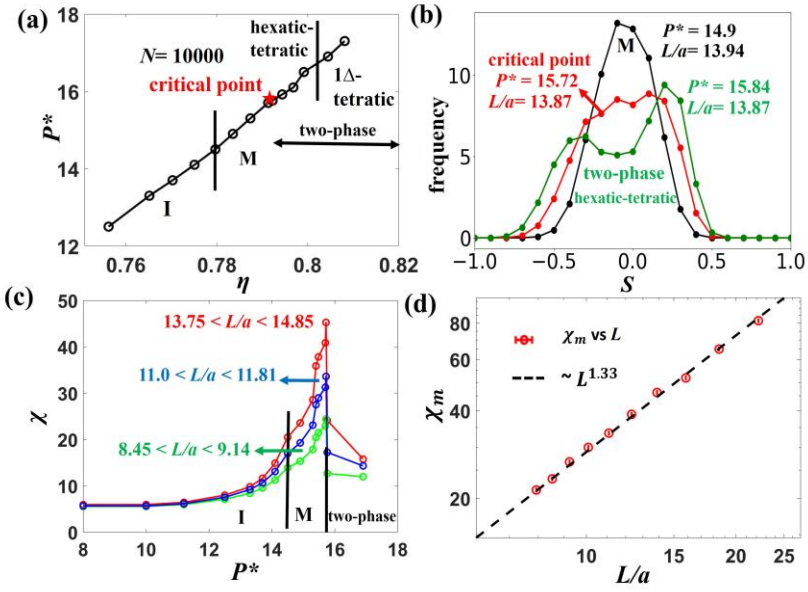

FIG. 3 (color online). Critical behavior of the equimolar disks+squares mixture with ξ = 1.1 and N = 10000. (a) Equation of state, P^* vs. η; the star marks the critical point at P^*= 15.72 and η= 0.791 and the vertical solid lines mark approximate boundaries between the I phase-M state and (hexatic-tetratic)-(1Δ-tetratic) two-phase regions. (b) Distribution of the local order parameter, S for states along the M→hexatic-tetratic two-phase transition, obtained by using 8×8 sub-cells (of dimension L). (c) Local compositional susceptibility, χ, measured as a function of P^* for different sub-cell lengths, L. Approximate phase boundaries are shown. (d) Relation between the maximum local compositional susceptibility, χ_m, and L on a logarithmic scale. The error bar indicates the fluctuations observed in L and the dashed line is a fit with the critical exponent value, $\frac{\gamma}{\upsilon}$ = 1.33. I = isotropic phase, M = mosaic state and a = square side length.

The critical point shown in Fig. 3a was estimated as follows. Using fss analysis, we measured the local compositional susceptibility, χ [see Eq. (6)] for different system sizes to gauge the local compositional fluctuation as shown in Fig. 3c and observed that the χ value diverges as the critical point is approached from either the M state or the two-phase region. Movie 1 in SI shows a sample simulation at the estimated critical point. The criteria for identifying the square-rich tetratic (red) and disk-rich hexatic (blue) phases in Movie 1 are discussed in Sec. VI and Fig. S8 in the SI. We quantitatively evaluate the dependence of the maximum local compositional susceptibility, χ_m with the sub-cell size, L as shown in Fig. 3d and estimated the critical exponent $\frac{\gamma}{\upsilon}$= 1.33$\pm$0.01 by using the scaling relation, $\chi_m \propto L^{\frac{\gamma}{\upsilon}}$. The power-law scaling nature of the local compositional susceptibility with the system size observed at the critical point reflects that the I→M→ (hexatic-tetratic) two-phase behavior is consistent with the continuous phase transition having critical exponents belonging to the Ising universality class. The $\frac{\gamma}{\upsilon}$ value, however, is inconsistent with the two-dimensional Ising universality class ($\frac{\gamma}{\upsilon}$=1.75), a difference that could reflect the nature of hexatic and tetratic phases at coexistence. However, at least part of this deviation can also be attributed to some of the limitations of our computational approach, e.g., the moderate range of sub-cell size, L used in our analysis. While much larger L values can allow detection of longer-range correlations of the composition within the sub-cells, much longer runs and specialized moves would be required to address the critical slowing down behavior that ensues as the critical point is approached. While our analysis is based on the variations of a single order parameter (S), field mixing with a second order parameter into an ordering operator (via suitably chosen nonuniversal scaling factors) may allow matching to the universal Ising distribution of the ordering operator at criticality [52–54]; such an approach, however, would require simulations in a semigrand isobaric ensemble to allow extensive sampling of global density and composition fluctuations in a finite-size system [55–57]. Further investigation into studying the phase transition behaviors using the classical XY spin model systems could also provide additional insights on characteristics of the system as the critical point is approached [58].

The near-critical point fluctuations of the local composition observed in the M state region engenders distinctive local structural properties. To characterize and distinguish the M state

from the hexatic and tetratic phases, we examined the six and four-fold local bond-orientational correlation functions, $g_6(r^*)$ and $g_4(r^*)$ [defined in Eq. (5)] and the pair correlation function, $g(r^*)$ (see Fig. 4) for x_s= 0.5. At P^*= 14.9 and η = 0.783, the M state showed algebraic decay of both $g_6(r^*)$ and $g_4(r^*)$ with an exponent value < −¼, and short-range layering (liquid-like behavior) of $g(r^*)$. We selected the −¼ exponent value as threshold to align with the KTHNY theory prediction for the scaling parameter lower-bound for the fluid to (n-fold)-atic phase transition (where n= 4 or 6). The M state has a long-ranged $g_6(r^*)$ and $g_4(r^*)$ orientational order compared to the I phase at P^*= 13.7 and η= 0.770, where we observed a quick decay in the $g_6(r^*)$ and $g_4(r^*)$ peaks. The large-r behavior of the $g_6(r^*)$ and $g_4(r^*)$ shows algebraic decay exponents, η_6 and η_4 for the M state that lie within the range ~ -0.4 < η_6 < -0.25 and -0.55 < η_4 < -0.25, respectively; whereas for the I phase $g_4(r^*)$ decays exponentially and $g_6(r^*)$ decays algebraically with η_6= -0.6 (see Fig. 4c). The six-fold ordering is stronger than the four-fold ordering in the M state due to the contribution from the RB clusters in the square-rich regions. This continuous change in the correlation of the $g_6(r^*)$ and $g_4(r^*)$ orientational order from I→M signals a significant change in the size of the network of six and four-fold clusters, which correlates with the sharp growth of χ as the M state region is crossed (*en route* to the critical point) for all sub-cell sizes, L (Fig. 3c). This leads to the formation of ordered micro-domains with both hexagonal-like and square-like structural motifs suggesting that the disks and squares have comparable proclivity to form stable six-fold and four-fold connections, respectively, that coexist across the system. Figure 5 shows that the algebraic decay of $g_6(r^*)$ and $g_4(r^*)$ orientational order of the M state is sustained even for a larger system size, a result that correlates with the observation that χ increases with sub-cell size, L (see Fig. S12 in SI), indicative that the local compositional fluctuations of the M state increase with system size. The M state was also observed for x_s=0.49 and 0.52 (see Sec. VI Fig. S10 in SI). As we approached the disk-rich (or the square-rich) region, we observed the hexatic (or tetratic) phase with quasi-long ranged $g_6(r^*)$ (or $g_4(r^*)$) orientational order (see Fig. 2a and b). Results similar to those in Fig. 4 are shown in Fig. S11 for the transitions I → hexatic at x_s= 0.45 and I → tetratic at x_s= 0.55. Although the M state was observed within a narrow x_s range between 0.48 and 0.53, the hexatic (or tetratic) phase region at x_s= 0.45 (or 0.55) and P^* > 15.3 (or P^* > 14.9) also shows concomitant characteristics of the M state where both $g_6(r^*)$ and $g_4(r^*)$ orientational

order functions decay algebraically along with large values of χ (see SI Fig. S11).

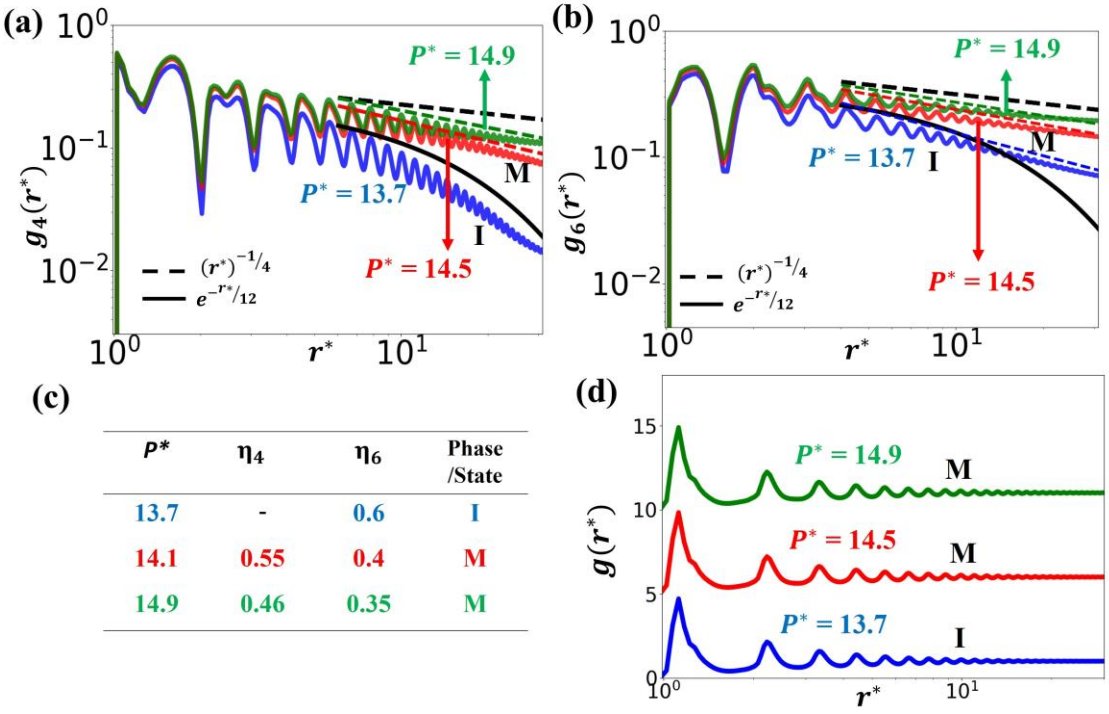

P^*	η_4	η_6	Phase /State
13.7	-	0.6	I
14.1	0.55	0.4	M
14.9	0.46	0.35	M

FIG. 4 (online color). Selected properties of equimolar disks+squares mixture with $\xi = 1.1$ and $N = 10000$. (a, b) Bond orientational order correlation functions for the I phase and the M state: $g_4(r^*)$ (a) and $g_6(r^*)$ (b). The black dashed and solid lines indicate algebraic and exponential decay of the orientational correlation with exponent $-1/4$ and $-1/12$, respectively. The algebraic decay exponent values η_4 and η_6 corresponding to the green and blue dashed lines shown in (a and b) for the I phase and M state are reported in table (c). (d) 2D pair correlation functions shifted uniformly to distinguish peaks for the phases and conditions indicated (by pressures P^*). I = isotropic phase, M = mosaic state.

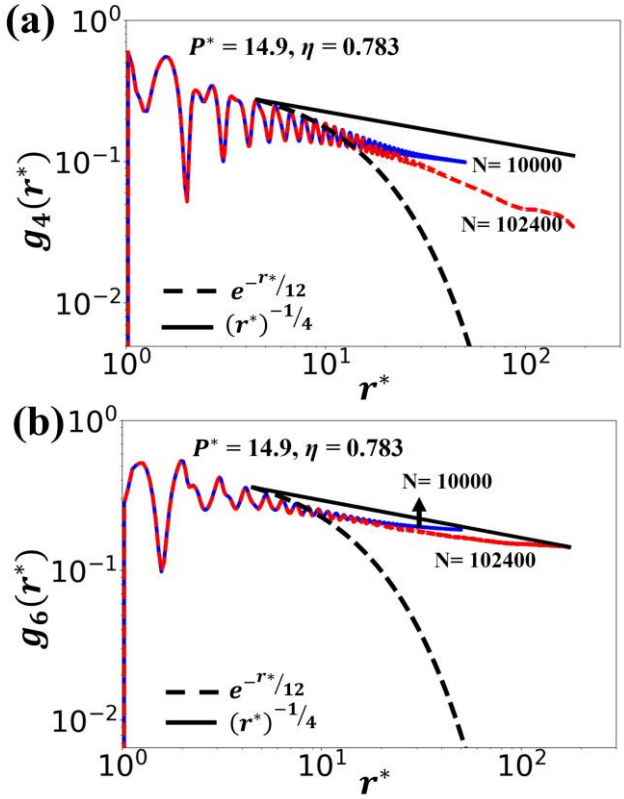

Fig. 5 (color online). Bond orientational order functions $g_4(r^*)$ (a) and $g_6(r^*)$ (b) for the M state of equimolar disks+squares mixture with ξ = 1.1 for N= 10000 and 102400 particles. The dashed and solid lines indicate algebraic and exponential decays with exponent $-1/4$ and $-1/12$, respectively.

Figures 6a and 6d (inset) show configurations of the M state and the two-phase coexistence state at P^*= 14.9 and η= 0.783, and P^*= 16.5 and η = 0.80, respectively. The clusters of six-fold and four-fold ordered domains are shown by coloring the particles based on the local values of Φ_6 (Fig. 6b) and Φ_4 (Fig. 6c). For the M state, the coloring reveals a complementary correlation between the disk-rich regions with high six-fold clusters and square-rich regions with high four-fold ordered clusters, that are randomly distributed throughout the simulated domain. We also detected regions of RB order formed by squares with high local values of Φ_6. To test that the M state is not just a system that has become kinetically arrested *en route* to macro-phase separation, we simulated a system started at a state of complete phase separation of squares and disks at P^*=14.9, and confirmed that the macro-domains gradually disintegrated

to form the M state micro-domains. Movie 2 in the SI shows this transition for an equimolar mixture with N= 39712 particles. Overall, our analysis indicates that the M state is indeed a near-critical state having a heterogeneous microstructure resembling a *"mosaic"* of different ordered micro-domains which locally resemble *tetratic/RB-like* and *hexatic-like* regions.

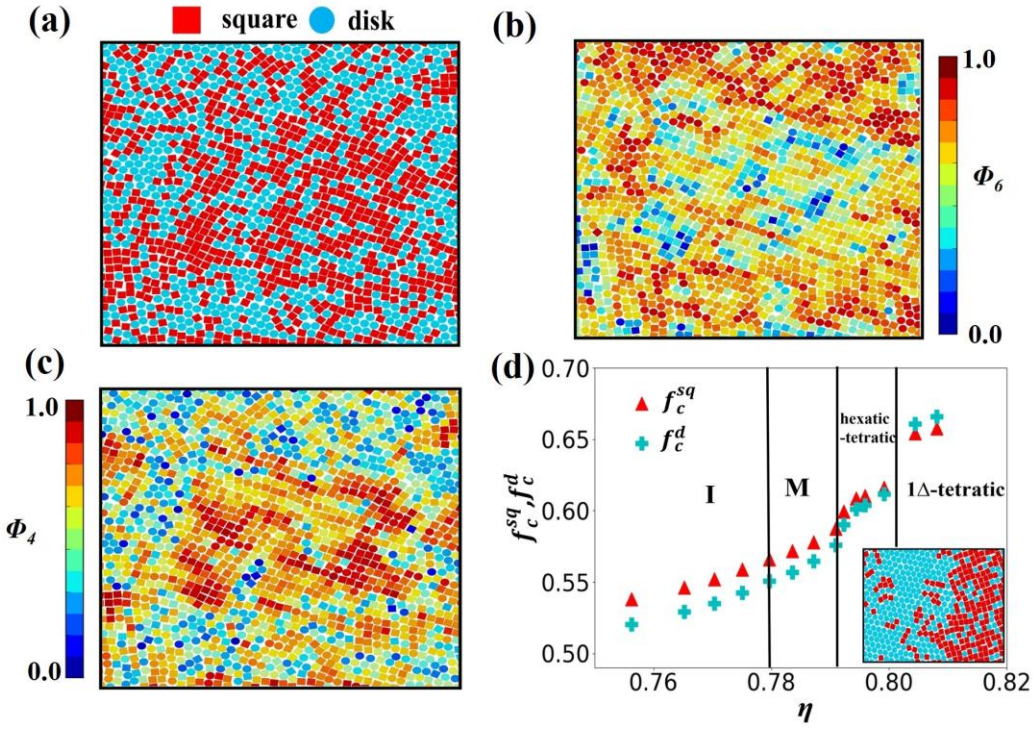

Fig. 6 (color online). Local bond orientational and compositional order for the equimolar disks+squares mixture with ξ = 1.1 and N = 10000. (a)-(c) correspond to the M state at η= 0.783 where the particles are colored based on type (a) and the local values of Φ_6 (b) and Φ_4 (c). Each snapshot represents a ~1/10th section of the entire simulation box. (d) Approximate phase boundaries and local composition parameters, f_c^{sq} and f_c^d, as a function of area fraction, η. The inset shows a representative snapshot of two-phase coexistence state at η = 0.8. I = isotropic phase, M = mosaic state.

To understand the mechanism associated with the I → M transition, we computed the local composition parameters, f_c^{sq} and f_c^d to detect the correlation between the local compositional heterogeneity and the presence of ordered domains formed by squares and disks (see Fig. 6d).

Parameters f_c^{sq} and f_c^{d} are the average fraction of the like-shaped nearest neighbors to a square and disk, respectively (normalized such that particles with all like-shaped neighbors corresponds to 1). For the I phase, the average values of both f_c^{sq} and f_c^{d} are close to a well-mixed value of 0.5, reflecting the overall equimolar composition. Upon compression, both f_c^{sq} and f_c^{d} increase gradually in the M state (for $\eta > 0.78$), and then more steeply as the hexatic-tetratic two-phase separated region is reached ($\eta > 0.791$). The loss of the particles' local compositional mixing observed in the M state compared to the I phase, reveals that the entropic bonding [59,60], which favors contacts between like-shaped particles, becomes sufficiently strong to seed the formation of disk-rich six-fold and square-rich four-fold micro-domains. The grain boundaries around these micro-domains contain particles with both f_c^{sq} and f_c^{d} values close to 0.5, which can be viewed as compositional *"defects"* contributing to the structural disorder in the M state. The migration of these defects was monitored at $\eta = 0.783$ using *"pseudo dynamic"* Monte Carlo simulations in the *NVT* ensemble. Movie 3 in the SI shows that, although the migration of these defects is restricted to the grain boundary regions, their compositions decorrelate much faster compared to particles inside ordered domains (see Fig. S8c Sec. VI of SI). This suggests that both the growth of ordered M domains from the I state, and the slow restructuring of the M domain patterns would be mediated by the accrual of local rearrangements at the grain boundaries. The compositional defects observed in the M state are expected to be correlated with the topological defects typically observed in the melting transition of two-dimensional solids.

The growth of the six-fold and four-fold ordered domains during the I → M transition was tracked by performing a cluster analysis. The protocol used to identify such clusters is described in the SI Sec. IV. The fraction of particles belonging to the largest four-fold and the largest six-fold clusters increased as the system transitions from the I phase to the M state (see Figs. 7a and 7b). In the M state, these largest *n*-fold (where *n*= 4 or 6) cluster tend to form a loose, interconnected network that is randomly distributed percolating the simulation box as shown in the snapshots in Fig 7. While we expect the *n*-fold clusters to form a percolating network at the critical point, we observed that the six-fold clusters also percolated the sample at the M state, likely due to the finite size effects. In the I phase in contrast, the largest *n*-fold clusters are isolated and much smaller. We also observed a higher fraction of particles in the six-fold

clusters compared to the four-fold clusters as the local RB order formed in the square-rich region also contributes to the six-fold symmetry (see Sec.VI Fig.S9 in SI). The fractal nature of the six-fold and four-fold clusters is consistent with a continuous phase transition. Figure 8 shows the relative orientational angle between the largest six-fold and the largest four-fold clusters in selected states of the I phase, M and (hexatic-tetratic) two-phase regions (see Sec. IV in SI). As the system transitions in the sequence I → M → (hexatic-tetratic) two-phase, the orientational correlation between the neighboring six-fold and four-fold ordered clusters increases ($|\theta_6-\theta_4| \to 0$), consistent with the growing correlation length of bond-ordering in the whole system and indicative of the preferential alignment of the particles between the square-rich and disk-rich domains.

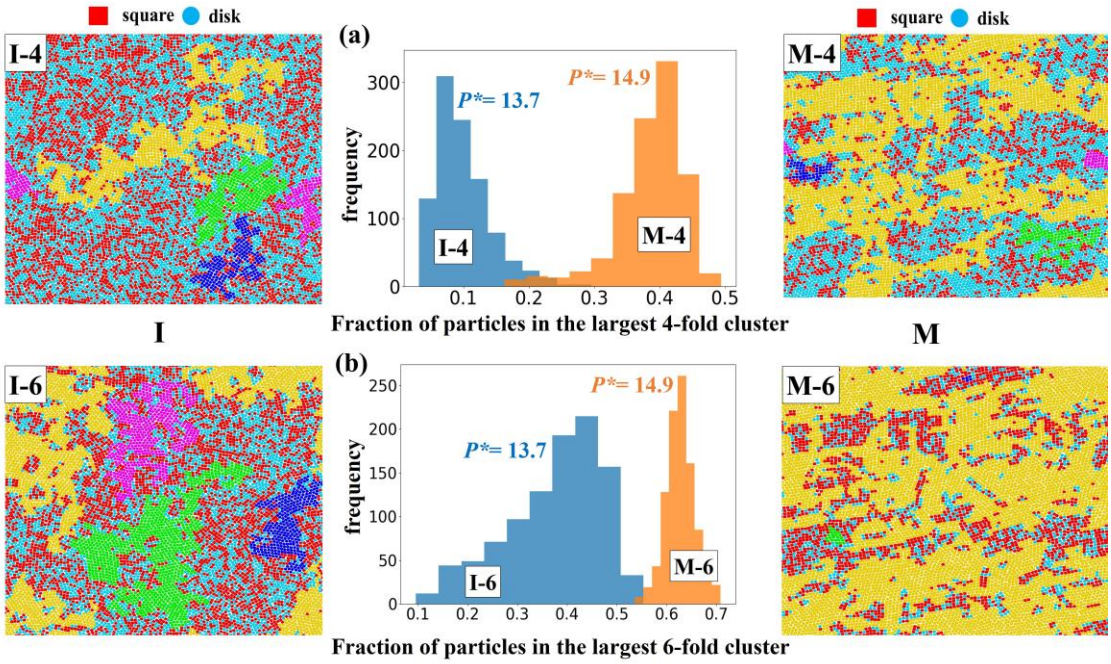

Fig. 7 (color online). Growth of the four-fold and six-fold ordered domains for the equimolar disks+squares mixture with $\xi = 1.1$ and $N = 10000$ for I phase (at P^*=13.7) and the M state (at P^*=14.9). Distribution function of the fraction of particles belonging to the largest four-fold (a) and six-fold (b) clusters. Representative snapshots for the I and M states are labelled as I-4 and M-4 for four-fold clusters and I-6 and M-6 for six-fold clusters. The particles belonging to the first, second, third, and fourth largest clusters are colored in yellow, green, magenta and blue, respectively.

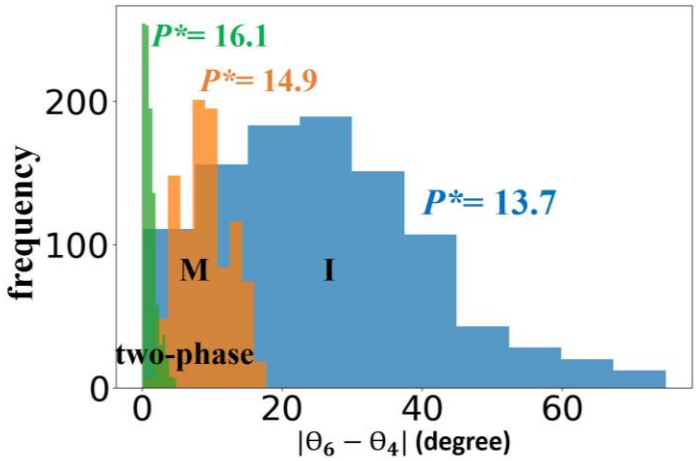

Fig. 8 Relative orientational angle between the largest six-fold and the largest four-fold clusters for representative I (blue), M (orange), and two-phase (green) states. I = isotropic phase, M = mosaic state.

Unlike most other near-critical point phenomena described in the literature, particle energetics play no role in the underlying phase transition and it is hence instructive to discuss entropy effects. The overall mixing entropy of the M state, while lower than that in the I phase (where nearly ideal mixing occurs), must be significant. Indeed, while limited mixing happens at the length scale of individual particles inside clusters (as in the solid solutions) and at the grain boundaries, *'random'* mixing also occurs at the length scale of the six-fold and four-fold ordered clusters due to the local compositional fluctuations near the critical point that scale in proportion to the correlation length of the ordered clusters. The result is a system with transient but well-defined *micro*-phase segregated regions which is quite distinct to the *macro*-phase segregated state observed above the critical pressure.

In our athermal system, pressure and the associated pressure×volume (*PV)* "enthalpic" contribution to the free energy, act as the knob that controls the strength of the packing entropy that optimizes local particle arrangements and its interplay with mixing entropy. At low pressure, the local compositions are uncorrelated and the interparticle coupling is weak, with a neighboring site to a square or disk being indistinctly occupied by another square or disk (quasi

random distribution). At higher pressure, compositional correlations and coupling is strong due to the loss in mixing entropy, favoring the formation of denser, orientationally aligned six-fold (disk-rich) and four-fold (square-rich) clusters that minimize the free energy by enhancing $P\Delta V < 0$ effects. Note that a more efficient packing is typically associated with a gain in vibrational motion (and associated entropy) of individual particles. The M state observed in this work thus engenders when there is a close balance between the packing entropy favoring optimal packing of the particles and the mixing entropy favoring contact between unlike particles.

We posit then that the M state behavior engenders when, at a suitable range of compositions and densities, the two competing entropic forces, namely, entropic bonding favoring like-particle contacts and mixing entropy favoring random contacts, are in such a close balance that are able to coexist by attaining a *"compromise"* state exhibiting both segregated like-particle domains and random mixing of those domains. As the M state is compressed to a higher density, the entropic cost of unlike contacts overpowers any gain in mixing entropy, leading (upon crossing a critical point) to the phase separation of the individual components into disk-rich and square-rich ordered phases. Conceptually, the transitions I $\rightarrow$ M $\rightarrow$ two-solid-phases with pressure for an equimolar mixture could be seen as the coarsening in the correlation length of the ordered domains, which goes from being very short ranged (I phase), to mesoscopic (M state) to macroscopic (two-phase state).

To underscore the significance of the optimal component size ratio, ξ, we also simulated phase diagrams for other ξ values for the disk+square mixture. We varied the ξ values by $\pm$ 27% from the representative optimal value of 1.1 so that the associated ΔF_x values are significantly higher than those in the relatively flat region for $1.04 < \xi < 1.2$ (see Fig. 1). Specifically, Fig. 9 shows results for $\xi = 0.8$ and 1.4 for which, unlike the $\xi = 1.1$ case in Fig. 2, no M state region was detected. In both cases, the stability region of the hexatic phase is much narrower compared to the $\xi = 1.1$ case. Furthermore, while for the $\xi = 1.1$ case both the disk-rich and square-rich phases and solid solution regions are large and comparable in size (giving the phase diagram a symmetric look), those regions become very asymmetric for the other ξ values; i.e., the hexatic and 1Δ regions are small, especially for the $\xi = 0.8$ case. These results clearly show that a system with a (near) optimal choice of ξ promotes the stability of ordered phases with substitutional disorder over wider ranges of composition and pressure and, by construction of ΔF_x [see Eq.

(1)], it does so in a way that *both* pure-component ordered phases are similarly represented (see Sec. VII). Arguably, the microscopic substitutional symmetry favored by a minimal ΔF_x gets translated into a macroscopic symmetry in the substitutionally disordered solids and partially ordered phases in the phase diagram.

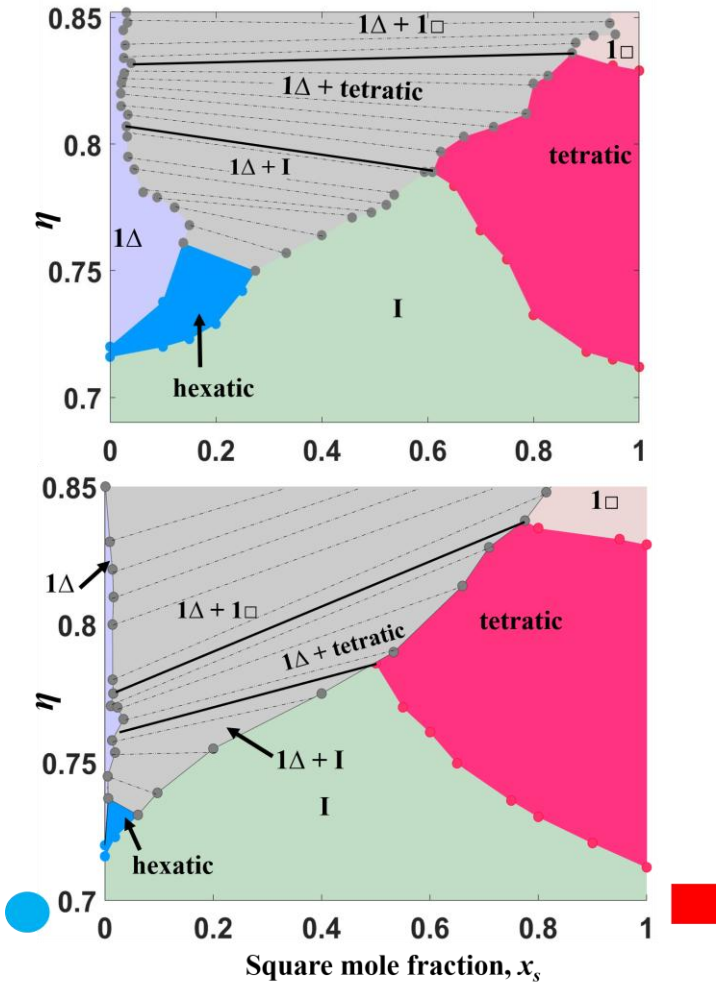

Fig. 9 (color online). Area fraction-composition phase diagrams for disks (diameter σ) and squares (side edge a) with different size ratios, $\xi = \sigma/a$. Top: $\xi = 0.8$, bottom: $\xi = 1.4$. The tie lines in the two-phase regions are shown as dashed lines. 1Δ = triangular solid, 1□ = square solid, and I = isotropic phase.

4. Final Remarks and Outlook

In summary, for the crystal-symmetry incompatible mixture of disk+squares with optimized size ratio ($\xi = 1.1$), we mapped the pressure-composition phase diagram which revealed broad ranges of compositions and pressures where the hexagonal solid and hexatic phase (favored by disks) and square solid and tetratic phase (favored by squares) form. Moreover, we identified a distinctive M state that resides near the critical point for the hexatic-tetratic phase coexistence region and is characterized by randomly distributed, persistent micro-domains corresponding to four-fold and six-fold regions. In contrast, for the crystal-symmetry compatible mixture of disks and hexagons with optimized size ratio ($\xi = 1.82$), the corresponding phase diagram shows that a 1Δ solid solution and the hexatic phase form over the entire range of compositions.

While the competition between 1Δ/hexatic and 1□/tetratic ordering is not uncommon in 2D or quasi-2D systems, structures resembling the M state have only been seen under very restrictive conditions. For example, cuboctahedral nanoparticles pinned at 2D fluid-fluid interfaces have been observed to transition from a hexagonal to a square lattice only as transient, non-equilibrium states (e.g., as surface ligands are removed and particles bond through their <100> facets) [61]. 2D simulations of hard rounded squares [62] of a particular degree of roundedness have predicted the formation of a *"polycrystalline"* phase with a patchy-domain structure loosely reminiscent to that of the M state. Through the rounding of square-corners, such a system provides a physical interpolation (in a single-component system) between disks and squares to reach a state where the entropic tendencies towards the formation of hexagonal and square lattices are in close balance, like that achieved in the M region by our disks+squares binary mixture.

The M state found in the disks+squares mixture could display interesting optical phenomenon such as critical opalescence since the near-critical point fluctuations of the local composition cause the sizes of both four-fold and six-fold symmetry domains to fluctuate over large length scales. Alternatively, the dual structural symmetric property observed in the M state could be leveraged for specialty applications, e.g., to fabricate a synthetic Chameleon skin [63], optical switches [64], or optical biosensors [65]. Indeed, the M state can be seen as a phase with pervading seeds of both hexatic and tetratic phases, whose global order could then be readily biased (through a suitable external field) to switch between one phase and the other. The

methods used and principles unveiled in this work should be general and applicable to many other athermal mixtures.

Acknowledgement

Funding support from NSF award CBET-1907369 is gratefully acknowledged. The authors thank Yangyang Sun, Unmukt Gupta, Srinath Ranya and Isabela Quintela Matos for useful exchanges and to Abhishek Sharma and Ankita Mukhtyar for valuable suggestions on the cluster analysis.

References

(1) Henzie, J.; Grünwald, M.; Widmer-Cooper, A.; Geissler, P. L.; Yang, P. Self-Assembly of Uniform Polyhedral Silver Nanocrystals into Densest Packings and Exotic Superlattices. *Nat. Mater.* **2012**, *11* (2), 131–137. https://doi.org/10.1038/nmat3178.

(2) Seo, D.; Ji, C. P.; Song, H. Polyhedral Gold Nanocrystals with Oh Symmetry: From Octahedra to Cubes. *J. Am. Chem. Soc.* **2006**, *128* (46), 14863–14870. https://doi.org/10.1021/ja062892u.

(3) Penterman, S. J.; Singh, A.; Zipfel, W. R.; Liddell Watson, C. M. Anisometric Colloidal Fullerene Rod and Platelet Solvates with Enhanced Photoluminescence. *Adv. Opt. Mater.* **2014**, *2* (11), 1024–1030. https://doi.org/10.1002/adom.201400266.

(4) Badaire, S.; Cottin-Bizonne, C.; Woody, J. W.; Yang, A.; Stroock, A. D. Shape Selectivity in the Assembly of Lithographically Designed Colloidal Particles. *J. Am. Chem. Soc.* **2007**, *129* (1), 40–41. https://doi.org/10.1021/ja067527h.

(5) Hernandez, C. J.; Mason, T. G. Colloidal Alphabet Soup: Monodisperse Dispersions of Shape-Designed LithoParticles. *J. Phys. Chem. C* **2007**, *111* (12), 4477–4480. https://doi.org/10.1021/jp0672095.

(6) Agarwal, U.; Escobedo, F. A. Mesophase Behaviour of Polyhedral Particles. *Nat. Mater.* **2011**, *10* (3), 230–235. https://doi.org/10.1038/nmat2959.

(7) Glotzer, S. C.; Solomon, M. J. Anisotropy of Building Blocks and Their Assembly into Complex Structures. *Nat. Mater.* **2007**, *6* (8), 557–562. https://doi.org/10.1038/nmat1949.

(8) Min, Y.; Akbulut, M.; Kristiansen, K.; Golan, Y.; Israelachvili, J. The Role of Interparticle and External Forces in Nanoparticle Assembly. *Nat. Mater.* **2008**, *7* (7), 527–538. https://doi.org/10.1038/nmat2206.

(9) Lim, Y. F.; Choi, J. J.; Hanrath, T. Facile Synthesis of Colloidal CuO Nanocrystals for Light-Harvesting Applications. *J. Nanomater.* **2012**, *2012*, 393160. https://doi.org/10.1155/2012/393160.

(10) Von Freymann, G.; Ledermann, A.; Thiel, M.; Staude, I.; Essig, S.; Busch, K.; Wegener, M. Three-Dimensional Nanostructures for Photonics. *Adv. Funct. Mater.* **2010**, *20* (7), 1038–1052. https://doi.org/10.1002/adfm.200901838.

(11) Kabashin, A. V.; Evans, P.; Pastkovsky, S.; Hendren, W.; Wurtz, G. A.; Atkinson, R.; Pollard, R.; Podolskiy, V. A.; Zayats, A. V. Plasmonic Nanorod Metamaterials for Biosensing. *Nat. Mater.* **2009**, *8* (11), 867–871. https://doi.org/10.1038/nmat2546.

(12) Novo, C.; Funston, A. M.; Mulvaney, P. Direct Observation of Chemical Reactions on Single Gold Nanocrystals Using Surface Plasmon Spectroscopy. *Nat. Nanotechnol.* **2008**, *3* (10), 598–602. https://doi.org/10.1038/nnano.2008.246.

(13) Henry, C. R. 2D-Arrays of Nanoparticles as Model Catalysts. *Catal. Letters* **2015**, *145* (3), 731–749. https://doi.org/10.1007/s10562-014-1402-6.

(14) Zhou, Z. Y.; Tian, N.; Li, J. T.; Broadwell, I.; Sun, S. G. Nanomaterials of High Surface Energy with Exceptional Properties in Catalysis and Energy Storage. *Chem. Soc. Rev.* **2011**, *40* (7), 4167–4185. https://doi.org/10.1039/c0cs00176g.

(15) Conway, J. H.; Jiao, Y.; Torquato, S. New Family of Tilings of Three-Dimensional Euclidean Space by Tetrahedra and Octahedra. *Proc. Natl. Acad. Sci. U. S. A.* **2011**, *108* (27), 11009–11012. https://doi.org/10.1073/pnas.1105594108.

(16) Bautista-Carbajal, G.; Gurin, P.; Varga, S.; Odriozola, G. Phase Diagram of Hard

Squares in Slit Confinement. *Sci. Rep.* **2018**, *8* (1), 1–13. https://doi.org/10.1038/s41598-018-26922-3.

(17) Torquato, S.; Jiao, Y. Dense Packings of the Platonic and Archimedean Solids. *Nature* **2009**, *460* (7257), 876–879. https://doi.org/10.1038/nature08239.

(18) Khadilkar, M. R.; Escobedo, F. A. Phase Behavior of Polyhedral Nanoparticles in Parallel Plate Confinement. *Soft Matter* **2016**, *12* (5), 1506–1516. https://doi.org/10.1039/c5sm02570b.

(19) Damasceno, P. F.; Engel, M.; Glotzer, S. C. Crystalline Assemblies and Densest Packings of a Family of Truncated Tetrahedra and the Role of Directional Entropic Forces. *ACS Nano* **2012**, *6* (1), 609–614. https://doi.org/10.1021/nn204012y.

(20) Teich, E. G.; Van Anders, G.; Klotsa, D.; Dshemuchadse, J.; Glotzer, S. C. Clusters of Polyhedra in Spherical Confinement. *Proc. Natl. Acad. Sci. U. S. A.* **2016**, *113* (6), E669–E678. https://doi.org/10.1073/pnas.1524875113.

(21) Anderson, J. A.; Antonaglia, J.; Millan, J. A.; Engel, M.; Glotzer, S. C. Shape and Symmetry Determine Two-Dimensional Melting Transitions of Hard Regular Polygons. *Physical Review X*. 2017, p 021001. https://doi.org/10.1103/PhysRevX.7.021001.

(22) Ye, X.; Collins, J. E.; Kang, Y.; Chen, J.; Chen, D. T. N.; Yodh, A. G.; Murray, C. B. Morphologically Controlled Synthesis of Colloidal Upconversion Nanophosphors and Their Shape-Directed Self-Assembly. *Proc. Natl. Acad. Sci. U. S. A.* **2010**, *107* (52), 22430–22435. https://doi.org/10.1073/pnas.1008958107.

(23) Riley, E. K.; Liddell, C. M. Confinement-Controlled Self Assembly of Colloids with Simultaneous Isotropic and Anisotropic Cross-Section. *Langmuir* **2010**, *26* (14), 11648–11656. https://doi.org/10.1021/la100361y.

(24) Baumgardner, W. J.; Whitham, K.; Hanrath, T. Confined-but-Connected Quantum Solids via Controlled Ligand Displacement. *Nano Lett.* **2013**, *13* (7), 3225–3231. https://doi.org/10.1021/nl401298s.

(25) Evers, W. H.; Goris, B.; Bals, S.; Casavola, M.; De Graaf, J.; Roij, R. Van; Dijkstra, M.;

Vanmaekelbergh, D. Low-Dimensional Semiconductor Superlattices Formed by Geometric Control over Nanocrystal Attachment. *Nano Lett.* **2013**, *13* (6), 2317–2323. https://doi.org/10.1021/nl303322k.

(26) Liu, B.; Besseling, T. H.; Hermes, M.; Demirörs, A. F.; Imhof, A.; Van Blaaderen, A. Switching Plastic Crystals of Colloidal Rods with Electric Fields. *Nat. Commun.* **2014**, *5*, 1–8. https://doi.org/10.1038/ncomms4092.

(27) Evers, W. H.; Schins, J. M.; Aerts, M.; Kulkarni, A.; Capiod, P.; Berthe, M.; Grandidier, B.; Delerue, C.; Van Der Zant, H. S. J.; Van Overbeek, C.; Peters, J. L.; Vanmaekelbergh, D.; Siebbeles, L. D. A. High Charge Mobility in Two-Dimensional Percolative Networks of PbSe Quantum Dots Connected by Atomic Bonds. *Nat. Commun.* **2015**, *6*, 1–8. https://doi.org/10.1038/ncomms9195.

(28) Danek, M.; Jensen, K. F.; Murray, C. B.; Bawendi, M. G. Synthesis of Luminescent Thin-Film CdSe/ZnSe Quantum Dot Composites Using CdSe Quantum Dots Passivated with an Overlayer of ZnSe. *Chem. Mater.* **1996**, *8* (1), 173–180. https://doi.org/10.1021/cm9503137.

(29) Halperin, B. I.; Nelson, D. R. Theory of Two-Dimensional Melting. *Phys. Rev. Lett.* **1978**, *41* (2), 121–124. https://doi.org/10.1103/PhysRevLett.41.121.

(30) Young, A. P. Melting and the Vector Coulomb Gas in Two Dimensions. *Phys. Rev. B* **1979**, *19* (4), 1855–1866. https://doi.org/10.1103/PhysRevB.19.1855.

(31) Nelson, D. R.; Halperin, B. I. Dislocation-Mediated Melting in Two Dimensions. *Phys. Rev. B* **1979**, *19* (5), 2457–2484. https://doi.org/10.1103/PhysRevB.19.2457.

(32) kosterlitz, J. M.; Thouless, D. J. Ordering, Metastability and Phase Transitions in Two-Dimensional Systems. *J. Phys. C Solid State Phys.* **1973**. https://doi.org/10.1088/0022-3719/6/7/010.

(33) Bernard, E. P.; Krauth, W. Two-Step Melting in Two Dimensions: First-Order Liquid-Hexatic Transition. *Phys. Rev. Lett.* **2011**, *107* (15), 1–4. https://doi.org/10.1103/PhysRevLett.107.155704.

(34) Millan, J. A.; Ortiz, D.; Van Anders, G.; Glotzer, S. C. Self-Assembly of Archimedean Tilings with Enthalpically and Entropically Patchy Polygons. *ACS Nano* **2014**, *8* (3), 2918–2928. https://doi.org/10.1021/nn500147u.

(35) Russo, J.; Wilding, N. B. Disappearance of the Hexatic Phase in a Binary Mixture of Hard Disks. *Phys. Rev. Lett.* **2017**, *119* (11), 1–5. https://doi.org/10.1103/PhysRevLett.119.115702.

(36) Buhot, A.; Krauth, W. Phase Separation in Two-Dimensional Additive Mixtures. *Phys. Rev. E - Stat. Physics, Plasmas, Fluids, Relat. Interdiscip. Top.* **1999**, *59* (3), 2939–2941. https://doi.org/10.1103/PhysRevE.59.2939.

(37) Vink, R. L. C.; Horbach, J.; Binder, K. Critical Phenomena in Colloid-Polymer Mixtures: Interfacial Tension, Order Parameter, Susceptibility, and Coexistence Diameter. *Phys. Rev. E - Stat. Nonlinear, Soft Matter Phys.* **2005**, *71* (1), 1–10. https://doi.org/10.1103/PhysRevE.71.011401.

(38) Trefz, B.; Siebert, J. T.; Speck, T.; Binder, K.; Virnau, P. Estimation of the Critical Behavior in an Active Colloidal System with Vicsek-like Interactions. *J. Chem. Phys.* **2017**, *146* (7). https://doi.org/10.1063/1.4975812.

(39) Stenhammar, J.; Wittkowski, R.; Marenduzzo, D.; Cates, M. E. Activity-Induced Phase Separation and Self-Assembly in Mixtures of Active and Passive Particles. *Phys. Rev. Lett.* **2015**, *114* (1), 1–5. https://doi.org/10.1103/PhysRevLett.114.018301.

(40) Han, M.; Yan, J.; Granick, S.; Luijten, E. Effective Temperature Concept Evaluated in an Active Colloid Mixture. *Proc. Natl. Acad. Sci. U. S. A.* **2017**, *114* (29), 7513–7518. https://doi.org/10.1073/pnas.1706702114.

(41) Rice, P. A.; McConnell, H. M. Critical Shape Transitions of Monolayer Lipid Domains. *Proc. Natl. Acad. Sci.* **1989**, *86* (17), 6445–6448. https://doi.org/10.1073/pnas.86.17.6445.

(42) Keller, S. L.; Mc Connell, H. M. Stripe Phases in Lipid Monolayers near a Miscibility Critical Point. *Phys. Rev. Lett.* **1999**, *82* (7), 1602–1605.

https://doi.org/10.1103/PhysRevLett.82.1602.

(43) Zhao, K.; Bruinsma, R.; Mason, T. G. Entropic Crystal-Crystal Transitions of Brownian Squares. *Proc. Natl. Acad. Sci.* **2011**. https://doi.org/10.1073/pnas.1014942108.

(44) Escobedo, F. A. Optimizing the Formation of Solid Solutions with Components of Different Shapes. *J. Chem. Phys.* **2017**, *146* (13). https://doi.org/10.1063/1.4979091.

(45) Khadilkar, M. R.; Escobedo, F. A. Heuristic Rule for Binary Superlattice Coassembly: Mixed Plastic Mesophases of Hard Polyhedral Nanoparticles. *Phys. Rev. Lett.* **2014**, *113* (16), 1–5. https://doi.org/10.1103/PhysRevLett.113.165504.

(46) Mazars, M. Bond Orientational Order Parameters in the Crystalline Phases of the Classical Yukawa-Wigner Bilayers. *Epl* **2008**, *84* (5), 55002. https://doi.org/10.1209/0295-5075/84/55002.

(47) Khadilkar, M. R.; Agarwal, U.; Escobedo, F. A. Phase Behavior of Binary Mixtures of Hard Convex Polyhedra. *Soft Matter* **2013**, *9* (48), 11557–11567. https://doi.org/10.1039/c3sm51822a.

(48) Gilbert, E. G.; Johnson, D. W.; Keerthi, S. S. A Fast Procedure for Computing the Distance Between Complex Objects in Three-Dimensional Space. *IEEE J. Robot. Autom.* **1988**, *4* (2), 193–203. https://doi.org/10.1109/56.2083.

(49) Schneider, P. J.; Eberly, D. H. *Geometric Tools for Computer Graphics*; Elsevier, 2003. https://doi.org/10.1016/B978-1-55860-594-7.X5000-0.

(50) Weber, H.; Marx, D.; Binder, K. Melting Transition in Two Dimensions: A Finite-Size Scaling Analysis of Bond-Orientational Order in Hard Disks. *Phys. Rev. B* **1995**, *51* (20), 14636–14651. https://doi.org/10.1103/PhysRevB.51.14636.

(51) Engel, M.; Anderson, J. A.; Glotzer, S. C.; Isobe, M.; Bernard, E. P.; Krauth, W. Hard-Disk Equation of State: First-Order Liquid-Hexatic Transition in Two Dimensions with Three Simulation Methods. *Phys. Rev. E - Stat. Nonlinear, Soft Matter Phys.* **2013**, *87* (4), 1–8. https://doi.org/10.1103/PhysRevE.87.042134.

(52) Wilding, N. B. Critical-Point and Coexistence-Curve Properties of the Lennard-Jones

Fluid: A Finite-Size Scaling Study. *Phys. Rev. E* **1995**, *52* (1), 602–611. https://doi.org/10.1103/PhysRevE.52.602.

(53) Bruce, A. D.; Wilding, N. B. Scaling Fields and Universality of the Liquid-Gas Critical Point. *Phys. Rev. Lett.* **1992**, *68* (2), 193–196. https://doi.org/10.1103/PhysRevLett.68.193.

(54) Stutzman, L. B.; Escobedo, F. A.; Tester, J. W. Heat Capacities of Supercritical Fluids via Grand Canonical Ensemble Simulations. *Mol. Simul.* **2018**, *44* (2), 147–155. https://doi.org/10.1080/08927022.2017.1355553.

(55) Wilding, N. B. Simulation Studies of Fluid Critical Behaviour. *J. Phys. Condens. Matter* **1997**, *9* (3), 585–612. https://doi.org/10.1088/0953-8984/9/3/002.

(56) Góźdź, W. T. Critical-Point and Coexistence Curve Properties of a Symmetric Mixture of Nonadditive Hard Spheres: A Finite Size Scaling Study. *J. Chem. Phys.* **2003**, *119* (6), 3309–3315. https://doi.org/10.1063/1.1589746.

(57) Góźdź, W. T.; Ciach, A. Critical Point Calculation for Binary Mixtures of Symmetric Non-Additive Hard Disks. *Condens. Matter Phys.* **2016**, *19* (1), 1–8. https://doi.org/10.5488/CMP.19.13002.

(58) Casiulis, M.; Tarzia, M.; Cugliandolo, L. F.; Dauchot, O. Ferromagnetism-Induced Phase Separation in a Two-Dimensional Spin Fluid. *J. Chem. Phys.* **2019**, *150* (15). https://doi.org/10.1063/1.5064590.

(59) Van Anders, G.; Ahmed, N. K.; Smith, R.; Engel, M.; Glotzer, S. C. Entropically Patchy Particles: Engineering Valence through Shape Entropy. *ACS Nano* **2014**, *8* (1), 931–940. https://doi.org/10.1021/nn4057353.

(60) Van Anders, G.; Klotsa, D.; Ahmed, N. K.; Engel, M.; Glotzer, S. C. Understanding Shape Entropy through Local Dense Packing. *Proc. Natl. Acad. Sci. U. S. A.* **2014**, *111* (45), E4812–E4821. https://doi.org/10.1073/pnas.1418159111.

(61) Whitham, K.; Hanrath, T. Formation of Epitaxially Connected Quantum Dot Solids: Nucleation and Coherent Phase Transition. *J. Phys. Chem. Lett.* **2017**, *8* (12), 2623–2628.

https://doi.org/10.1021/acs.jpclett.7b00846.

(62) Avendaño, C.; Escobedo, F. A. Phase Behavior of Rounded Hard-Squares. *Soft Matter* **2012**, *8* (17), 4675–4681. https://doi.org/10.1039/c2sm07428a.

(63) Teyssier, J.; Saenko, S. V.; Van Der Marel, D.; Milinkovitch, M. C. Photonic Crystals Cause Active Colour Change in Chameleons. *Nat. Commun.* **2015**, *6*, 1–7. https://doi.org/10.1038/ncomms7368.

(64) Ge, J.; Hu, Y.; Zhang, T.; Huynh, T.; Yin, Y. Self-Assembly and Field-Responsive Optical Diffractions of Superparamagnetic Colloids. *Langmuir* **2008**, *24* (7), 3671–3680. https://doi.org/10.1021/la7039493.

(65) Damborský, P.; Švitel, J.; Katrlík, J. Optical Biosensors. *Essays Biochem.* **2016**, *60* (1), 91–100. https://doi.org/10.1042/EBC20150010.

SUPPLEMENTARY INFORMATION

Bridging hexatic and tetratic phases in binary mixtures through near-critical point fluctuations

B.P. Prajwal and Fernando A. Escobedo*

I. Relation between ΔF_x and mixing free-energy and mixing entropy

Let solid solution s_1 have N_{s_1} total particles and N_2 particles of the guest component 2, and hence a composition x_2:

$$x_2 = N_2/N_{s_1} \tag{S1}$$

and likewise, the solid solution s_2 has N_{s_2} total particles and N_1 particles of guest component 1, so that,

$$x_1 = N_1/N_{s_2} \tag{S2}$$

At the temperature (T) and pressure (P) of interest, the mixing free energy per particle associated with both solutions in going from the pure solids to the mixed states is:

$$\Delta g_{\text{mixing}} = \frac{1}{N_{s_1}}\{\Delta G_{s_1}\}_{\text{mixing}} + \frac{1}{N_{s_2}}\{\Delta G_{s_2}\}_{\text{mixing}} \tag{S3}$$

$$\Delta g_{\text{mixing}} = \left[g_{s_1}(x_2) - (1-x_2)g^0_{s_1} - x_2 g^0_{s_2}\right] + \left[g_{s_2}(x_1) - (1-x_1)g^0_{s_2} - x_1 g^0_{s_1}\right] \tag{S4}$$

where $g^0_{s_i}$ is the free-energy per particle of pure solid s_i (for i = 1 or 2), and $g_{s_i}(\zeta)$ is the free-energy of solid solution s_i with composition "ζ" of the guest species.

Since we do not know *a-priori* what compositions the solid solutions can attain, we evaluate Δg_{mixing} at the most conservative and convenient compositions, namely, at infinite dilute conditions where $x_2 \to 0$ and $x_1 \to 0$; in such a case Eq. (S4) reduces to:

$$\Delta g^{\infty}_{mixing} = \left[g_{s_1}(x_2 \to 0) - g^0_{s_1}\right] + \left[g_{s_2}(x_1 \to 0) - g^0_{s_2}\right] \tag{S5}$$

To evaluate $g_{s_1}(x_2 \to 0)$, consider the expansion:

$$g_{s_1}(x_2 \to 0) \approx g_{s_1}^0 + \left(\frac{\partial g_{s_1}^0}{\partial x_2}\right)_{T,P,N_{s_1}} dx_2 = g_{s_1}^0 + \left(\frac{\partial g_{s_1}^0}{\partial N_2}\right)_{T,P,N_{s_1}} dN_2$$

where Eq. (S1) was used to transform the last term above. Since N_2 is an integer variable, the partial derivative can be approximated by a finite difference such that for $\delta N_2 = 1 - 0 = 1$:

$$g_{s_1}(x_2 \to 0) - g_{s_1}^0 = \frac{\left[g_{s_1}(N_2=1) - g_{s_1}(N_2=0)\right]_{T,P,N_{s_1}}}{\delta N_2} \delta N_2 = \left[g_{s_1}(N_2 = 1) - g_{s_1}^0\right]_{T,P,N_{s_1}}$$

Using this result and a similar expression for $g_{s_2}(x_1 \to 0)$, Eq. (S5) becomes:

$$\Delta g_{mixing}^{\infty} = \left[g_{s_1}(N_2 = 1) - g_{s_1}^0\right]_{T,P,N_{s_1}} + \left[g_{s_2}(N_1 = 1) - g_{s_2}^0\right]_{T,P,N_{s_2}} \quad \text{(S6)}$$

or:

$$\Delta g_{mixing}^{\infty} = \left[\delta g_{s_1}\right]_{T,P,N_{s_1}} + \left[\delta g_{s2}\right]_{T,P,N_{s_2}} \quad \text{(S7)}$$

where δ denotes a property change corresponding to the single guest-particle compositional change indicated in Eq. (S6). Each term inside a bracket in Eq. (S6) or (S7), upon multiplication by $\beta = 1/k_BT$, corresponds to the reduced excess chemical potential associated with "exchanging" (or mutating) a host particle of the pure phase into a guest particle, as defined in Eq. (1) of the main text and hence:

$$\beta \Delta g_{mixing}^{\infty} = \mu_{ex}^{s_1}(1 \to 2) + \mu_{ex}^{s_2}(2 \to 1) \quad \text{(S8)}$$

showing that $\Delta F_x = \beta \Delta g_{mixing}^{\infty}$.

The equations above can be rewritten by splitting the Gibbs free-energy into its enthalpic (H) and entropic (S) components; e.g., the counterpart for Eq. (S3) is:

$$\Delta g_{\text{mixing}} = \frac{\{\Delta H_{s_1}\}_{\text{mixing}}}{N_{s_1}} + \frac{\{\Delta H_{s_2}\}_{\text{mixing}}}{N_{s_2}} - \frac{T}{N_{s_1}}\{\Delta S_{s_1}\}_{\text{mixing}} - \frac{T}{N_{s_2}}\{\Delta S_{s_2}\}_{\text{mixing}}$$

and for Eq. (S7):

$$\Delta g^{\infty}_{mixing} = [\delta h_{s_1} + \delta h_{s_2}]_{\text{mixing}} - T[\delta s_{s_1} + \delta s_{s_2}]_{\text{mixing}} \quad \text{(S9)}$$

where h and s are enthalpy and entropy per particle. In Eq. (S9) the conditions of constant T, P and number of particles have been omitted for simplicity, and the subscript "mixing" made explicit as a reminder of the operation implied by each δ. For an athermal mixture like the ones studied in this work, Eq. (S9) can be simplified to:

$$\Delta F_x = \beta \Delta g^{\infty}_{mixing} = \beta P \left[\delta v_{s_1} + \delta v_{s_2}\right]_{\text{mixing}} - {}^{1}/_{k_B}\,[\delta s_{s_1} + \delta s_{s_2}]_{\text{mixing}} \quad \text{(S10)}$$

where v is specific volume. Just like molecular simulations are implemented to evaluate ΔF_x (see Sec. III below), simulations can also be used to evaluate the first term in Eq. (S10); this would allow us to isolate and indirectly evaluate the mixing entropy term in Eq. (S10). However, the volume changes (δv) associated with such minor compositional changes will be rather small unless the components were to have considerably different sizes; hence, assuming that the 2nd term in Eq. (S10) is dominant:

$$\Delta F_x \approx -{}^{1}/_{k_B}\,[\delta S_{s_1} + \delta S_{s_2}]_{\text{mixing}} \quad \text{(S11)}$$

which indicates that minimizing ΔF_x would tend to maximize the mixing entropy at the dilute limit of the guest component in each of the two solid phases. This minimal ΔF_x can be seen as a predictor, or a metric for a first-order extrapolation, of the mixing free-energy behavior at finite guest compositions.

II. Estimating p_m for calculating ΔF_x

For the mixture with components *i* and *j*, the relationship between ξ of the components and the corresponding pure component order disorder transition pressure (ODP), P_t^k (where k= *i* or *j*) is:

$$\frac{P_t^i}{P_t^j} = k\,\xi^2 \qquad (S12)$$

where *k* is the ratio of the ODPs when ξ= 1 (see Table S1). The relevant reduced pressure values of the pure components used in the exchange free energy calculations are reported in Table S2.

Table S1. Representative values of ξ and pressure, p_m, used in the exchange free energy calculation for the disks+squares and disks+hexagons mixtures. $\boldsymbol{P_t}^{\textbf{disk}}$ and $\boldsymbol{P_t}^{\textbf{polygon}}$ are the pressures at the isotropic→tetratic transition for pure squares and the hexatic→triangular solid (1Δ) transition for pure disks and pure hexagons. The reference polygon edge length is a = 2.

Mixture	ξ	$p_m = max(P_t^{disk}, P_t^{polygon})$
disks+squares	1.0	2.325 (2.325, 2.125)
	1.04 (equal ODP)	2.125
	1.1	2.125 (1.921, 2.125)
	1.13 (equal area)	2.125 (1.821, 2.125)
disks+hexagons	1.7	0.804 (0.804,0.687)
	1.82 (equal area)	0.702 (0.702,0.687)
	1.84 (equal ODP)	0.687
	1.9	0.687 (0.644,0.687)

Data for pure polygons and disk

Table S2. Equation of state data for pure polygons and disk systems from the literature [1,2]. The pure component reduced pressures P_L* and corresponding densities η for the ordered phases were used in the ΔF_x calculations. The range of densities for the relevant phases is also shown.

Shape	**Phase**	**Density, η**	**P_L* (η)**
Square	tetratic	0.72-0.832	17 (~0.722)
Hexagon	hexatic	0.686-0.708	10.9 (~0.713)
Disk	hexatic	0.716-0.720	9.3 (~0.721)

III. Interfacial simulation method

To test the relative stability of the phases near the transition region, we used interfacial simulations, where the box dimension was at least five times more elongated along one direction compared to the other perpendicular directions. A longer axis (say the x-axis) facilitated the formation of distinct two-phase regions under coexistence conditions, with the interfaces normal to the long axis. The box cross-sectional length (perpendicular to the long axis) was carefully chosen to accommodate pre-equilibrated unit cells of both distinct crystal phases, having at least 25-30 particle layers to minimize the finite-size effects. We allowed fluctuations in the box dimension along the x-axis only, using volume moves in the NP_xT ensemble [3]. To estimate the average equilibrium compositions of the individual phases in the interfacial simulations, we used a histogram method [4] where the simulation box was divided into sub-cells along the long axis and the compositions in each of the sub-cells was computed. An optimal sub-cell size was chosen (at least 5σ) such that each sub-cell gives a reasonable local estimate of the single-phase compositions. The resulting composition histogram obtained showed two peaks (Fig. S1) corresponding to the two phases in the box and the compositions of the individual phases was estimated by a simple weighted average of the appropriate peak (excluding the interfacial region).

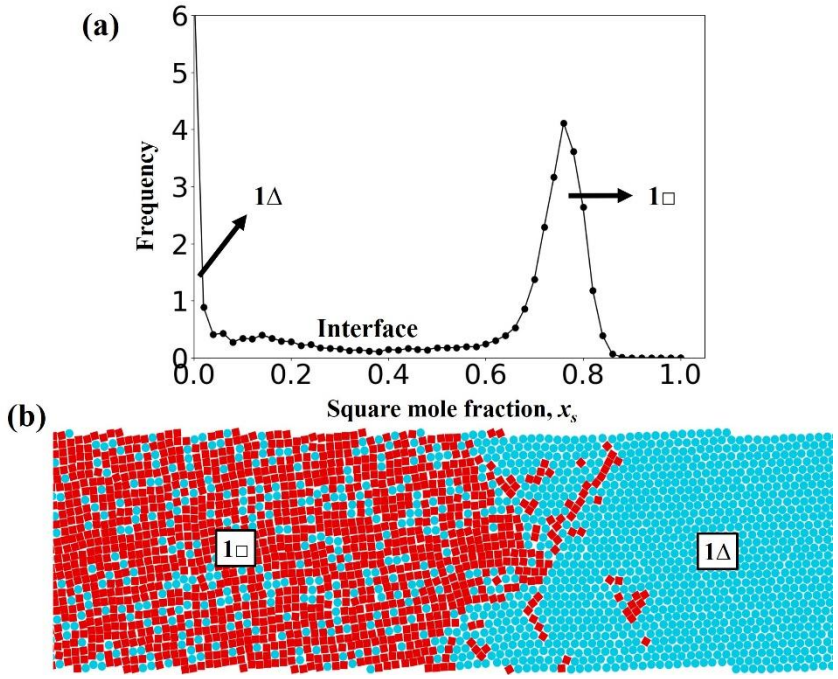

Fig S1 (color online). Distribution function of the (a) average square molar composition in the sub-cells constructed for the two-phase system obtained from the NP_xT Interfacial simulation for the disks+squares mixture at P^*= 18.9 and N= 4345 (2170 disks+ 2175 squares). The two peaks obtained correspond to the square compositions of the individual phases. (b) Snapshot showing the two-phase regions with the 1□ (square solid) in the leftmost region and 1Δ (triangular solid) in the rightmost region.

IV. Order parameters for structure determination

Cubatic order parameter

To determine global orientational order of the squares in the disks+squares mixtures we measure the cubatic order parameter, P_4, which is defined as,

$$P_4 = 1/(16N)\ \sum_{ij}(35|\boldsymbol{u_{ij}}.\ \boldsymbol{n}|^4 - 30|\boldsymbol{u_{ij}}.\ \boldsymbol{n}|^2 + 3\ ) \qquad (S13)$$

where $\boldsymbol{u_{ij}}$ is the unit vector along the axis j of square i and $\boldsymbol{n}$ is the unit vector that maximizes P_4 (normalized such that perfect order corresponds to 1). The director $\boldsymbol{n}$ is found by using the numerical recipe reported in [5].

Local compositional autocorrelation function

We analyzed the variation of the square composition, $\boldsymbol{LC_{sq}}$ in the local environment of each particles over the Monte Carlo (MC) cycles in the mosaic (M) state using the autocorrelation function, γ_s defined as,

$$\gamma_s = \frac{\sum_{j=0}^{N_{MC}-N_s} \widehat{\boldsymbol{\theta}}_j . \widehat{\boldsymbol{\theta}}_{j+s}}{N_{MC} - N_s} \qquad (S14)$$

where $\widehat{\boldsymbol{\theta}} = \frac{\boldsymbol{LC_{sq}} - \langle \boldsymbol{LC_{sq}} \rangle}{\| \boldsymbol{LC_{sq}} - \langle \boldsymbol{LC_{sq}} \rangle \|}$, $\boldsymbol{LC_{sq}} - \langle \boldsymbol{LC_{sq}} \rangle = \{x_1 - \bar{a}, x_2 - \bar{a}, x_3 - \bar{a}, \ldots, x_N - \bar{a}\}$, $\bar{a} = \frac{\sum_{i=1}^{N} x_i}{N}$ and x_i is a local composition defined as the fraction of particles that are squares within the cutoff distance, $r_c \sim 1.7\sigma$ from the position of particle *i*. N_s is the number of MC cycles over which the variation of $\boldsymbol{LC_{sq}}$ is measured, N_{MC} is the total number of MC cycles, and *N* is the number of particles. We performed these calculations with *NVT* ensemble simulations using only *"pseudo dynamic"* translation and rotation moves. The step size for these moves was kept constant and small, corresponding to an average acceptance probability between 75 and 80 %.

Cluster analysis

For an equimolar disks+squares mixture, we tracked the growth of the six-fold and four-fold ordered domains associated with the I → M → (hexatic-tetratic) two-phase transition. To perform this analysis, we adopted the clustering method reported in Ref. [6] that used the local order parameter to study the nucleation and growth mechanism of complex ordered structures like the lamellar, cylinder and the alternating gyroid phases. We identified the particles belonging to the six-fold and four-fold clusters by estimating the correlation between the neighboring particles *i* and *j* using the *dot* product of the *n*-fold local bond orientational vectors defined as,

$$d_{p,n}(i,j) = \Phi_n(i)\, \Phi_n^*(j) \qquad (S15)$$

where * indicates the complex conjugate. The correlations, $d_{p,6}$ and $d_{p,4}$ are computed for all neighboring pairs (i,j) within the cutoff distance, $r_c \sim 1.7\sigma$ from the position of particle *i*. Figure S2a shows the frequency histogram of $d_{p,6}$ and $d_{p,4}$ for both hexatic and tetratic phases. The hexatic phase was simulated at x_s= 0.3, P^*= 14.1, η= 0.773 and the tetratic phase was simulated at x_s= 0.8, P^*= 12.1, η= 0.782. To categorize the two neighboring particles *i* and *j* into *hexatic-*

like and the *tetratic-like* connections, we set the threshold $d_{p,6}^{c}$ and $d_{p,4}^{c}$ as 0.33 and 0.31, respectively (where the cumulative $d_{p,6}$ and $d_{p,4}$ distributions for the hexatic and tetratic phases intersect). We then checked the number of connections per particle which were *tetratic-like,* $N_{c,4}$, and *hexatic-like,* $N_{c,6}$, for both the tetratic and hexatic phases. Figure S2b and S2c show the cumulative distribution functions for $N_{c,6}$ and $N_{c,4}$ obtained by considering $d_{p,6}$> 0.33 and $d_{p,4}$> 0.31, respectively. Using this distributions, we estimated a second threshold parameter, $\mathfrak{E}_{c,6}$ (or $\mathfrak{E}_{c,4}$) such that if $N_{c,6}(i)$ (or $N_{c,4}(i)$) > $\mathfrak{E}_{c,6}$ (or $\mathfrak{E}_{c,4}$) then the particle *i* is considered *hexatic-like* (or *tetratic-like*). Based on the distributions shown in Fig. S2b and S2c, we set $\mathfrak{E}_{c,6}$ and $\mathfrak{E}_{c,4}$ as 4. The particles identified as *hexatic-like* and *tetratic-like* were clustered based on the nearest-neighbor cutoff condition where $r_c \sim 1.7\sigma$. Using this clustering protocol, we determined the four largest six-fold and four-fold ordered domain. We also computed the relative orientational alignment between the largest six-fold and the largest four-fold clusters by estimating the $|\theta_6 - \theta_4| = \left|\frac{\arg(\Psi_6^{N_L})}{6} - \frac{\arg(\Psi_4^{N_L})}{4}\right|$, where $\Psi_n^{N_L}$ (where n= 6, 4) is the n-fold bond orientational vector of the largest n-fold ordered clusters containing N_L particles.

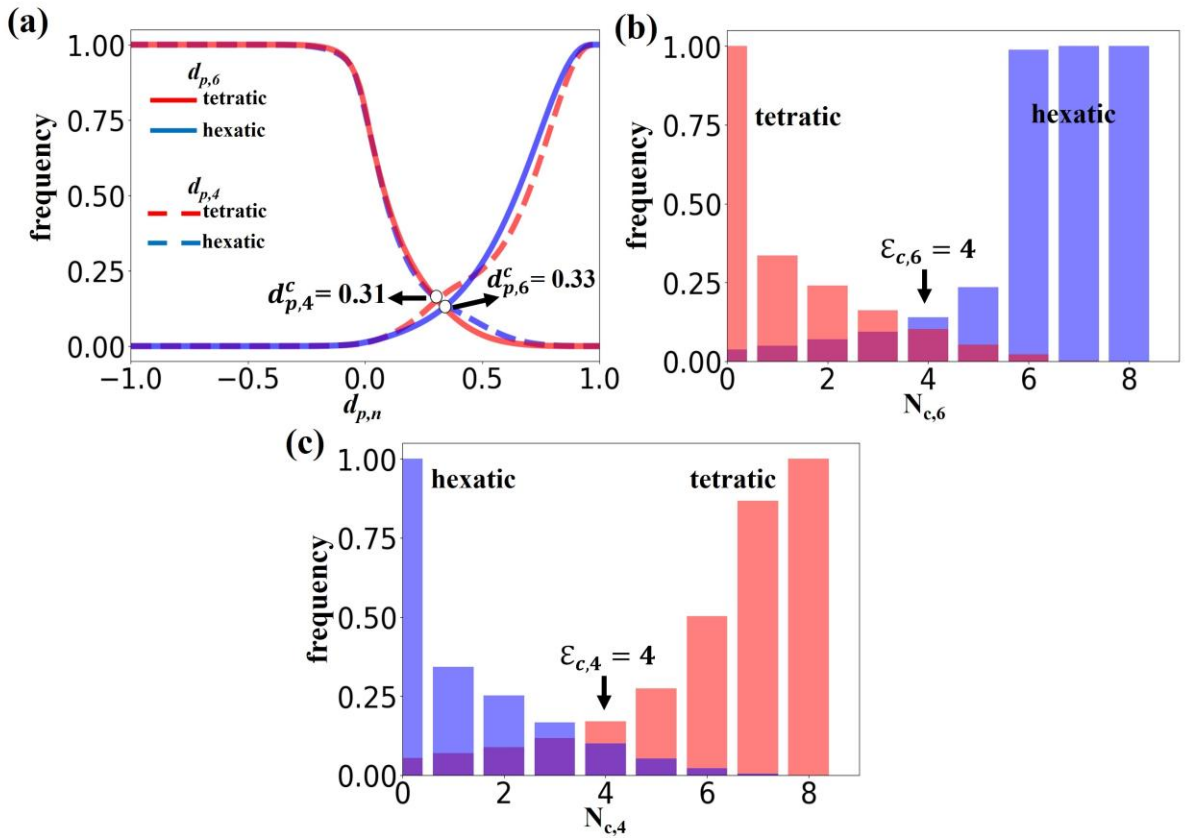

Fig S2 (color online). (a) Cumulative distributions of the correlation function $d_{p,6}$ and $d_{p,4}$ for the hexatic phase at x_s= 0.3, P*= 14.1, N= 8569, and the tetratic phase at x_s= 0.8, P*= 12.1, N=11203. (b,c) Distributions showing the number of connections per particle for the hexatic and tetratic phases. Two particles are considered to be connected if their correlation function $d_{p,6}$ and $d_{p,4}$ is greater than 0.33 and 0.31, respectively. The particles having $N_{c,6} \geq 4$ and $N_{c,4} \geq 4$ are defined as possessing *tetratic-like* and *hexatic-like* connections.

V. Phase behavior of disks+squares mixture

Equation of state (EoS) for 20% and 80% square compositions

EoS curves for x_s= 0.2 and 0.8 are shown in Fig. S3, where the state points were obtained using compression runs starting from a low-pressure I phase. To characterize the structural difference between the I phase and the tetratic or hexatic phase, we calculated the global six-fold (Ψ_6) and four-fold (Ψ_4) bond orientational order parameters. For the x_s= 0.2 case (Fig. S3a), both Ψ_6 and Ψ_4 ~ 0 at low η, demarking the I phase, and upon compression Ψ_6 increased significantly for η > 0.72, indicating the onset of six-fold order in the system. The Ψ_4 values remained low for the entire range of the I and hexatic phases, indicating low four-fold order. For the x_s= 0.8 case (Fig. S3b), the Ψ_4 values increased for η > 0.737, indicating the formation of four-fold order in the system.

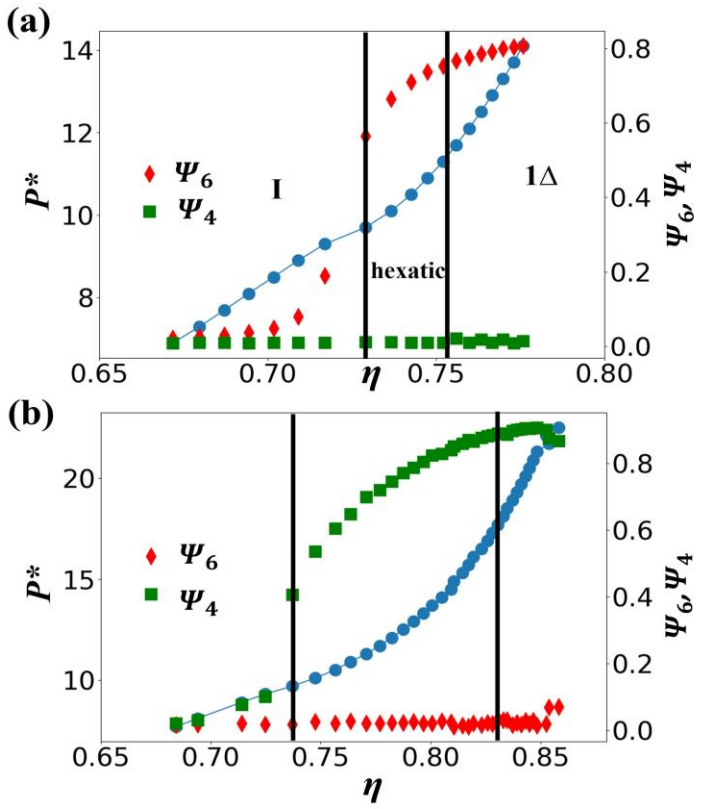

Fig. S3 (color online). Equation of state (EoS) for (a) 20% and (b) 80% squares composition in the disk + square mixture with ξ = 1.1 (optimal) size ratio. The EoS curves (continuous curve + circles in blue) were obtained for (a) 90000 and (b) 11203 particle system. Approximate phase boundaries are also marked. The pressure P^*, bond orientational order parameters Ψ_6 (diamonds) and Ψ_4 (squares) are shown as a function of area fraction, η. The symbols 1Δ, 1□, and I denote the triangular solid, square solid and isotropic phase, respectively.

Analysis to identify hexatic-solid and tetratic-solid transition boundaries

The global values of Ψ_6 and Ψ_4 only detect the presence of the four-fold or six-fold clusters in the system that are aligned to the global Ψ_4 and Ψ_6 orientational director vector. To identify the existence of the hexatic (or tetratic) phase and mark their phase boundaries with the solid phase, we analyzed the trends in local positional and bond orientational distribution functions using the 2D histogram of positional pair-correlation function, $g(\Delta \boldsymbol{x}^*, 0)$ and bond orientational correlation function, $g_n(r^*)$, where n= 6 or 4 [1,2]. $g(\Delta \boldsymbol{x}^*, 0)$ was obtained by orienting the

Δx^* axis of each configuration with the global Ψ_6 or Ψ_4 orientational director vector. We carried out MC simulations in the *NPT* ensemble for systems with x_s= 0.2 and 0.8 having 9000 and 11203 particles, respectively. Figure S5a shows $g(\Delta x^*, 0)$ and $g_6(r^*)$ for the hexatic and 1Δ solid phases. We observed that at η = 0.737, the peaks in $g(\Delta x^*, 0)$ decay rapidly after 10σ indicating a short-range translational order, while the corresponding $g_6(r^*)$ orientational correlation function is long-ranged. These characteristics are consistent with hexatic phase behavior. At η = 0.756, $g(\Delta x^*, 0)$ decays algebraically with an exponent $\approx -1/3$ while $g_6(r^*)$ decays negligibly, indicators of quasi-long-range translational and six-fold bond orientational order in the system. Thus, the positional order increases gradually with density from the hexatic phase at η = 0.737 to a 1Δ solid phase at η = 0.756, where the $g(\Delta x^*, 0)$ function crosses over to a power-law behavior whose $\approx -1/3$ exponent marks the stability limit of the solid phase in the KTHNY scenario. Figure S4b shows snapshots and associated structure factors, which display six-fold patterns due to the hexagonal order in the hexatic and 1Δ solid phase. To corroborate these conclusions, we obtained the 2D pair correlation histogram [2] for the configurations in Fig. S5. They show that the positional order peaks persist for the 1Δ solid throughout the simulation domain at much longer length scales (~ 50σ) for η = 0.756, while the peaks disappear for the hexatic phase at ~ 10σ for η = 0.737.

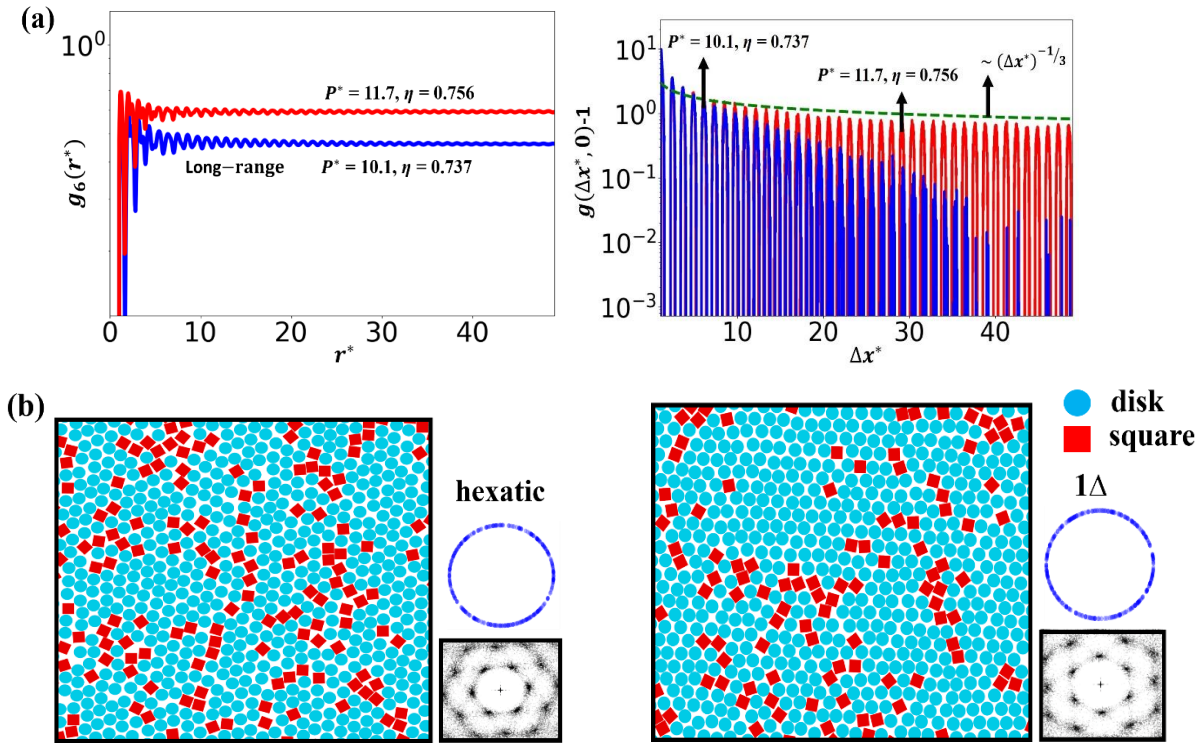

Fig. S4 (color online): Correlation functions obtained from MC-*NPT* simulations for the 20% squares (80% disks) mixture composition with $\xi = 1.1$ and $N = 9000$ particles. (a) Bond order $g_6(r^*)$ and 2D pair $g(\Delta x^*, 0)$ correlation functions for the hexatic, and triangular solid (1Δ) phases corresponding to η = 0.737, and 0.756, respectively. The dashed-line indicates the algebraic decay with exponent $\sim -1/3$ (the KTHNY theory prediction for hexatic-solid transition). (b) Snapshots, structure factors, and scatter plots for the orientation unit vectors of squares for the hexatic (left) and 1Δ (right) phases. The snapshots represent only a section of the entire simulated phase.

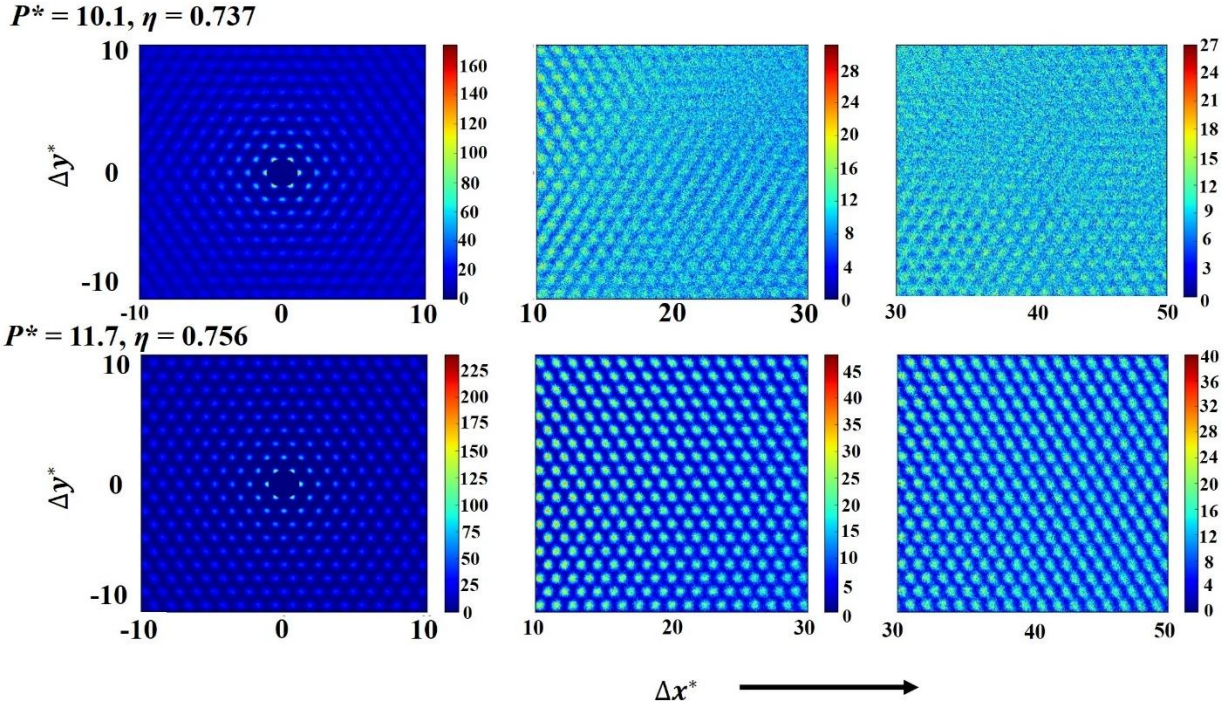

Fig. S5 (color online). 2D positional pair-correlation histograms for a single configuration (N = 9000) at different sections along the x-axis. Top panel: hexatic phase at P^*= 10.1, η = 0.737, where the peaks disappear at length scales greater than ~10σ indicating short-range positional order. Bottom panel: triangular solid (1Δ) phase at P^*= 11.7, η = 0.756, where the positional order is sustained for a length scale of ~ 50σ. The scale bar indicates the intensity of the peaks.

Similar analyses were carried out to obtain the tetratic to 1□ solid phase boundary for the square-rich region with $x_s = 0.8$ (see Fig. S6). At the density η = 0.787, $g(\Delta x^*, 0)$ decayed quickly for $\Delta x^* > 5\sigma$ indicating short-range positional order but $g_4(r^*)$ is long-ranged, indicative of the tetratic phase. For the 1□ solid phase at η = 0.831, $g(\Delta x^*, 0)$ decays algebraically with an exponent $\approx -1/3$ indicating quasi-long range positional order, and $g_4(r^*)$ shows long-range four-fold orientational order. The 2D pair correlation histogram also shown in Fig. S7 confirms a transition from short-range (tetratic) to long-range (1□ solid) positional order. Figure S6b shows representative snapshots and structure factors, which display four-fold patterns indicative of square order in the tetratic and 1□ solid phase. Overall, these trends suggest that the hexatic→1Δ solid and tetratic→1□ solid transitions follow the continuous KTHNY mechanism. However, a rigorous analysis using simulations of much larger systems

would be required to more definitely establish the mechanism and map the boundaries of these transitions.

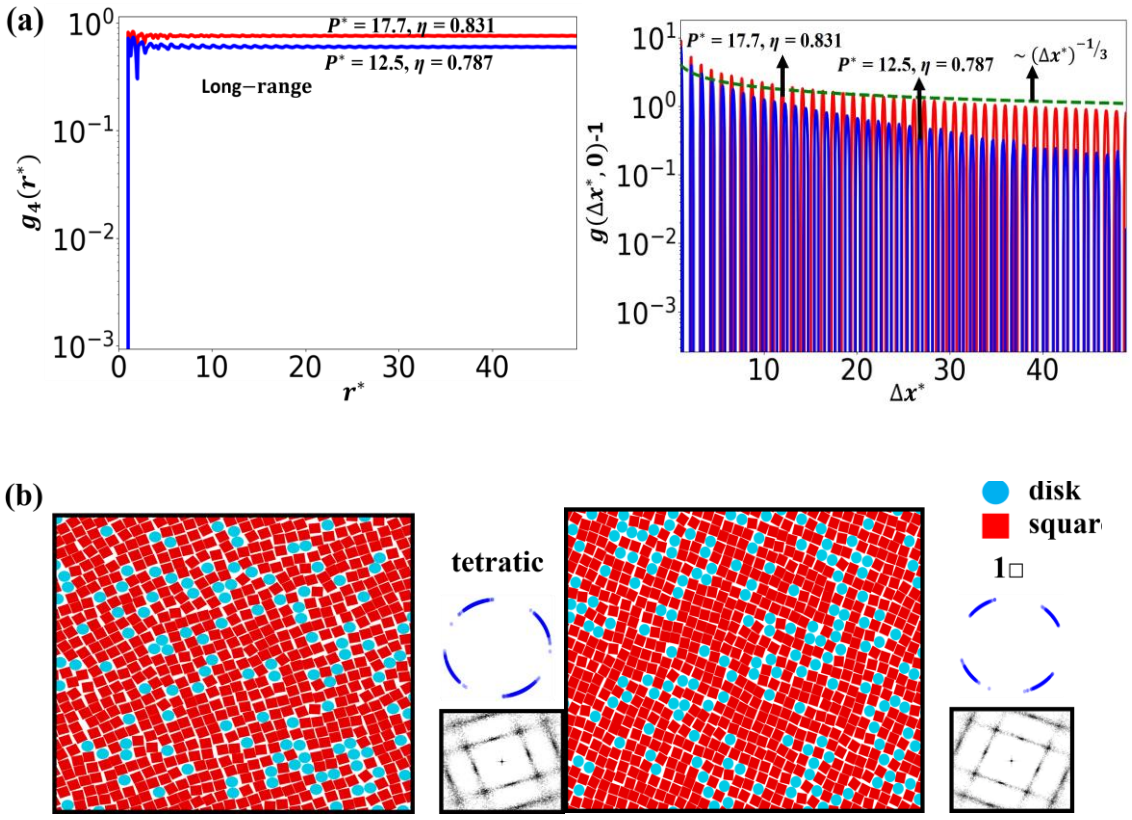

Fig. S6 (color online). Correlation functions obtained from MC-*NPT* simulations for the 80 % squares (20% disks) mixture with $N = 11203$ and $\xi = 1.1$. (a) Bond order $g_4(r^*)$ and 2D pair $g(\Delta x^*, 0)$ correlation functions for the tetratic phase at $\eta = 0.787$ and square solid (1□) phase at $\eta = 0.831$. The dashed-line indicates an algebraic decay with exponent $\sim -1/3$ corresponding to the tetratic-solid transition predicted by the KTHNY theory. (b) Snapshots and structure factor for the tetratic (left) and 1□ (right) phases. The snapshots show only a section of the entire simulated phase.

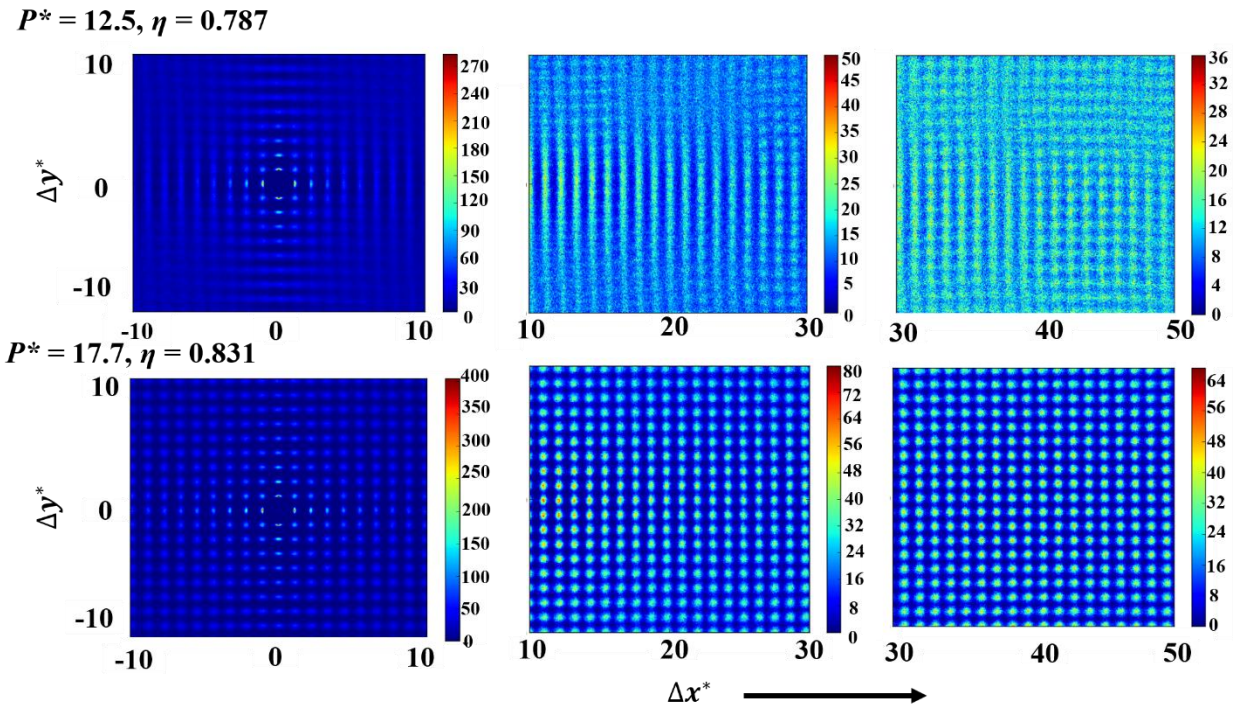

Fig. S7 (color online). 2D positional pair-correlation histograms (N = 11203) for a single configuration at different sections along the x-axis. Top panel: tetratic phase at P^* = 12.5, η = 0.787, where the peaks become blurred at larger length scales indicating short-range positional order. Bottom panel: square solid (1□) phase at P^* = 17.7, η = 0.831, where sharper peaks are observed for a longer length scales ~ 50 σ. The scale bar indicates the intensity of the peaks.

VI. Characteristics of the mosaic (M) state

Local compositional analysis

The well-mixed isotropic (I) phase transitions into the M state upon compression, where the contribution from the entropic bonding gives rise to the formation of disk-rich hexatic and square-rich tetratic/rhombic micro-domains in the system. The clustering of the like-shaped particles is shown in Fig. S8a by analyzing the square composition, $\boldsymbol{LC_{sq}}$, in the local environment of each particle. We observed regions of *'defective'* particles having $\boldsymbol{LC_{sq}}$ near 0.5

occupying mainly the grain boundaries. We analyzed the migration of these defects using the local square compositional autocorrelation function, γ_s (defined in Eq. S14 Sec. IV) for the particles that were tagged as defective and, for comparison, for the particles that belongs to the six and four-fold ordered (not defective) micro-domain clusters (Fig. S8a). To evaluate γ_s over the Monte Carlo (MC) cycles, the particles were categorized as defective and not defective for the initial configuration (MC cycle= 0) and such categorization was retained throughout. We observed a slower decay in the local square compositions with MC cycles for the particles belonging to the ordered clusters compared to the defective particles (Fig. S8c). This behavior can also be seen in the Movie 3.

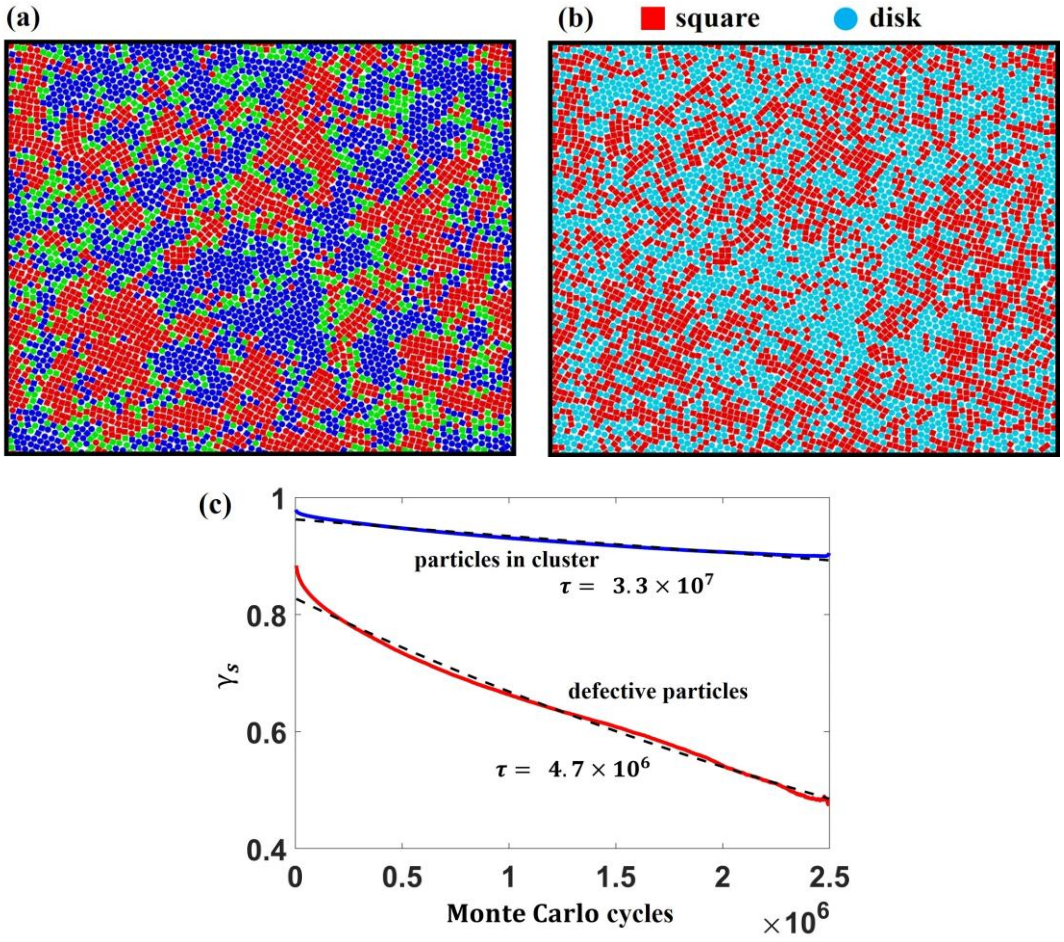

Fig. S8 (color online). Representative snapshots, (a) and (b), and local square compositional autocorrelation function, γ_s, (c), of the M state at P^*= 14.9 and η = 0.783 for the equimolar disks+squares mixture with N = 10000 particles. γ_s is shown for the defective particles and the

particles that belongs to the ordered clusters. (a) The particles (i = 1 to N) are colored based on the local square composition, x_i, that is estimated within 1.7σ from the particle's position. Red, green, and blue particles have x_i> 0.52, 0.48 < x_i < 0.52 and x_i < 0.48, respectively. Fitted exponential decay curve is shown as dashed lines along with the corresponding time constant, τ value (in units of MC cycles).

Identifying rhombic (RB) clusters

To further detect any underlying ordered domains in the system, we plot in Fig. S9a the global Ψ_6^{sq} for squares and Ψ_4^d for disks. The global Ψ_6^{sq} and Ψ_4^d values are evaluated by calculating the average of the n-fold (where n= 4 or 6) local bond orientational order, Φ_6^{sq} for squares and Φ_4^d disks in the system. Ψ_6^{sq} increased from a low value to an intermediate value in the M state region while Ψ_4^d remained constant with a low value throughout. This is due to the formation of oblique rhombic (RB)-like lattice domains by the square particles as corroborated by the lattice angle distribution function (see Fig. S10b). At P*= 14.9 and η = 0.783, the lattice angle distribution function exhibits a broad peak with the lattice angles populated similarly over the 75º-105º range, which bracket the limiting angle value of 80.435º [7] for RB order. This distribution function also shows significant number of particles having close to 90º (and 180º) lattice angles, indicative of tetratic-like ordered domains. Since the M state forms at intermediate pressures, local RB order likely arises from the squares having enough free volume to rotate and translate within the tetratic-like ordered domains. At P*= 17.3 and η = 0.807, the system phase separated into tetratic and 1Δ crystal structures, and Ψ_6^{sq} decreases sharply while the global Ψ_4 values increase as the lattice angle distribution of 1□ phase forms a single peak centered at 90º (see Fig. S9b). Note also that the scatter plot obtained for the square orientation vectors in the M state (see Fig. S9a) shows weak four-fold orientational order, which can also be detected by the higher P_4 (see Eq. S13 Sec. IV) values compared to the I phase.

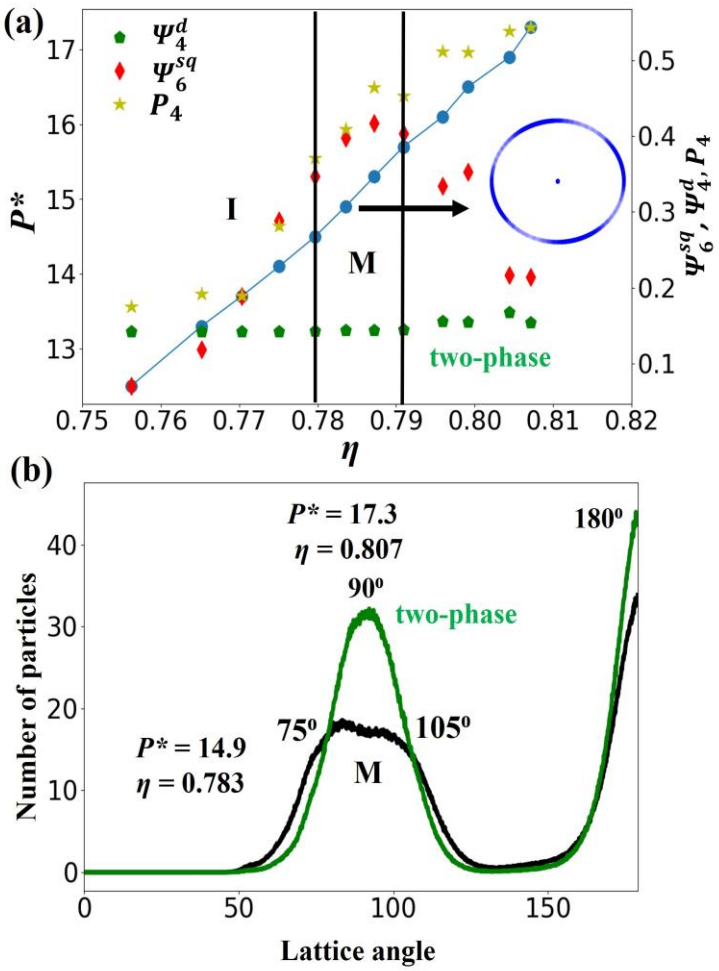

Fig. S9 (color online). Equation of state (a) and lattice angle distribution function (b) for equimolar disks + squares mixture with $\xi = 1.1$ (*optimal*) size ratio. The equation of state curves (continuous curve and circles in blue) is for $N = 10000$ particles. The Ψ_4^d, Ψ_6^{sq} and P_4 order parameters are plotted as a function of area fraction, η. The lattice angles for the RB clusters are calculated with the vectors obtained using the coordinates of the four nearest neighbors of the central square particles [7].

Local bond orientational functions, $g_4(r^*)$ and $g_6(r^*)$ at x_s = 0.49 and 0.52

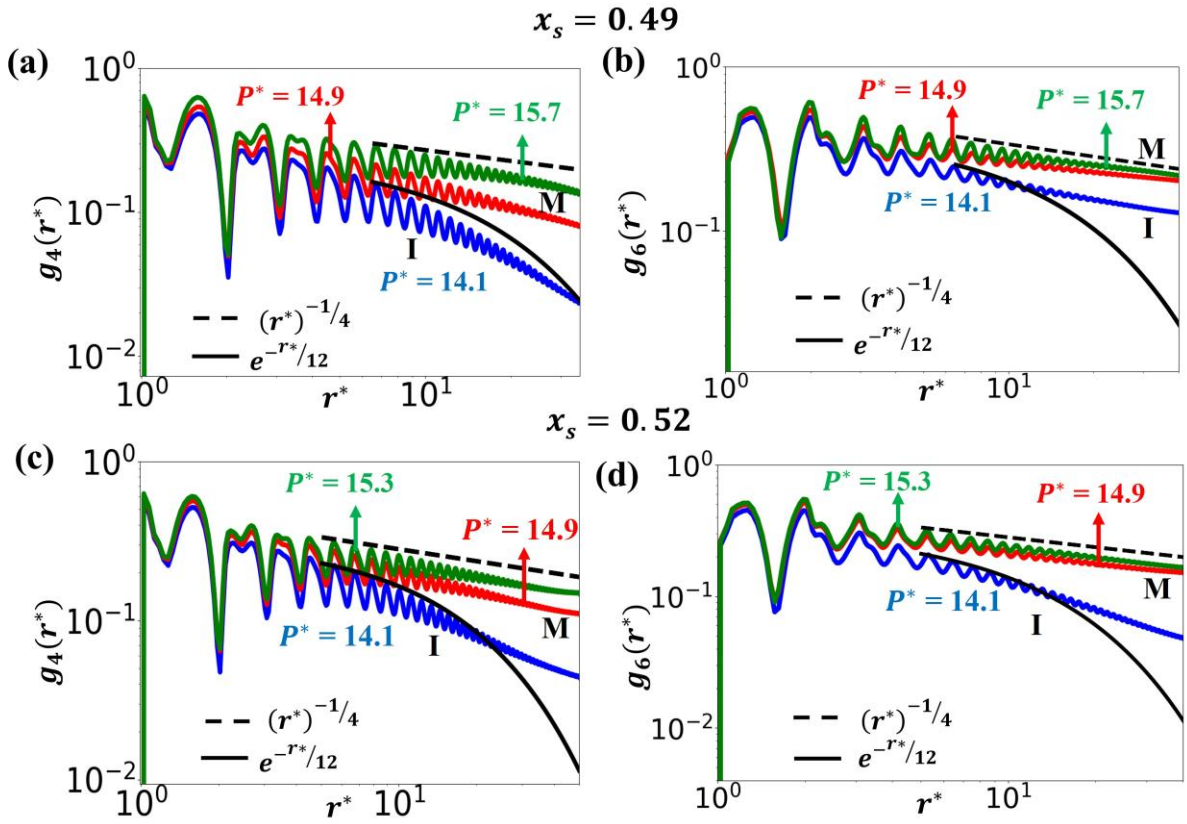

Fig. S10 (color online). Bond orientational order functions $g_4(r^*)$ and $g_6(r^*)$ for the I, hexatic, and M state with N = 10000. The orientational correlation functions are shown for x_s= 0.49 (a,b) and 0.52 (c,d). The dashed and solid lines indicate algebraic and exponential decay of the orientational correlation with exponent $-1/4$ and $-1/12$, respectively. I= isotropic phase; M= mosaic state.

Local bond orientational functions, $g_4(r^*)$ and $g_6(r^*)$ at x_s = 0.45 and 0.55

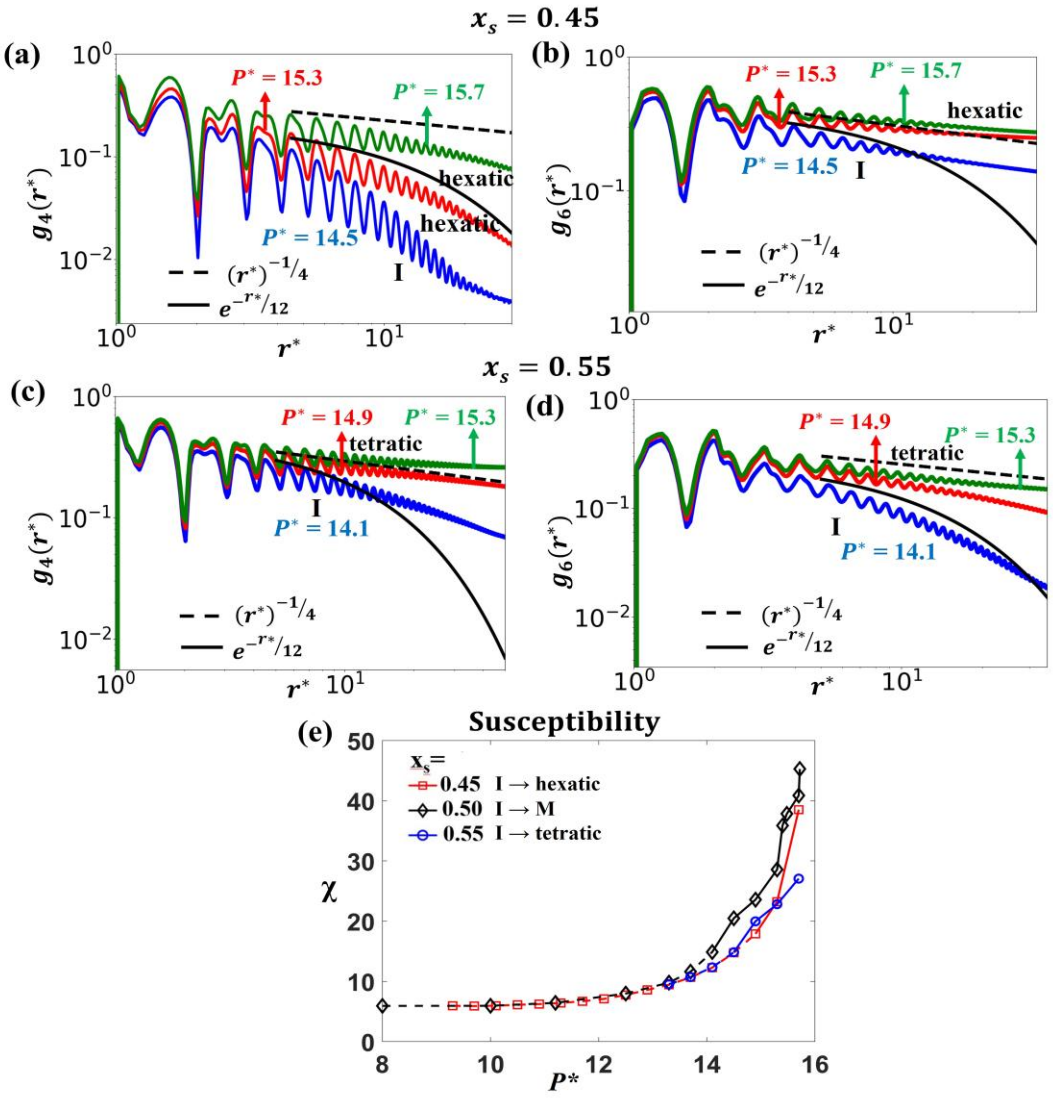

Fig. S11 (color online). Bond orientational order functions $g_4(r^*)$ and $g_6(r^*)$ for the I, hexatic, and tetratic phases. The orientational correlation functions are shown for x_s= 0.45 (a,b) and 0.55 (c,d). The dashed and solid lines indicate algebraic and exponential decay of the orientational correlation with exponent $-1/4$ and $-1/12$, respectively. (e) Variation of susceptibility χ with P^* at different global square composition, x_s evaluated for the single-phase region. Solid lines represent the hexatic phase, M state, and tetratic phase region for x_s= 0.45, 0.5, and 0.55, respectively. The dashed lines correspond to the I phase. For clarity, the maximum χ is not shown at x_s= 0.45 and 0.55. The χ values are obtained by using 8×8 sub-cells and N = 10000 particles. I = isotropic phase; M = mosaic state.

Finite size scaling analysis of the M state

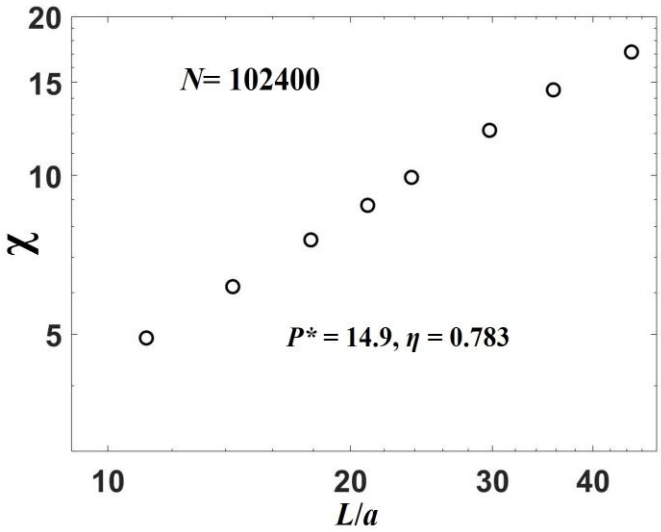

Fig. S12 (color online). Relationship between the local compositional susceptibility, χ and the sub-cell size, L for the M state of equimolar disks+squares mixture with $\xi = 1.1$ and $N = 102400$ particles. a = square side.

VII. Data for disks+squares mixtures of different size ratios

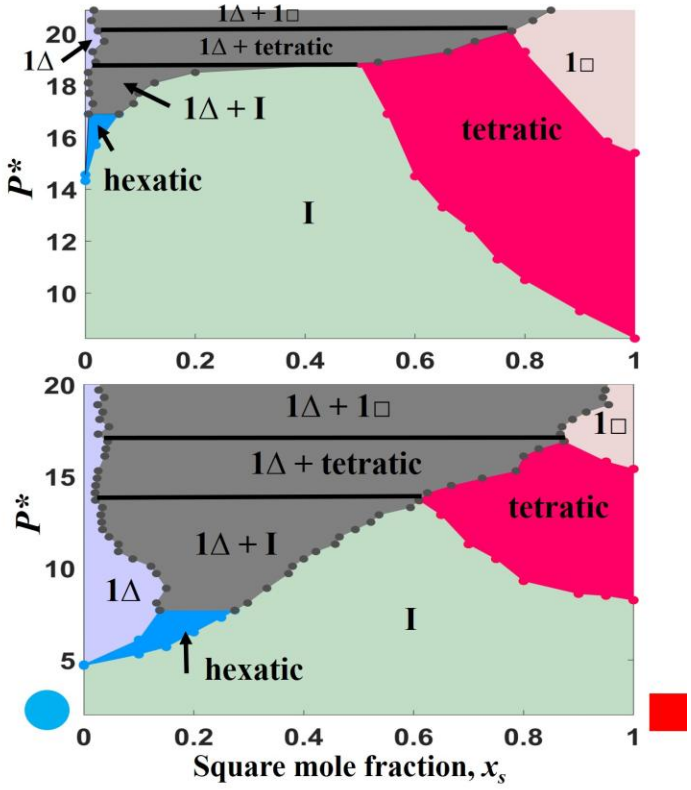

Fig. S13 (color online). Pressure-composition phase diagrams for disks (diameter σ) and squares (side edge a) with different size ratios, $\xi = \sigma/a$. Top: $\xi = 0.8$, bottom: $\xi = 1.4$. 1Δ = triangular solid, 1□ = square solid, and I = isotropic phase.

Table S3. Simulation data for disks+squares mixture at three different size ratios. $\Delta ODP = ODP_4 - ODP_6$, where ODP_x is the reduced pressure of individual components at I → (n-fold)atic (where n= 4 or 6) transition. P_{co}^* is the minimum pressure where the two phases coexist. P_M^* indicates the stable range of pressure values for the M state. $x_s^{1\Delta}$ and $x_s^{1\square}$ shows the maximum difference in the square compositions where the disk-rich and square-rich solid solution regions are stable.

Size ratio	ΔODP	P_{co}^*	P_M^*	$x_s^{1\Delta}$	$x_s^{1\square}$
0.8	≈ -6.06	16.9	-	0.01	0.22
1.1	≈ 0.67	15.7	14.5-15.7	0.3	0.26
1.4	≈ 3.57	7.7	-	0.14	0.13

VIII. Phase behavior of disks+hexagons mixture

Analysis to identify hexatic-solid transition boundaries at equimolar composition

Figure S14a shows $g(\Delta x^*, 0)$ and $g_6(r^*)$ for the hexatic and 1Δ solid phases. We observed that the hexatic phase is stable within a narrow range of pressures, P^*, and density, η. At η = 0.706, the peaks in $g(\Delta x^*, 0)$ decay rapidly after 10σ indicating short-range translational order while $g_6(r^*)$ is long-ranged. At η = 0.718, $g(\Delta x^*, 0)$ decays algebraically with an exponent ≈ $-1/3$ while $g_6(r^*)$ is long-ranged, indicators of quasi-long-range translational and long-range six-fold bond orientational order in the system. Figure S14b shows snapshots and associated structure factors, which display six-fold patterns due to the hexagonal order in the hexatic and 1Δ solid phase. The equation of state curves for x_h= 0.5 are shown in Fig. S14c, where we observed a first-order like transition from the I phase to hexatic phase and a continuous-like transition from hexatic phase to 1Δ solid phase. To characterize the structural difference

between the I phase and the hexatic phase, we calculated the global six-fold (Ψ_6) bond orientational order parameters. Upon compressing the I phase, Ψ_6 increased significantly for η > 0.706 indicating the onset of six-fold order in the system.

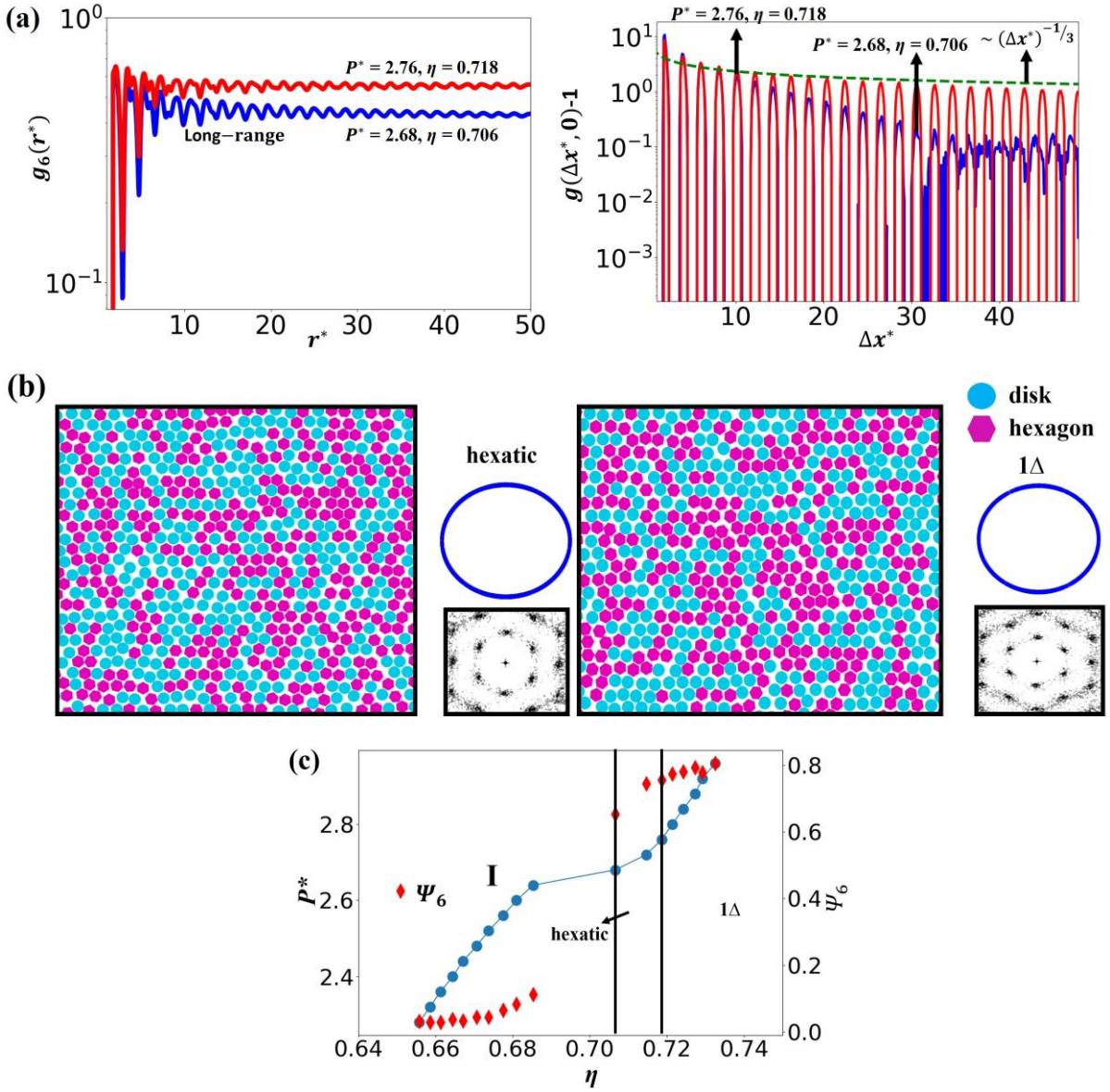

Fig. S14 (color online). Correlation functions and equation of state obtained from MC-*NPT* simulations for the 50% hexagons (50% disks) mixture with N = 8100 and ξ = 1.82. (a) Bond

order $g_6(r^*)$ and 2D pair $g(\Delta x^*, 0) - 1$ correlation functions for the hexatic phase at $\eta = 0.706$ and 1Δ phase at $\eta = 0.715$. The dashed-line indicates an algebraic decay with exponent $\sim -1/3$ corresponding to the hexatic-solid transition predicted by the KTHNY theory. (b) Snapshots and structure factor for the hexatic (left) and 1Δ (right) phases. The snapshots show only a section of the entire simulated phase. (c) The pressure, P^*, bond oriental order parameters Ψ_6 (diamonds) are shown as a function of area fraction, η. Approximate phase boundaries are also marked. The symbols 1Δ, and I denote the triangular solid, and isotropic phase, respectively.

References

[1] J. A. Anderson, J. Antonaglia, J. A. Millan, M. Engel, and S. C. Glotzer, Phys. Rev. X **7**, 021001 (2017).

[2] E. P. Bernard and W. Krauth, Phys. Rev. Lett. **107**, 155704 (2011).

[3] D. Frenkel, Eur. Phys. J. Plus **128**, 10 (2013).

[4] F. Martínez-Veracoechea and E. A. Muller, Mol. Simul. **31**, 33 (2005).

[5] B. S. John, C. Juhlin, and F. A. Escobedo, J. Chem. Phys. **128**, 044909 (2008).

[6] A. J. Mukhtyar and F. A. Escobedo, Macromolecules **51**, 9769 (2018).

[7] C. Avendaño and F. A. Escobedo, Soft Matter **8**, 4675 (2012).

CHAPTER 4: Atomistic modeling approach for predicting association of photoacid generators in extreme ultraviolet polymeric photoresists

B.P. Prajwal[‡], James M. Blackwell[†], Patrick Theofanis[†], and Fernando A. Escobedo*[‡]

[‡]Robert Fredrick Smith School of Chemical and Biomolecular Engineering, Cornell University, Ithaca, New York

[†]Intel Corporation, Hillsboro, Oregon

Abstract

This work advances a computational framework to probe the molecular inhomogeneities that occur in chemically amplified photoresists intended for extreme ultraviolet (EUV) lithography. Atomistic molecular dynamics simulations were used to probe the effect of ionic and steric interactions on the dispersibility of photoacid generators (PAGs) in the polymer medium before EUV exposure, as poor dispersibility is a potential source of post-exposure feature roughness. The PAGs studied include ionic salts containing Triphenyl sulfonium (TPS) cation with trifluoromethane (TFMeS), nonafluorobutane (NFBuS), perfluorophenyl (PFPS) and adamantyltetrafluoroethyl (ATFEtS) sulfonate anions, and a nonionic naphthalimide sulfonate PAG. The model photoresists studied are sequence-defined polypeptoids, poly(tert-butyl methacrylate) (PtBMA) and poly(4-hydroxy styrene) (PHS) homopolymers and alternating copolymers thereof. The dissociation free-energy of isolated single and dimer PAGs in the different polymers indicates that PHS segments provide a better solvation environment for ionic PAGs than PtBMA segments and that the nonionic naphthalimide PAG has the highest dispersibility, while TPS-TFMeS solvates better than the bulkier TPS-NFBuS and TPS-ATFEtS salts. The dissociation free-energies were consistent with a trend of increasing PAG clustering in less polar media at high PAG concentrations (7 to 36 wt%), and of increasing dipole moments for PAGs in less polar implicit solvation media as estimated from density functional theory. Both simulations and infrared spectroscopy on the copolymer provide evidence of hydrogen bonded carbonyl groups whose prevalence diminishes upon the addition

of ionic PAGs. For TPS-TFMeS loadings between 25-29 wt%, our analysis revealed short string-like salt clusters in PHS homopolymer, large globular clusters in PtBMA homopolymer, and a heterogenous distribution of string-like and globular PAG aggregates in the alternating copolymer. In the case of polypeptoids with similar chemistries, the aggregation tendency of ionic PAGs depends on the sequence of side groups attached to the backbone atoms. For all PAG loadings, TPS-ATFEtS and TPS-NFBuS PAGs exhibited the highest extent of aggregation. In the case of polypeptoids with similar chemistries, the aggregation tendency of ionic PAGs depends on the sequence of side groups attached to the backbone atoms. Altogether, the advocated methodology is a potentially effective tool to rank and identify polymer and PAG chemistries with improved compatibility and mixing homogeneity.

1. Introduction

In the context of semiconductor manufacturing, downsizing the transistors in a circuit to sub-10 nm scales has been a key goal to attain the next level of device performance. Extreme ultraviolet (EUV) lithography has proven to be one of the promising tools to achieve such small device features by exposing chemically amplified resists (CAR) to EUV short-wavelength light sources [1–3]. These photoresists are a complex blend of components that includes the acid-sensitive polymer, photoacid generator (PAG), and photo decomposable quencher (PDQ). Chemical inhomogeneities in these mixtures are an aggravating factor that increases the likelihood of stochastic defects during lithography and decreasing inhomogeneity is one way to decrease defectivity. As target critical dimensions continue to shrink, understanding the dispersibility of PAGs and PDQs in the polymer base is important to minimize defects that may arise from PAG agglomerates which may affect line edge roughness (LER) and stochastic defects [4,5]. Many experimental [6–14] and molecular modeling [6,14–19] studies have mostly concentrated on the processes occurring during and post EUV exposure, e.g., to track chemical reactions that induce acid generation and estimate their effect on feature resolution and defects. Stochastic defects are inherent in the processing of photoresists even in the pre EUV exposure conditions where the intermolecular interactions among the polymer base, PAGs, and PDQs can lead to nano-segregated domains whose sizes are in the same order of magnitude as that of

the desired sub-10 nm features. Recent experimental work has begun to probe such intrinsic PAG inhomogeneities at a 10-15 nm feature scale in a photoresist film through a technique termed massive cluster secondary ion mass spectroscopy [20–24].

In this work, we focus on understanding the complex interactions between PAGs and polymer medium that occur at the pre EUV exposure conditions and examine the inherent inhomogeneities that may arise in the chemically amplified photoresist blend after spin coating and soft bake process (see Figure 1a). We hypothesize that predicting the solvation behavior of PAGs at infinite dilution, mainly single and dimer PAGs can provide a relative metric of dispersion quality in the polymer medium, i.e., how homogenously PAG disperses at high concentrations. To validate our hypothesis and also characterize the near-equilibrium nano structural organization of the PAGs in photoresists, we probed the affinity of ionic and nonionic PAG candidates in polypeptoids, poly(4-hydroxy styrene) (PHS) and poly(tert-butyl methacrylate) (PtBMA) homopolymer and the alternating copolymer therefrom (see Figure 1b) using atomistic molecular dynamics (MD) simulations. The PAG candidates chosen for this study are: ionic PAGs containing triphenyl sulfonium (TPS) cation with trifluoromethane sulfonate (TFMeS), nonafluorobutane sulfonate (NFBuS), perfluorophenyl sulfonate (PFPS), and adamantyltetrafluoroethyl sulfonate (ATFEtS) anions, and nonionic naphthalimide sulfonate PAG (see Figure 1c). The selected polymer and PAG chemistries are representative of commercially available chemically amplified resists and of recent studies focused on the complex reactions occurring in photoresists exposed to EUV radiation [13,14,25–27]. By choosing the above PAG chemistries, with their varying steric and ionic interactions, we are able to assess their effect on the interplay between PAG-PAG and polymer-PAG interactions.

The PHS-PtBMA alternating copolymer, wherein PHS and PtBMA segments are maximally interspersed and hence have minimal compositional segregation, was chosen for study as a limiting realization of realistic random copolymers. The random copolymer structure is representative of the polymers used in commercially available CAR materials which are typically comprised of a polar component like hydroxystyrene and a less polar deprotectable acrylic ester component. By probing the solvation behavior of PAGs in the homopolymers and their alternating copolymer media, our simulations provide the basis for understanding PAG aggregation in realistic random copolymer photoresists where PAGs will encounter local

environments intermediate between the extreme cases of homopolymer rich domains and alternating copolymer domains. To understand the intrinsic tendency of segregation between PHS and PtBMA chemistries we also analyzed the inhomogeneities present in both homopolymer blends and block copolymer. Using simulations and Fourier transform infrared (FTIR) spectroscopy experiments, we provide evidence of the hydrogen bonding interactions between PHS and PtBMA segments in the copolymer media.

To quantify the relative strengths of the polymer-PAG and PAG-PAG interactions, we implemented an enhanced umbrella sampling technique to calculate the potential of mean force (PMF) of single and dimer PAG dissociation in the different polymers. The dissociation free energy of a PAG, $\triangle G$, as obtained from the PMF, provides a direct measure of the solvation quality of the media wherein higher dissociation free energy indicates larger aggregation tendency, i.e., poor PAG solvation quality. $\triangle G$ values are not system-size dependent and can be used to estimate the dissociation rate, k_d of PAGs at infinite dilution through the Eyring equation's $k_d \propto \exp(-\triangle G/k_bT)$ where T is the temperature and k_b is the Boltzmann constant.

The trends observed for $\triangle G$ in different polymers were also validated by (i) estimating dipole moments of the associated salts in implicit and explicit polymer solvation medium using Density Functional Theory (DFT), and (ii) simulating concentrated PAG systems using MD. Overall, the trends observed for the high concentration PAG simulations with different PAG chemistries validate our hypothesis that $\triangle G$ obtained at the super dilute conditions can be used to predict the concentrated-PAG dispersion quality in the polymer media. The results from the PAG concentrated simulations also provide insights on the local hydrogen bonding interactions and how the local PAG solvation environment determines the shape and size of the PAG clusters. Using Flory-Huggins polymer solution theory, we also study the effect of temperature on the dispersibility of PAGs in different polymer media.

The outline of this paper is as follows. Section II details our overall simulation strategy, and methodology for PMF and dipole moment calculations using MD and DFT. Section IIIA present results quantifying heterogeneity in the polymer matrix without PAGs and provide evidence for hydrogen bonding between PHS and PtBMA, Section IIIB discusses the trends in dissociation free energies and solvation behavior of single and dimer PAGs in homopolymer and alternate copolymer media, and Section IIIC presents results for high PAG concentrations.

Finally, Section IV presents closing remarks and an outlook of our study.

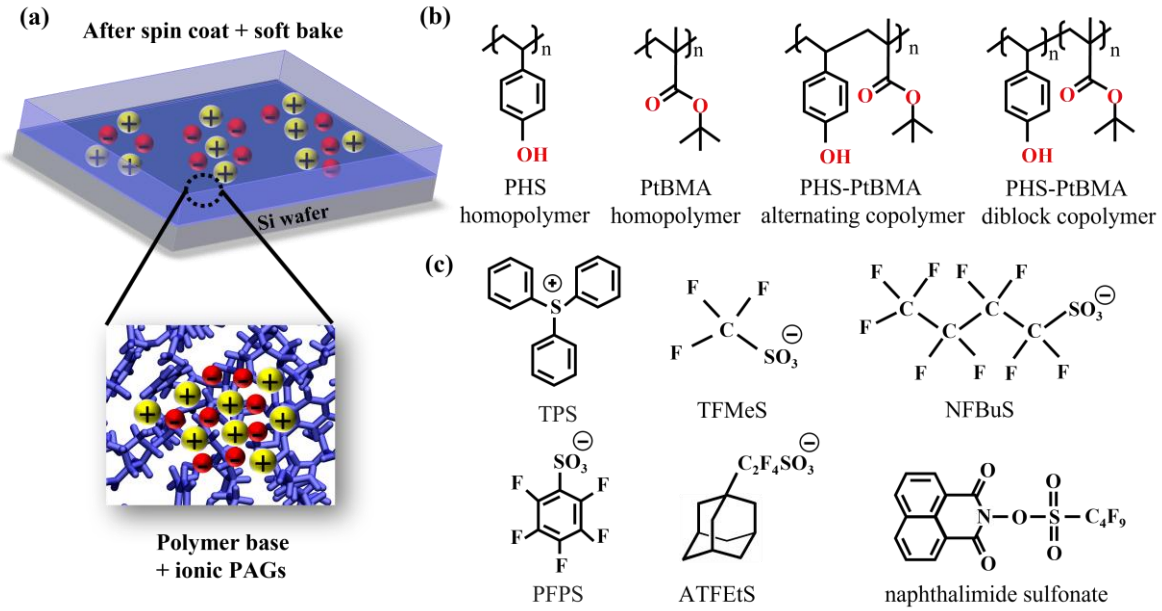

Figure 1. Representation of chemically amplified photoresist and chemical structures of simulated photoresist components. (a) Illustration of nonhomogeneous distribution of ionic PAGs (yellow and red spheres) in the polymer base (blue) after spin coating and soft bake. (b) Repeating units of n-mer PHS and PtBMA homopolymers, alternating and diblock copolymers. The polar oxygen and hydroxyl groups are colored red. (c) Ionic and nonionic PAG chemistries selected for this study. PHS = poly(4-hydroxy styrene), PtBMA = poly(tert-butyl methacrylate), TPS = triphenyl sulfonium, TFMeS = trifluoromethane sulfonate, NFBuS = nonafluorobutane sulfonate, PFPS= perfluorophenyl sulfonate, ATFEtS = adamantyltetrafluoroethyl sulfonate.

2. Methodology

2.1 Overall simulation strategy

In principle, simulations performed with random PHS-PtBMA copolymers at the experimentally relevant temperatures and PAG concentrations would provide a direct probe of PAG aggregation behavior. In practice, this is not a suitable strategy because: (i) The polymer

would be below its glass transition temperature, T_g where segmental mobility and relaxation are greatly arrested, (ii) statistics on PAG cluster sizes and morphologies would not be very reproducible and hence only be of qualitative value, and (iii) results would exhibit high variability depending on sequence used in the random copolymer. We addressed these issues as follows. First, we conducted all production simulations at 600 K (well above the polymers' T_g's) to allow timely thermal relaxation of the solvation environment around PAGs which would be expected to occur during the photoresist processing steps prior to EUV exposure. Second, we obtained the PAG dissociation free energy, $\triangle$G, from simulations at very dilute conditions, as these provide a distinct, quantitative, reproducible, and efficient metric that captures the solvation quality of the medium (i.e., lower ΔG indicating better solvation). We hypothesize that these $\triangle$G'*s* can fully capture the association tendencies of PAGs at high concentration. We then tested such a hypothesis by performing concentrated PAG simulations (also at 600 K) which although very expensive and largely qualitative, can corroborate the trends predicted by $\triangle$G. Third, by studying the well-defined alternating copolymer and the pure PHS and PtBMA polymers, we systematically probe the effect of the different limiting local environments that would be present in a random copolymer.

2.2 Molecular dynamics simulation model

In this study, we used an all-atom MD simulation to model the complex interactions within the photoresist components. We parameterized the interactions in PHS, and PtBMA homopolymers and copolymers, and different PAG chemistries (see Figures 1b and 1c) using optimized potentials for liquid simulations-all atom (OPLS-AA) [28–33]. We also modelled the polymer tacticity by adding an improper dihedral harmonic constraint to maintain the relative stereochemistry of adjacent chiral centers of pendant groups within the polymer chain. A detailed list of bonded and nonbonded parameters for all the polymer and PAG chemistries simulated is provided in Sec. I of the supplementary information (SI). The OPLS-AA model has been previously used to efficiently study the nano-scale structures, conformations, and dynamics of syndiotactic, isotactic, and atactic PMMA polymer melts within a classical description [29,34]. We parameterized the interactions in polypeptoid sequences using Chemistry at Harvard Macromolecular Mechanics (CHARMM) forcefield. We also incorporated the

correction factor in the Berthelot mixing rule between Hydrogen and Fluorine atoms to accurately describe the interactions of fluorinated compounds [24,35]. All MD simulations were performed in a cubic periodic box using Large-scale Atomic/Molecular Massively Parallel Simulator (LAMMPS 29th September 2021 version) open source package [36]. The timestep, δt for velocity-Verlet integration in both isothermal-isochoric (NVT) and isothermal-isobaric (NPT) simulations was set to 1 fs. The Nosé-Hoover thermostat and barostat[37–39] damping parameters were set to 0.1 ps and 1 ps, respectively. The compositions of alternating and diblock copolymers were fixed at 50% PHS and 50% PtBMA segments (see Figure 1b). Unless stated otherwise, all simulations with homopolymers and copolymers consist of 70 molecules of 12-mer polymer chains. The chosen length of the polymer was similar to the average length used in experiments[26,40,41] and simulations[15,18,42]. Figure S2 shows the simulated polymer chain structures in this work. In all the bulk homopolymer and copolymer simulations, the end-to-end distance between the terminal backbone carbon atoms of the chains is within 20-23 Å which is less than half the simulation box length that ranges between 58-60 Å. Figure S2 shows the simulated polymer and polypeptoid chain structures in this work.

To validate the forcefield, we estimated T_g for the homopolymers and alternating copolymer. These simulations were carried out by first generating a well equilibrated disordered initial configuration at 600 K (above T_g) by following a rigorous protocol mentioned in Sec. IIA in the SI. The generated configuration was then cooled from 600 K to 300 K in 25 K steps and 3 ns equilibration per step in an NPT ensemble at fixed pressure of 1 bar. The T_g values were estimated as the point where the trend of specific volume vs. temperature exhibits a change in slope or an inflexion[34,43–45]. We simulated isotactic, syndiotactic, and atactic PtBMA homopolymers to study the effect of tacticity on T_g values. Figure S9 in Sec. IIB in the SI shows the predicted T_g values and the mobility of polymer chains below and above T_g. We find that the simulated T_g for PtBMA is between 380-470 K depending on tacticity, with the observed trend being similar to experimental values of PMMA polymers where the T_g decreases going from syndiotactic to atactic to isotactic[34]. We also find that the T_g value for atactic PHS homopolymers is ~450 K (within the experimental range: 410 K-470 K[46,47]) and for atactic alternating copolymers is ~440 K.

We also analyzed the effect of segmental blocking at 300 K that can contribute to the nano-

segregations or heterogeneity in the polymer only medium (without PAGs). To compare the structural heterogeneity in PHS-PtBMA blends, alternating, and diblock copolymers we used the Ripley's K-function analysis [48] that provides both an extent-of-clustering parameter, K(r) and a clustering length scale:

$$\mathrm{K}(r) = \frac{1}{\rho N} \sum_{i=1}^{N} \sum_{j=1,\, j\neq i}^{N} I(r) \qquad (1)$$

where $\rho=N/V$ is the number density and N is the number of PHS or PtBMA atoms in a simulation box volume, V in Å^3. I(r) is the number of PHS or PtBMA atoms present within the sample volume of radius r. If atom positions were homogenously distributed (following a Poisson distribution), the values of K(r) would vary as ~$4/3\pi r^3$, and positive or negative deviations from this ideal scenario indicates clustering or dispersion of atoms, respectively. Simulations for analyzing polymer heterogeneity were carried out with atactic diblock and alternating copolymers and 140 molecules for equimolar blend of atactic 6-mer PHS and 6-mer PtBMA (see Figure S2).

2.3 Dissociation and aggregation simulations

The free energy for dissociation of a single PAG, $\triangle G_S$, and a PAG dimer, $\triangle G_D$, in the polymer medium was estimated as the difference between the maximum and minimum free energy values (representing the dissociated and associated states, respectively) from the PMF curve found via the umbrella sampling technique (US). To improve the sampling of configurations across different US windows we implemented the Hamiltonian Replica Exchange (HREX) [49] method at constant temperature and pressure; this required a modification of the LAMMPS source script. We simulated one and two PAG molecules in atactic alternating copolymer, and atactic homopolymers of PHS and PtBMA. To validate our PMF methodology, we also simulated the dissociation of TPS-TFMeS PAG in a nonpolar 12-mer atactic polystyrene (PS) homopolymer, which is expected to give the highest $\triangle G$ compared to the other polymers studied in this work (see Figure S2h for PS chain structure). The probability distributions obtained for the series of umbrella windows are combined using the weighted histogram analysis method (WHAM) and error bars were computed using the bootstrapping technique [50,51]. For the (cation-anion dissociation) PMF of a single ionic PAG, we chose the distance, r_{SO}

between the center of masses of the sulfur atom in TPS cation and the oxygen atoms in TFMeS, NFBuS, and ATFEtS anions as the reaction coordinate that separates the associated and dissociated states for single PAG. A similar reaction coordinate was used to study the dissociation of electron attached TPS-TFMeS PAG in vacuum [15]. For the PMF of PAG dimers, we selected the center of mass distance, $r_{PAGscom}$ between the two PAGs as the reaction coordinate. The simulated system sizes were large enough to avoid any unphysical long ranged coulombic interactions with the periodic images when the PAGs are dissociated. More details on the protocol for implementing HREX simulations are provided in Sec. IIC in the SI. PMF calculations for PAG singlets and dimers in vacuum were also performed to understand the effect of the polymer medium on dissociation.

To probe the aggregation tendency of PAGs at high concentrations, we simulated mixtures of 50, 100, 150, and 200 PAGs in 140 12-mers of atactic alternating copolymer, and homopolymers of PHS and PtBMA. These choices correspond to PAG concentrations ranging between 7 to 36 wt% which align with experimental PAG loadings [13,25]. We also probed the variation in the extent of hydrogen bonding interactions between PHS and PtBMA due to the presence of PAGs in the alternating copolymers. To obtain representative structures at different PAG loadings, we followed a rigorous equilibration routine which includes a series of energy minimization, compression/decompression, and annealing steps [52–54] (see Sec. IID in the SI for more details). These steps were particularly important to achieve near-equilibrium structures by minimizing local kinetic traps or defects (like void pockets). The consistency of the results for all PAG loadings was checked by simulating three MD runs with different initial configuration and random seeds to initialize the atomic trajectories.

2.4 Estimating dipole moments using ab initio calculations

We computed the dipole moment, D of a single associated PAG molecule in different implicit solvation environment using a polarizable continuum model (PCM) [55–57] in the open source GAMMES package [58]. PCM captures the effective electrostatic interactions between a continuum (or implicit) dielectric solvent and a quantum mechanical description of a solute molecule (i.e., a PAG). We selected benzyl methanol and butyl acetate implicit solvation models with the dielectric constant of 12.5 and 5, respectively, as they closely match the

pendant group chemistries in PHS and PtBMA homopolymers. These solvent models include the quantum mechanical density of the PAG for electrostatic calculations[56]. For the PHS-PtBMA alternating copolymer, we used the explicit polymer environment around the associated TPS-TFMeS PAG to estimate the dipole moment. The protocol for these calculations is described in the SI Sec. IIE.

2.5 Resist formulation and FTIR measurements

Two resists were prepared by spin-casting onto bare silicon wafers and subjected to pre-exposure baking at 110℃ for 1 minute. The first resist consisted of pure 40:60 random copolymer of PHS-PtBMA, while the other consisted of the same copolymer with a 20wt% TPS-PFPS PAG loading. We obtained the spectral intensities of the C=O stretching bands for the two resists through transmission IR spectra. These IR spectra were compared to quantify the effect of PAGs on hydrogen bonding between PHS and PtBMA segments.

3. Results and discussions

3.1 Quantifying heterogeneity in the polymer matrix without PAG

In this section, we study the intrinsic nano segregation of PtBMA and PHS segments within the polymer matrix (in the absence of any PAGs) for alternating copolymer, diblock copolymer, and blend systems, as any such segregation can be a factor contributing to the ensuing heterogeneity in the distribution of PAGs. Indeed, the structure of the polymer and the compatibility of its pendant group chemistries largely influences the solvation and post-EUV activation of PAGs, which is one of the crucial steps that controls LER in the final features.

3.1.1 Copolymers minimize spatial heterogeneity

Figures 2a to 2c show the structures for the simulated systems at 300 K. Visually, the level of segregation for the blend system, which shows well-defined PtBMA and PHS domains, is larger than that for the alternating copolymer, with the diblock copolymer showing an intermediate level of domain segregation. For the alternating copolymer, we observed smaller nanodomains of PHS and PtBMA rich segments that are randomly distributed throughout the simulation box. These observations are consistent with the estimated Flory's mixing parameter of $\chi N = 7.3$ for the PHS and PtBMA polymers from the Hildebrand-Scott equation, which is close to the $(\chi N)_{ODT} = 10.5$ [59,60] (for the symmetric diblock copolymer) indicating that the PHS and PtBMA are moderately incompatible.

Figure 2d shows the variation of Ripley's K(r) values (see Eq. 1) with the sample radius, *r* for the diblock and blend systems relative to the alternating copolymer system ($K_{alt}(r)$), chosen as reference, because in that case the PHS and PtBMA segments are nearly well dispersed (see Figure S10 in Sec. III in the SI). The blends have higher relative K values indicating higher clustering of PHS and PtBMA atoms with a well-defined interfacial boundary while the diblock has expectedly lower values indicative of increased spatial homogeneity relative to the blends. In both blend and diblock cases, we observed a higher $K(r)-K_{alt}(r)$ values for PHS compared to PtBMA indicating that the PHS segments have higher packing density (higher number of atoms in a given volume) compared to PtBMA segments. The *r* values corresponding to the maximum $K(r)-K_{alt}(r)$ mark the correlation lengths of the cluster domains. For the blends we estimated an average PHS and PtBMA cluster domain size of ~18.0 Å which is greater than the average end-to-end distance of PHS and PtBMA chains (i.e., ~13.5 Å). For the diblock copolymer system, the characteristic domain length scale is between 11.5-12.0 Å that roughly corresponds to the average end-to-end distance of the chains (see Figure S11 in Sec. IV in the SI), with a small depletion ($K(r)-K_{alt}(r) < 0$) zone of PHS and PtBMA segments at $r > 20$ Å which suggests segregated domains like in the blend system (although at smaller length scale).

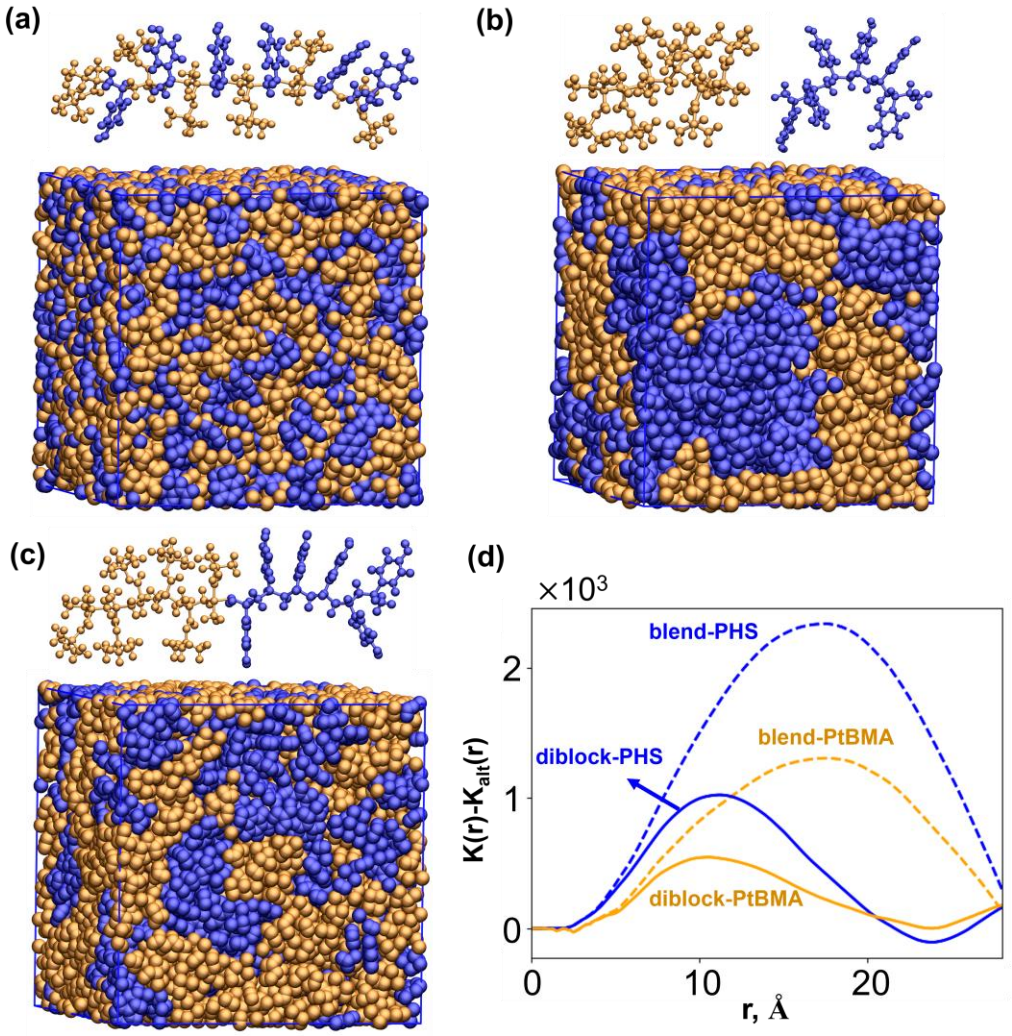

Figure 2. Simulation snapshots for PHS-PtBMA (a) alternating, (b) blend, and (c) diblock systems at 300 K. The cubic simulation box length is between 54-58 Å. The PHS and PtBMA atoms are colored blue and light orange, respectively. (d) Ripley's K-function analysis for PHS (blue) and PtBMA (light orange) segments in the blend (dashed lines) and diblock copolymer (solid lines). The effective K-function values are estimated relative to the alternating copolymer.

3.1.2 Hydrogen bonding between PHS and PtBMA segments enhance matrix homogeneity

We probed hydrogen bonding interactions between the polar groups in PHS and PtBMA segments in the copolymer media as these are experimentally detectable by IR spectroscopy. We identified the hydrogen bonds by estimating the spatial time averaged density, $\rho g(r)$, between H-H atoms in the phenol groups, H-O atoms in the phenol and carbonyl groups, respectively (see Figure 3a and Figure S12a in Sec. V in the SI). This analysis indicates that the nearest neighbor distance between H-O atoms in the phenol and carbonyl groups is about 1.9 Å and closer than the H-H distance (~2.5 Å) between the phenol groups. The presence of hydrogen bonded carbonyl groups was corroborated through FTIR measurements where we observed two distinct C=O stretching bands at 1720 cm^{-1} and 1696 cm^{-1} for the PHS-PtBMA random copolymer film (see Figure 3b). Figure 3c and Figure S12b in the SI show a simulation snapshot of hydrogen bonding in the alternating copolymer matrix; similar interactions were observed in the diblock copolymer. Due to the proximity of PHS and PtBMA segments in the alternating copolymers, we estimated ~ 37% increase in the concentration of H-O interactions between the phenol and carbonyl groups as compared to the diblock case (see Figure 3a). This increase in the H-O interactions improves mixing between PHS and PtBMA segments in their respective nanodomains, countering the aggregation tendency between like-polymer segments (PHS-PHS and PtBMA-PtBMA).

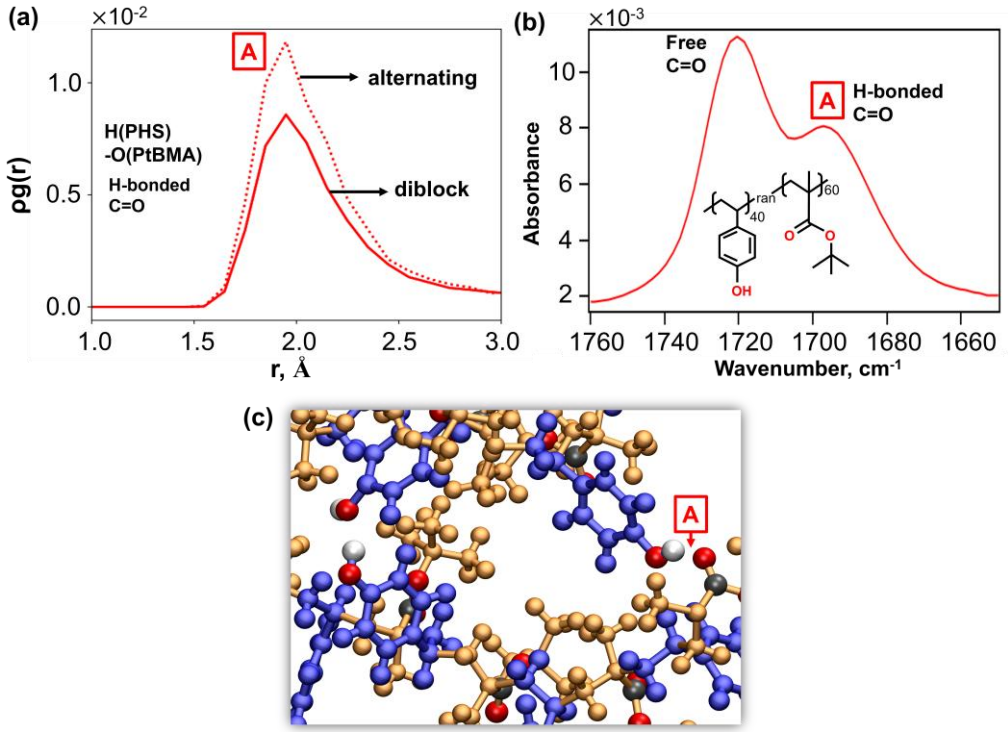

Figure 3. (a) Time averaged density, ρg(r), obtained from MD simulations between H-O atoms (blue) in phenol and carbonyl groups, and between H-H atoms (red) in phenol groups for the structure formed by diblock (solid lines), and alternating (dotted lines) copolymers at 300 K. (b) IR spectra for random copolymers showing two distinct C=O stretching bands at 1720 cm^{-1} and 1696 cm^{-1} for PHS-PtBMA film (red). (c) Local environment for alternating copolymer shows hydrogen bonding between phenol groups in the PHS segments (blue) and between H-O atoms in PHS phenol and PtBMA carbonyl groups (light orange); functional group carbon, hydrogen, and oxygen atoms are colored gray, white, and red, respectively. The boxed letter A marks the hydrogen bonding.

3.1.3 Dissociation free energies of single and dimer PAGs

The PAG dissociation free energy for a single PAG $\triangle G_S$, and dissociation free energy for a dimer, $\triangle G_D$, depend on the interplay of two main opposing forces: (i) Cation-anion attraction in a single PAG or PAG-PAG attraction in a PAG dimer, and (ii) interactions between PAG and polymer that promote PAG solvation and dissociation. In this section, we probe the relative strength of the above competing interactions by extracting $\triangle G_S$ and $\triangle G_D$ from the PMF in different polymer media and use them to understand the key interactions in the PAG solvation

environment. The $\triangle G_S$ and $\triangle G_D$ barriers are shown in Figure 4 with their numerical values provided in Table S36 and the PMF curves in Sec. VI of the SI.

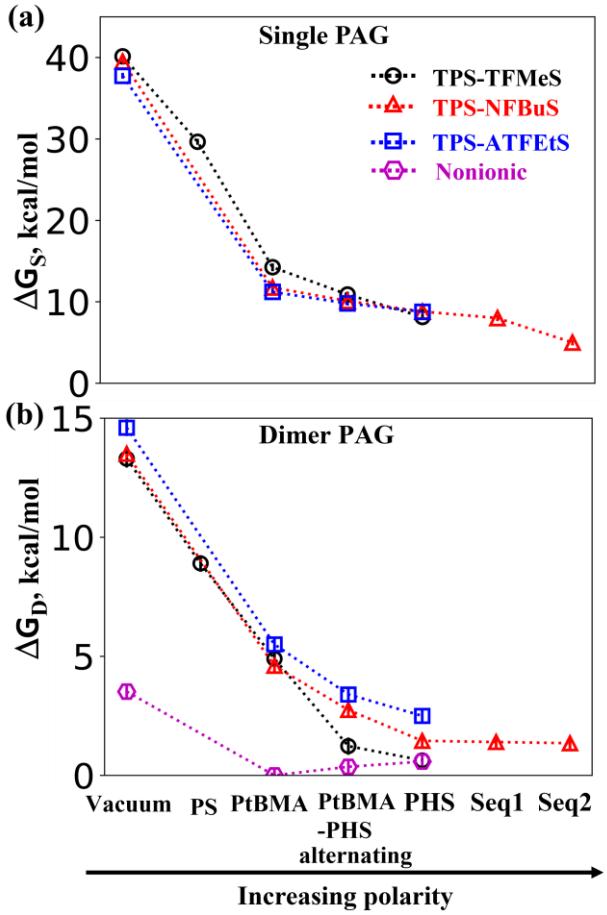

Figure 4. Dissociation free energy of single, $\triangle G_S$ (a) and dimer, $\triangle G_D$ (b) for TPS-TFMeS (black circles), TPS-NFBuS (red triangles), TPS-ATFEtS (blue squares), and nonionic naphthalimide (magenta hexagons) sulfonate PAGs in vacuum, polypeptoids sequences (Seq1 and Seq2), PHS-PtBMA alternating copolymer, and homopolymers of PS, PHS, and PtBMA. Error bars are from bootstrapping technique.

3.2 Single and dimer PAGs in vacuum have the highest ionic bond strengths

We first estimated the association strengths of the PAG singlet and dimer without any influence of the solvation medium, i.e., in vacuum. We found that the $\triangle G_S$ and $\triangle G_D$ for ionic TPS-

TFMeS, TPS-NFBuS, and TPS-ATFEtS PAGs are between 38-40 kcal/mol and 13-15 kcal/mol, respectively (see Figure 4). As expected, $\triangle G_S$ is much greater (~2.5-3.0 times) than $\triangle G_D$ due to the strong electrostatic interactions between cation's TPS sulfur and the anion's sulfonate oxygen that stabilize the associated state. Since the nonionic naphthalimide PAG has the least electrostatic strength to associate, its $\triangle G_D$ values were about 75% smaller than those of the ionic PAG dimers. The PMF profiles for the single and dimer PAGs are shown in Figures S13 and S14 in Secs. V1A and VIB in the SI. The profiles for the single ionic PAGs show two potential wells roughly at r_{SO} distances of 3.5-4.0 Å and 5.0-5.3 Å, respectively, with a difference between well depths less than 0.5 kcal/mol, indicating that both states have similar likelihood. The associated PAG structure at the first and second wells have different orientations of the TPS cation relative to the anion (see Figure S13 for representative MD snapshots). In the first 3.5-4.0 Å well, the closeness of the TPS sulfur and sulfonate oxygen atoms causes the TPS phenyl rings to orient away from the anion, whereas in the second 5.0-5.3 Å well hydrogen bonding between sulfonate oxygen and TPS hydrogen atoms pull the TPS phenyl rings towards the anion. These two associated configurations closely match the isolated PAG associated structures predicted using DFT methods [15,61,62].

3.3. Low polar media and bulky ionic PAGs favor associated dimer state

PAG dissociation in polymer media yields $\triangle G_S$ and $\triangle G_D$ barriers that are 8-32 kcal/mol and 3-15 kcal/mol smaller than those in vacuum, respectively (see Figure 4). This bond strength reduction occurs due to the favorable electrostatic interactions between the polar groups in the polymer and PAG that facilitate dissociation. Figures S15 and S16 in the SI show the full PMF profiles for single and dimer PAGs in PHS and PtBMA homopolymers and alternating copolymer media.

For ionic PAGs both $\triangle G_S$ and $\triangle G_D$ in pure PHS are lower than those in pure PtBMA, while they have intermediate values in the alternating copolymer. This indicates that the polar hydroxyl groups in PHS are more effective than the less polar carbonyl groups in PtBMA in facilitating cation-anion or PAG-PAG dissociation. Ionic PAGs have the highest $\triangle G_D$ values ranging between 4.6-5.5 kcal/mol with a deeper potential well in PtBMA homopolymer. In the alternating copolymer and PHS homopolymer, the bulky TPS-ATFEtS PAG has the highest

$\triangle G_D$ value, the smaller TPS-TFMeS PAG has the lowest, and the TPS-NFBuS PAG has an intermediate $\triangle G_D$ value. The dissociation strengths of single and dimer TPS-NFBuS PAGs in polypeptoid sequences are comparable to the PHS homopolymer indicating the polar nature of peptoid backbones. Slightly lower PAG strength for the single TPS-NFBuS PAG case suggests that the polypeptoid with sequence 2 is more polar compared to sequence 1. Our PMF calculations capture the screening effect of bulky hydrophobic side groups on the electrostatic interactions between the ionic PAG and polar hydroxyls in PHS. This screening is more pronounced in dimers, compared to a single PAG, due to the doubling in the number of side groups in the associated state.

For the nonionic naphthalimide PAG, the dimer dissociation has hardly any energetic cost (i.e., $\triangle G_D < 0.6$ kcal/mol) in all the media tested (see Figures 4b and S16a). The PMF profiles show a relatively flat profile for $r_{PAGscom} > 12.5$ Å in PtBMA homopolymer and for 7.5 Å$< r_{PAGscom} <15$ Å in PHS homopolymer and the alternating copolymer with the interactions becoming repulsive for smaller $r_{PAGscom}$ values, indicative of a tendency to disfavor PAG aggregates. We observed a very small increase (less than 0.6 ± 0.3 kcal/mol) in $\triangle G_D$ for PHS homopolymer and the alternating copolymer, likely due to relative orientations between the naphthalimide rings that allow more favorable interactions with the PAG polar groups (see Figure S16b).

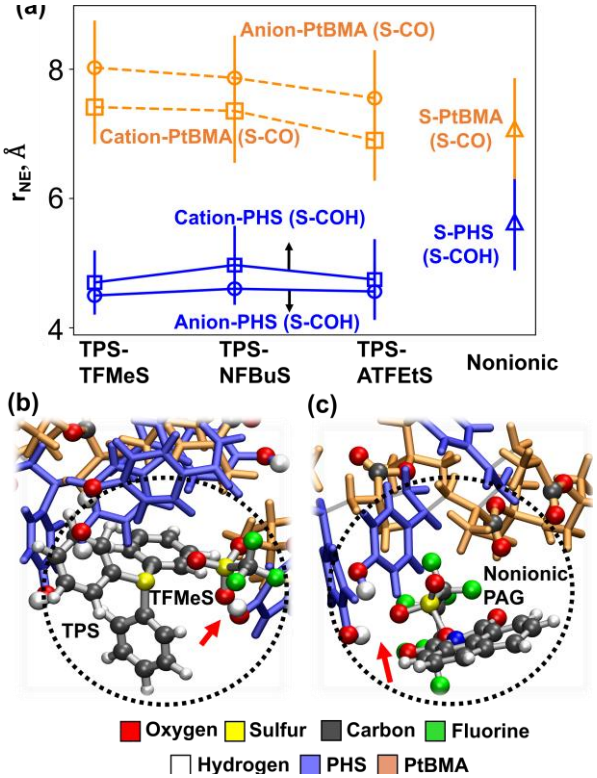

Figure 5. Solvation calculations for associated single PAGs in alternating copolymer. (a) Time average nearest distances, r_{NE} from MD simulations between anion (circle)/cation (square)/nonionic (triangle) sulfur atoms in a single PAG and functional-group carbon atoms in PHS (solid blue lines) and PtBMA (dashed orange lines). Error bars are also shown. Representative snapshot of a TPS-TFMeS PAG (b) and a nonionic PAG (c) surrounded by PHS and PtBMA segments. The associating atoms are encircled, and the red arrows show the hydrogen bonding interaction.

3.4 Hydrogen bonding interactions mediate solvation of PAG by PHS polar groups

The competing hydrogen bonding interactions between the PAG and the polar groups in PHS and PtBMA segments were probed by estimating the average nearest distance, r_{NE} between sulfur atoms in PAG and carbon atoms in the hydroxyl and carbonyl groups of the alternating copolymer. Figure 5 shows these statistics as obtained from the last 3 ns of a 10 ns NPT simulation of the associated PAG singlet corresponding to the first PMF well (corresponding probability distributions are shown in Figure S17). Figure 5a shows that the r_{NE} between sulfur

atom in TFMeS, NFBuS, and ATFEtS anions and the hydroxyl group is ~ 4.5-4.6 Å [27] which is lower than the r_{NE} between the anion sulfur and carbonyl group that ranges between 7.5-8.0 Å. Given the strong anion-cation attraction and co-localization, a similar trend was observed for the TPS cation where the TPS-hydroxyl distance is about 2.0-3.0 Å shorter than the TPS-carbonyl distances. Also, the bulkiness of the tertiary butyl groups in the PtBMA pendant chains tends to screen the electrostatic interactions between negatively charged oxygen atoms in the carbonyl group and positively charged sulfur atoms in the TPS cation. We observed similar trends for r_{NE} whether the associated PAG state was taken to be at the first PMF well (at r_{so} ~ 3.6-4.3 Å) or the second well (at r_{so} ~ 5.5-6.2 Å, see Figure S18).

For the single nonionic PAG in the alternating copolymer, we observed that the r_{NE} distance for sulfur-hydroxyl is larger compared to the ionic PAG cases, indicating a comparatively weaker tendency to hydrogen bond with the PHS hydroxyl groups. The difference between sulfur-hydroxyl and sulfur-carbonyl r_{NE} distances is about ~1.4 Å which is about half that for the ionic PAG cases implying that the nonionic PAGs have almost no preference for interacting with either PHS or PtBMA polar groups. Figures 5b and 5c show sample configurations depicting the interactions between the sulfonate oxygen and PHS hydroxyl groups for the single associated TPS-TFMeS PAG and single nonionic PAG.

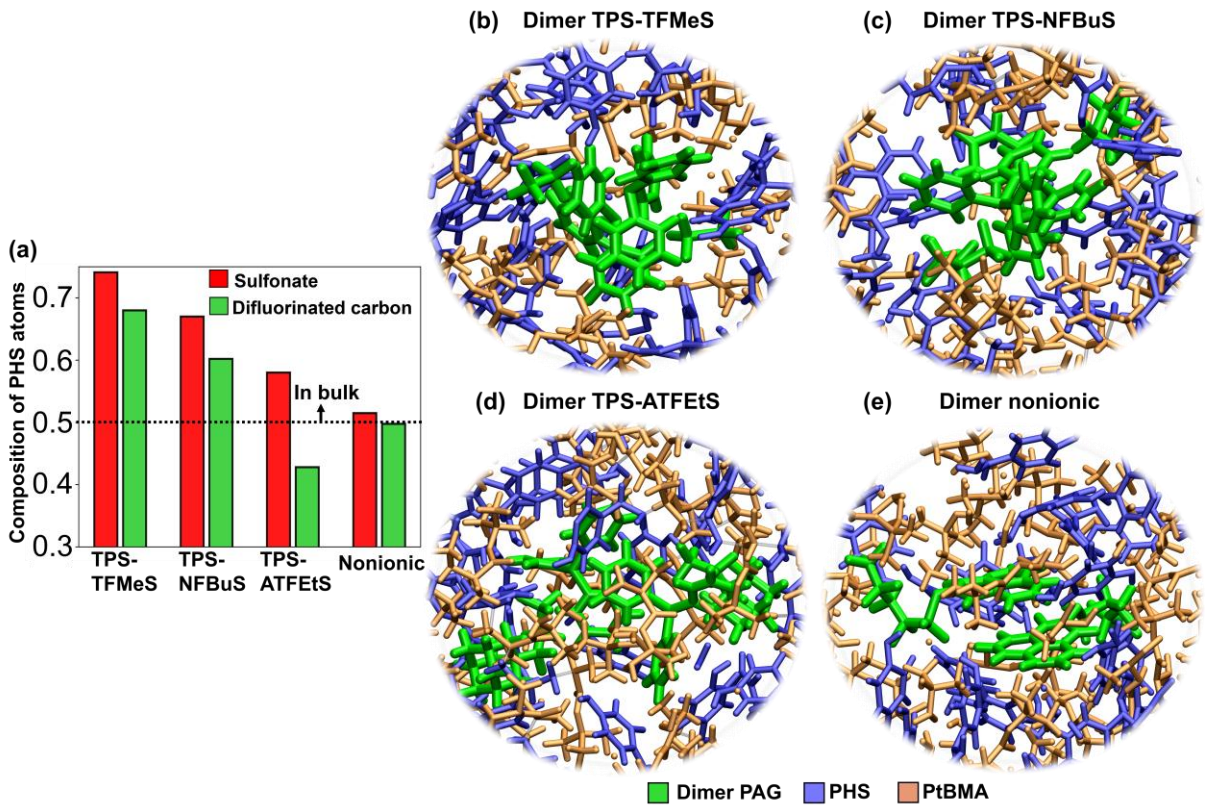

Figure 6. Solvation of associated dimer PAGs in alternating copolymer. (a) Composition of PHS atoms within 8 Å radial distance around sulfur and terminal difluorinated carbon of TFMeS, NFBuS, ATFEtS, and nonionic dimer PAGs. The dashed line indicates the bulk PHS composition. (b-e) Representative simulation snapshots showing the local environment (< 10 Å) of dimer PAGs (green). The atomic color scheme is shown at the bottom.

3.5. Bulky PAGs with hydrophobic side group hinder solvation by polar PHS segments

Although the sulfonate oxygen in the ionic PAGs has a relatively stronger attraction towards the PHS hydroxyl group than the PtBMA carbonyl group, changing the PAG side group chemistry affects the effective solvation environment around the PAG. To understand this effect, we calculated the composition of PHS atoms excluding the hydrogens bonded to carbons in the alternating copolymer within 8 Å radial distance around the polar sulfur and hydrophobic terminal difluorinated carbon (CF_2) groups in the PAG associated (see Figure 6a). The compositions were averaged over the last 3 ns from 10 ns NPT simulation run.

As shown in Figure 6a, smaller TPS-TFMeS PAG had ~68-74% of PHS atoms around the polar sulfonate and hydrophobic CF2 groups which is about 1.4-1.5 times the bulk composition. In contrast, making the anions bulkier with hydrophobic side groups in TPS-NFBuS and TPS-ATFEtS PAGs, leads to a ~10-20% and 12-37% decrease in the composition of PHS atoms around the sulfonate and CF2 groups, respectively. Since any change in the solvation-shell PHS composition is accompanied by the opposite change in PtBMA composition, these results indicate that having a hydrophobic bulky side group in PAGs allows them to be better solvated by the more hydrophobic PtBMA groups (like t-butyls and chain backbone) than by the more polar PHS segments. A complementary analysis based on the local densities of PHS and PtBMA segments is given in the SI (Figure S19). Overall, the trends observed in the solvation behavior for different ionic PAGs aligns with the predicted $\triangle G_S$ and $\triangle G_D$ trends where we see a higher drop in dissociation barrier from PtBMA to PHS homopolymers for TPS-TFMeS as compared to TPS-NFBuS and TPS-ATFEtS (see Figure 4).

For the nonionic PAG, the dimer has similar preference for (mixes equally well with) both PHS and PtBMA, exhibiting a similar solvation shell peaking at ~10-12 Å (see Figures S19a and S19b in the SI) and also compositions close to the bulk. Figures 6b to 6e show representative snapshots of associated ionic PAGs and nonionic PAG dimers solvated by PHS and PtBMA segments. We can visually discern that the number of PtBMA atoms increases in the solvation shell for the bulkier TPS-ATFEtS and TPS-NFBuS as compared to the smaller TPS-TFMeS, while for nonionic PAG dimers, both PHS and PtBMA atoms participate in the solvation shell.

3.6. Validating the PMF framework using MD and DFT methods

As a first test of the proposed PMF methodology, we estimated $\triangle G_S$ and $\triangle G_D$ from HREX MD simulations for TPS-TFMeS PAG in PS homopolymer where we expect a higher barrier compared to PHS and PtBMA homopolymers. The results in Figure 4 and Figure S20 in the SI show an increase of about 15.5 kcal/mol and 4 kcal/mol in $\triangle G_S$ and $\triangle G_D$ barriers, respectively, compared to the PtBMA homopolymer. This suggests that PS segments in any polymer medium will hinder the dispersibility of ionic PAGs, which is consistent with reported experimental observation of a higher fraction of perfluoro ionic PAG aggregates in a polymer containing PS and/or acrylic segments [20,63].

In the second consistency test, we calculated the effective dipole moment of the single nonionic and associated ionic PAGs in implicit and explicit solvation medium from DFT methods (see Sec. IIE for more details) where a higher dipole moment in low-polar solvation medium would be expected to correlate with higher $\triangle G_D$ barriers from HREX MD simulations. A similar trend was also observed in a salt-doped polymer electrolyte system where decreasing the polymer polarity led to the formation of larger Li-TFSi aggregates[64].

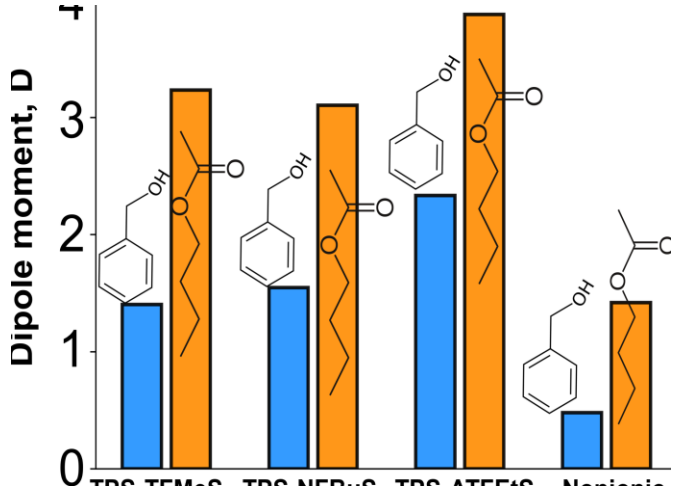

Figure 7. Dipole moments from DFT implicit-solvation model for the single associated ionic and nonionic PAGs in benzyl methanol (blue) and butyl acetate (light orange). The chemical structures of the solvent media are shown.

Figure 7 shows the variation of dipole moment for the ionic PAGs in the implicit benzyl methanol and butyl acetate solvation medium. Note that besides embodying similar pendant group chemistries in PHS and PtBMA, benzyl methanol and butyl acetate also have a contrast in polarities similar to the PHS and PBA homopolymers whose dielectric constants for 1kHz and room temperature are 9.5 and 4.4, respectively [65,66]. Figure 7 shows that the dipole moment of the ionic PAGs is higher in the implicit butyl acetate medium (> 3 D) than in benzyl methanol (< 2 D). This aligns with the trends observed for $\triangle G_D$ (Figure 4b) where the ionic PAGs were found to have higher $\triangle G_D$ in PtBMA than in PHS homopolymer. We also captured the effective change in the dipole moment for PAGs with bulky hydrophobic groups where we estimated an increase of ~10% and 65% in the dipole moment in the more polar benzyl methanol for TPS-

NFBuS and TPS-ATFEtS compared to TPS-TFMeS (see Figure 7). The dipole moment in the alternating copolymer, calculated with explicit chains around a single associated TPS-TFMeS PAG, was found to have an intermediate value compared to those of the homopolymers (see Figure S21 in the SI).

For the nonionic PAG, we observed an overall decrease in dipole moment compared to the ionic PAGs for both benzyl methanol and butyl acetate media (see Figure 7) corroborating the observed decrease in ΔG_D barriers. Although the PMF for the nonionic PAG is barrier-less, we observed a higher dipole moment (~1.4 D) in butyl acetate than in benzyl methanol (~0.5 D).

4. High PAG concentrations in homopolymers and alternating copolymer

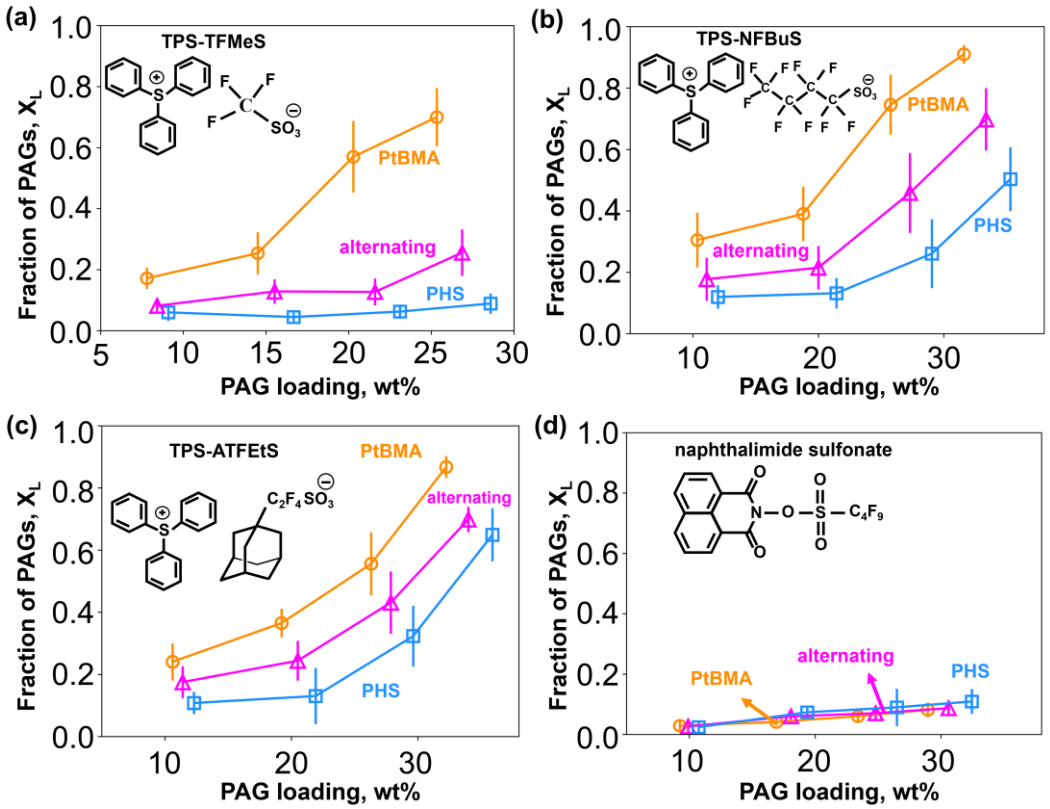

Figure 8. Fraction, X_L of (a-c) ionic and (d) nonionic sulfonate PAGs in the largest cluster for different PAG wt% loadings in PHS (cyan square), PtBMA (orange circle) homopolymers, and alternating copolymer (magenta triangle). Error bars are also shown.

4.1 PAG aggregation at high concentrations follows trends predicted by ΔG_D

To validate our hypothesis that the trends observed in super dilute $\triangle G_D$ can be correlated to the PAG aggregation behavior at high concentrations, we carried out simulations for 7-36 wt% PAG systems as described in Sec. IID in the SI. We evaluated the extent of PAG aggregation by grouping the centers of mass of anion and cation for the ionic PAGs and the PAG molecule for the nonionic PAG within the cutoff distance, r_c and recursively constructed the connected clusters till all the centers of mass are accounted for. For ionic PAGs, we chose r_c values of 7.25 Å, 8.3 Å, and 8.5 Å for TPS-TFMeS, TPS-NFBuS, and TPS-ATFEtS, respectively, which correspond to the minimum after the first peak in the radial density distribution of anions and cations (see Figure S22a). For the nonionic PAG, we selected r_c of 9.5 Å corresponding to the position of first peak in the PAG center of mass radial density distribution function (see Figure S22b).

Figure 8 shows representative fractions of PAGs in the largest connected cluster, X_L for different PAG loadings. For the ionic PAGs, we observed that for any PAG loading the X_L value is higher in PtBMA homopolymer than in PHS homopolymer, having an intermediate value for the alternating copolymer (see Figures 8a to 8c). In the PtBMA homopolymer, X_L increased sharply for ionic PAG loadings > 15-20 wt% and reached up to values between 0.6-0.9 at the highest PAG loading. For TPS-TFMeS PAG, we observed a relatively flat profile with $X_L < 0.25$ in the PHS homopolymer and alternating copolymer media. For the bulky TPS-NFBuS and TPS-ATFEtS PAGs, the size of the largest cluster increased with increasing PAG loading for all polymers and at concentrations between 30-35wt%, X_L varied between 0.5-0.6 even in the PHS homopolymer.

Representative simulation snapshots show the four largest clusters for the mixtures containing 200 TPS-TFMeS (Figures 9a-9c), 200 TPS-NFBuS (Figures 9d-9f), and 200 nonionic (Figures 9g-9i) PAGs in 140 polymer molecules (note that this fixed molar composition generates slightly different wt% PAG loadings). The snapshots for TPS-ATFEtS PAG are shown in Figure S23 in the SI. It is seen that TPS-TFMeS forms small PAG clusters in pure PHS that are distributed randomly throughout the simulation box; in contrast, it forms a large PAG segregated cluster in pure PtBMA. The bulky TPS-NFBuS and TPS-ATFEtS PAGs, having a stronger tendency to form dimers, form large percolating networks of PAG aggregates in all the polymer media. Nonionic PAGs in homopolymer and alternate copolymer media form well

dispersed small-size clusters with $X_L \leq 0.1$ for all PAG concentrations (see Figure 8d).

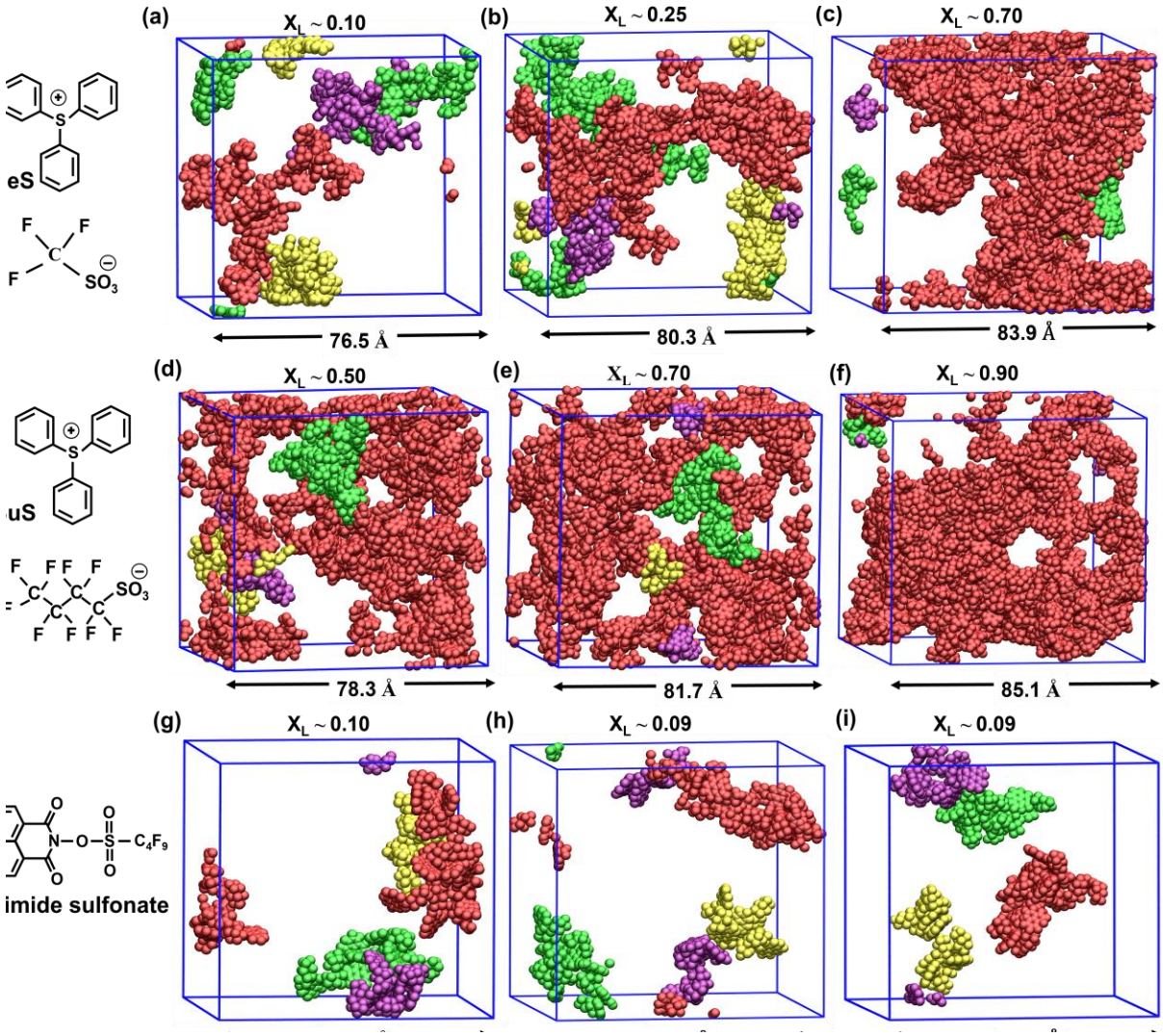

Figure 9. Representative simulation snapshots of cubic periodic box showing the first (red), second (green), third (purple), and fourth (yellow) largest PAG clusters formed in a mixture of (a-c) TPS-TFMeS (25-29 wt%), (d-f) TPS-NFBuS (31-35 wt%), and (g-i) nonionic naphthalimide sulfonate (28-33 wt%) PAGs in PHS homopolymer, alternating copolymer, and PtBMA homopolymer. The polymer chains are not shown for clarity. The fraction, X_L of PAGs in the largest red cluster and box dimension are also shown.

4.2 PAG aggregation, solubility, and effect of temperature

Our high PAG concentration results from Sec. C1 allows us to roughly estimate the limiting solubility of PAGs in different polymer media; these data can be used to parameterize an equation of state model to estimate, e. g., the effect of temperature on the dispersibility of PAGs. We illustrate this approach using the Flory-Huggins (FH) theory for polymer solutions[67–69] for the case of TPS-NFBuS PAG in PHS and PtBMA homopolymers and their alternating copolymer. Accordingly, first the PAG solubility limit, X_{PAG} was estimated from MD simulation data at 600 K as the PAG composition where $X_L \sim 0.5$ (see Figure 8b) and used to obtain an effective Flory's χ parameter for the polymer-PAG pair at hand; the resulting FH model is then used to calculate the phase boundaries at different temperatures above T_g (> 430 K) (see Sec.VIIC in the SI for details).

Figure 10 shows the binodal and spinodal TPS-NFBuS composition bound for varying temperature for the different polymers. We expectedly find that in all cases the predicted stability range of the well mixed (or the two-phase) region becomes narrower (or wider) with decreasing temperature. The range of PAG loading in the well-mixed stable region is widest for PHS (6-15 wt%), narrowest for PtBMA (1-3 wt%), and intermediate for the alternating copolymer (3-8 wt%) (see Figure 10). These differences reflect a larger effective FH χ parameter between the PAG and the different polymers (see Table S39 in the SI), consistent with the clustering trends in Figure 8b. Increasing PAG loadings near or beyond the spinodal boundary increases the segregation tendency (or X_L) resulting in percolating networks of PAG aggregates (see Figure 8b, Figure 9d-9f, and Figure 10). We note here that the phase boundaries in Figure 10 are sensitive to the choice of X_{PAG} and the empirical models that correlate χ with temperature (see Sec.VIIC in the SI); however, the qualitative trends of PAG solubility in different polymer media will remain unchanged. Phase diagrams for other aggregating PAGs can be similarly generated (e.g., from the data in Figures 8a and 8c) and expected to show trends similar to those in Figure 10.

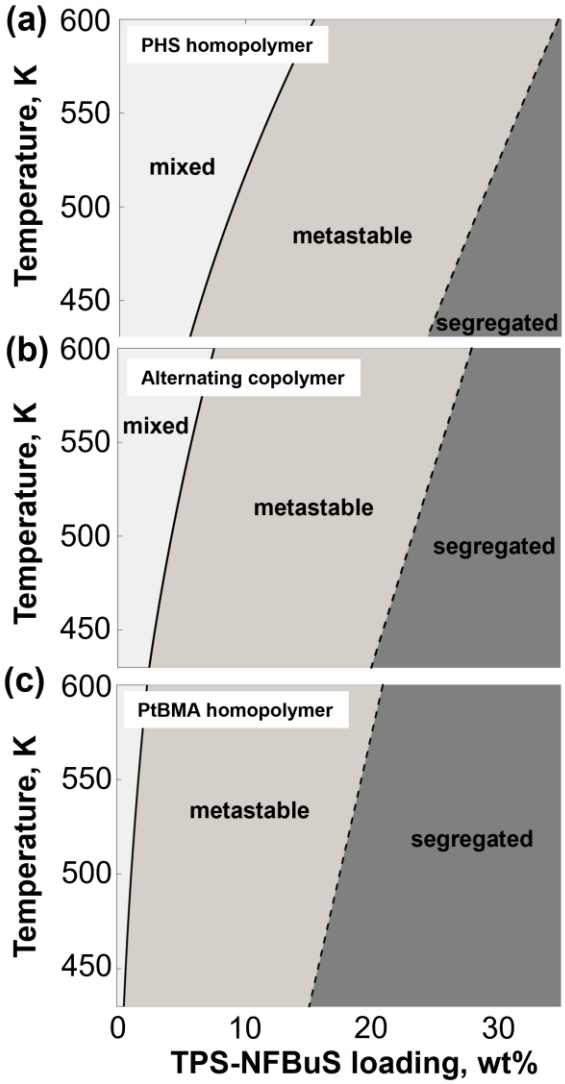

Figure 10. Temperature-PAG loading phase diagrams obtained using Flory-Huggins theory for a mixture of TPS-NFBuS PAG with (a) PHS, (b) alternating copolymer, and (c) PtBMA. The shaded regions separated by the binodal (solid line) and spinodal (dashed lines) boundaries indicate mixtures that are in well-mixed (stable mixing), metastable mixing, and segregated (unstable mixing) states.

4.3 Ionic PAGs screen the hydrogen bonding interactions between PHS and PtBMA

Our solvation analysis for the single ionic PAGs in Sec. III B3 showed stronger interactions between the PAG ions and PHS polar groups that could significantly affect the number of hydrogen bonding interactions between PHS and PtBMA segments at high PAG concentrations. To understand this effect, we analyzed the spatial distribution between H-O atoms in the phenol and carbonyl groups for different PAG loadings in the alternating copolymer. We focused on H-O atoms as any screening of the interactions between them can reduce local mixing of PHS and PtBMA segments and foster nanosegregation.

Figure 11a shows the spatial density obtained from MD simulations between phenol and carbonyl groups in alternating copolymer with and without TPS-PFPS PAGs at 600 K. By increasing the PAG loadings from 10 to 31 wt%, the density of hydrogen bonded carbonyls at ~2 Å decreased from 12% to 45% compared to the PAG-free case (a similar behavior was observed for TPS-TFMeS, TPS-NFBuS, and TPS-ATFEtS as shown in Figure S25 in the SI). This decrease in the concentration of hydrogen bonded carbonyls is consistent with the FTIR spectra for the random copolymer wherein the two distinct peaks (at 1720 cm^{-1} and 1696 cm^{-1}) for the pure system merges with the primary C=O peak at 1718 cm^{-1} when mixed with 20wt% TPS-PFPS (see Figure 11b).

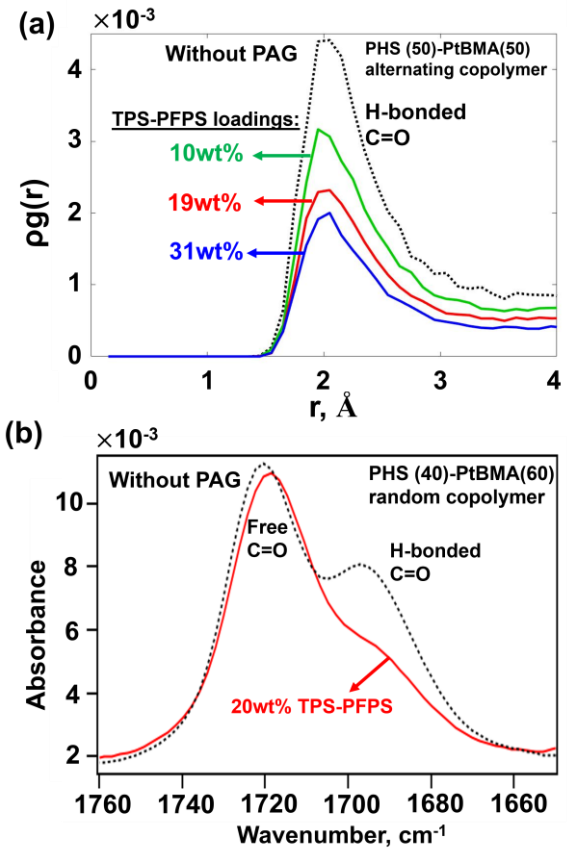

Figure 11. Variation in the concentration of hydrogen bonds between hydroxyl and carbonyl groups in copolymer media. (a) Time averaged density, ρg(r), obtained from MD simulations between H-O atoms in phenol and carbonyl groups for the structure formed by alternating copolymers with (solid lines) and without (dashed lines) TPS-PFPS PAGs at 600 K. (b) IR spectra for PHS-PtBMS random copolymer film with (solid line) and without (dashed line) TPS-PFPS PAGs. The corresponding PAG loadings in wt% for simulations and experiments are shown.

4.4 Local solvation environment influences shape and size of the TPS-TFMeS PAG clusters

Although our solvation analysis for single/dimer TPS-TFMeS PAG showed their strong affinity towards the PHS segments, the presence of multiple PAGs at high concentrations shifts the balance to favor PAG-PAG contacts over polymer-PAG interactions. Figure 12 shows representative snapshots of the largest PAG clusters solvated in different polymers at PAG 25-29 wt% loadings. We observe a string-like network containing 15 ion pairs ~50 Å long in the PHS homopolymer and a segregated cluster with 140 ion pairs in the PtBMA homopolymer (see Figures 12a and 12c). For the alternating copolymer, the PAGs form a heterogenous structure with 51 ion pairs that spans the entire simulation box length of ~ 80 Å (see Figure 9b) with both string-like and globular aggregates likely reflecting the inhomogeneous solvation provided by PHS and PtBMA segments (see Figure 12b). Similar trends were observed for the other ionic PAGs.

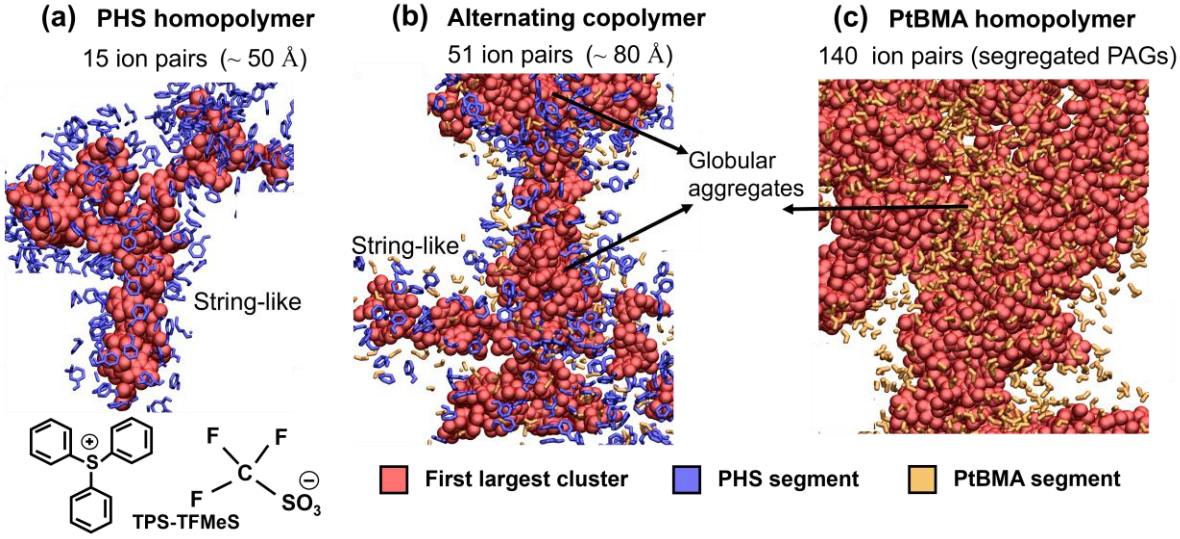

Figure 12. Representative simulation snapshots showing structures of the largest PAG cluster (red) along with the solvating PHS (blue) and PtBMA (orange) segments in different polymers. For simplicity, only PHS phenols and PtBMA ester groups within 8Å radial distance from the clustered PAG atoms are shown. The PAG loadings are between 25-29 wt%.

5. Conclusions and Outlook

Using atomistic models and molecular dynamics simulations, we demonstrated that the dissociation free-energy of dilute PAGs can be used as a predictive tool to rank different polymers and PAG chemistries to identify photoresist components with improved compatibility and mixing homogeneity. The performance of EUV resists at the post-exposure stage depends on the number and size of the PAG aggregates present within the photoresist at the pre-exposed conditions i.e., after spin coating and baking. If the PAG molecules are aggregated, i.e., heterogeneously distributed in the polymer medium, then post exposure of such a resist would lead to nonuniform acid production and partially deprotected regions with suboptimal or unexpected dissolution behaviors that may nucleate defects[25].

We first analyzed the inherent inhomogeneities present in the polymer matrix (without PAGs) using the Ripley's K-function method where we observed that the PHS and PtBMA blends have higher level of segregation with well-defined PtBMA and PHS domains compared to the diblock and alternating copolymer. These results highlight the appeal of alternating (at best) or random (at least) copolymers as a way to minimize compositional segregation. Our analysis of simulation structures and FTIR experiments revealed hydrogen bonding interactions between the PHS and PtBMA segments, which are expected to promote some level of mixing and matrix homogeneity.

Our PMF calculations for single and dimer ionic TPS-TFMeS, TPS-NFBuS, and TPS-ATFEtS PAGs predicted a lower PAG dissociation barrier in PHS homopolymer compared to PtBMA homopolymer, with an intermediate value for the alternating copolymer. This indicates that the polar hydroxyl groups in PHS aid PAG dissociation, while the less polar PtBMA segments allow for more PAG association. In pure PHS, our study also showed that the presence of bulky hydrophobic side groups in TPS-NFBuS, and TPS-ATFEtS screen the electrostatic interactions with the polar hydroxyl groups and hence increases the $\triangle G_D$ by a factor of 2-4 compared to that for the smaller TPS-TFMeS PAG. For nonionic napthalimide PAG, we predicted a barrier-less dissociation with relatively flatter PMF profiles in both PHS and PtBMA homopolymers and alternating copolymer media indicating a higher dispersibility compared to the ionic PAGs. The trend of higher $\triangle G_D$ in less polar media was correlated with a higher effective dipole moment for PAGs in less polar solvation media as found from implicit and explicit solvent DFT

calculations.

We also performed MD simulations that validated our hypothesis that the pairwise $\triangle G_D$ at super dilute conditions can predict the multibody PAG association at high PAG concentrations. We observed that for PAG loadings between 7-36wt% the ionic PAGs have larger aggregates in PtBMA homopolymer compared to PHS homopolymer, and intermediate values in the alternating copolymer. Through simulations and FTIR experiments, we showed that the number of hydrogen bonded carbonyls between PHS and PtBMA decreases with increasing ionic PAG concentration. Our simulations also captured the effect of hydrophobic side groups on PAG aggregation, showing that for TPS-ATFEtS and TPS-NFBuS PAG loadings between 28-35wt% the aggregates form a large percolating network spanning the entire simulation box in the polymers tested. Using the FH theory, we estimated that by decreasing the temperature from 600 K to 430 K, the solubility range of TPS-NFBuS PAGs in polymer media is reduced by ~60-70%. For the smaller TPS-TFMeS and at concentrations ranging between 25-29wt%, we observed short string-like clusters dispersed randomly in pure PHS while a large segregated PAG cluster in pure PtBMA. In the alternating copolymer medium, we observed a heterogenous distribution of string-like and globular TPS-TFMeS aggregates reflecting the inhomogeneous solvation environment of PHS and PtBMA segments. The nonionic PAGs had the least aggregation among all the PAGs studied with less than 10% of PAGs in the largest clusters for all concentrations in different polymer media.

Overall, the systematic computational methodology developed in this study can be used to build more complex molecular models with polymer + PAG + PDQ mixtures under different preparation conditions and PAG/PDQ concentrations. Such tools could also be applied to understand PAG aggregation tendencies in other promising photoresist polymer chemistries, including polymer-bound PAG or sequence-defined peptoid photoresists[40,41]. Work on such more complex systems in bulk and in thin photoresist films with thickness ~15 nm is currently under way. In realistic processing scenarios where the system is cooled relatively fast and the system's dynamics slow down approaching its T_g, the system's structure will be largely arrested in a state representative of a melt state. Our simulations were intended to characterize those *melt-like* states, which could be used as the starting point for studies at sub-T_g conditions. Indeed, the simulated nanostructures of PAG clusters and solvating polymer segments from this

work can be used as an input to DFT models to study the PAG activation due to the post exposure secondary electron attachment- a key step during acid generation [13,18]. Our increasing understanding and detailed modeling of the pre-EUV exposure characteristics of the photoresist nanostructures can pave future modeling efforts to examine post exposure behaviors like acid evolution and diffusion, dissociation of PAGs, structure evolution upon polymer degradation, and finally LER after development.

Supporting Information

The document contains more details on the OPLS forcefield parameters, protocols for MD and ab initio calculations. Supporting simulation results for polymer media with and without PAGs at dilute and high concentrations are also discussed. The LAMMPS scripts can be accessed using the following link: https://github.com/escobedo-lab/Hamiltonian-Replica-Exchange

Acknowledgements

This work was supported by the Semiconductor Research Corporation (SRC). The authors thank Mohammed Alshammasi and Manish Kumar Das for useful exchanges and Dr. Vikram Thapar for all the valuable discussions and assistance while implementing the Hamiltonian replica simulations. The authors also thank Dr. Srinath Ranya for all the valuable exchanges while carrying out the DFT calculations. We thank Dr. Eric Mattson from Intel for providing the FTIR plots. This work used computational resources from Extreme Science and Engineering Discovery Environment (XSEDE), which is supported by the National Science Foundation grant number CHE-2101829.

Abbreviations

EUV, extreme ultraviolet; PAGs, photoacid generators; PDQs, photo decomposable quenchers; TPS, triphenyl sulfonium; TFMeS, trifluoromethane sulfonate; NFBuS, nonafluorobutane sulfonate; PFPS, perfluorophenyl sulfonate; ATFEtS, adamantyltetrafluoroethyl sulfonate; PtBMA, poly(tert-butyl methacrylate); PHS, poly(4-hydroxy styrene); PS, polystyrene; CAR, chemically amplified resists; LER, line edge roughness.

References

(1) Wu, B.; Kumar, A. Extreme Ultraviolet Lithography and Three Dimensional Integrated Circuit—A Review. *Appl. Phys. Rev.* **2014**, *1* (1), 011104. https://doi.org/10.1063/1.4863412.

(2) Silverman, P. J. Extreme Ultraviolet Lithography: Overview and Development Status. *J. Micro/Nanolithography, MEMS, MOEMS* **2005**, *4* (1), 011006. https://doi.org/10.1117/1.1862647.

(3) Gwyn, C. W.; Stulen, R.; Sweeney, D.; Attwood, D. Extreme Ultraviolet Lithography. *J. Vac. Sci. Technol. B Microelectron. Nanom. Struct. Process. Meas. Phenom.* **1998**, *16* (6), 3142–3149. https://doi.org/10.1116/1.590453.

(4) Mack, C. A. Reducing Roughness in Extreme Ultraviolet Lithography. *J. Micro/Nanolithography, MEMS, MOEMS* **2018**, *17* (04), 1. https://doi.org/10.1117/1.JMM.17.4.041006.

(5) Naulleau, P. P.; Niakoula, D.; Zhang, G. System-Level Line-Edge Roughness Limits in Extreme Ultraviolet Lithography. *J. Vac. Sci. Technol. B Microelectron. Nanom. Struct. Process. Meas. Phenom.* **2008**, *26* (4), 1289–1293. https://doi.org/10.1116/1.2932100.

(6) Narasimhan, A.; Grzeskowiak, S.; Srivats, B.; Herbol, H.; Wisehart, L.; Kelly, C.; Earley, W.; Ocola, L. E.; Neisser, M.; Denbeaux, G.; Brainard, R. L. Studying Secondary Electron Behavior in EUV Resists Using Experimentation and Modeling. In *Extreme Ultraviolet (EUV) Lithography VI*; Wood, O. R., Panning, E. M., Eds.; 2015; Vol. 9422, p 942208. https://doi.org/10.1117/12.2086596.

(7) Narasimhan, A.; Grzeskowiak, S.; Ackerman, C.; Flynn, T.; Denbeaux, G.; Brainard, R. L. Mechanisms of EUV Exposure: Electrons and Holes. In *Extreme Ultraviolet (EUV) Lithography VIII*; Panning, E. M., Goldberg, K. A., Eds.; 2017; Vol. 10143, p 101430W. https://doi.org/10.1117/12.2258321.

(8) Kang, S.; Wu, W.; Choi, K.-W.; De Silva, A.; Ober, C. K.; Prabhu, V. M. Characterization of the Photoacid Diffusion Length and Reaction Kinetics in EUV Photoresists with IR Spectroscopy. *Macromolecules* **2010**, *43* (9), 4275–4286.

https://doi.org/10.1021/ma902548a.

(9) Grzeskowiak, S.; Denbeaux, G. H.; Brainard, R. L.; Kaminsky, J.; Murphy, M.; Gibbons, S.; Chandonait, J. Polymer Effects on PAG Acid Yield in EUV Resists (Conference Presentation). In *Advances in Patterning Materials and Processes XXXV*; Hohle, C. K., Gronheid, R., Eds.; SPIE, 2018; p 12. https://doi.org/10.1117/12.2297692.

(10) Cheng, Y.-C.; Wu, P.-J.; Wang, Y.-F.; Wang, C.-W.; Cheng, J.; Chang, V.; Chen, W.-C.; Chang, C.-Y.; Lin, J. Nanoscale Inhomogeneity and Photoacid Generation Dynamics in Extreme Ultraviolet Resist Materials. In *Advances in Patterning Materials and Processes XXXV*; Hohle, C. K., Gronheid, R., Eds.; SPIE, 2018; p 60. https://doi.org/10.1117/12.2316308.

(11) Grzeskowiak, S.; Kaminsky, J.; Gibbons, S.; Narasimhan, A.; Brainard, R. L.; Denbeaux, G. Electron Trapping: A Mechanism for Acid Production in Extreme Ultraviolet Photoresists. *J. Micro/Nanolithography, MEMS, MOEMS* **2018**, *17* (03), 1. https://doi.org/10.1117/1.JMM.17.3.033501.

(12) Lee, C.-T.; Wang, M.; Gonsalves, K. E.; Yueh, W.; Roberts, J. M.; Younkin, T. R.; Henderson, C. L. Effect of PAG and Matrix Structure on PAG Acid Generation Behavior under UV and High-Energy Radiation Exposure. In *Advances in Resist Materials and Processing Technology XXV*; Henderson, C. L., Ed.; 2008; Vol. 6923, p 69232F. https://doi.org/10.1117/12.782634.

(13) Deng, J.; Bailey, S.; Jiang, S.; Ober, C. K. High-Performance Chain Scissionable Resists for Extreme Ultraviolet Lithography: Discovery of the Photoacid Generator Structure and Mechanism. *Chem. Mater.* **2022**, *34* (13), 6170–6181. https://doi.org/10.1021/acs.chemmater.2c01444.

(14) Bottoms, C. M.; Bauman, G. E.; Stein, G. E.; Doxastakis, M. Role of Counter-Anion Chemistry, Free Volume, and Reaction Byproducts in Chemically Amplified Resists. *J. Micro/Nanopatterning, Mater. Metrol.* **2023**, *22* (03), 20. https://doi.org/10.1117/1.JMM.22.3.034601.

(15) Kim, M.; Moon, J.; Choi, J.; Park, S.; Lee, B.; Cho, M. Multiscale Simulation Approach on Sub-10 Nm Extreme Ultraviolet Photoresist Patterning: Insights from

Nanoscale Heterogeneity of Polymer. *Macromolecules* **2018**, *51* (17), 6922–6935. https://doi.org/10.1021/acs.macromol.8b01290.

(16) Park, J.; Lee, S.-G.; Vesters, Y.; Severi, J.; Kim, M.; De Simone, D.; Oh, H.-K.; Hur, S.-M. Molecular Modeling of EUV Photoresist Revealing the Effect of Chain Conformation on Line-Edge Roughness Formation. *Polymers (Basel).* **2019**, *11* (12), 1923. https://doi.org/10.3390/polym11121923.

(17) Ma, J. H.; Wang, H.; Prendergast, D.; Neureuther, A.; Naulleau, P. Investigating Extreme Ultraviolet Radiation Chemistry with First-Principles Quantum Chemistry Calculations. *J. Micro/Nanolithography, MEMS, MOEMS* **2020**, *19* (03), 1–11. https://doi.org/10.1117/1.JMM.19.3.034601.

(18) Lee, H.; Park, S.; Kim, M.; Moon, J.; Lee, B.; Cho, M. Multiscale Simulation of Extreme Ultraviolet Nanolithography: Impact of Acid–Base Reaction on Pattern Roughness. *J. Mater. Chem. C* **2021**, *9* (4), 1183–1195. https://doi.org/10.1039/D0TC04104A.

(19) Kim, M.; Park, S.; Choi, J.; Moon, J.; Cho, M. Tailoring Polymer Microstructure for the Mitigation of the Pattern Collapse in Sub-10 Nm EUV Lithography: Multiscale Simulation Study. *Appl. Surf. Sci.* **2021**, *536* (April 2020), 147514. https://doi.org/10.1016/j.apsusc.2020.147514.

(20) Hou, X.; Li, M.; Eller, M. J.; Verkhoturov, S. V.; Schweikert, E. A.; Trefonas, P. Understanding Photoacid Generator Distribution at the Nanoscale Using Massive Cluster Secondary Ion Mass Spectrometry. *J. Micro/Nanolithography, MEMS, MOEMS* **2019**, *18* (03), 1. https://doi.org/10.1117/1.JMM.18.3.033502.

(21) Eller, M. J.; Li, M.; Hou, X.; Verkhoturov, S. V.; Schweikert, E. A.; Trefonas, P. Nano-Scale Molecular Analysis of Positive Tone Photo-Resist Films with Varying Dose. In *Metrology, Inspection, and Process Control for Microlithography XXXIV*; Adan, O., Robinson, J. C., Eds.; SPIE, 2020; p 85. https://doi.org/10.1117/12.2551941.

(22) Eller, M. J.; Verkhoturov, S. V.; Schweikert, E. A. Testing Molecular Homogeneity at the Nanoscale with Massive Cluster Secondary Ion Mass Spectrometry. *Anal. Chem.* **2016**, *88* (15), 7639–7646. https://doi.org/10.1021/acs.analchem.6b01466.

(23) Spampinato, V.; Franquet, A.; De Simone, D.; Pollentier, I.; Pirkl, A.; Oka, H.; van der

Heide, P. SIMS Analysis of Thin EUV Photoresist Films. *Anal. Chem.* **2022**, *94* (5), 2408–2415. https://doi.org/10.1021/acs.analchem.1c04012.

(24) Escobedo, F. A.; Chen, Z. Liquid Crystalline Behavior of a Semifluorinated Oligomer. *J. Chem. Phys.* **2004**, *121* (22), 11463–11473. https://doi.org/10.1063/1.1811071.

(25) Cruz, J.; Verkhoturov, S. V.; Verkhoturov, D. S.; Robinson, M. A.; Blackwell, J. M.; Eller, M. J.; Schweikert, E. A. Evaluating Nanoscale Molecular Homogeneity in Extreme Ultraviolet Resists with Nanoprojectile Secondary Ion Mass Spectrometry. *J. Micro/Nanopatterning, Mater. Metrol.* **2022**, *21* (04), 1–13. https://doi.org/10.1117/1.JMM.21.4.044001.

(26) Deng, J.; Bailey, S.; Ai, R.; Delmonico, A.; Denbeaux, G.; Jiang, S.; Ober, C. K. Synthesis of End-Cap Enabled Self-Immolative Photoresists for Extreme Ultraviolet Lithography. *ACS Macro Lett.* **2022**, *11* (9), 1049–1054. https://doi.org/10.1021/acsmacrolett.2c00395.

(27) Bottoms, C. M.; Terlier, T.; Stein, G. E.; Doxastakis, M. Ion Diffusion in Chemically Amplified Resists. *Macromolecules* **2021**, *54* (4), 1912–1925. https://doi.org/10.1021/acs.macromol.0c02052.

(28) Jorgensen, W. L.; Maxwell, D. S.; Tirado-Rives, J. Development and Testing of the OPLS All-Atom Force Field on Conformational Energetics and Properties of Organic Liquids. *J. Am. Chem. Soc.* **1996**, *118* (45), 11225–11236. https://doi.org/10.1021/ja9621760.

(29) Chen, C.; Maranas, J. K.; García-Sakai, V. Local Dynamics of Syndiotactic Poly(Methyl Methacrylate) Using Molecular Dynamics Simulation. *Macromolecules* **2006**, *39* (26), 9630–9640. https://doi.org/10.1021/ma0610562.

(30) Jorgensen, W. L.; Tirado-Rives, J. Potential Energy Functions for Atomic-Level Simulations of Water and Organic and Biomolecular Systems. *Proc. Natl. Acad. Sci.* **2005**, *102* (19), 6665–6670. https://doi.org/10.1073/pnas.0408037102.

(31) Canongia Lopes, J. N.; Pádua, A. A. H. Molecular Force Field for Ionic Liquids Composed of Triflate or Bistriflylimide Anions. *J. Phys. Chem. B* **2004**, *108* (43), 16893–16898. https://doi.org/10.1021/jp0476545.

(32) Gouveia, A. S. L.; Bernardes, C. E. S.; Tomé, L. C.; Lozinskaya, E. I.; Vygodskii, Y.

S.; Shaplov, A. S.; Lopes, J. N. C.; Marrucho, I. M. Ionic Liquids with Anions Based on Fluorosulfonyl Derivatives: From Asymmetrical Substitutions to a Consistent Force Field Model. *Phys. Chem. Chem. Phys.* **2017**, *19* (43), 29617–29624. https://doi.org/10.1039/C7CP06081E.

(33) Dodda, L. S.; Cabeza de Vaca, I.; Tirado-Rives, J.; Jorgensen, W. L. LigParGen Web Server: An Automatic OPLS-AA Parameter Generator for Organic Ligands. *Nucleic Acids Res.* **2017**, *45* (W1), W331–W336. https://doi.org/10.1093/nar/gkx312.

(34) F. Behbahani, A.; Vaez Allaei, S. M.; H. Motlagh, G.; Eslami, H.; Harmandaris, V. A. Structure and Dynamics of Stereo-Regular Poly(Methyl-Methacrylate) Melts through Atomistic Molecular Dynamics Simulations. *Soft Matter* **2018**, *14* (8), 1449–1464. https://doi.org/10.1039/C7SM02008B.

(35) Pierce, F.; Tsige, M.; Borodin, O.; Perahia, D.; Grest, G. S. Interfacial Properties of Semifluorinated Alkane Diblock Copolymers. *J. Chem. Phys.* **2008**, *128* (21). https://doi.org/10.1063/1.2924120.

(36) Thompson, A. P.; Aktulga, H. M.; Berger, R.; Bolintineanu, D. S.; Brown, W. M.; Crozier, P. S.; in 't Veld, P. J.; Kohlmeyer, A.; Moore, S. G.; Nguyen, T. D.; Shan, R.; Stevens, M. J.; Tranchida, J.; Trott, C.; Plimpton, S. J. LAMMPS - a Flexible Simulation Tool for Particle-Based Materials Modeling at the Atomic, Meso, and Continuum Scales. *Comput. Phys. Commun.* **2022**, *271*, 108171. https://doi.org/10.1016/j.cpc.2021.108171.

(37) Hoover, W. G. Canonical Dynamics: Equilibrium Phase-Space Distributions. *Phys. Rev. A* **1985**, *31* (3), 1695–1697. https://doi.org/10.1103/PhysRevA.31.1695.

(38) Nosé, S. A Unified Formulation of the Constant Temperature Molecular Dynamics Methods. *J. Chem. Phys.* **1984**, *81* (1), 511–519. https://doi.org/10.1063/1.447334.

(39) Hoover, W. G. Constant-Pressure Equations of Motion. *Phys. Rev. A* **1986**, *34* (3), 2499–2500. https://doi.org/10.1103/PhysRevA.34.2499.

(40) Meng, X. Z.; Käfer, F. H.; Wallraff, G. M.; Ober, C. K.; Segalman, R. A. Controlled Sequence Peptoids as Photoresist Platforms for High-Resolution DUV/EUV Photoresists. **2022**, No. December, 54. https://doi.org/10.1117/12.2642965.

(41) Käfer, F. H.; Ober, C. K.; Meng, Z.; Segalman, R. A.; Read de Alaniz, J. Sequence-

Defined Polypeptoid CARs for Electron-Beam and EUV Lithography. In *Advances in Patterning Materials and Processes XL*; Guerrero, D., Amblard, G. R., Eds.; SPIE, 2023; Vol. 1249817, p 41. https://doi.org/10.1117/12.2658413.

(42) Theofanis, P. L.; Tazetdinov, O. Monte Carlo EUV Stochastic Simulator (MESS): A Chemistry-Oriented Lithography Simulator. In *Optical and EUV Nanolithography XXXV*; Lio, A., Burkhardt, M., Eds.; SPIE, 2022; Vol. PC12051, p 35. https://doi.org/10.1117/12.2617292.

(43) Mohammadi, M.; Fazli, H.; Karevan, M.; Davoodi, J. The Glass Transition Temperature of PMMA: A Molecular Dynamics Study and Comparison of Various Determination Methods. *Eur. Polym. J.* **2017**, *91* (March), 121–133. https://doi.org/10.1016/j.eurpolymj.2017.03.056.

(44) Han, J.; Gee, R. H.; Boyd, R. H. Glass Transition Temperatures of Polymers from Molecular Dynamics Simulations. *Macromolecules* **1994**, *27* (26), 7781–7784. https://doi.org/10.1021/ma00104a036.

(45) Wen, C.; Liu, B.; Wolfgang, J.; Long, T. E.; Odle, R.; Cheng, S. Determination of Glass Transition Temperature of Polyimides from Atomistic Molecular Dynamics Simulations and machine-learning Algorithms. *J. Polym. Sci.* **2020**, *58* (11), 1521–1534. https://doi.org/10.1002/pol.20200050.

(46) Deokar, S.; Ghadage, R. S.; Rajan, C. R.; Ponrathnam, S. Facile Synthesis of Poly(4-hydroxy Styrene) from Polystyrene. *J. Appl. Polym. Sci.* **2004**, *91* (5), 3192–3201. https://doi.org/10.1002/app.13488.

(47) Himuro, S.; Sakamoto, N.; Arichi, S. Miscibility Behavior of Poly(4-Hydroxystyrene) with Poly(4-Acetoxystyrene). *Polym. J.* **1992**, *24* (12), 1371–1376. https://doi.org/10.1295/polymj.24.1371.

(48) Dixon, P. M. Ripley's *K* Function. In *Encyclopedia of Environmetrics*; Wiley, 2001. https://doi.org/10.1002/9780470057339.var046.

(49) Fukunishi, H.; Watanabe, O.; Takada, S. On the Hamiltonian Replica Exchange Method for Efficient Sampling of Biomolecular Systems: Application to Protein Structure Prediction. *J. Chem. Phys.* **2002**, *116* (20), 9058–9067. https://doi.org/10.1063/1.1472510.

(50) Kumar, S.; Rosenberg, J. M.; Bouzida, D.; Swendsen, R. H.; Kollman, P. A. THE Weighted Histogram Analysis Method for Free-Energy Calculations on Biomolecules. I. The Method. *J. Comput. Chem.* **1992**, *13* (8), 1011–1021. https://doi.org/10.1002/jcc.540130812.

(51) Hub, J. S.; de Groot, B. L.; van der Spoel, D. G_wham—A Free Weighted Histogram Analysis Implementation Including Robust Error and Autocorrelation Estimates. *J. Chem. Theory Comput.* **2010**, *6* (12), 3713–3720. https://doi.org/10.1021/ct100494z.

(52) Molinari, N.; Mailoa, J. P.; Kozinsky, B. Effect of Salt Concentration on Ion Clustering and Transport in Polymer Solid Electrolytes: A Molecular Dynamics Study of PEO–LiTFSI. *Chem. Mater.* **2018**, *30* (18), 6298–6306. https://doi.org/10.1021/acs.chemmater.8b01955.

(53) Molinari, N.; Khawaja, M.; Sutton, A. P.; Mostofi, A. A. Molecular Model for HNBR with Tunable Cross-Link Density. *J. Phys. Chem. B* **2016**, *120* (49), 12700–12707. https://doi.org/10.1021/acs.jpcb.6b07841.

(54) Kucukpinar, E.; Doruker, P. Molecular Simulations of Gas Transport in Nitrile Rubber and Styrene Butadiene Rubber. *Polymer (Guildf).* **2006**, *47* (22), 7835–7845. https://doi.org/10.1016/j.polymer.2006.08.062.

(55) Tomasi, J. Selected Features of the Polarizable Continuum Model for the Representation of Solvation. *WIREs Comput. Mol. Sci.* **2011**, *1* (5), 855–867. https://doi.org/10.1002/wcms.54.

(56) Marenich, A. V.; Cramer, C. J.; Truhlar, D. G. Universal Solvation Model Based on Solute Electron Density and on a Continuum Model of the Solvent Defined by the Bulk Dielectric Constant and Atomic Surface Tensions. *J. Phys. Chem. B* **2009**, *113* (18), 6378–6396. https://doi.org/10.1021/jp810292n.

(57) Wang, Y.; Cheng, X.; Yang, X.; Yang, X. DFT Study of Solvent Effects for Some Organic Molecules Using a Polarizable Continuum Model. *J. Solution Chem.* **2006**, *35* (6), 869–878. https://doi.org/10.1007/s10953-006-9034-0.

(58) Barca, G. M. J.; Bertoni, C.; Carrington, L.; Datta, D.; De Silva, N.; Deustua, J. E.; Fedorov, D. G.; Gour, J. R.; Gunina, A. O.; Guidez, E.; Harville, T.; Irle, S.; Ivanic, J.; Kowalski, K.; Leang, S. S.; Li, H.; Li, W.; Lutz, J. J.; Magoulas, I.; Mato, J.; Mironov,

V.; Nakata, H.; Pham, B. Q.; Piecuch, P.; Poole, D.; Pruitt, S. R.; Rendell, A. P.; Roskop, L. B.; Ruedenberg, K.; Sattasathuchana, T.; Schmidt, M. W.; Shen, J.; Slipchenko, L.; Sosonkina, M.; Sundriyal, V.; Tiwari, A.; Galvez Vallejo, J. L.; Westheimer, B.; Włoch, M.; Xu, P.; Zahariev, F.; Gordon, M. S. Recent Developments in the General Atomic and Molecular Electronic Structure System. *J. Chem. Phys.* **2020**, *152* (15). https://doi.org/10.1063/5.0005188.

(59) Arceo, A.; Green, P. F. Ordering Transition of Block Copolymer Films. *J. Phys. Chem. B* **2005**, *109* (15), 6958–6962. https://doi.org/10.1021/jp050636i.

(60) Ho, R.-M.; Chiang, Y.-W.; Chen, C.-K.; Wang, H.-W.; Hasegawa, H.; Akasaka, S.; Thomas, E. L.; Burger, C.; Hsiao, B. S. Block Copolymers with a Twist. *J. Am. Chem. Soc.* **2009**, *131* (51), 18533–18542. https://doi.org/10.1021/ja9083804.

(61) Okamoto, K.; Kozawa, T. Estimation of Electron Affinity of Photoacid Generators: Density Functional Theory Calculations Using Static and Dynamic Models. *Jpn. J. Appl. Phys.* **2021**, *60* (SC), SCCC03. https://doi.org/10.35848/1347-4065/abf469.

(62) Petsalakis, I. D.; Theodorakopoulos, G.; Lathiotakis, N. N.; Georgiadou, D. G.; Vasilopoulou, M.; Argitis, P. Theoretical Study on the Electronic Structure of Triphenyl Sulfonium Salts: Electronic Excitation and Electron Transfer Processes. *Chem. Phys. Lett.* **2014**, *601*, 63–68. https://doi.org/10.1016/j.cplett.2014.03.086.

(63) Liu, E.; Hegazy, A.; Choi, H.; Weires, M.; Brainard, R.; Denbeaux, G. Characterization of Surface Variation of Chemically Amplified Photoresist to Evaluate Extreme Ultraviolet Lithography Stochastics Effects. *J. Photopolym. Sci. Technol.* **2021**, *34* (1), 63–70. https://doi.org/10.2494/photopolymer.34.63.

(64) Wheatle, B. K.; Lynd, N. A.; Ganesan, V. Effect of Polymer Polarity on Ion Transport: A Competition between Ion Aggregation and Polymer Segmental Dynamics. *ACS Macro Lett.* **2018**, *7* (10), 1149–1154. https://doi.org/10.1021/acsmacrolett.8b00594.

(65) El-Gamal, A. A. Enhancement of the Dielectric Properties of Polyvinyl Alcohol by Adding TiO 2 Nanoparticles. *Phys. status solidi* **2022**, *219* (19). https://doi.org/10.1002/pssa.202200190.

(66) Hayakawa, T.; Adachi, K. Dielectric Relaxation of Poly(n-Butyl Acrylate). *Polym. J.* **2000**, *32* (10), 845–848. https://doi.org/10.1295/polymj.32.845.

(67) Flory, P. J. Thermodynamics of High Polymer Solutions. *J. Chem. Phys.* **1942**, *10* (1), 51–61. https://doi.org/10.1063/1.1723621.

(68) Huggins, M. L. Solutions of Long Chain Compounds. *J. Chem. Phys.* **1941**, *9* (5), 440–440. https://doi.org/10.1063/1.1750930.

(69) Qian, D.; Michaels, T. C. T.; Knowles, T. P. J. Analytical Solution to the Flory–Huggins Model. *J. Phys. Chem. Lett.* **2022**, *13* (33), 7853–7860. https://doi.org/10.1021/acs.jpclett.2c01986.

SUPPLEMENTARY INFORMATION

Atomistic modeling approach for predicting association of photoacid generators in extreme ultraviolet polymeric photoresists

B.P. Prajwal[‡], James M. Blackwell[†], Patrick Theofanis[†], and Fernando A. Escobedo*[‡]

[‡]Robert Fredrick Smith School of Chemical and Biomolecular Engineering, Cornell University, Ithaca, New York- 14853

[†]Intel Corporation, Hillsboro, Oregon- 97124

1 Forcefield parameters

We model the interactions in polymer chains, polymer-photoacid generator (PAG) molecules using the all-atom optimized potentials for liquid simulations (OPLS-AA) parameters. This force field contains components for constraining bonds, angles, and dihedrals within a molecule and incorporates non-bonded interactions such as coulombic and dispersion forces for each atom. The OPLS potential energy function, U_{total} in kcal/mol is given by equation,

$$U_{total} = \sum_{bonds} K_r\,(r - r_o)^2 + \sum_{angles} K_\theta\,(\theta - \theta_o)^2 + \sum_{n=1}^{4} \frac{1}{2}\,K_n\,[1 + (-1)^{n+1}\cos(n\phi)]$$
$$+K_\omega\,(\omega - \omega_o)^2 + \sum_{i>j} 4\,\varepsilon_{ij}\left[\left(\frac{\sigma_{ij}}{r_{ij}}\right)^{12} - \left(\frac{\sigma_{ij}}{r_{ij}}\right)^{6}\right] + \frac{C\,q_i q_j}{\varepsilon\,r_{ij}} \quad \text{when } r_{ij} < r_c \qquad (1)$$

where, K_r (kcal mol^{-1}Å^{-2}), K_θ (kcal mol^{-1} rad^{-2}), K_n (kcal/mol), and K_ω (kcal/mol) are the constants for harmonic bonds, harmonic angles, opls dihedral, and improper dihedral equations, respectively. r (Å) and θ (degrees) are the distance and angle between the bonded atoms and r_o, θ_o are the corresponding equilibrium constants. ϕ (degrees) is the dihedral angle and ω_o (degrees) is the equilibrium improper angle. ε_{ij} (kcal/mol) and σ_{ij} (Å) are the Lennard-Jones (LJ) dispersion energy and distance parameters between atoms i and j, respectively, with unlike-pair parameters estimated based on the geometric mixing rules. The coulombic pairwise interaction parameters, q_i, and q_j are the atom charges, C is an energy-conversion constant, and

ε is the dielectric constant set to 1.0. r_{ij} (Å) is the distance between atoms i and j and r_c is the cutoff for LJ and coulombic interactions. All molecular dynamics (MD) simulations were carried out in LAMMPS [1] real units. The corresponding units for each input parameter in Eq. 1 are defined in LAMMPS (more information in lammps.sandia.gov). The OPLS-AA bonded and nonbonded forcefield parameters were obtained from literature sources (details provided in Sec. IA and Sec. IB) that use ab initio quatum chemical calculations to optimize the parameters for organic and ionic liquid systems. The developed parameters have also been validated by comparing experimental thermodynamics and physical properties such as heats of vaporization and densities.

A. Bonded and non-bonded interaction parameters for polymer chains

Figures S1 and S2 show the chemical structures of the poly(4-hydroxy styrene) (PHS) and poly(tert-butyl methacrylate) (PtBMA) segments along with the atom labels used for defining the bonded and non-bonded parameters in the simulation. The segmental parameters can be used to construct the alternating, diblock, or random copolymers. The forefield parameters for PHS and PtBMA atoms listed in Tables S1 to S5 were obtained from Jorgensen et. al. [2], Chen et.al [3], Price et. al. [4] . In the case of PtBMA segments, the tortional parameters for the ester side group were obtained from Chen et. al [3] as the rotation of the ester group were compared with experiments. For all other atoms including PHS segments, the tortional parameters were obtained from Jorgensen et. al. [2] where the rotational energy profiles from ab initio calculations were used for comparison. The charges and Lennard-Jones parameters were optimized by comparing the conformational dynamics/energetics, and liquid properties [2–4].

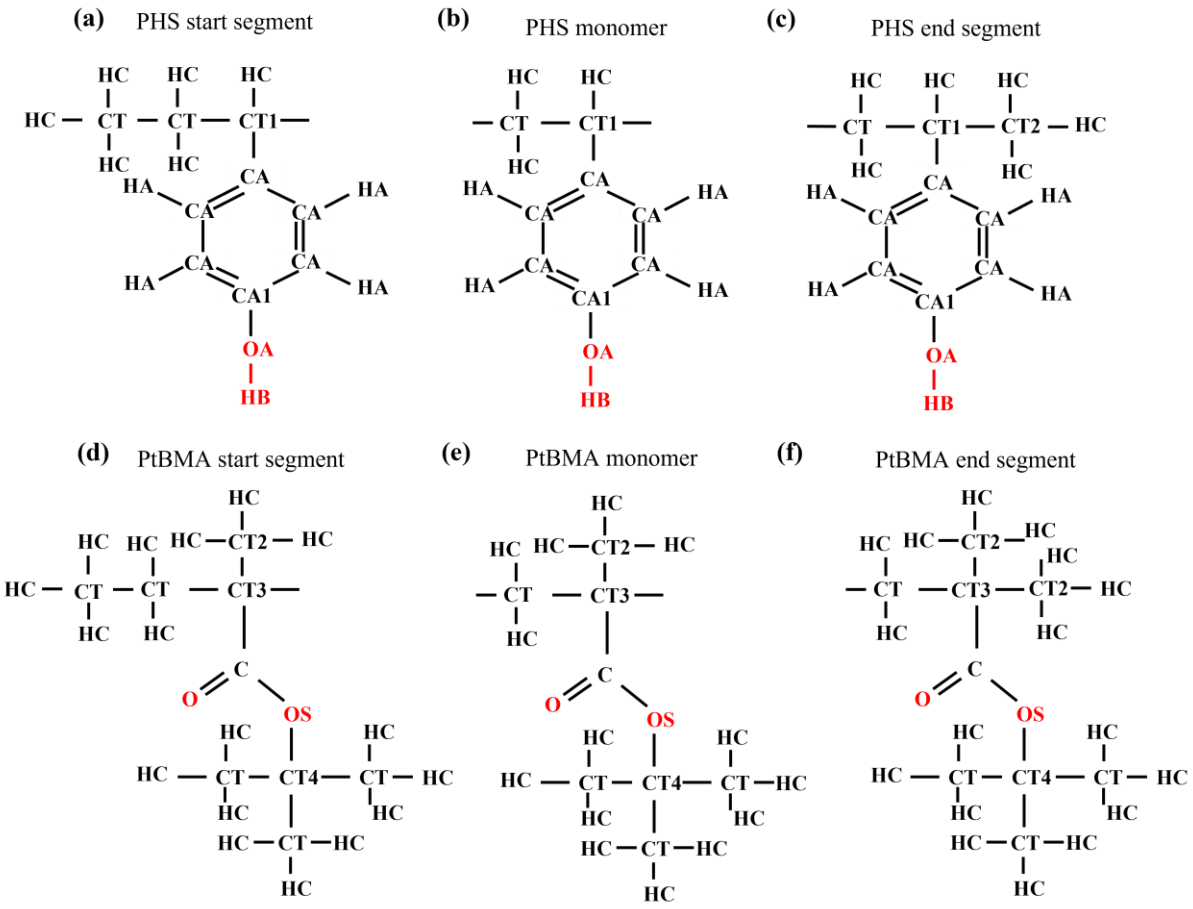

Figure S1. Chemical structures of (a-c) PHS, and (d-e) PtBMA segments showing atom labels. C, CA, CT, CT1-CT4 = carbon; HC, HA, HB = hydrogen; O, OA, OS = oxygen.

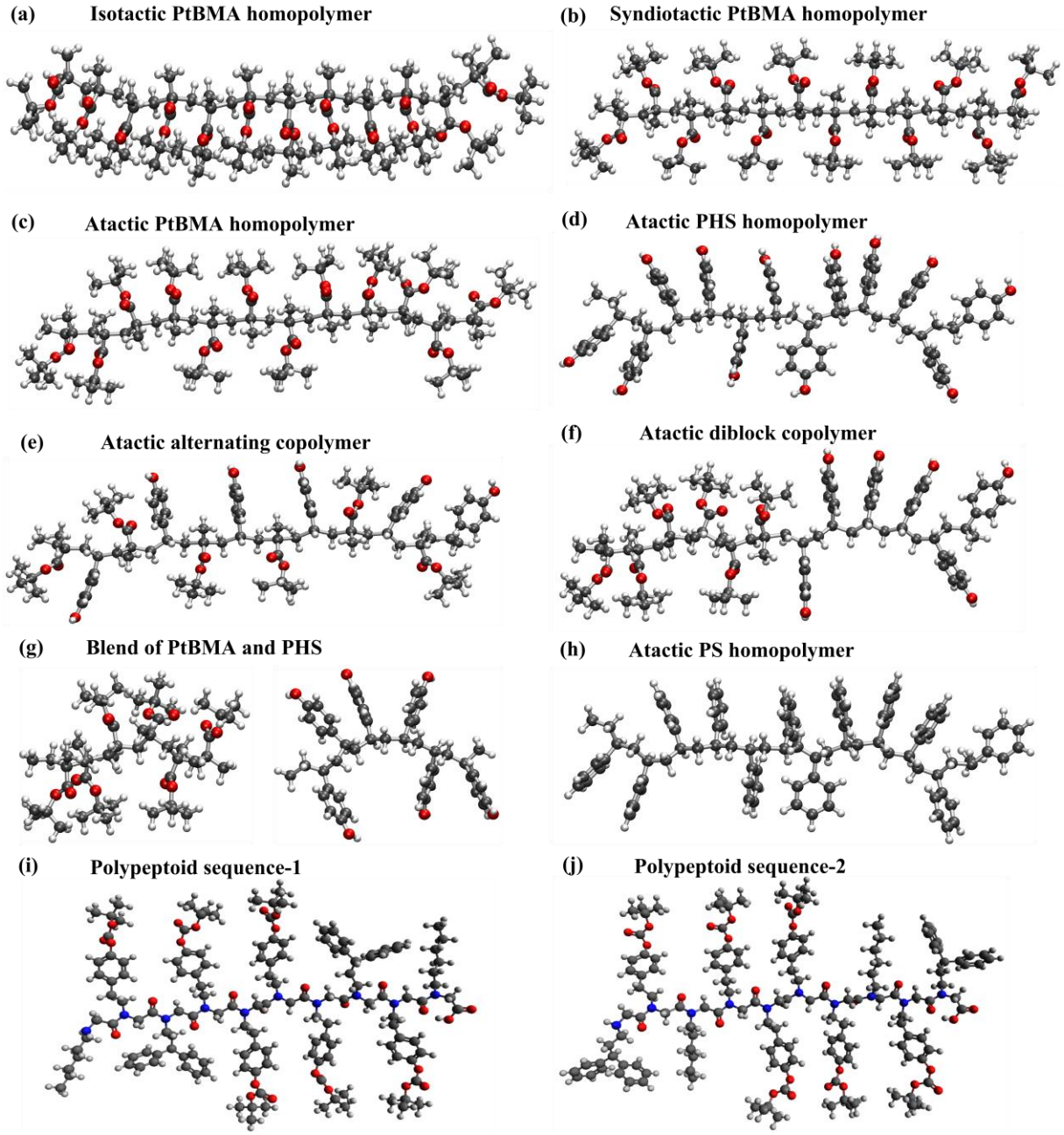

Figure S2. Simulated polypeptoid, PHS and PtBMA polymer structures. (a-c) isotactic, syndiotactic, and atactic PtBMA homopolymer structures. (d) Atactic PHS homopolymer. (e,f) Atactic PHS-PtBMA alternating and diblock copolymers. (g) Atactic PS homopolymer. (h) Atactic 6-mer PtBMA and 6-mer PHS blend structures. (i,j) Polypeptoids with identical chemistries but different sequence. Atom colors: carbon = gray, hydrogen = white, Oxygen = red.

Table S1. Nonbonded LJ and columbic parameters

Atom type	ε_i (kcal mol^{-1})	σ_i (Å)	q_i (e^-)
HC	0.030	2.50	0.045
CT/CT2	0.066	3.50	-0.135
CT1	0.066	3.50	0.055
CA	0.070	3.55	-0.115
CA1	0.070	3.55	0.165
HA	0.030	2.42	0.115
OA	0.170	3.07	-0.585
HB	0.0	0.0	0.435
CT3	0.051	3.20	0.0
C	0.105	3.75	0.51
O	0.210	2.96	-0.43
OS	0.170	3.00	-0.33
CT4	0.066	3.50	0.25

Table S2. Bonded potential parameters

Bond type	K_r (kcal mol^{-1}Å^{-2})	r_o (Å)
CT-CT/CT1-CT2/CT3-CT2/CT-CT4	368.0	1.539
CT-HC/CT1-HC/CT2-HC	331.0	1.090
CT-CT1/CT-CT3	300.0	1.549
CT1-CA	317.0	1.510
CA-CA/CA-CA1	469.0	1.400
CA-HA	367.0	1.080
CA1-OA	450.0	1.364
OA-HB	553.0	0.945
CT1-C	326.0	1.517
C-O	968.0	1.209
C-OS	471.0	1.360
OS-CT4	342.0	1.446

Table S3. Bending potential parameters

Angle type	K_θ (kcal mol^{-1} rad^{-2})	θ_o (degrees)
HC-CT-HC/HC-CT2-HC	35.0	109.5
HC-CT-CT/HC-CT-CT1/HC-CT1-CT/HC-CT1-CT2/HC-CT2-CT1/HC-CT-CT3/HC-CT-CT4/HC-CT2-CT3	35.0	109.5
HC-CT1-CA	35.0	109.5
CT-CT1-CA/CT2-CT1-CA	63.0	114.0

HA-CA-CA	35.0	120.0
CA-CA-CA/CA-CA1-CA	63.0	120.0
CA-CA1-OA	70.0	120.0
CA1-OA-HB	35.0	113.0
CT-CT-CT1/CT1-CT-CT1/CT-CT4-CT/CT-CT-CT3/CT3-CT-CT3/CT1-CT-CT3	89.5	113.3
CT-CT1-CT/CT-CT1-CT2/CT-CT3-CT2/CT-CT3-C/CT2-CT3-C/CT-CT3-CT	87.0	109.5
CT3-C-O	63.3	125.6
CT3-C-OS	74.5	111.4
O-C-OS	126.5	123.0
C-OS-CT4	84.8	116.40
OS-CT4-CT	50.0	109.5

Table S4. Dihedral potential parameters

Dihedral type	K_1 (kcal mol^{-1})	K_2 (kcal mol^{-1})	K_3 (kcal mol^{-1})	K_4 (kcal mol^{-1})
HC-CT-CT-HC/HC-CT-CT1-HC/HC-CT-CT2-HC/	0.0	0.0	0.300	0.0
HC-CT-CT1-CA/HC-CT2-CT1-CA	0.0	0.0	0.462	0.0
HC-CT1-CA-CA	0.0	0.0	0.0	0.0
CT1-CA-CA-HA/CT1-CA-CA-CA	0.0	7.25	0.0	0.0
HA-CA-CA-CA/HA-CA-CA1-CA/HA-CA-CA-CA1	0.0	7.25	0.0	0.0
CA-CA-CA-CA/CA-CA1-CA-CA/CA-CA-CA1-CA/CA-CA-CA-CA1	0.0	7.25	0.0	0.0
HA-CA-CA1-OA	0.0	7.25	0.0	0.0
CA-CA1-OA-HB	0.0	1.682	0.0	0.0
CT-CT1-CA-CA/CT2-CT1-CA-CA	0.0	0.0	0.0	0.0
HC-CT-CT-CT1/HC-CT-CT1-CT2/HC-CT2-CT1-CT/HC-CT-CT1-CT/HC-CT-CT-CT3	0.0	0.0	0.366	0.0
CA-CA-CA1-OA	0.0	7.25	0.0	0.0
HA-CA-CA-HA	0.0	7.25	0.0	0.0
HC-CT-CT3-CT2/HC-CT2-CT3-CT/HC-CT-CT4-CT/HC-CT2-CT3-CT2/HC-CT-CT3-CT	0.0	0.0	0.366	0.0
HC-CT-CT3-C/HC-CT2-CT3-C	0.0	0.0	-0.10	0.0
CT-CT3-C-O/CT2-CT3-C-O	5.20	0.1	-5.10	0.0
CT-CT3-C-OS/CT2-CT3-C-OS	1.61568	0.0	0.0	-1.61568
O-C-OS-CT4	0.0	5.124	0.0	0.0
CT3-C-OS-CT4	4.669	5.124	0.0	0.0
OS-CT4-CT-HC	0.0	0.0	0.468	0.0
CT-CT-CT1-CT/CT-CT1-CT-CT1/CT1-CT-CT1-CT2/CT-CT1-CT-CT3/CT1-CT-CT3-CT/CT-CT3-CT-CT1/CT3-CT-CT1-CT	1.74	-0.157	0.279	0.0

CT-CT-CT3-CT/CT-CT3-CT-CT3/CT2-CT3-CT-CT3/CT3-CT-CT1-CT2/CT1-CT-CT3-CT2	1.74	-0.157	0.279	0.0

Table S5. Improper dihedral potential parameters

Improper dihedral type	K_ω (kcal mol^{-1})	ω_o (degrees)
CA-CT-CT1-CT/HC-CT-CT1-CT/CA-CT-CT1-CT2/HC-CT-CT1-CT2/C-CT-CT3-CT/CT2-CT-CT3-CT/C-CT-CT3-CT2/CT2-CT-CT3-CT2	300.0	109.5

B. Bonded and non-bonded interaction parameters for PAGs

In this section, we provide the forcefield parameters for the PAGs shown in Figs. S3 to S8. The OPLS parameters for triphenyl sulfonium (TPS) cation with charge +1, adamantyltetrafluoroethyl sulfonate (ATFEtS) and anion with charge -1.0, and nonionic naphthalimide sulfonate were obtained from LigParGen (http://zarbi.chem.yale.edu/ligpargen/) [5,6]. The structures were first optimized in Avogadro software (version 1.2.0) [7] before generating the parameters from the LigParGen server [5]. Note that the LigParGen database provides forcefield parameters using the CM1A [8] partial atomic charge model for condensed-phase simulations. For charged molecules, LigParGen database does not scale the CM1A charges by a factor of 1.14 which is typically done for neutral molecules. This scaling factor is obtained by minimizing the errors for predicting condensed-phase properties such as free energies of hydration, densities, and heats of vaporization. For trifluoromethane sulfonate (TFMeS) and nonafluorobutane sulfonate (NFBuS) anions with charge -1.0, the OPLS parameters were obtained from Lopes et. al. [9] and Gouveia et. al. [10], respectively. The parameters for both TFMeS and NFBuS were validated through ab initio calculations and reproducing crystal structures and liquid-state densities. The OPLS parameters for hexafluoro benzene were obtained from Tinker distribution and phenyl sulfonate anion from LigParGen server were used to parameterize the bonded and nonbonded interactions for perfluorophenyl sulfonate (PFPS) anion with charge -1.0.

B1. Interaction parameters for TPS cation

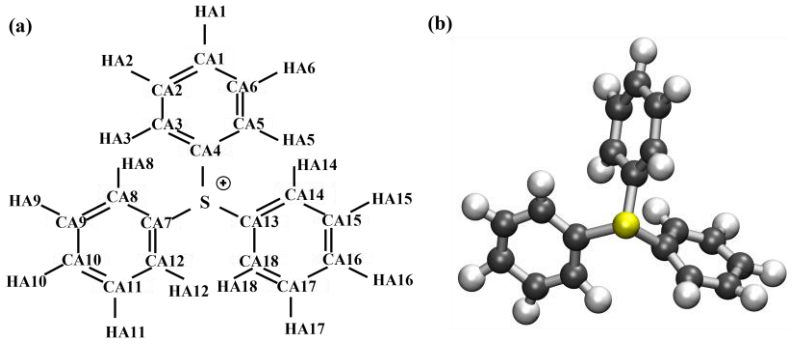

Figure S3. (a) Chemical structure of TPS cation along with the atom labels. (b) TPS cation structure after 10 ns MD simulations in vacuum using OPLS forcefield. CA1-CA18 = carbon (gray), HA1-HA18 = hydrogen (white), S- sulfur (yellow). TPS = triphenyl sulfonium.

Table S6. Nonbonded LJ parameters for S, CA, and HA atom types

Atom type	ε_i (kcal mol^{-1})	σ_i (Å)
HA	0.030	2.42
CA	0.070	3.55
S	0.355	3.60

Table S7. Atom charges

Atom type	q_i (e^-)
HA1	0.1627
CA1	-0.0561
HA2	0.1645
CA2	-0.1181
HA3	0.1462
CA3	-0.0614
CA4	-0.1958
HA5	0.1525
CA5	-0.0531
HA6	0.1626
CA6	-0.1247
S	0.4609
CA7	-0.1962
HA8	0.1525
CA8	-0.0541
HA9	0.1622
CA9	-0.1245

HA10	0.1648
CA10	-0.0558
HA11	0.1628
CA11	-0.1184
HA12	0.1465
CA12	-0.0601
CA13	-0.196
HA14	0.1468
CA14	-0.0608
HA15	0.1642
CA15	-0.1181
HA16	0.1629
CA16	-0.0562
HA17	0.1626
CA17	-0.1242
HA18	0.1526
CA18	-0.0537

Table S8. Bonded potential parameters between S, CA, and HA atom types

Bond type	K_r (kcal mol^{-1}Å^{-2})	r_o (Å)
CA-HA	367.0	1.08
CA-CA	469.0	1.40
CA-S	250.0	1.76

Table S9. Bending potential parameters between S, CA, and HA atom types

Angle type	K_θ (kcal mol^{-1} rad^{-2})	θ_o (degrees)
HA-CA-CA	35.0	120.0
CA-CA-CA	63.0	120.0
S-CA-CA	85.0	119.4
CA-S-CA	62.0	104.2

Table S10. Dihedral potential parameters between S, CA, and HA atom types

Dihedral type	K_1 (kcal mol^{-1})	K_2 (kcal mol^{-1})	K_3 (kcal mol^{-1})	K_4 (kcal mol^{-1})
HA-CA-CA-CA/HA-CA-CA-HA/CA-CA-CA-CA	0.0	7.25	0.0	0.0
CA-CA-S-CA	0.0	0.60	0.0	0.0
S-CA-CA-CA/S-CA-CA-HA	0.0	7.25	0.0	0.0

B2. Interaction parameters for TFMeS

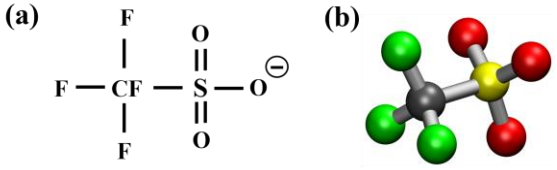

Figure S4. (a) Chemical structure of TFMeS anion showing atom labels. (b) TFMeS anion structure after 10 ns MD simulations in vacuum using OPLS forcefield. CF = carbon (gray), F = fluorine (green), S- sulfur (yellow), O- oxygen (red). TFMeS = trifluoromethane sulfonate.

Table S11. Nonbonded LJ and coulombic parameters

Atom type	ε_i (kcal mol^{-1})	σ_i (Å)	$q_i(e^-)$
F	0.0599	2.95	-0.16
CF	0.0659	3.50	0.35
S	0.25	3.55	1.02
O	0.21	2.96	-0.63

Table S12. Bonded potential parameters

Bond type	K_r (kcal mol^{-1}Å^{-2})	r_o (Å)
CF-F	441.80	1.323
S-O	637.07	1.442
CF-S	235.42	1.818

Table S13. Bending potential parameters

Angle type	K_θ (kcal mol^{-1} rad^{-2})	θ_o (degrees)
F-CF-F	93.33	107.1
F-CF-S	82.93	111.8
CF-S-O	103.96	102.6
O-S-O	115.79	115.3

Table S14. Dihedral potential parameters

Dihedral type	K_1 (kcal mol^{-1})	K_2 (kcal mol^{-1})	K_3 (kcal mol^{-1})	K_4 (kcal mol^{-1})
F-CF-S-O	0.0	0.0	1.451	0.0

B3. Interaction parameters for NFBuS

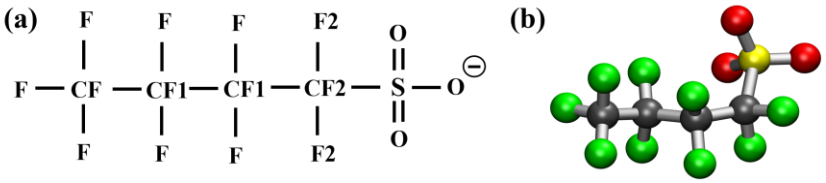

Figure S5. Chemical structure of NFBuS anion showing atom labels. (b) NFBuS anion structure after 10 ns MD simulations in vacuum using OPLS forcefield. CF, CF1, CF2 = carbon (gray), F, F2 = fluorine (green), S- sulfur (yellow), O- oxygen (red). NFBuS = nonafluorobutane sulfonate.

Table S15. Nonbonded LJ and coulombic parameters

Atom type	ε_i (kcal mol^{-1})	σ_i (Å)	$q_i(e^-)$
F	0.0530	2.95	-0.12
F2	0.0530	2.95	-0.2
CF	0.0659	3.50	0.36
S	0.25	3.55	1.18
O	0.20	3.15	-0.68
CF1	0.0659	3.50	0.24
CF2	0.0659	3.50	0.26

Table S16. Bonded potential parameters

Bond type	K_r (kcal mol^{-1}Å^{-2})	r_o (Å)
CF-F/CF1-F/CF2-F2	366.835	1.332
S-O	637.054	1.455
CF2-S	235.42	1.792
CF-CF1/CF1-CF1/CF1-CF2	267.93	1.529

Table S17. Bending potential parameters

Angle type	K_θ (kcal mol^{-1} rad^{-2})	θ_o (degrees)
F-CF-F/F2-CF2-F2/F-CF1-F	76.93	109.1
F2-CF2-S	82.90	111.7
CF2-S-O	103.96	104.4
O-S-O	115.79	114.0
CF1-CF2-S	69.64	113.3
F-CF-CF1/F-CF1-CF1/F-CF1-CF2/F2-CF2-CF1	49.93	109.5
CF-CF1-CF1/CF1-CF1-CF2	58.292	112.7

Table S18. Dihedral potential parameters

Dihedral type	K_1 (kcal mol^{-1})	K_2 (kcal mol^{-1})	K_3 (kcal mol^{-1})	K_4 (kcal mol^{-1})
F2-CF2-S-O	0.0	0.0	0.3466	0.0
CF-CF1-CF1-CF2	6.6191	0.9476	1.387	2.12
F2-CF2-CF1-CF1/F-CF1-CF1-CF/F-CF-CF1-CF1/F-CF1-CF1-CF2	0.3	0.0	0.4	0.0
F-CF-CF1-F/F-CF1-CF1-F/F-CF1-CF2-F2	-2.5	0.0	0.25	0.0
S-CF2-CF1-CF1	-3.85	-0.479	0.1833	0.0
S-CF2-CF1-F	0.0	0.0	0.330	0.0
CF1-CF2-S-O	0.0	0.0	0.333	0.0

B4. Interaction parameters for ATFEtS

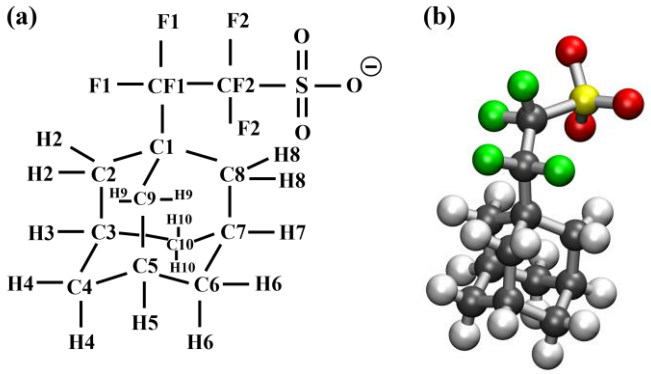

Figure S6. Chemical structure of ATFEtS anion showing atom labels. (b) ATFEtS anion structure after 10 ns MD simulations in vacuum using OPLS forcefield. C1-C10, CF1, CF2 = carbon (gray), F1, F2 = fluorine (green), S= sulfur (yellow), O = oxygen (red), H2-H10 = hydrogen (white). ATFEtS = adamantyltetrafluoroethyl sulfonate.

Table S19. Nonbonded LJ parameters for S, C, CF, H, O, and F atom types

Atom type	ε_i (kcal mol^{-1})	σ_i (Å)
C/CF	0.066	3.50
H	0.03	2.5
S	0.25	3.55
O	0.170	2.96
F1/F2	0.06	2.90

Table S20. Atom charges

Atom type	q_i (e^-)
C1	-0.0675
C2	-0.1487
C3	-0.0958
H2	0.0877
C10	-0.148
C7	-0.0978
H10	0.0703
C8	-0.1386
H8	0.1164
C4	-0.1465
H3	0.0764
C5	-0.0965
H4	0.0681
C6	-0.1483
H7	0.0881
H6	0.0715
C9	-0.1458
H5	0.0776
H9	0.0935
CF1	0.2213
CF2	-0.1864
S	1.2758
O	-0.5889
F1	-0.1517
F2	-0.1321

Table S21. Bonded potential parameters between S, C, CF, H, O, and F atom types

Type	K_r (kcal mol^{-1}Å^{-2})	r_o (Å)
C-C/C-CF/CF-CF	267.93	1.529
C-H	340.0	1.090
S-CF	340.0	1.770
S-O	700.0	1.440
CF-F	367.0	1.360

Table S22. Bending potential parameters between S, C, CF, H, O, and F atom types

Type	K_θ (kcal mol^{-1} rad^{-2})	θ_o (degrees)
C-C-C/C-C-CF/C-CF-CF	58.35	112.7
H-C-C	37.5	110.7
S-CF-CF	50.0	114.7
O-S-CF	74.0	108.9
C-CF-F/S-CF-F/F-CF-CF	50.0	109.5
H-C-H	33.0	107.8
F-CF-F	77.0	109.1
O-S-O	104.0	119.0

Table S23. Dihedral potential parameters between S, C, CF, H, O, and F atom types

Type	K_1 (kcal mol^{-1})	K_2 (kcal mol^{-1})	K_3 (kcal mol^{-1})	K_4 (kcal mol^{-1})
C-C-C-C/C-C-C-CF/C-C-CF-CF/C-C-C-CF	1.30	-0.2	0.2	0.0
C-CF-CF-S	1.262	-0.198	0.465	0.0
CF-CF-S-O/F-CF-S-O/C-C-CF-F/C-CF-CF-F	0.0	0.0	0.0	0.0
H-C-C-C/H-C-C-H/H-C-C-CF	0.0	0.0	0.30	0.0
F-CF-CF-S	0.0	0.450	0.0	0.0
F-CF-CF-F	-2.50	0.0	0.250	0.0

B5. Interaction parameters for PFPS

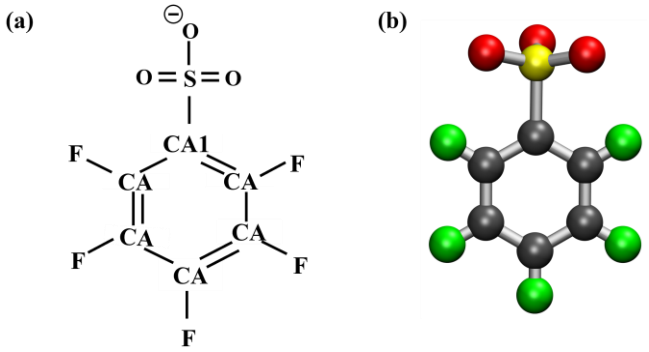

Figure S7. Chemical structure of PFPS anion showing atom labels. (b) PFPS anion structure after 10 ns MD simulations in vacuum using OPLS forcefield. CA1, CA = carbon (gray), F = fluorine (green), S = sulfur (yellow), O = oxygen (red). PFPS = perfluorophenyl sulfonate.

Table S24. Nonbonded LJ parameters for CA, S, F, and O atom types

Atom type	ε_i (kcal mol^{-1})	σ_i (Å)
CA/CA1	0.07	3.55
F	0.061	2.85
S	0.25	3.55
O	0.17	2.96

Table S25. Atom charges

Atom type	q_i (e^-)
CA	0.13
CA1	-0.4041
F	-0.13
S	1.3118
O	-0.6359

Table S26. Bonded potential parameters between CA, CA1, F, S, and O atom types

Atom type	q_i (e^-)
CA	0.13
CA1	-0.4041
F	-0.13
S	1.3118
O	-0.6359

Table S27. Bonded potential parameters between CA, CA1, F, S, and O atom types

Type	K_r (kcal mol^{-1}Å^{-2})	r_o (Å)
S-O	700.0	1.44
S-CA1	340.0	1.77
CA1-CA/CA-CA	469.0	1.40
F-CA	420.0	1.354

Table S28. Bending potential parameters between CA, CA1, F, S, and O atom types

Type	K_θ (kcal mol^{-1} rad^{-2})	θ_o (degrees)
O-S-O	104.0	119.0
O-S-CA1	74.0	107.2
S-CA1-CA	85.0	119.4
F-CA-CA	80.0	120.0
CA-CA-CA	63.0	120.0

Table S29. Dihedral potential parameters between CA, CA1, F, S, and O atom types

Type	K_1 (kcal mol^{-1})	K_2 (kcal mol^{-1})	K_3 (kcal mol^{-1})	K_4 (kcal mol^{-1})
O-S-CA1-CA	0.0	0.0	0.0	0.0
S-CA1-CA-CA/S-CA1-CA-F/F-CA-CA-F/CA-CA-CA-CA/CA1-CA-CA-CA/CA-CA1-CA-CA/F-CA-CA-CA/F-CA-CA1-CA/F-CA-CA-CA1	0.0	7.25	0.0	0.0

B6. Interaction parameters for nonionic naphthalimide sulfonate PAG

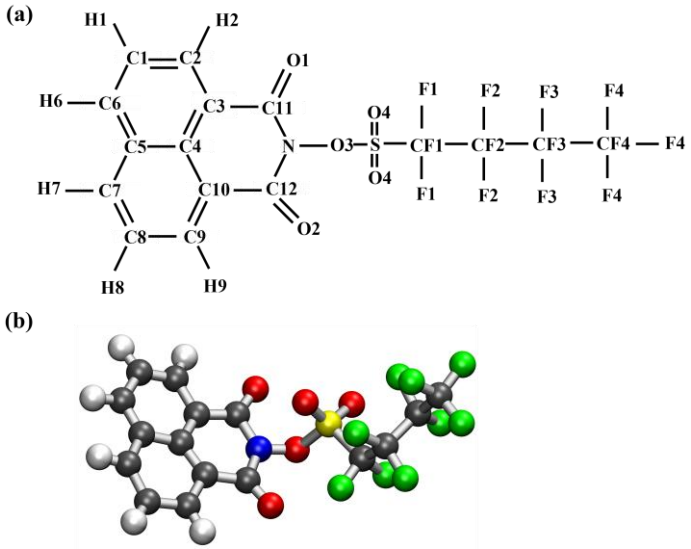

Figure S8. (a) Chemical structure of nonionic naphthalimide sulfonate showing atom labels. (b) Nonionic PAG structure after 10 ns MD simulations in vacuum using OPLS forcefield. C1-C12, CF1-CF4 = carbon (gray), F1-F4 = fluorine (green), N = nitrogen (blue), S= sulfur (yellow), O1-O4 = oxygen (red), H1-H12 = hydrogen (white).

Table S30. Nonbonded LJ and coulombic parameters

Atom type	ε_i (kcal mol^{-1})	σ_i (Å)	q_i (e^-)
C2	0.076	3.55	-0.0155
C1	0.07	3.55	-0.1779
C6	0.07	3.55	-0.0673
H1	0.03	2.42	0.1715
C5	0.08	3.50	-0.0737
H6	0.03	2.42	0.1632
C4	0.08	3.50	0.0393
C3	0.08	3.50	-0.1672
H2	0.03	2.42	0.1899
C7	0.07	3.55	-0.0688
C8	0.07	3.55	-0.1762
H7	0.03	2.42	0.1629
C9	0.076	3.55	-0.0122
H8	0.03	2.42	0.1713
C10	0.08	3.50	-0.1635
H9	0.03	2.42	0.1904
C11	0.07	3.55	0.6423
N	0.17	3.25	-0.6673
C12	0.07	3.55	0.6519
O1	0.21	2.96	-0.3577
O2	0.21	2.96	-0.3720

O3	0.14	2.90	-0.2082
S	0.25	3.55	1.3572
O4	0.17	2.96	-0.4561
CF1	0.066	3.50	-0.1423
CF2	0.066	3.50	0.1583
CF3	0.066	3.50	0.1671
F1	0.06	2.90	-0.0698
F2	0.06	2.90	-0.0914
F3	0.06	2.90	-0.0937
CF4	0.066	3.50	0.3979
F4	0.06	2.90	-0.1238

Table S31. Bonded potential parameters

Bond type	K_r (kcal mol^{-1}Å^{-2})	r_o (Å)
C1-C2/C2-C3/C8-C9/C9-C10	427.0	1.433
C1-C6/C7-C8	469.0	1.400
C1-H1/C6-H6/C7-H7/C8-H8	367.0	1.080
C6-C5/C5-C7	469.0	1.404
C5-C4/C4-C10/C3-C4	520.0	1.370
C2-H2/C9-H9	412.52	1.050
C3-C11/C10-C12	447.0	1.419
C11-N/C12-N	418.0	1.388
C11-O1/C12-O2	570.0	1.229
N-O3	467.3	1.320
O3-S	293.97	1.660
S-O4	700.0	1.440
S-CF1	340.0	1.770
CF1-CF2/CF2-CF3/CF3-CF4	267.93	1.529
CF1-F1/CF2-F2/CF3-F3/CF4-F4	367.0	1.360

Table S32. Bending potential parameters

Angle type	K_θ (kcal mol^{-1} rad^{-2})	θ_o (degrees)
C6-C1-C2/C7-C8-C9	70.00	124.00
H1-C1-C2/H8-C8-C9	64.51	118.99
C1-C6-C5	63.00	120.00
H6-C6-C1/H7-C7-C5/H8-C8-C7/H1-C1-C6/C5-C6-H6/H7-C7-C8	35.00	120.00
C6-C5-C4/C5-C4-C3/C10-C4-C3/C7-C5-C4	85.00	117.30
C1-C2-C3/C1-C2-H2/C8-C9-H9/C10-C9-H9/C3-C2-H2/C8-C9-C10	60.00	122.26
C6-C5-C7	85.00	134.90
C5-C7-C8	63.00	120.00
C5-C4-C10	85.00	134.00
C2-C3-C11/C9-C10-C12	77.27	119.73
C3-C11-N/C10-C12-N	70.00	111.30
C4-C10-C12/C4-C3-C11	85.00	119.20
C3-C11-O1/C10-C12-O2	80.00	128.80
C11-N-O3/C12-N-O3	63.00	112.40
N-O3-S	69.51	114.54
O3-S-O4/O3-S-CF1	78.67	104.36
S-CF1-CF2	50.00	114.70
CF1-CF2-CF3/CF2-CF3-CF4	58.35	112.70
S-CF1-F1/CF1-CF2-F2/CF2-CF3-F3/CF3-CF4-F4/F2-CF2-CF3/F1-CF1-CF2/F3-CF3-CF4	50.00	109.50
F2-CF2-F2/F4-CF4-F4/F3-CF3-F3	77.00	109.10
N-C11-O1/N-C12-O2	80.00	120.60
C4-C10-C9/C4-C3-C2	70.00	124.00
O4-S-CF1/	74.00	108.90
C11-N-C12	70.00	126.40
O4-S-O4	104.00	119.00

Table S33. Dihedral potential parameters

Dihedral type	K_1 (kcal mol^{-1})	K_2 (kcal mol^{-1})	K_3 (kcal mol^{-1})	K_4 (kcal mol^{-1})
C5-C6-C1-C2/C5-C7-C8-C9/H7-C7-C8-H8/C9-C10-C4-C3/H7-C7-C5-C4/H8-C8-C7-C5/C8-C9-C10-C4/C7-C5-C4-C3/C3-C4-C10-C12/C5-C6-C1-H1/H6-C6-C5-C4/C5-C4-C10-C9/H1-C1-C2-C3/H1-C1-C6-H6/C6-C5-C4-C3/C5-C4-C3-C11/H1-C1-C2-H2	0.0	7.25	0.0	0.0
C6-C5-C4-C10/C7-C5-C4-C10/C5-C4-C10-C12/H6-C6-C1-C2/C11-C3-C4-C10/C2-C3-C4-C5/H8-C8-C9-H9/H7-C7-C5-C6/H8-C8-C9-C10/C1-C2-C3-C4/H7-C7-C8-C9/C1-C2-C3-C11/CF1-CF2-CF3-CF4/H6-C6-C5-C7/C2-C3-C4-C10	0.0	7.25	0.0	0.0
C1-C6-C5-C4/C6-C5-C7-C8/C2-C3-C11-N/C9-C10-C12-N/C4-C5-C7-C8/C4-C10-C12-N/C2-C3-C11-O1/O1-C11-C3-C4/C1-C6-C5-C7/C9-C10-C12-O2/C4-C10-C12-O2/C4-C3-C11-N	0.0	7.00	0.0	0.0
C6-C1-C2-C3/C7-C8-C9-C10	1.241	3.353	-0.286	0.0
C11-N-O3-S/C12-N-O3-S	3.0	3.0	0.0	0.0
N-O3-S-O4	0.75	0.0	0.0	0.0
O3-S-CF1-CF2/CF1-CF2-CF3-F3/CF2-CF3-CF4-F4/O4-S-CF1-CF2/O3-S-CF1-F1/O4-S-CF1-F1/CF2-CF3-CF4-F4/F1-CF1-CF2-CF3/O4-S-CF1-F1/F2-CF2-CF3-CF4	0.0	0.0	0.0	0.0
S-CF1-CF2-CF3	1.262	-0.198	0.465	0.0
S-CF1-CF2-F2/S-CF1-CF2-F2	0.0	0.450	0.0	0.0
C11-N-C12-O2/C10-C12-N-C11/C3-C11-N-C12/O1-C11-N-C12	0.0	4.90	0.0	0.0
H9-C9-C10-C12/C6-C1-C2-H2/C7-C8-C9-H9/H2-C2-C3-C11/H2-C2-C3-C4/H9-C9-C10-C4	0.0	0.0	-0.372	0.0
F2-CF2-CF3-F3/F2-CF2-CF3-F3/F1-CF1-CF2-F2/F4-CF4-CF3-F3/F3-CF3-CF4-F4	-2.5	0.0	0.25	0.0
O2-C12-N-O3/O1-C11-N-O3	0.0	6.603	0.0	0.0
C10-C12-N-O3/O3-N-C11-C3	0.0	14.0	0.0	0.0
N-O3-S-CF1	-0.75	0.0	0.0	0.0

7 Protocols for molecular dynamics and ab initio calculations

A. Protocol for generating an unbiased initial configuration at 600 K

To generate a representative initial configuration, we first placed the polymer chains on a grid in a very large cubic box (~50 times the expected final volume) with periodic boundary conditions applied in all directions and simulated at high temperature (1000 K) to randomize the system for 1 ns in an isothermal-isochoric (NVT) ensemble using Nose-Hoover thermostat with damping parameter of 0.1 ps. During this process, coulombic interactions are turned off and the LJ cutoff is set to 12 Å. Relaxation and decorrelation from the starting configuration was facilitated by using the LAMMPS *fix adapt* procedure for 1 ns that turns off the LJ interactions (while retaining the bonded interactions) and ramps them back to normal strength. After this step, we equilibrated the system with both coulombic and LJ interactions including long-ranged LJ tail corrections (setting 12 Å as cutoff) at 1000 K using Nose-Hoover thermostat and barostat (NPT ensemble) for 1.0 ns. We then further equilibrated the system for 1 ns by adding the *pppm* model with 10^{-5} error tolerance for coulombic interactions. After generating a dense configuration at 1000 K, a stepwise cooling is performed at 100 K/ns in the NPT ensemble until 600 K is reached. The system is relaxed at 600 K by further equilibrating for 5 ns in the NPT ensemble. The pressure was set to 1 atm for all the NPT runs and the timestep to 1 fs for the velocity-Verlet integration, checking the conservation of atomic linear momentum (p_x, p_y, p_z) every 5 ps during all the simulation stages. The Nosé-Hoover thermostat and barostat damping parameters were set to 0.1 ps and 1 ps, respectively.

B. Glass transition temperature and mean square displacement of the polymer media

Figures S9c and S9d track the mean square displacement (MSD) of the polymer atoms at 600 K (well above T_g) and 400 K (below T_g) and as expected we observed a significant drop in the MSD values with a flatter profile at longer times for all the polymers at 400 K compared to the MSD values at 600 K. We also observed that the drop in MSD values is larger in PHS than in PtBMA. These MSD trends hint towards nano structural differences (e.g., in local packing of the chains or the available free volume) of the atactic PHS, and PtBMA homopolymers, and PHS-PtBMA alternating copolymer chains as the system is cooled below T_g.

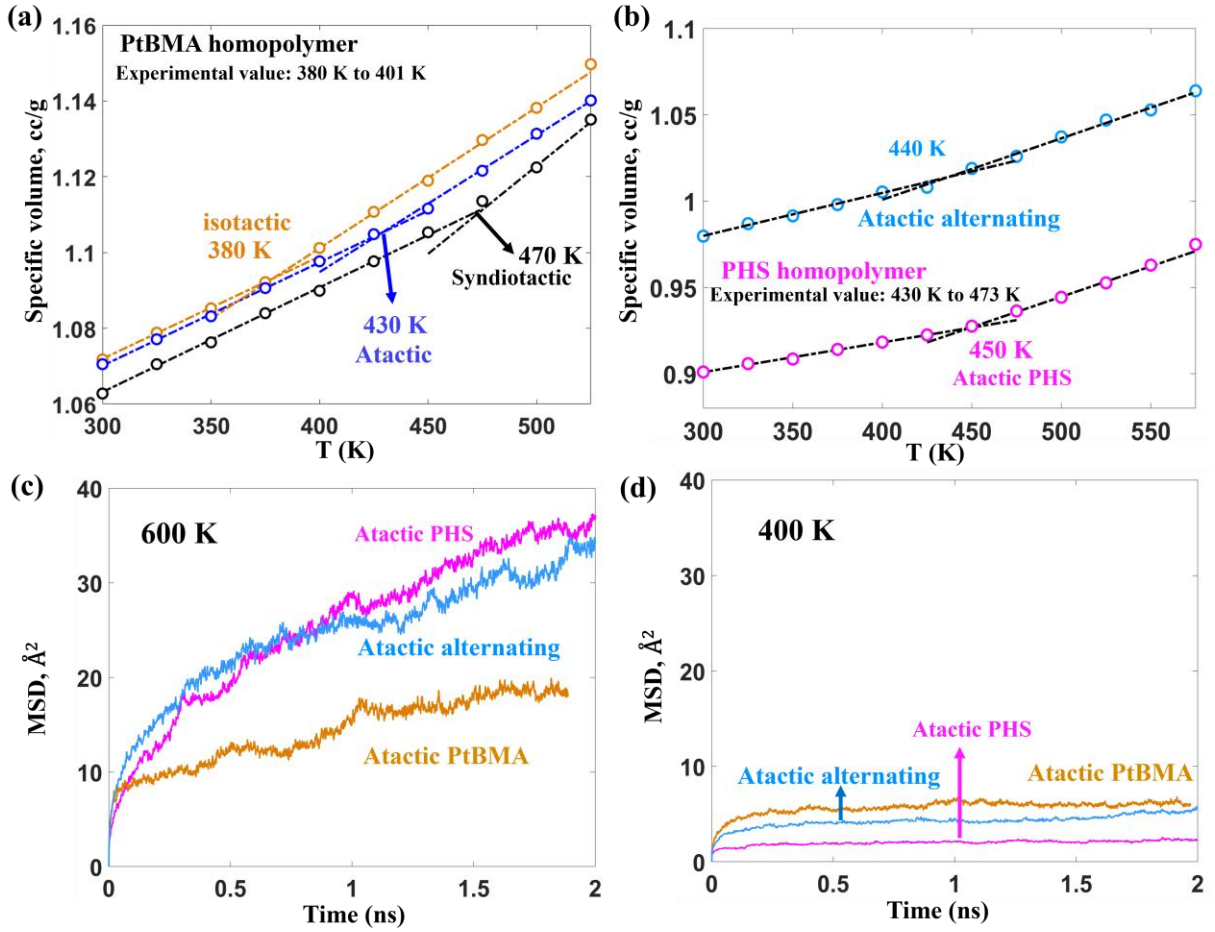

Figure S9. Glass transition temperature (T_g) estimation and MSD analysis for the PHS and PtBMA homopolymers, and PHS-PtBMA alternating copolymer. (a,b) Specific volume as a function of temperature during gradual cooling of polymers with different tacticity. The experimental T_g values for PtBMA and PHS (from https://www.polymerdatabase.com/ archive accessed on 18th March 2023) are also shown. Dotted lines are two-piece linear functions whose intersection marks the T_g. MSD vs. simulation time is shown at (c) 600K (above T_g) and (d) 400 K (below T_g).

C. Protocol for Hamiltonian replica exchange (HREX) simulations

The free energy or the potential of mean force (PMF) for dissociation of a single and dimer PAGs with and without the polymer medium was estimated using umbrella sampling (US) withing a HREX framework. HREX is intended to improve the sampling of the configurational space in different US windows by allowing windows to swap configurations and thus escaping

possible configurational traps. The HREX method allows for swapping of configurations belonging to neighboring umbrella sampling replica windows based on the Metropolis acceptance criterion, P_{acc}. For windows, i = 1 and 2, for example, P_{acc} = min {1, exp(-β_1[U(k_1, r_1^{ref}, r_2) – U(k_1, r_1^{ref}, r_1)]- β_2[U(k_2, r_2^{ref}, r_1) – U(k_2, r_2^{ref}, r_2)])} where $\beta_1 = \beta_2 = 1/k_bT$ and U(k_i, r_i^{ref}, r_i)= $\frac{1}{2}$ k_i (r_i- r_i^{ref})^2 is a harmonic spring potential with parameters, k_i and r_i^{ref}, and r_i (= r_{SO} or $r_{PAGscom}$) is the reaction coordinate distance. The replica swap move was attempted every 0.2 ps by randomly selecting an odd or even replica pairing. We fixed the value of k_i for all i windows to be 15 kcal/(mol·Å^2) and the r_i^{ref} is varied with 0.5 Å increments from 3.0 Å to 22.5 Å for single PAG and 5.0 Å to 20.5 Å for dimer PAG simulations. The choice of k_i's and the spacing between each replica windows determine the neighboring window swap acceptance rate, and we selected the spring parameters such that the swap acceptance rate for all HREX simulations is between 15-30%. In each i^{th} reaction coordinate window, a harmonic bias potential, U(r_i)= $\frac{1}{2}$ k (r_i- r_i^{ref})^2 is applied to keep the system close to the reference separation distance r_i^{ref}. In the case of ionic PAG dimer HREX simulations, we included an additional harmonic bias potential with k= 15 kcal/(mol·Å^2) between the cation and anion to constrain r_{SO} distance in the associated PAGs at different $r_{PAGscom}$ values. Note that the equilibrium r_{SO} distance for each associated ionic PAG in the dimer calculations is obtained from the single ionic PAG PMFs where the first potential well was observed (see Figure S13 and Table S37 in Sec. VI for numerical values). 1 fs timestep is used in all the HREX simulations.

We first performed the HREX simulations for the single and dimer PAG molecules in vacuum using NVT ensemble at 600 K in a very large periodic box (~1000 Å) with distance cutoff for the LJ and coulombic interactions set to 50 Å (disregarding long ranged columbic interactions). We then relaxed the initial configurations by equilibrating them for 10 ns in their respective replica windows (without any swaps). After the equilibration step, we performed the HREX simulations. Due to small number of degrees of freedom present in the vacuum simulations, we used a Langevin thermostat with 1 ps as the damping parameter and conserved the linear (p_x, p_y, p_z) and angular (L_x, L_y, L_z) momentums of all the atoms for every 2 ps during the simulation. The HREX simulations were also performed at 600 K in NPT ensemble for single and dimer PAGs in atactic PHS-PtBMA alternating copolymer, and atactic homopolymers of PS, PHS, and PtBMA. The Nosé-Hoover thermostat and barostat damping parameters during the runs

were set to 0.1 ps and 1 ps, respectively. The LJ and coulombic cutoffs were set at 12 Å and included long-ranged LJ tail corrections and a coulombic *pppm* model with 10^{-5} error tolerance. First, the equilibrated configuration for the PAG-free polymer is obtained by following the protocol described in Sec. IIA. We then inserted an associated single or a dimer PAG obtained from the vacuum HREX simulations with random orientation at a random location in the polymer-containing simulation box, and the entire structure was minimized to avoid any unphysical overlaps. Using the minimized structure, we then generated more reliable initial configurations for each umbrella window in the HREX simulations by performing series of energy minimization, and annealing cycles for a total of 9 ns (see Table S34). The HREX simulations for single and dimer PAGs were performed for 5 ns and 6 ns, respectively and sampled values for the corresponding reaction coordinate distances for each window were dumped for every 1 ps. The probability distribution obtained for the series of windows from the last 2.5 ns for single PAG and 3 ns for PAG dimer simulations are eventually combined with the weighted histogram analysis method (WHAM) [11] to compose the PMF curve. The atomic linear momentum (p_x, p_y, p_z) was conserved for every 2 ps in the HREX simulations and 5 ps in the annealing runs. The consistency of the PMF profiles was checked by performing two independent HREX runs with different initial configurations and different random seeds for atom trajectories and replica exchanges.

Table S34. Equilibration stages to generate initial configurations for the single and dimer HREX simulations. All simulations are performed at 1 atm and 1 fs timestep. The temperature is ramped over the entire duration of the heating and cooling stages.

Stage	Simulation time (ns)	Temperature (K)
Energy minimization	-	-
NPT	0.5	600
NPT (heating)	1.0	600→800
NPT	2.0	800
NPT (cooling)	1.0	800→600
NPT	0.5	600
Energy minimization	-	-
NPT (heating)	1.0	600→800
NPT (cooling)	1.0	800→600
NPT	2.0	600

D. Protocol for PAG concentrated simulations in polymer medium

Mixtures with 140 molecules of a given polymer and 50, 100, 150, and 200 PAG molecules are placed on a grid in a very large cubic periodic box (~ 50 times the expected final volume). We performed NVT simulations at 1000 K for 1 ns using Nose-Hoover thermostat with a damping parameter of 0.1 ps. The coulombic interactions are turned off during this stage to help the random disperse the PAG molecules and polymer chains in the large box. We used the LAMMPS *fix adapt* function that ramps up the LJ interactions (while retaining the bonded interactions). The LJ interaction cutoff was set to 12 Å. Note that the ionic PAGs are completely dissociated at this stage. After this step, we performed an energy minimization, and the minimized structure was simulated at 600 K and 1 atm in the NPT ensemble for 1 ns with both coulombic and LJ interactions set to 12 Å cutoff including LJ tail corrections. We then added the *pppm* model with 10^{-5} error tolerance for coulombic interactions and performed a series of stages containing minimization, annealing, compression, and decompression runs for 9 ns (see Table S35). During all the stages, the timestep was set at 1 fs and the atomic linear momentum (p_x, p_y, p_z) was conserved for every 5 ps. The total simulation time is 11 ns and the statistics for the cluster analysis and local hydrogen bonding interactions are obtained from the configurations that dumped every 10 ps during the last 3 ns.

Table S35. Equilibration stages for PAG concentrated simulations. Temperature is ramped over the entire duration of the heating or colling stages. Total simulation time is 9 ns.

Stage	Simulation Time (ns)	Temperature (K)	Pressure (atm)
Energy minimization	-	-	-
NPT	0.5	600	1
NPT (compression)	0.5	600	1→4000
Energy minimization	-	-	-
NPT	0.5	600	4000
NPT (decompression)	0.5	600	4000→1
NPT (heating)	1.0	600→800	1
NPT (cooling)	1.0	800→600	1
NPT (compression)	0.5	600	1→4000
NPT	0.5	600	4000
NPT (decompression)	0.5	600	4000→1
Energy minimization	-	-	-
NVT	0.5	600	-
NPT	3.0	600	1

E. Protocol for estimating dipole moment using ab initio methods

The protocol for the dipole moment calculation in implicit solvent model is as follows: (i) The geometry of the associated PAG structure obtained from the vacuum HREX MD simulations is optimized (see Sec. IIC) using the R-B3LYP 6-31++G(d,p) basis set. The net charge of the PAG is set to 0 and the multiplicity of the electron state to 1. (ii) The resulting optimized structure was then used to carry out the energy minimization run with benzyl methanol and butyl acetate implicit solvent model.

For estimating dipole moment of TPS-TFMeS PAG in the explicit polymer environment, we selected the polymer atoms in the first solvation shell around the associated TPS-TFMeS PAG from a MD equilibrated structure and chose the distance cutoffs from the PAG center of mass such that similar number (~10) of hydroxyl and carbonyl groups were included for the calculations. We then minimized the energy of the structure using the R-B3LYP 6-31G(d) basis.

8 Heterogeneity analysis in alternating copolymer medium

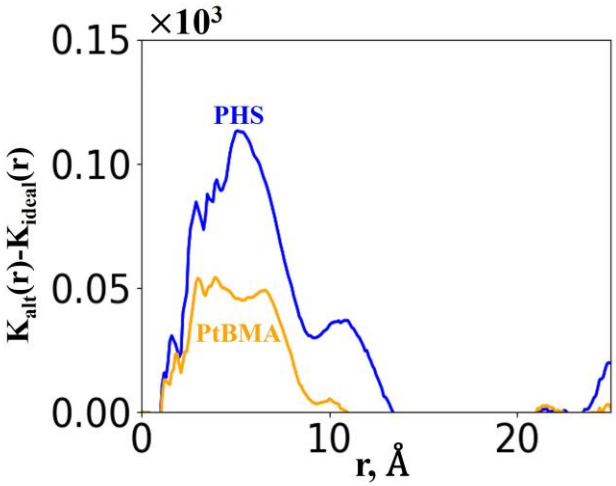

Figure S10. Ripley's K-function analysis for PHS (blue) and PtBMA (light orange) segments in the alternating copolymer. The effective K values are estimated relative to ideal scenario where the atoms are homogenously distributed.

9 End-to-end distance of PHS and PtBMA segments in blend and diblock copolymer systems

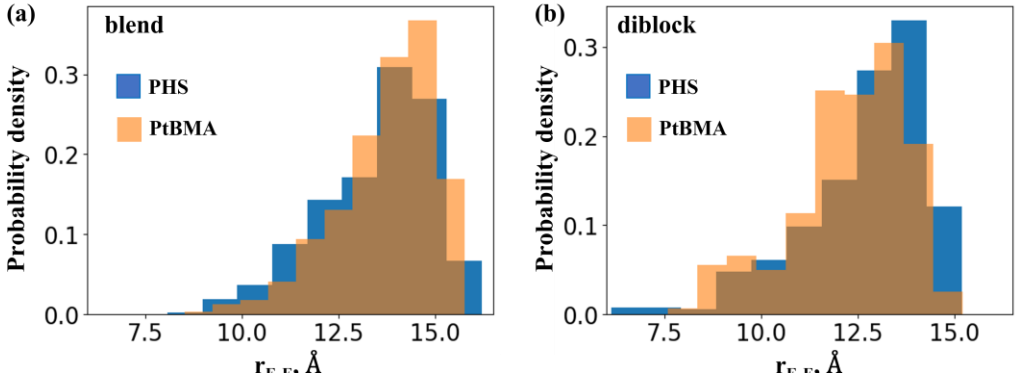

Figure S11. End-to-end distance, $r_{E\text{-}E}$ of PHS and PtBMA segments in (a) blend and (b) diblock copolymer systems. The average $r_{E\text{-}E}$ is 13.5 Å for PHS and ~13.7 Å for PtBMA in the blend (a), and ~12.7 Å and 12.0 Å, in the diblock copolymer (b). The distances are calculated between the head and tail carbon atoms of the chain.

10 Hydrogen bonding between PHS segments in alternating and diblock copolymers

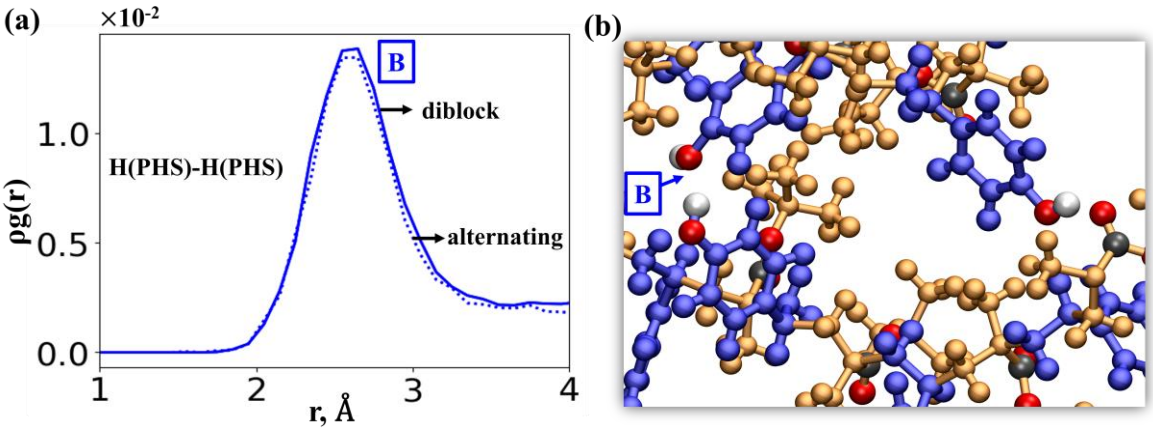

Figure S12. (a) Time averaged density, ρg(r), obtained from MD simulations between H-H atoms (blue) in phenol groups for the structure formed by diblock (solid lines), and alternating (dotted lines) copolymers at 300 K. (b) Local environment for alternating copolymer showing hydrogen bonding between phenol groups in the PHS segments (blue); functional group carbon, hydrogen, and oxygen atoms are colored gray, white, and red, respectively. The boxed letter B marks the hydrogen bonding.

11 PMF results for single and dimer ionic and nonionic PAGs at 600 K

Table S36. Numerical values of dissociation free energy (in kcal/mol) of single, $\triangle G_S$, and dimer, $\triangle G_D$, PAGs in vacuum (polymer-free medium), homopolymers, and alternating copolymer from HREX simulations. Error bars are estimated using bootstrapping technique.

$\triangle G_S$ in kcal/mol for single PAGs					
PAG chemistry	Vacuum	PS homopolymer	PtBMA homopolymer	Alternating PHS-PtBMA copolymer	PHS homopolymer
TPS-TFMeS	40.2±0.2	29.7±0.4	14.2±0.5	10.9±0.4	8.1±0.4
TPS-NFBuS	39.5±0.3	-	11.8±0.3	10.1±0.4	8.8±0.4
TPS-ATFEtS	37.8±0.4	-	11.2±0.4	9.8±0.3	8.8±0.3
$\triangle G_D$ in kcal/mol for dimer PAGs					
PAG chemistry	Vacuum	PS homopolymer	PtBMA homopolymer	Alternating PHS-PtBMA copolymer	PHS homopolymer
TPS-TFMeS	13.3±0.4	8.9±0.4	4.9±0.3	1.2±0.4	0.63±0.3
TPS-NFBuS	13.5±0.3	-	4.6±0.3	2.8±0.3	1.45±0.3
TPS-ATFEtS	14.6±0.4	-	5.5±0.2	3.4±0.3	2.5±0.3
Nonionic naphthalimide	3.5±0.3	-	0.0±0.3	0.4±0.3	0.58±0.3

A. Dissociation free energy profiles and simulation snapshots of single ionic PAGs at 600 K in vacuum

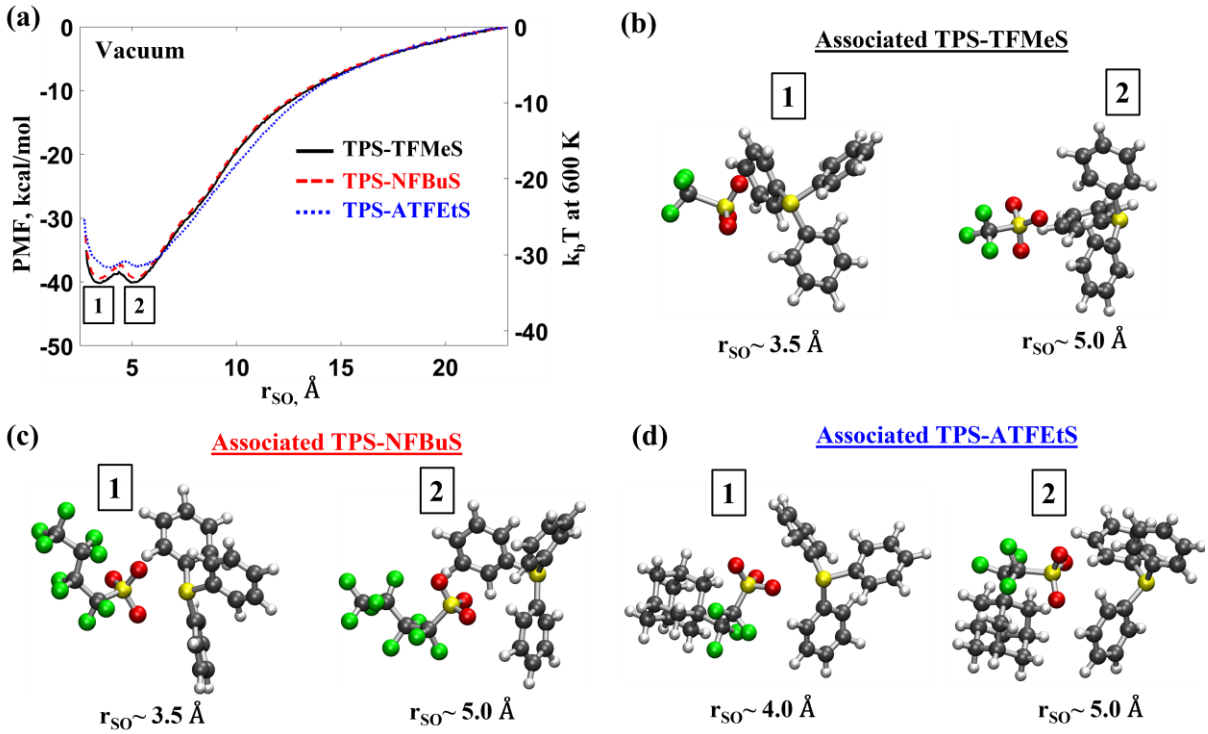

Figure S13. (a) PMF in kcal/mol and k_bT at 600K for dissociation of single ionic TPS-TFMeS (black solid line), TPS-NFBuS (red dashed line), and TPS-ATFEtS (blue dotted line) PAGs in vacuum. r_{so} is the distance between TPS sulfur and center of mass of oxygen atoms in the sulfonate anion. (b-d) Snapshots of the associated PAG configuration with r_{so} corresponding to the minimum of first and second potential wells. The boxed numbers 1 and 2 indicate the potential wells in (a) and the corresponding PAG configurations in (b-d). Note that the difference in PMF values between states 1 and 2 is less than 0.5 kcal/mol. Atom colors: carbon = gray, hydrogen = white, sulfur = yellow, oxygen = red, and fluorine = green.

B. Dissociation free energy profiles and simulation snapshots of dimer ionic and nonionic PAGs at 600 K in vacuum

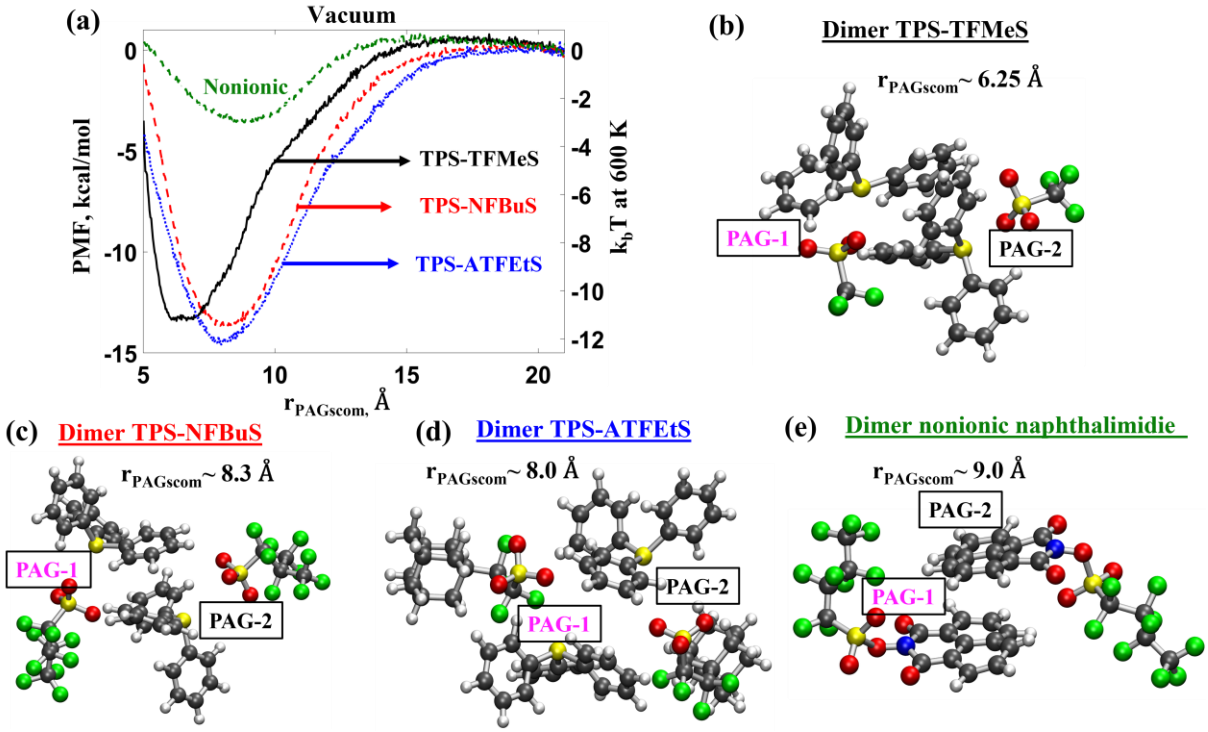

Figure S14. (a) PMF in kcal/mol and k_bT at 600K for dissociation of dimer ionic TPS-TFMeS (black solid line), TPS-NFBuS (red dashed line), and TPS-ATFEtS (blue dotted line), and nonionic naphthalimide PAGs in vacuum. $r_{PAGscom}$ is the center of mass distance between associated PAG-1 and PAG-2. (b-e) Snapshots of the dimer PAG configurations. For the ionic PAGs, the r_{so} values for PAG-1 and PAG-2 correspond to the minimum of the first potential wells. Atom colors: carbon = gray, hydrogen = white, sulfur = yellow, oxygen = red, fluorine = green, nitrogen = blue.

C. Dissociation free energy profiles for single and dimer ionic PAGs at 600 K in homopolymer and copolymer media

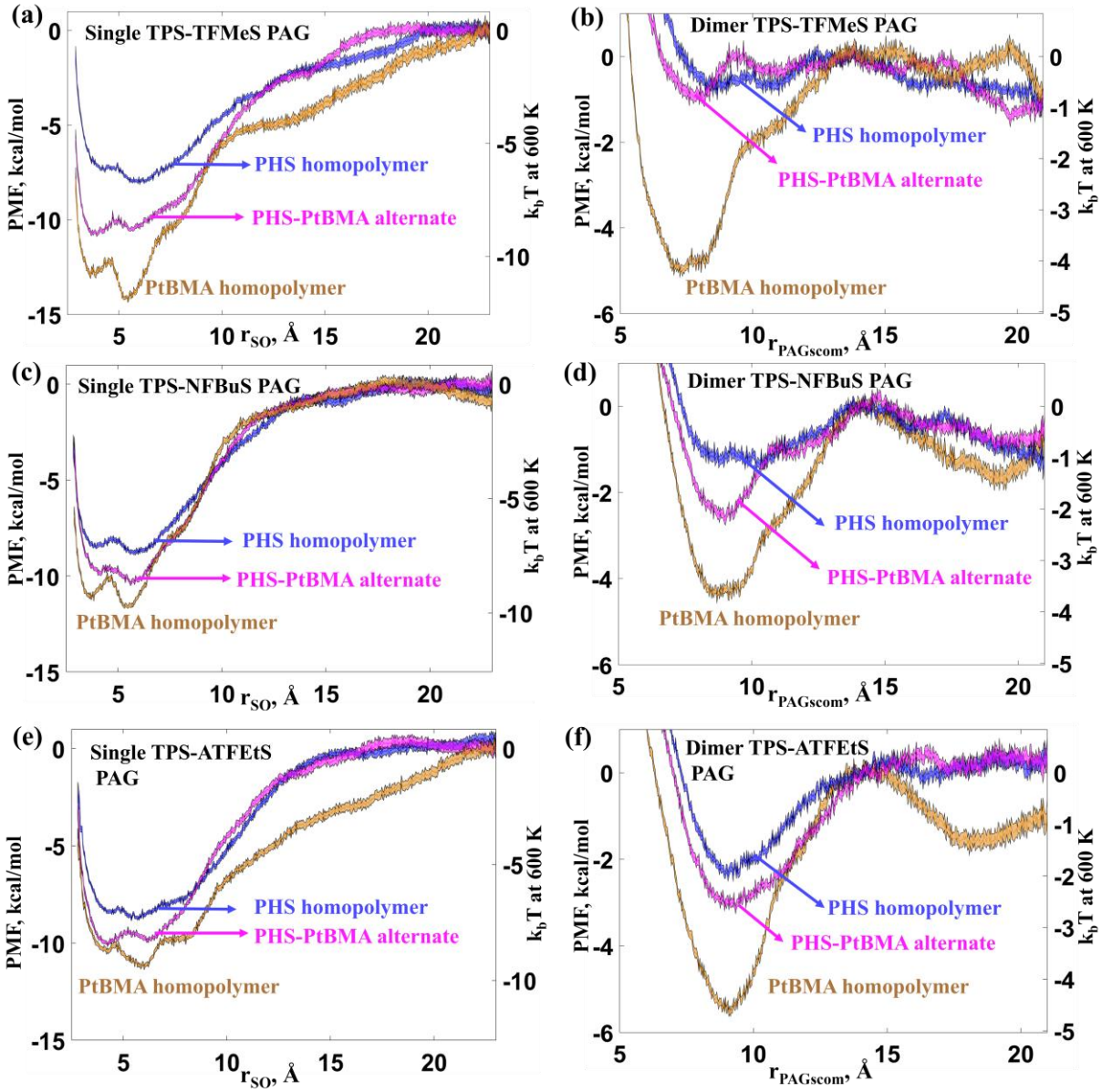

Figure S15. PMF profiles in kcal/mol and k_bT at 600K for dissociation of single and dimer PAGs. (a,b) TPS-TFMeS, (c,d) TPS-NFBuS, and (e,f) TPS-ATFEtS in PHS (blue) and PtBMA (orange) homopolymers, and alternating copolymer (magenta). The shaded regions represent the error bars.

Table S37. Approximate r_{so} values at the first, r_{FW} (Å) and second, r_{SW} (Å) well minima from the single ionic PAG PMFs in Figs. S13, S15, and S20. Note that difference in PMF values between r_{FW} and r_{SW} is less than 1.5 kcal/mol.

PAG chemistry	Vacuum		PS homopolymer		PtBMA homopolymer		Alternating PHS-PtBMA		PHS homopolymer	
	r_{FW} (Å)	r_{SW} (Å)	r_{FW} (Å)	r_{SW} (Å)	r_{FW} (Å)	r_{SW} (Å)	r_{FW} (Å)	r_{SW} (Å)	r_{FW} (Å)	r_{SW} (Å)
TPS-TFMeS	3.5	5.0	3.56	5.2	3.62	5.25	3.65	5.5	4.2	6.0
TPS-NFBuS	3.5	5.1	-	-	3.63	5.5	4.2	5.6	4.0	5.8
TPS-ATFEtS	3.9	5.3	-	-	4.2	5.85	4.3	6.2	4.5	6.0

Table S38. Approximate $r_{PAGscom}$ (Å) values at the first well minimum from the dimer ionic and nonionic PAG PMFs in Figs. S14, S15, and S20. Simulations were not performed for the unfilled columns under PS homopolymers.

PAG chemistry	Vacuum	PS homopolymer	PtBMA homopolymer	Alternating PHS-PtBMA	PHS homopolymer
TPS-TFMeS	6.25	7.0	7.0	8.0	0
TPS-NFBuS	8.15	-	9.0	9.0	9.0
TPS-ATFEtS	8.0	-	9.0	9.2	9.2
Nonionic naphthalimide	9.0	-	0	10.0	10.0

D. Dissociation free energy profiles for dimer nonionic PAGs and preferred orientations between associated dimer PAGs at 600 K in homopolymer and copolymer media

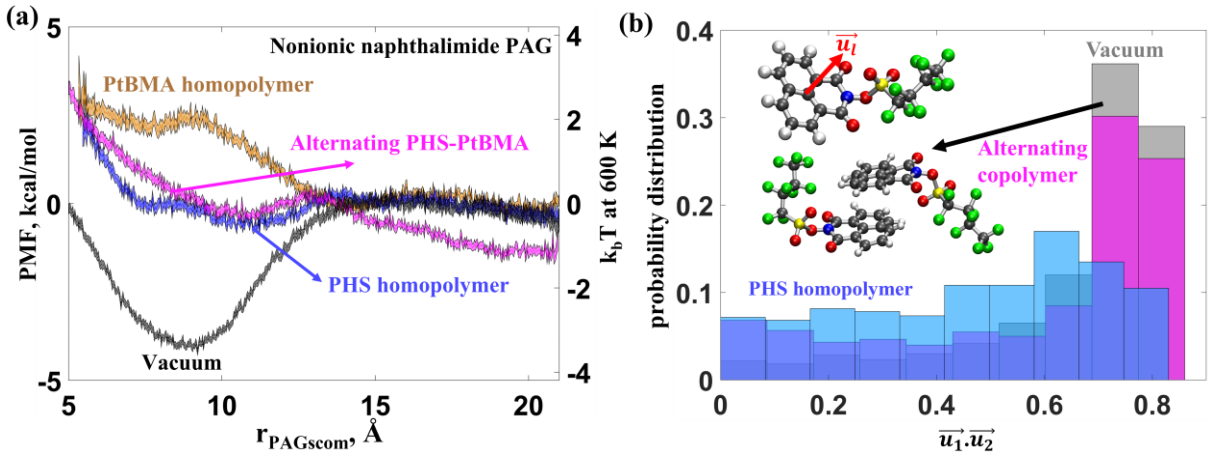

Figure S16. (a) PMF profiles in kcal/mol and k_bT at 600K for dissociation of dimer nonionic naphthalimide PAG in PHS and PtBMA homopolymers and alternating copolymer. (b) Probability distribution of the relative orientations between the dimer PAGs in vacuum, alternating copolymer, and PHS homopolymer mediums. $\overrightarrow{u_l}$ (l = 1 or 2) is the unit vector perpendicular to the naphthalimide rings. The statistics are obtained at PMF minima where r_{PAGcom} is 9 Å for vacuum and 10 Å for both alternating copolymer and PHS homopolymer.

E. Probability distribution of the nearest distances from the anion and cation of the single associated PAG to the PHS and PtBMA functional groups

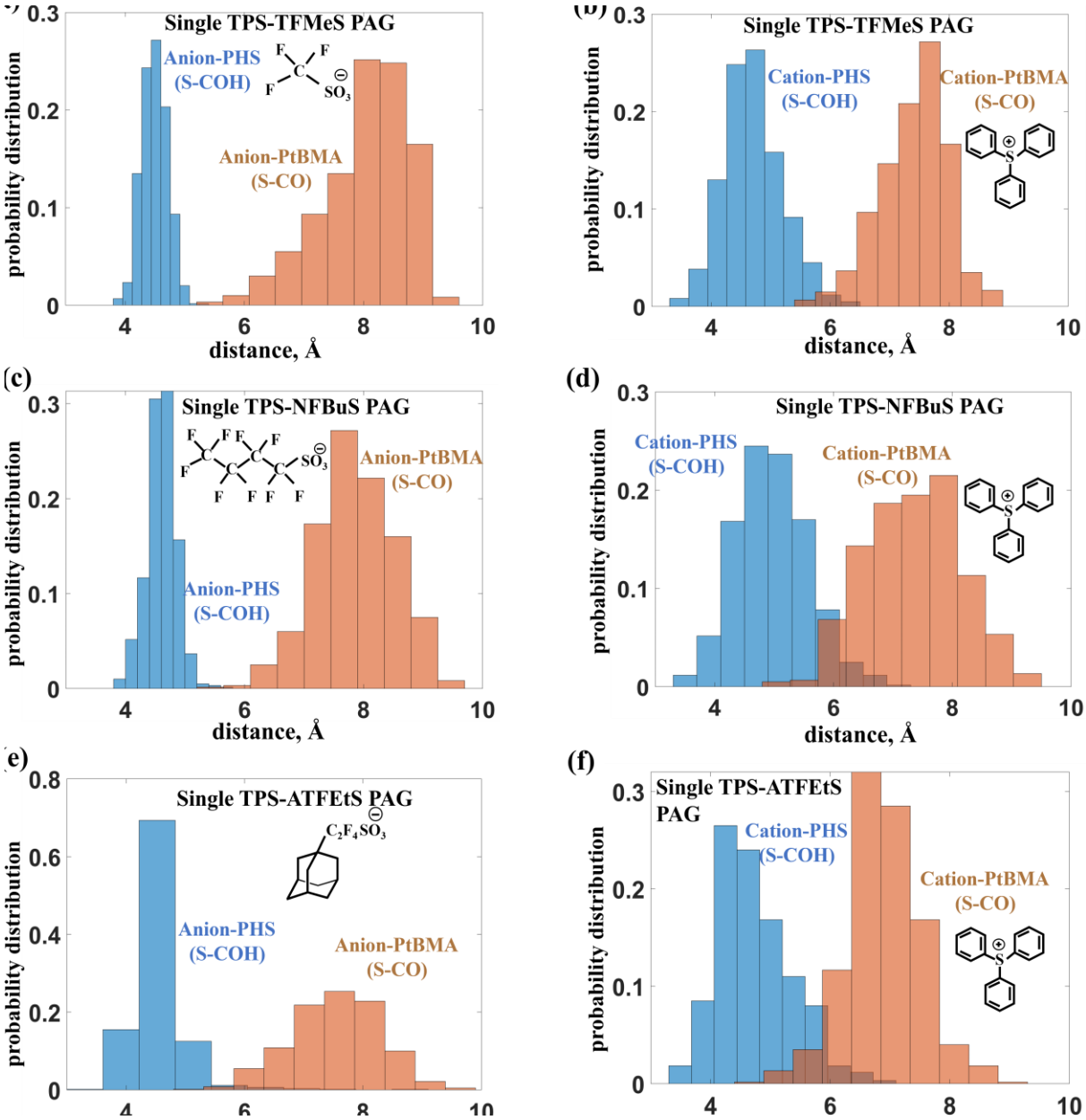

Figure S17. Probability distribution of the closest distances from the sulfur atoms in anion and cation to the phenol (blue) and carbonyl (light orange) functional groups in the alternating copolymers. The calculations correspond to single associated TPS-TFMeS, TPS-NFBuS, and TPS-ATFEtS PAGs where the r_{so} distance is 3.6-4.3 Å (position of first PMF well shown in Figure S14 and Table S37).

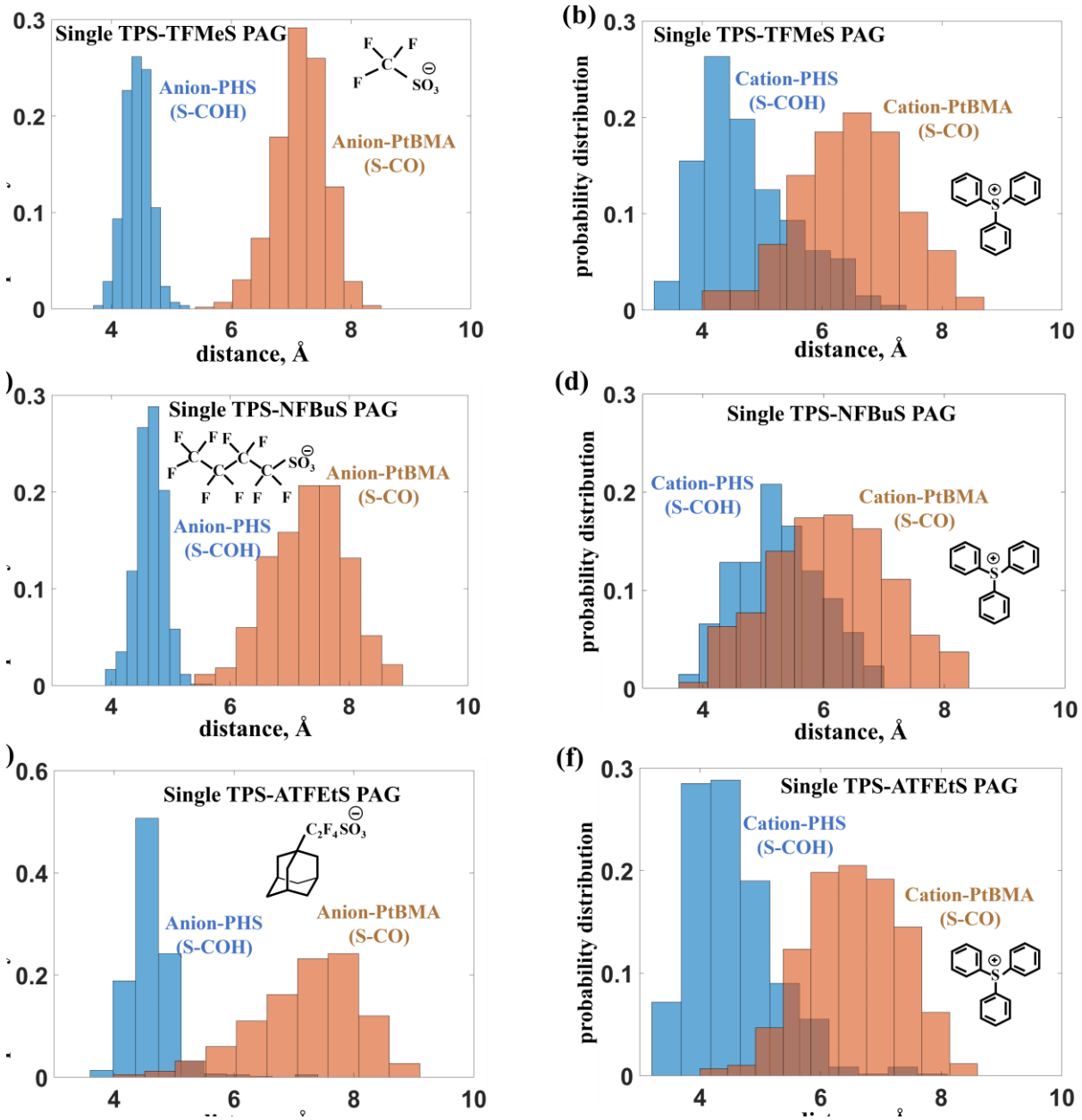

Figure S18. Probability distribution of the closest distances from the sulfur atoms in anion and cation to the phenol (blue) and carbonyl (orange) functional groups in the alternating copolymers. The calculations correspond to single associated TPS-TFMeS, TPS-NFBuS, and TPS-ATFEtS PAGs where the r_{so} distance is 5.5-6.2 Å (position of second PMF well shown in Figure S14 and Table S37).

F. Solvation density of PHS and PtBMA atoms around associated dimer PAGs

We analyzed the spatial densities of PHS and PtBMA segments excluding the hydrogen atoms connected to carbon in the alternating copolymer at different radial distances, *r*, from the center of mass (COM) of dimer associated PAG states (see Figure S19). We observed that the effective interaction distance between dimer PAG and the polar PHS segments is larger compared to that for the smaller TPS-TFMeS PAG case. This is confirmed by the decrease in density of PHS segments in the first solvation shell ($r < 10$ Å) as compared to the TPS-TFMeS PAG case. The change in PtBMA solvation density is evident where more PtBMA atoms populate at solvation distances less than 8.5-9.0 Å for TPS-NFBuS and TPS-ATFEtS as compared to the TPS-TFMeS (see Figs. S19a and S19b).

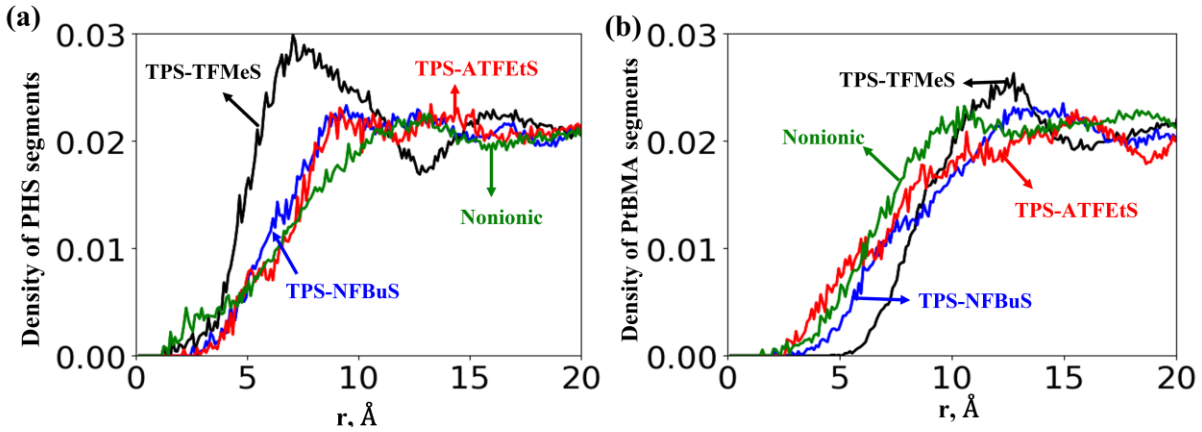

Figure S19. Density of (a) PHS and (b) PtBMA atoms away from the center of mass of dimer associated TPS-TFMeS, TPS-NFBuS, TPS-ATFEtS, and nonionic PAGs.

G. Dissociation free energy profiles for TPS-TFMeS PAG at 600 K in vacuum, PS and PtBMA homopolymer mediums

To validate the PMF methodology, we compared the dissociation free energy of single and dimer TPS-TFMeS PAG in vacuum, and in both PS and PtBMA homopolymers. As expected, we observed that the dissociation barrier increases with decreasing polarity (or dielectric constant) of the medium.

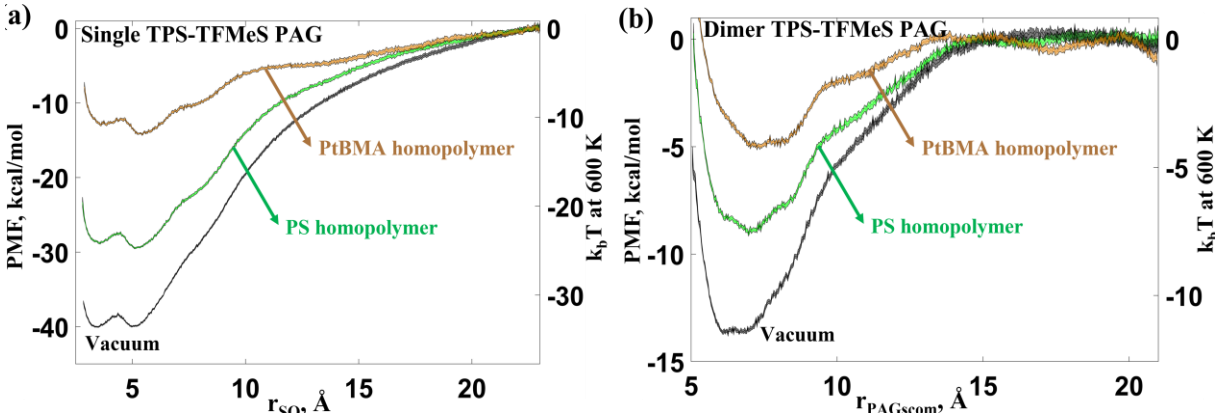

Figure S20. PMF profiles in kcal/mol and k_bT at 600 K for dissociation of single, $\triangle G_S$, and dimer, $\triangle G_D$, TPS-TFMeS PAG in vacuum (black), PS (green), and PtBMA (orange) homopolymers. The shaded regions represent the error bars.

H. Estimating Dipole moment of single associated TPS-TFMeS PAG in explicit alternating copolymer medium

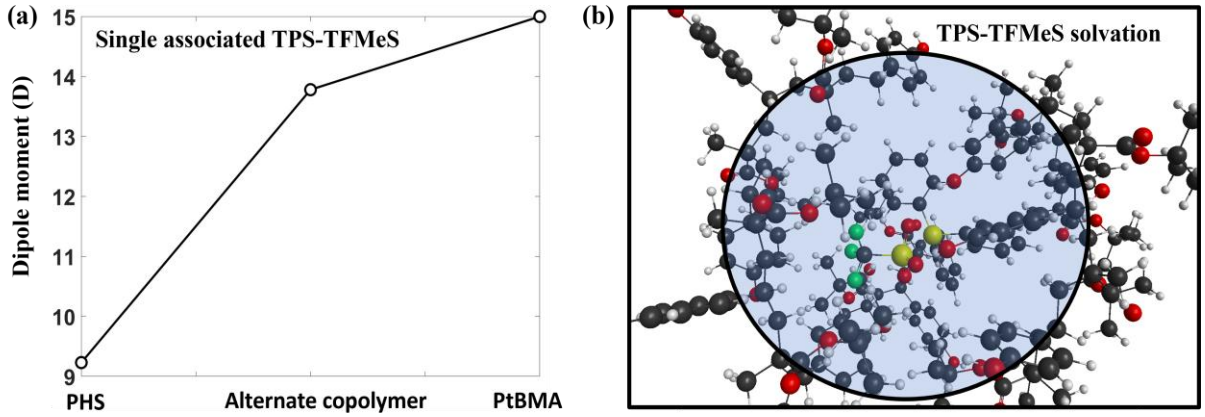

Figure S21. (a) Variation of the dipole moment, D for associated TPS-TFMeS PAG system in explicit alternating copolymer. (b) Configuration showing associated TPS-TFMeS PAG (circled) solvated by PHS and PtBMA segments. Atom colors: carbon = gray, hydrogen = white, sulfur = yellow, oxygen = red, and fluorine = green.

12 Results for high concentration PAGs in homopolymer and alternating copolymer media

A. Radial density distribution function for the ionic and nonionic PAGs

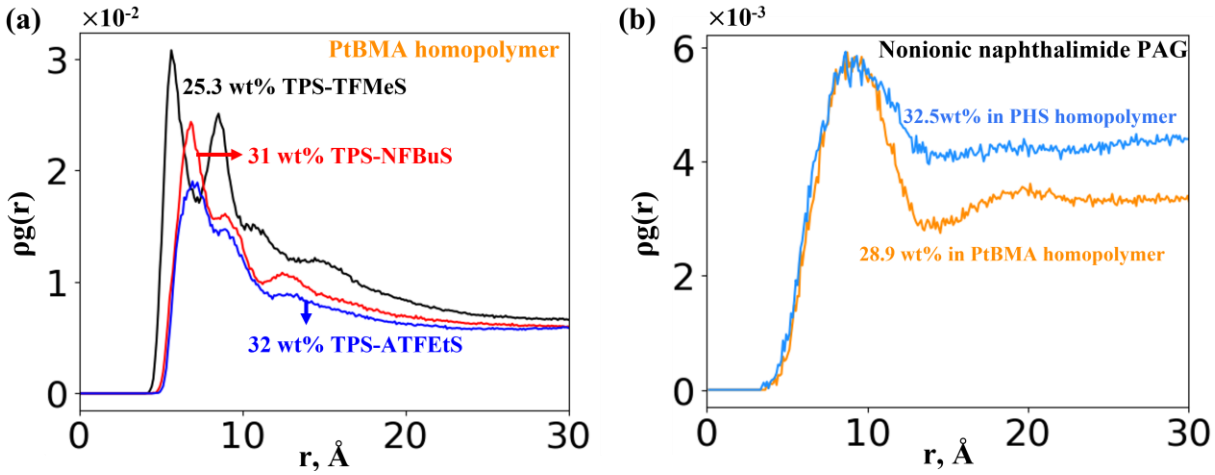

Figure S22. Time averaged density, ρg(r), of the (a) anion and cation centers of mass in PtBMA homopolymer for ionic PAGs, and (b) center of mass of nonionic naphthalimide PAG in PHS and PtBMA homopolymers. The wt% is calculated based on 200 PAGs in 140 12-mers of PHS and PtBMA.

B. TPS-ATFEtS PAG clusters in PHS and PtBMA homopolymers and alternating copolymer media

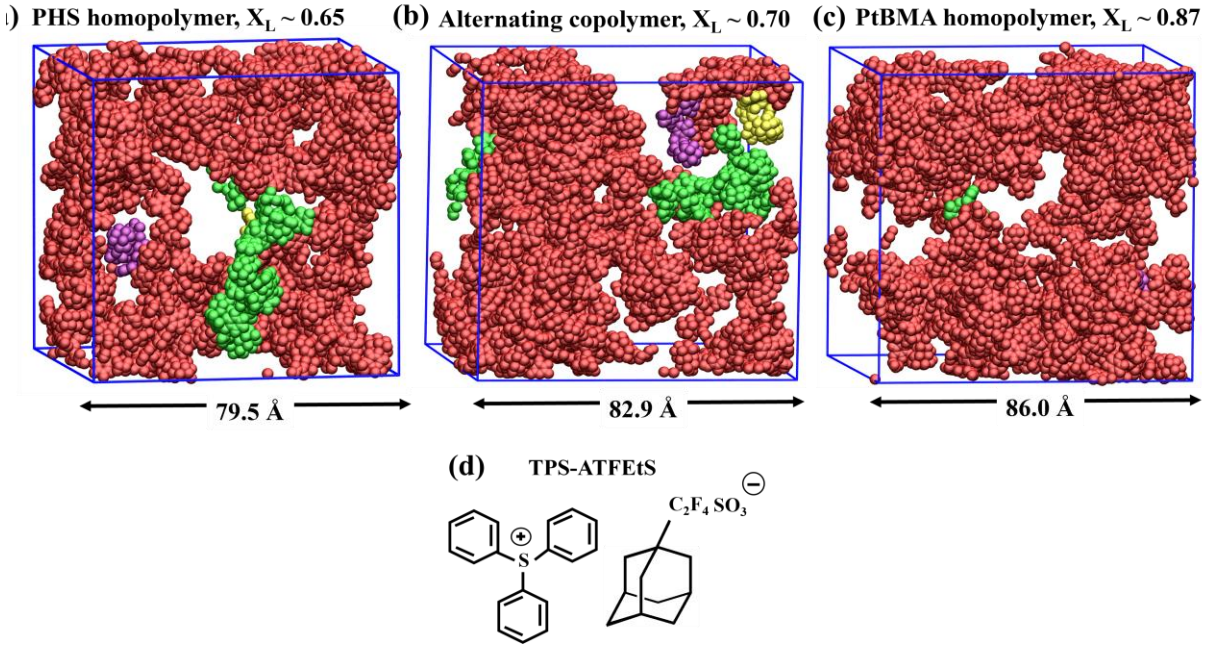

Figure S23. Representative simulation snapshots of cubic periodic box showing the first (red), second (green), third (purple), and fourth (yellow) largest PAG clusters formed in a mixture of TPS-ATFEtS PAGs in (a) PHS homopolymer, (b) alternating copolymer, and (c) PtBMA homopolymer media. The polymer chains are not shown and the corresponding TPS-ATFEtS concentrations are between 32-36wt%. The fraction, X_L, of PAGs in the first largest cluster (red) along with the simulation box dimension are also shown. (d) Chemical structure of TPS-ATFEtS PAG.

C. Phase diagrams for mixture of TPS-NFBuS PAG in PHS and PtBMA homopolymers and alternating copolymer media

To construct a phase diagram for the mixture of PAG and polymer, we start with the Flory-Huggins equation[12,13] for the mixing free energy, $\triangle F_{mix}$, of polymer solution,

$$\triangle F_{mix} = k_b T \left[\frac{\phi}{N_p} \ln \phi + (1-\phi)\ln(1-\phi) + \chi\,\phi(1-\phi)\right] \qquad (2)$$

where, k_b, ϕ, and N_p are the Boltzmann constant, composition of polymer in the mixture, and number of lattice sites occupied by each polymer chain, respectively. The Flory interaction parameter, χ is represented as: $\chi = \triangle E/k_b T$, where T is temperature, and $\triangle E$ is the difference in pairwise interaction energies between the components in a mixture and components in pure states.

The binodal phase boundary is determined by numerically solving the following equations derived from the common tangent of the free energy (Eq. 2) at polymer compositions $\phi^{\alpha 1}$ and $\phi^{\alpha 2}$ that corresponds to two equilibrium coexisting phases,[14]

$$\left(\frac{\partial \triangle F_{mix}}{\partial \phi}\right)_{\phi=\phi^{\alpha 1}} = \left(\frac{\partial \triangle F_{mix}}{\partial \phi}\right)_{\phi=\phi^{\alpha 2}} \qquad (3)$$

$$\phi^{\alpha 1}\left(\frac{\partial \triangle F_{mix}}{\partial \phi}\right)_{\phi=\phi^{\alpha 1}} - (\triangle F_{mix})_{\phi=\phi^{\alpha 1}} = \phi^{\alpha 2}\left(\frac{\partial \triangle F_{mix}}{\partial \phi}\right)_{\phi=\phi^{\alpha 2}} - (\triangle F_{mix})_{\phi=\phi^{\alpha 2}} \qquad (4)$$

The spinodal boundary is determined by equating second derivative of $\triangle F_{mix}$ to zero, leading to

$$\chi_s = \frac{1}{2}\left[\frac{1}{N_p\phi} + \frac{1}{1-\phi}\right] \qquad (5)$$

The critical points (ϕ_c, χ_c) in the phase diagram are determined by using,

$$\phi_c = \frac{1}{1+\sqrt{N_p}} \text{ and } \chi_c = \frac{1}{2}\left[\frac{1}{\sqrt{N_p}} + 1\right]^2 \qquad (6)$$

To estimate the effective N_p occupied by 12-mer PHS and PtBMA homopolymer and alternating copolymer chain, we calculate the ratio between the molar volumes of polymer chain and associated TPS-NFBuS PAG. We approximate N_p to the nearest integer value (see Table S39). Simulated polymer chain molecular weights and bulk densities of pure TPS-NFBuS PAGs, PHS and PtBMA homopolymers and alternating copolymer media at 600 K and 1 atm are also provided in Table S39. Figure S24 shows the χ *vs* PAG composition phase diagram for the homopolymers and alternating copolymer.

To construct the temperature *vs* PAG composition phase diagram, we first estimated TPS-NFBuS PAG solubility limit, X_{PAG} (vol%) from MD simulation data for different PAG loadings at 600 K (Table S39) where the X_{PAG} values correspond to concentration with 50% of PAGs present in the largest aggregated cluster. We note that the PAGs which are not part of the largest clusters also form nanocluster domains that are randomly distributed throughout the mixture. At X_{PAG}, the segregation tendency between polymer and PAG is high which indicates that the mixture is in a metastable state between the binodal and spinodal boundaries of the two-phase region. For concreteness, we assume that the X_{PAG} estimated from the MD data approximates the onset of the spinodal region in the phase diagram (see points 1, 2, and 3 in Figure S24a). Using this assumption, we estimated $\triangle E$ at 600 K from: $\triangle E = \chi_s k_b T$, where χ_s is the spinodal interaction parameter corresponding to X_{PAG} in different polymer media (see Table S39 for values). We then construct the temperature-composition phase diagram by extrapolating the estimated fit parameter for different temperatures.

Table S39. Physical properties and parameters estimated at 600 K for constructing phase diagram for mixture of TPS-NFBuS PAG in PHS and PtBMA homopolymers and alternating copolymer media. k_b= 0.0019858 kcal/ (mol K). Densities (g/cc) and PAG solubility limit, X_{PAG} (vol%) are obtained from simulations. χ_s is the spinodal interaction parameter corresponding to X_{PAG} values.

Polymer/PAG	Density (g/cc)	Molecular weight (g/mol)	N_p	X_{PAG} (vol%)	χ_s	$\triangle E$ (kcal/mol)
PHS	0.974	1471.9	3	29	1.96	2.33
Alternating copolymer	0.923	1604.2	4	22	2.43	2.90
PtBMA	0.844	1736.4	5	15	3.45	4.11
TPS-NFBuS	1.267	562.5	-	-	-	-

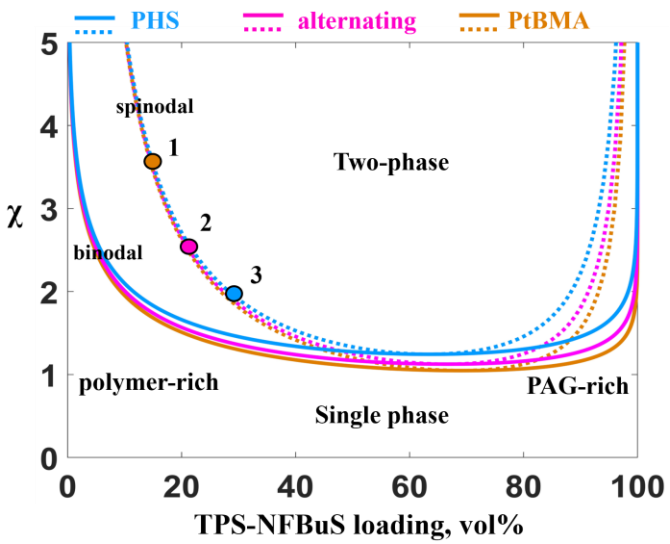

Figure S24. Phase diagrams estimated from Flory-Huggins theory, showing variation of interaction parameter, χ for different TPS-NFBuS PAG loadings (wt%) in PHS and PtBMA homopolymers, and alternating copolymer media. State points 1 (PtBMA), 2 (alternating), and 3 (PHS) correspond to the PAG solubility limit, X_{PAG} estimated from MD simulations at 600 K.

D. Hydrogen bonding interactions in alternating copolymer at high PAG concentration MD simulations at 600 K

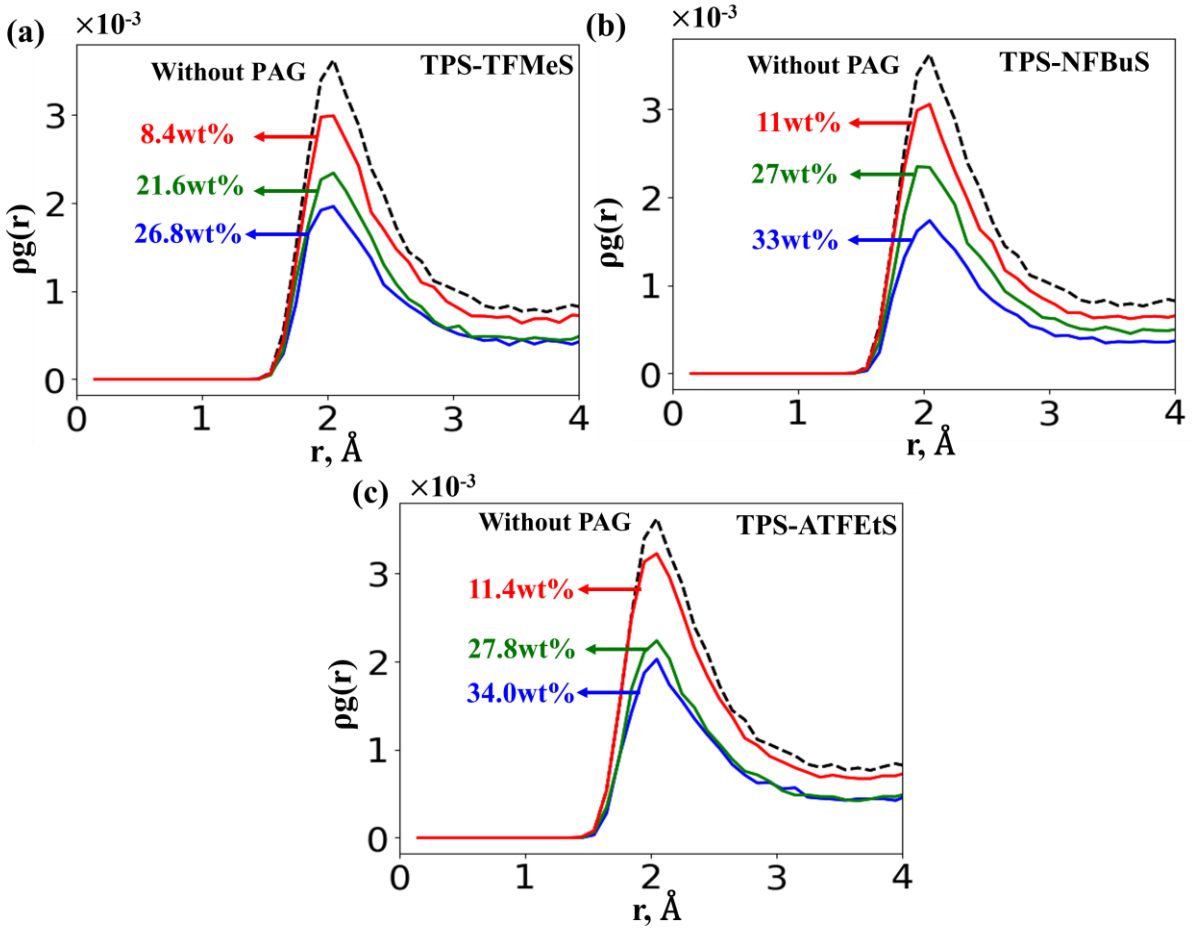

Figure S25. Variation in density, ρg(r), of hydrogen bonding interactions between hydroxyl and carbonyl groups in alternating copolymer medium with (solid lines) and without (dashed lines) (a) TPS-TFMeS, (b) TPS-NFBuS, and (c) TPS-ATFEtS at 600 K. The corresponding PAG loadings in wt% is shown.

References

(1) Thompson, A. P.; Aktulga, H. M.; Berger, R.; Bolintineanu, D. S.; Brown, W. M.; Crozier, P. S.; in 't Veld, P. J.; Kohlmeyer, A.; Moore, S. G.; Nguyen, T. D.; Shan, R.; Stevens, M. J.; Tranchida, J.; Trott, C.; Plimpton, S. J. LAMMPS - a Flexible Simulation Tool for Particle-Based Materials Modeling at the Atomic, Meso, and Continuum Scales. *Comput. Phys. Commun.* **2022**, *271*, 108171. https://doi.org/10.1016/j.cpc.2021.108171.

(2) Jorgensen, W. L.; Maxwell, D. S.; Tirado-Rives, J. Development and Testing of the OPLS All-Atom Force Field on Conformational Energetics and Properties of Organic Liquids. *J. Am. Chem. Soc.* **1996**, *118* (45), 11225–11236. https://doi.org/10.1021/ja9621760.

(3) Chen, C.; Maranas, J. K.; García-Sakai, V. Local Dynamics of Syndiotactic Poly(Methyl Methacrylate) Using Molecular Dynamics Simulation. *Macromolecules* **2006**, *39* (26), 9630–9640. https://doi.org/10.1021/ma0610562.

(4) Price, M. L. P.; Ostrovsky, D.; Jorgensen, W. L. Gas-Phase and Liquid-State Properties of Esters, Nitriles, and Nitro Compounds with the OPLS-AA Force Field. *J. Comput. Chem.* **2001**, *22* (13), 1340–1352. https://doi.org/10.1002/jcc.1092.

(5) Dodda, L. S.; Cabeza de Vaca, I.; Tirado-Rives, J.; Jorgensen, W. L. LigParGen Web Server: An Automatic OPLS-AA Parameter Generator for Organic Ligands. *Nucleic Acids Res.* **2017**, *45* (W1), W331–W336. https://doi.org/10.1093/nar/gkx312.

(6) Jorgensen, W. L.; Tirado-Rives, J. Potential Energy Functions for Atomic-Level Simulations of Water and Organic and Biomolecular Systems. *Proc. Natl. Acad. Sci.* **2005**, *102* (19), 6665–6670. https://doi.org/10.1073/pnas.0408037102.

(7) Hanwell, M. D., Curtis, D. E., Lonie, D. C., Vandermeersch, T., Zurek, E., Hutchison, G. R. Avogadro: An Advances Semantic Chemical Editor, Visualization, and Analysis Platform. *J. Cheminform.* **2012**, *4* (1), 1–17. https://doi.org/10.1016/j.aim.2014.05.019.

(8) Dodda, L. S.; Vilseck, J. Z.; Tirado-Rives, J.; Jorgensen, W. L. 1.14∗CM1A-LBCC: Localized Bond-Charge Corrected CM1A Charges for Condensed-Phase Simulations. *J. Phys. Chem. B* **2017**, *121* (15), 3864–3870. https://doi.org/10.1021/acs.jpcb.7b00272.

(9) Canongia Lopes, J. N.; Pádua, A. A. H. Molecular Force Field for Ionic Liquids Composed of Triflate or Bistriflylimide Anions. *J. Phys. Chem. B* **2004**, *108* (43), 16893–16898. https://doi.org/10.1021/jp0476545.

(10) Gouveia, A. S. L.; Bernardes, C. E. S.; Tomé, L. C.; Lozinskaya, E. I.; Vygodskii, Y. S.; Shaplov, A. S.; Lopes, J. N. C.; Marrucho, I. M. Ionic Liquids with Anions Based on Fluorosulfonyl Derivatives: From Asymmetrical Substitutions to a Consistent Force Field Model. *Phys. Chem. Chem. Phys.* **2017**, *19* (43), 29617–29624. https://doi.org/10.1039/C7CP06081E.

(11) Kumar, S.; Rosenberg, J. M.; Bouzida, D.; Swendsen, R. H.; Kollman, P. A. THE Weighted Histogram Analysis Method for Free-Energy Calculations on Biomolecules. I. The Method. *J. Comput. Chem.* **1992**, *13* (8), 1011–1021. https://doi.org/10.1002/jcc.540130812.

(12) Flory, P. J. Thermodynamics of High Polymer Solutions. *J. Chem. Phys.* **1942**, *10* (1), 51–61. https://doi.org/10.1063/1.1723621.

(13) Huggins, M. L. Solutions of Long Chain Compounds. *J. Chem. Phys.* **1941**, *9* (5), 440–440. https://doi.org/10.1063/1.1750930.

(14) Qian, D.; Michaels, T. C. T.; Knowles, T. P. J. Analytical Solution to the Flory–Huggins Model. *J. Phys. Chem. Lett.* **2022**, *13* (33), 7853–7860. https://doi.org/10.1021/acs.jpclett.2c01986.